A320-HACK Final Report

Hydrogen Assisted Combustion of Kerosene

Design Synthesis Exercise

Group 11

Delft University of Technology

TU Delft

(This page was left blank intentionally)

A320-HACK Final Report

Hydrogen Assisted Combustion of Kerosene

by

Group 11

Student Name	Student Number
Coelho Antunes, Sofia	4886747
De Hauwere, Tota	4551699
Gheorghe, Nico	4853245
Giobbio, Martino	4814096
Homola, Marek	4828542
Nikitin, Mikhail	4855418
Sequeira Raposeiro, Sara	4827554
Urzica, Elena	4835573
van Stuyvesant Meijen, Johan	4794141
Vemulapalli, Datta	4447441

Coordinator: Dr. Arvind Gangoli Rao
Coaches: Dr. Ivan Langella
MSc Flavio Domingos de Azevedo Quadros
Maleen Hiestermann
Teaching Assistant: Tristan Hamers
Institution: Delft University of Technology
Place: Faculty of Aerospace Engineering, Delft

Project Duration: April, 2021 - July, 2021

TU Delft Delft University of Technology

Preface

This report was written by ten Aerospace Engineering students at TU Delft, during the ten-week final BSc project *Design Synthesis Exercise*. The goal of the team is to design the A320-HACK - a more environmentally friendly successor of the A320neo - by implementing a hybrid propulsion system, based on hydrogen assisted combustion of kerosene.

While writing the current report, it was assumed that the reader has a basic knowledge of aircraft systems. Readers interested in the general problem that is tackled in this report and in the proposed solution, will find these from Chapter 2 to 8. Readers with a larger interest on the technical design aspects of the A320-HACK subsystems, will find these from Chapter 11 to 13. Readers interested in the actual impact of the A320-HACK on different levels, as well as in the eventual next phases of the project, will find these from Chapter 14 to 21.

We would like to thank our coordinator Dr. Arvind Gangoli Rao and coaches Dr. Ivan Langella, Ir. Flavio Domingos de Azevedo Quadros, and Maleen Hiestermann for their support. In addition, we would like to thank our teaching assistant Tristan Hamers for his advice.

Group 11
Delft, June 2021

Executive Summary

The aviation industry is one of the top 10 contributors towards the global emissions that promote global warming and climate change. In addition, the increasing popularity and affordability of air transport is set to result in the growth of not just the industry, but also its share of global emissions. Thus, the aviation industry needs to become more sustainable in order to contribute to climate change mitigation. The A320-HACK project has as objective, the design of a more sustainable yet market competitive successor of the Airbus A320neo, using Hydrogen Assisted Combustion of Kerosene. The HACK system has as a primary strength the reduced emissions due to lower hydrocarbon combustion products resulting in lower greenhouse gas (GHG) emissions. However, this system brings along challenges regarding onboard hydrogen storage. Nonetheless, the apparent challenge of onboard hydrogen storage, offers opportunities to reduce the emissions further by replacing the former kerosene-combustion auxiliary power unit (APU) system with a fuel cell dedicated power unit (DPU). Ensuring that these technologies are economically and technically feasible by the year 2035, when the A320-HACK is set to enter into service, are the challenges that were tackled. The proposed solutions are detailed in the subsequent sections.

Detailed A320-HACK Design

Liquid hydrogen (LH_2) was chosen as the optimal storage state considering criteria such as energy density, refuelling possibilities, structural weight, cost and the requirement that at most 1/3 of the energy stored onboard the A320-HACK must be provided by hydrogen. The maximum LH_2 volume and mass stored onboard the HACK is 33.54 m^3 and 2,385 kg respectively. From the available LH_2 volume and the aim to reduce emissions, it was determined that only hydrogen would be used as fuel for the idle, taxi out and taxi in phase, both in the HACK system of the main engines, as well as in the DPU. In the flight phases (climb, cruise, and descent), the mass split of the LH_2 and kerosene fuels is 14% and 86%. This results in the following differences in emissions during the landing and take-off (LTO) cycle, and cruise phase:

Table 1: Comparison between the cruise and LTO emissions of A320-HACK compared to A320neo.

Species	CO_2	CO	H_2O	NOx	$Soot$	UHC
Cruise Differences [%]	-70.9	-95.7	+19	-40.9	-61.4	-61.4
LTO Differences [%]	-92.2	-95.5	+8.9	-79.4	-98.8	-89.7

The engines of A320-HACK were modified with respect to the LEAP-1A engine option of the A320neo in multiple ways. Firstly, for cruise, the bypass ratio was increased from 11.1 to 15.8. Additionally, the engine is now geared, meaning that it requires fewer compressor and turbine stages. By being a geared turbofan the fan's pressure ratio can be reduced which is beneficial for the engine's duct efficiency but requires the duct nozzle to have a variable area. Lastly, the fuel injection system relies on the Lean Direct Injection concept, which reduces NO_x emissions by lowering the peak flame temperature.

The original Auxiliary Power Unit of the A320neo was changed to a Dedicated Power Unit (DPU) consisting of a proton-exchange membrane fuel cell (PEMFC). The DPU provides a power of 400 kW for the whole aircraft. To be able to deliver this amount of power, the DPU consisted of PEMFC and a battery to assist when needed. The PEMFC will operate at 90 $°C$ using pressurised cabin air, have a voltage of 1200 V and a current of 333 A. The PEMFC has a battery to assist when needed. It consists of 325 battery cells in series and 30 cells in parallel, resulting in a total of 9750 cells. It can store 320 MJ of energy and has a mass of 296 kg. Both the PEMFC and battery need water cooling. The PEMFC will use bipolar plates with a serpentine flow layout and the battery cooling system is based on the Tesla model S battery cooling system. The whole system costs about €20,000 which is only 5% of the cost of the A320neo APU. With respect to the original APU, the new DPU system is also 300% more efficient and 70% quieter. However, it weights 4.4 times more and cover 9.8 times more volume.

Another change introduced by the HACK system are the new liquid hydrogen storage tanks and fuelling system. It was chosen to store the LH_2 in wing podded tanks, mounted on top of the main wing. This solution allows for a safe storage of the hydrogen, far from passengers and the ground. It also permits to maintain the fuselage similar to the original A320neo, thereby reducing developments costs and necessary investments. The tanks will have an aluminium Al-2090-T81 double-walled structure, with a multi-layer insulation system used as thermal protection, and are designed as cylinders with spherical caps. The drawback of this design is the drag penalty introduced by the tanks, estimated to increase the cruise drag by 7.68 % compared to A320neo. The final layout of the plane new systems is shown in Figure 1.

Operations & Logistics

Introducing hydrogen in a complex industry such as commercial aviation requires to analyse the implications in terms of operations and infrastructure. The A320-HACK will retain the same turnaround time of the A320neo, equal to 44 min. This is based on the projection that in the next decade, LH_2 technology will allow for a refuelling rate in the order of 1000 L/m, comparable to the current one for kerosene.

An operations and logistics plan needs to be tailored to each airport. For this project, the Rotterdam The Hague airport is used as a case study. The proximity of the Rotterdam The Hague airport to the port of Rotterdam means that the airport can rely on the port's plan to fully execute the "Hydrogen backbone" plan that would see itself being a source of 2.25 GW green hydrogen electrolyser and a terminal for the import of overseas green/blue liquid hydrogen. This is particularly handy because the liquefaction of the hydrogen in the airport vicinity alone presented several challenges. The excessive investment of €90 million and a need for 11 GWh green energy per year at inception in 2035, a further 31 GWh by the end of 2050, are required for liquefaction alone. Therefore, based on the forecasts for the LH_2 to be used at the airport, which is equivalent to 1.5 truck loads a day in 2035 and 8 truck loads per day in 2050, outsourcing of liquid hydrogen would be ideal for the case study.

Costs

The A320-HACK has an estimated development cost of around €2.8 billion, and a production cost of €100.3 M per aircraft, which is 14.2 % higher than for the A320neo. The aircraft will be listed at

€ 103.6. The break-even point of the program will be reached in the year 2041, after 848 aircraft have been sold by Airbus. Airliners can expect a maximum increase in operational costs per block hour of 11% compared to the A320neo when using blue hydrogen. For a fleet of 10 aircraft per airliner, a cost of € 6.58 billion is expected over the lifetime of this fleet.

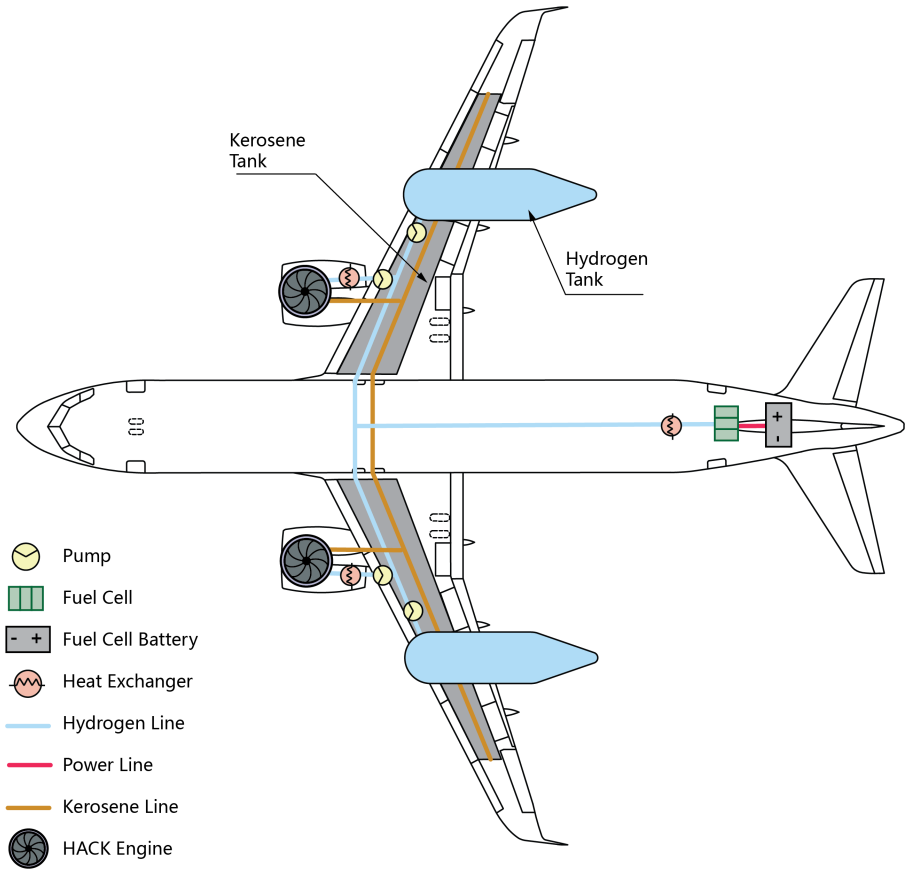

Figure 1: Propulsion system architecture of the A320-HACK

Contents

1 | Introduction

With the rise in globalization and the resulting development in sectors such as international trade and tourism, the air transport is becoming increasingly important. However, besides being of immense value for the modern world, the rapid growth in the number of aircraft in operation results also in several negative consequences. Air transport largely contributes to the emission of greenhouse gases, such as CO_2 and NO_x, to the extent that "someone flying from Lisbon to New York and back generates roughly the same level of emissions as the average person in the EU does by heating their home for a whole year"[1]. As these gases result from the combustion in jet engines, a lot of effort is invested in developing novel technologies with the aim of increasing the efficiency of propulsion units. However, the current designs are already highly optimized and their efficiencies nearly reach the theoretical maximum values. This makes it difficult to increase the efficiency of engines by more then 1-2% per year[2], which is by far not sufficient to compensate for a much faster increasing use of aircraft. Therefore, a more radical solution is required, possibly transforming the conventional engine technology entirely.

One of the candidates for such a transition are electric motors. However, although electricity can support small aircraft, it is currently infeasible for larger airplanes as large and heavy batteries would be required to be carried on-board. As a consequence, combustion engines are still seen as a more viable option for this type of aircraft and efforts are rather put into investigating alternative fuels. A strong candidate among these is hydrogen, as it offers a high energy content and it is producible through green methodologies. Although hydrogen has a potential of shaping the future aviation, the current technology and infrastructure is not entirely ready to support the transition to this fuel. One of the strategies to approach this challenge is to make this transition gradual rather than abrupt.

For this reason, a team of 10 students of Aerospace Engineering at Delft University of Technology is investigating the feasibility of the transition from kerosene to hydrogen fuel in civil aviation. Their task is to design the successor of the A320neo implementing a hybrid propulsion system, based on the combination of hydrogen and kerosene. The team will not only look into the design of the aircraft, but also into the extent of the required changes in the infrastructure.

This document constitutes the final report, the last from a series written during the project. This document is divided in three main parts: the first one analyses the problem that is aimed to be tackled and proposes a solution. The second part is concerned with the actual design of the proposed concept; in more detail, the engines, the fuel system, the wing and the Dedicated Power Unit (DPU) design processes are described. Lastly, the third part investigates the impact of the proposed concept from various standpoints and gives an outlook to the eventual next phases of the project.

Part I

Problem Analysis & Solution

[1] https://ec.europa.eu/clima/policies/transport/aviation_en, accessed:19-May-2021

[2] https://www.iata.org/en/programs/ops-infra/fuel/fuel-efficiency/, accessed:19-May-2021

2 | Problem Analysis

This chapter states problem analysed and briefly describes the proposed solutions concerning the fuel used, the propulsion method of the main engine, and the redesign of the auxiliary power unit.

2.1 Problem Statement

The increasing popularity and affordability of air transportation is leading to the growth of this industry and to an increasing share of this sector to the global human-kind emissions. The A320-HACK (Hydrogen Assisted Combustion of Kerosene) project aims to implement a hydrogen and kerosene hybrid system to a single-aisle aircraft, resulting in a market competitive option to the A320neo. This is captured by the Mission Need Statement and the Project Objective Statement.

Mission Need Statement: Contribute to climate change mitigation through the aviation sector.

Project Objective Statement: Design the A320-HACK, a more sustainable yet market competitive successor of the Airbus A320neo utilizing Hydrogen Assisted Combustion of Kerosene, in a team of 10 students within 10 weeks.

2.2 Proposed Solution

Three main functional choices were made when designing the A320-HACK. Firstly, both kerosene and hydrogen are used as fuel. Secondly, the Auxiliary Power Unit is converted into a Dedicated Power Unit, providing power and compressed air during the whole mission through an hydrogen based fuel cell. Finally, the main engines solely provide thrust by using either only hydrogen or a combination of hydrogen and kerosene. These factors together will allow to achieve a 30% reduction in the climate impact of CO, NO_x, unburned hydrocarbons, and soot during cruise and a 50% decrease during the Landing and Take-off (LTO) cycle. The use of only hydrogen on ground will contribute to reaching this goal. Concerning the topology of the aircraft, wing podded engines and tanks are used.

2.2.1 Use of Hydrogen

To reduce the environmental impact of aviation, alternative energy sources must be sought. Figure 2.1 shows the specific volumetric and mass energy density for several fuels. Kerosene is good at both energy densities, while batteries are bad at both. Biofuels are somewhere in between batteries and kerosene, but their poor yield efficiency [1, 2], scalability, availability, and ethical implications pose some concerns. Hydrogen has a very high mass energy density but a rather low volumetric one. Its volume, temperature and pressure requirements for storage are quite challenging, however it is attractive for being a carbon neutral option which can be produced from renewable energy sources. Availability and scalability are not concerns either as hydrogen is the most abundant element in the universe. For these reasons, hydrogen as a fuel was integrated in this project. However, fully hydrogen aircraft requires extreme adaptations to the aircraft and the airports' infrastructure. For now it is advantageous to use hybrid systems in a synergistic way, idea elaborated upon in Section 2.2.2.

2.2.2 Hydrogen Assisted Combustion of Kerosene

Combusting hydrogen and kerosene together significantly reduces emissions. Besides, unlike fully hydrogen planes, it does not have the disadvantages of storing huge volumes of hydrogen on-board or requiring drastic infrastructure changes. The HACK follows from the Lean Direct Injection concept [3, 4], in which fuel and air are not premixed. Instead, there are multiple, co-rotating, swirler injectors, with a layout as represented in Figure 2.2. This results in high shear between the air coming out of each injector, increasing the strain rate. Hence, the flame peak temperature decreases and so thus the NO_x production. The

A320-HACK uses the central swirler for hydrogen and the outer ones for kerosene.

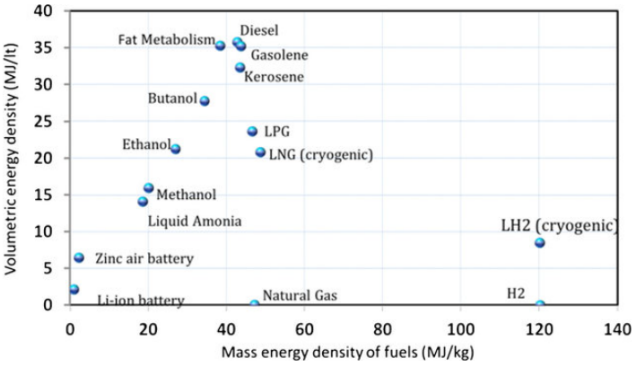

Figure 2.1: Volumetric and mass energy density for several energy sources [5]

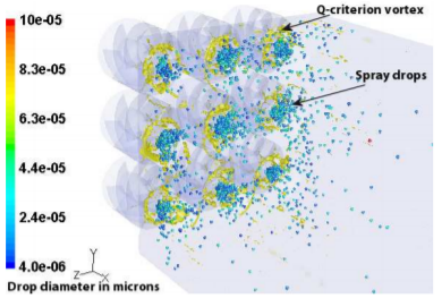

Figure 2.2: Swirler injectors of the Lean Direct Injection concept [4]

2.2.3 Fuel Cell for Dedicated Power Unit

The Auxiliary Power Unit of the A320neo, Honeywell 131-9A, is a gas generator, running on kerosene and producing 125.7 dB of noise at 1 m distance. The A320-HACK focuses on reducing emissions and so other options were considered. A Proton-Exchange Membrane fuel cell was selected. It only uses hydrogen and air to produce water vapour, thus reducing the CO_2 emissions. The fuel cell only generates 40-50 dB of noise in operation Which would reduce the noise intensity W/m^2 during idle phase by a factor of 1940.

3 | Requirements

To conduct the preliminary design of the A320-HACK, top-level requirements were established and relevant user guidelines were considered. These are categorised and presented below.

Performance

UR-PERF-01 A successor to the A320neo aircraft shall be designed with the HACK system.

UR-PERF-02 The design shall satisfy the CS25 rules [6].

UR-PROP-01 The amount of usable energy stored in H_2 shall not exceed 1/2 of the energy content in kerosene.

SR-PERF-02 The aircraft shall be able to transport 180 passengers excluding crew.

SR-PERF-03 The aircraft shall have a max fuel range of (at least) 6300 km.

Safety & Reliability

UR-SR-01 The LH_2 storage system shall store the fuel for 36 hours without boil-off at an ambient temperature of 45 °C.

UR-SR-04 The passenger evacuation time of A320-HACK shall not be greater than 90 s.

Sustainability

SR-SUST-01 The cruise emissions of NO_x, CO, unburnt hydrocarbon and soot emission shall be at least 30% lower than A320neo.

SR-SUST-02 The NO_x, CO, unburnt hydrocarbon and soot emission for the Landing and Take-Off (LTO) cycle shall be reduced by at least 50% when compared to the A320neo.

SR-SUST-04 The noise-level contour of A320-HACK shall be at most 85 dB, same as for the A320neo.

Operations, Engineering Budget & Cost

UR-OPER-01 The impact of refuelling LH_2 on the turn-around time of the aircraft shall not be more than 10 minutes.

SR-OPER-03 The engine idling and taxi process shall be performable utilising only hydrogen.

UR-COST-01 The total development cost of the aircraft shall not exceed 5 billion euros.

UR-COST-02 The production cost of the aircraft shall not exceed 15% than that of A320neo.

UR-EB-01 The entry into service of the aircraft shall be by 2035.

User Guidelines

UG-SUST-01 The supply and production of green hydrogen at the airport shall be investigated

UG-SUST-02 A life cycle analysis shall be carried out

UG-PERF-02 The aircraft refuelling and safety shall be taken into account

UG-PERF-03 The flight mechanics characteristics of the aircraft shall be evaluated

UG-SR-01 The issue of ground clearance and tail strike shall be considered

UG-SR-02 The safety of the LH_2 refuelling system shall be addressed

UG-SR-03 The storage of LH_2 at the airport shall be addressed

Part II

Problem Approach

4 | Market Analysis

This chapter will present the market analysis performed to assess the A320-HACK market positioning. Firstly, the aviation industry trends are presented, followed by a narrow-body market segment description. Finally, the A320-HACK will be analysed and information about its closest competitors will be reported.

4.1 General Trends

The aviation industry is expected to grow at a rate of 4.3% per annum, according to a global market forecast for the period 2019-2038 performed by Airbus [7]. This growing rate has been interrupted by the Covid-19 pandemic, which had disruptive effects: in April 2020, there was a decrease of 94.4% in passenger traffic, compared to April 2019. It is expected that the industry will recover to pre-pandemic levels and restart growing, although it is not fully clear in what time frame this recovery will actually take place[1]. In any case, the decreased air traffic had positive effect on the environment, due to the substantial emission reduction. The climate impact of aviation is an important aspect to consider, although the industry still only makes up around 2.5% of the global CO_2 emissions, it accounts for around 3.5% of effective radiative forcing [8]. These values will most likely continue to grow, as flight volumes increase at a rate higher than CO_2 emissions decrease[2].

The industry's evolution and eventual radical changes are determined by geopolitics and technology advancements. Currently, although a clear decarbonisation strategy is not defined[2], possibilities to reduce the emissions from the sector are being investigated, also in light of the sustainability targets set by ICAO, for instance. For example, Sustainable Aviation Fuels (SAFs) are becoming increasingly popular, and it is estimated that they could account for 75% of the total carbon emissions reduction in 2050 compared to the level in 2015[3]. Hydrogen is also very interesting as aircraft manufacturers have been researching the idea of a hydrogen combustion engine due to its high energy density. Nevertheless, due to the difficulty related to hydrogen storage and 'green' production, no hydrogen combustion aircraft has yet entered the market[4]. However, the interest is high and development are currently ongoing: for instance, Airbus is working on the ZeroE project, proposing three aircraft that are expected to enter the market from 2035. These concepts have already reached maturity in their design, and will drive innovation in the storage and handling of hydrogen technology[4].

For the time being, sustainability and emissions reduction goals are not binding, though they might be turned into laws in the future. The European Union, for example, aims at becoming carbon neutral (i.e. achieving net-zero CO_2 emissions) by 2050, and this objective could be translated into a legal obligation. This would force both airlines and aircraft manufacturers to revise their operations, in order to reduce CO_2 emissions. Currently, the European Union already requires all flights within the European Economic Area to monitor, report and verify their CO_2 emissions through the European Union Emissions Trading System CORSIA program. It has been confirmed that this program is compatible with international law and thus this means that a global regulation could be imposed[5].

In addition, airports worldwide are taking steps towards becoming more sustainable, and can start imposing their own rules regarding pollution, placing restrictions on aircraft allowed to operate in these airports. For instance, airports are already allowed to restrict airlines not conforming to noise pollution limits from operating[6]. Every ten or so years, a limit for the maximum effective perceived noise levels (EPNdB) allowed to be produced by aircraft is decreased, and aircraft that do not meet the new regulations,

[1] https://www.iata.org/en/pressroom/pr/2020-06-03-01/, accessed:28-May-2021
[2] https://ourworldindata.org/co2-emissions-from-aviation, accessed:05-May-2021
[3] https://aviationbenefits.org/environmental-efficiency/climate-action/waypoint-2050/, accessed:06-May-2021
[4] https://www.airbus.com/newsroom/stories/hydrogen-combustion-explained.html, accessed:06-May-2021
[5] https://ec.europa.eu/clima/policies/transport/aviation_en, accessed:05-May-2021
[6] https://www.loc.gov/law/help/airport-noise/regulations.php, accessed:28-May-2021

are restricted from operating in specific airports[7] [8].

4.2 Narrow-body Market Segment

Single aisle, narrow-body aircraft make up for the largest share of the market, and it is forecasted that this will exceed 56% before the end of the decade. Most of these aircraft are - and will - be used by Low Cost Carries (LCC) to operate short-haul flights. GlobalData[9] expects that the regional breakdown of the market will be as follows: Asia-Pacific will have the largest share, with 43%, Europe follows with 20.3%, North America accounts for 18.4%, the Middle East and Latin America have 8% and 7.9%, respectively, and finally Africa accounts for only 1.8%.

In more details, Airbus sold 642 aircraft of the A320 family in 2019, of which 551 were A320neo. The sales in 2020 - as a direct result of the Covid-19 pandemic - decreased by 21.8%, to 446 aircraft of the A320 family, of which 431 were A320neo. In 2020, 115 aircraft orders got cancelled as well[10]. Airbus' demand forecast for the next 20 years [7] amounts to 39,210 passenger and freight aircraft. 29,720 of these belong to the small segment, which constitutes 76% of the total deliveries. An aircraft is categorised as small when the maximum range is 3,000 *nmi*, thus the A220 and A320 families are part of this category. The majority of these new small segment airliners will go towards the Asia-Pacific region (12,765 planes) and Europe (5,760 planes). Note that this forecast was made before the Covid-19 pandemic, thus the actual numbers will most likely be lower than the estimations.

Nonetheless, another forecast - produced by Oliver Wyman - includes the effects of the Covid-19 pandemic, and estimates the total aircraft fleet in 2021 and 2031, as shown in Table 4.1. Moreover, it also states that the industry will most likely need more than 10 years to completely recover [9].

Table 4.1: Fleet forecast for 2021 and 2031 by Oliver Wyman for narrow-body aircraft [9]

Region	2021 fleet	2031 fleet	Fleet growth rate 2020-2031
Africa	380	566	0.8%
Middle East	425	1,289	2.8%
Asia Pacific	1,816	3,753	4.5%
China	2,999	4,451	4.5%
India	524	1,300	8.7%
Latin America	785	1,357	0.5%
North America	3,742	5,435	4,7%
Eastern Europe	874	1,648	1.4%
Western Europe	2,654	3,913	0.9%
World	14,199	23,712	2.5%

4.3 The A320-HACK

Now that the general industry structure and the market segment of interest have been outlined in the previous section, it is possible to consider how the A320-HACK will fit in the market. First, a Strengths, Weaknesses, Opportunities and Threats (SWOT) analysis will be performed in order comprehensively assess the product.Then, a deeper overview of the direct competitors will be given. Overall, the A320-HACK is expected to be a profitable product, given its positioning in a segment with an already high

[7] https://www.icao.int/Meetings/Green/Documents/day%201pdf/session%202/2-Dickson.pdf, accessed:05-May-2021

[8] https://hmmh.com/resources/news-insights/blog/stage-5-aircraft-noise-standards-approved-us-mean-airports/, accessed:05-May-2021

[9] https://www.researchandmarkets.com/reports/4583619/the-global-commercial-aircraft-market-2018-2028#:~:text=The%20single%20aisle%20aircraft%20segment,haul%20flight%20routes%20by%20LCCs,%20LA%2005-03-2021, accessed:03-May-2021

[10] https://www.airbus.com/newsroom/press-releases/en/2021/01/airbus-2020-deliveries-demonstrate-resilience.html, accessed:05-May-2021

market share, which is also expected to constantly grow, as previously mentioned. This assessment can be confirmed by evaluating the A320-HACK utilizing a growth share matrix[11].

4.3.1 Strengths, Weaknesses, Opportunities, & Threats Analysis

This assessment's outcomes are given in Figure 4.1. Summarizing the results, the A320-HACK has the potential of reducing emissions without compromising performances, while possibly paving the way for large-scale adoption of hydrogen in aviation, thus placing its manufacturer in a market leading position. Simultaneously, technical difficulties in implementing the HACK concept, infrastructure issues, and disregard for sustainability from the most growing economies might undermine the A320-HACK's success.

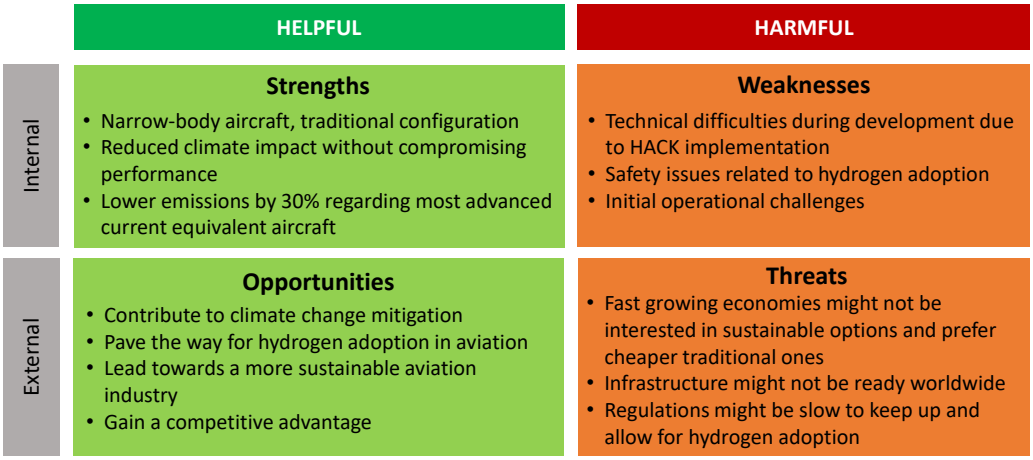

Figure 4.1: Strengths, Weaknesses, Opportunities, and Threats analysis for the A320-HACK

4.3.2 Competitors

The competitors - whose specifications are in Table 4.2 - were selected by their size, range and passenger capacity. The A320-HACK enters the market in 2035, which is the relative near future, and so it seems highly unlikely that radically new aircraft will be launched by then. Therefore, it can be assumed that the A320-HACK will have to compete with the by then latest development of the current competitors, such as the Boeing 737. Moreover, some competitive aircraft that are currently being developed are also considered, as they should reach the market by 2035.

At the moment, the A320neo is the most popular narrow-body aircraft on the market. The A320-HACK is intended to be the replacement/successor of the A320neo, and thus it should take up its market share. If a kerosene version of the aircraft was offered alongside the HACK one, it would be an internal competitor especially in those markets that are not interested in switching to alternative fuels to reduce emissions. Therefore, the A320-HACK has the option to only use kerosene. A downside would be the reduced maximum range of 3225 km, however this is still 82% of the A320neo range.

The Boeing 737 is a current competitor for the A320neo, thus its newest version in 2035 is also expected to compete with the A320-HACK. The Bombardier C-series, now the A220 family, specifically the A220-300 could also be considered a competitor of the A320-HACK, due to its similarities with the A320neo as is seen in Table 4.2. An Asian potential competitor could be the COMAC C919, which is currently being developed and tested by the Chinese aircraft manufacturer COMAC and should enter the market soon. Another potential competitor is the MC-21 developed by the Russian aircraft manufacturer Irkut. The MC-21 family is not yet on the market, but it is expected to be launched soon. The specifications of the MC-21 are very similar to the ones of the A320neo and Boeing 737 MAX 7, as can be seen in Table 4.2.

Table 4.2: Competitor aircraft specifications of the A320-HACK

[11] https://www.bcg.com/about/our-history/growth-share-matrix, accessed:04-May-2021

	A320-HACK	A320neo[12]	B737 MAX 7[13] [10]	A220-300[14]	C919 ER[15] [16]	MC-21-200[17]	MC-21-300[17]
Overall length [m]	37.57	37.57	35.56	38.7	38.9	36.8	42.2
Fuselage width [m]	3.95	3.95	3.76	3.5	3.95	4.06	4.06
Wing span [m]	35.8	35.8	35.9	35.1	35.8	35.9	35.9
Height [m]	11.76	11.76	12.3	11.5	11.95	11.5	11.5
Pax (2-class)	180	150-180	138-153	120-150	158	132	163
Range [km]	6,560	6,300	7,130	6,297	5,555	6,400	6,000
Cruise Mach Number	0.82	0.82	0.79	0.82	0.785	-	-
MTOW [kg]	73,500	73,500	80,285	70,900	77,300	72,560	79,250
MLW [kg]	66,300	66,300	66,043	60,600	66,600	63,100	69,100
MZFW [kg]	63,610	62,800	62,913	57,600	42,100	-	-

5 | Sustainability Development Strategy

This project aims at contributing to a sustainable future for aviation through a sustainable design process. The driver motive behind the implementation of the hydrogen assisted combustion of kerosene (HACK) is to reduce emissions. Thus contributing to tackling climate change, this project also aims to simultaneously create an economical and social environment, where all three dimensions can prosper.

One of the pillars of the A320-HACK is its propulsion system. Unlike any other commercially available aircraft, the A320-HACK has a hydrogen assisted combustion of kerosene. Furthermore, due to the systems' flexibility, the change between hydrogen and hydrogen assisted kerosene combustion is possible [11]. To go a step further, only hydrogen will be used for taxi and idle, and alternative options to the usual auxiliary power unit will be analysed. These design choices reduce the amount of emissions (CO_2, NO_x, soot) around the airport, which contributes to an improved air quality. Conversely, the noise produced by the A320-HACK, should be similar or lower compared to A320neo due to improvements in engine technology. Needless to say that the noise of A320neo already is already 50% lower than the current competition[1].

Concerning the environmental impact of ground operations, there is a distinct preference for green hydrogen, even though blue hydrogen is more cost attractive. A further analysis will be conducted on these hydrogen types. Furthermore, the manner to transport hydrogen to the airport will be analysed.

In order to make sure the A320-HACK follows the sustainability requirements, several analyses will be performed. These include assessing how, depending on different mission stages, the A320-HACK's climate impact can be minimised. Due to the lack of information on the climate impact of water vapor emissions, special care will be given to this type of emission. Furthermore, another very important analysis that shall be conducted is the life cycle analysis. The production, the operations, and the end-of-life phases will be rated while considering aspects such as emissions (CO_2, H_2O, NO_x, soot), climate impact, air quality,

[12] https://www.airbus.com/aircraft/passenger-aircraft/a320-family/a320neo.html, accessed:05-May-2021
[13] https://www.boeing.com/commercial/737max/, accessed:06-May-2021
[14] https://www.airbus.com/aircraft/passenger-aircraft/a220-family/a220-300.html, accessed:05-May-2021
[15] https://modernairliners.com/comac-c919/, accessed:05-May-2021
[16] https://web.archive.org/web/20170616174300/http://www.aspireaviation.com/2011/04/19/comac-c919-threat-overblown/, accessed:06-May-2021
[17] http://mc21eng.irkut.com/family/characteristics/?PAGEN_1=2&SIZEN_1=1, accessed:05-May-2021
[1] https://www.lufthansagroup.com/en/company/fleet/lufthansa-and-regional-partners/airbus-a320neo.html, accessed:19-May-2021

noise, waste production, recyclability of materials, and energy consumption. Finally, the noise around the airports and its effect on the quality of life of people will be modelled.

The sustainability requirements and analysis is detailed in Chapter 16.

6 | Functional Analysis

The functional analysis was performed as a tool to investigate all the functions A320-HACK is required to perform. Subsequently, it facilitated the definition of relevant requirements. This analysis is represented in this report by a functional flow diagram and a functional breakdown structure. The functional breakdown diagram (FBD) breaks down the phases of the missions into further detailed functions. This diagram can be viewed in Appendix C on page 140 and page 141. The functional flow diagram represents the functions in the order in which they need to be performed. The first-level of the diagram is illustrated in Figure 6.1, while the detailed diagrams can be found in Appendix C on page 142 and page 143.

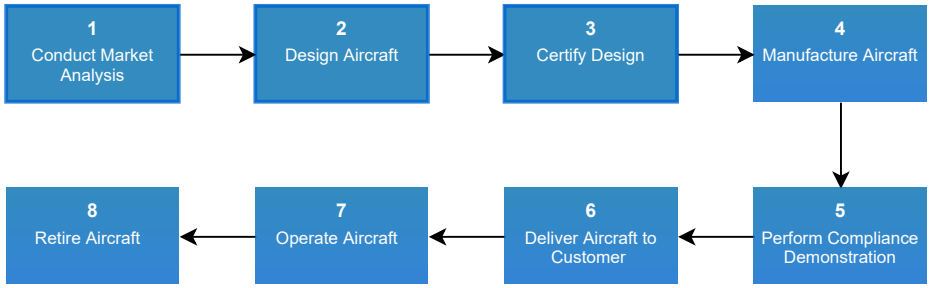

Figure 6.1: Simplified functional flow diagram

7 | Technical Risks

Risk management aims to identify the risks, evaluate them and then mitigate them if necessary. The evaluation was done for the probability of occurrence and consequence of the risk. The probability is scaled from 1 to 5, where 1 stands for a low probability and 5 stands for a very high probability. The consequence criteria has 4 levels: negligible (1), marginal (2), critical (3) and catastrophic (4). Six categories of risks were considered: financial (FR.#), schedule (SR.#), operations (OR.#), performance risks (PR.#), manufacturing risks (MR.#) and design risks (DR.#). The overview of these risks is provided in Table 7.1.

Table 7.1: Technical risk overview

Label	Risk Identification	Mitigation
FR.1	Production costs exceeding A320neo by more than 15%.	Conduct extensive research to procure the parts, materials for the best quality to price ratios. During the design phase, maintain good communication with the customer to ensure that they are aware of all the developments related to production costs.
FR.2	Lack of interest from the airlines in the final product.	Risk is in the tolerable zone.

FR.3	Development costs are exceeded.	Perform a thorough costs analysis and resource allocation at an early stage of the design. Allowing room for multiple reviews to ensure that everything is on track.
FR.4	Uncertainty of the unit cost in 14 years (effects of inflation, supply and demand).	Risk is in the tolerable zone.
SR.1	Not being able to complete the design in 10 weeks	By consulting the project logic diagrams and remaining in line with them and keeping them updated at every stage. By starting from the most important features of the design, delivering the concept and the main design adaptations without the more specific detail gives the team a chance of having the primary mission well defined despite not having completed the full deliverables.
SR.2	Technology and production methods not reaching TRL 7/8 by 2035.	Identify the technologies and production methods at risk and lobby for investment and research in those areas. When making design trade off, focus on concepts that are look promising to reach TRL 8 in time for Entry into service.
OR.1	Airports are unable to store and/or handle H_2.	By employing effective lobbying techniques to convince governments to either subsidise or oblige airports to handle/store H_2. Prevention measure was sufficient for exiting the non-tolerable risk zone.
OR.2	Certification is not possible due to the lack of regulations for H_2 propulsion.	Share the costs with other stakeholders such as investors, KLM, Airbus, Safran, Rotterdam-The Hague Airport and maybe governments.
OR.3	The supply of H_2 is too scarce for the demand.	Risk is in the tolerable zone.
OR.4	The effect of H_2 refueling on the turnaround time is more than 10 min.	Risk is in the tolerable zone.
OR.5	Stricter regulations on the use of H_2 for aviation.	Risk is in the tolerable zone.
OR.6	Operational costs are excessively higher than those of A320neo.	Risk is in the tolerable zone.
PR.1	The LH_2 cannot be stored for 36 h at 45 $^{\circ}C$ ambient temperature.	Ensure the effectiveness of insulation and use active cooling system with redundancy. Design in a flexible manner such that gaseous hydrogen is still a possibility.
PR.2	The selected materials do not meet the sustainability requirement.	Having the sustainability officers perform regular checks. Redirect some of the proceeds of this project to help other sustainability projects (e.g. initiative of planting trees in Panama[1]) achieve their objective.
PR.3	The aircraft does not meet the noise regulations at airport level.	Risk is in the tolerable zone.
PR.4	Measured performance is lower than the calculated performance.	Risk is in the tolerable zone.
PR.5	New structural elements not being able to meet certification requirements.	Aim to minimise the redesign of the structural elements. Seek additional resources from the Finance managers.
PR.6	The emissions requirements are not met.	By having the sustainability officers perform regular checks. This risk cannot be mitigated because it is the core of the mission, hence failing to meet this results in the complete failure of the project.
PR.7	Range is lower than the value defined in SR-PERF-03.	Risk is in the tolerable zone.
PR.8	Passenger capacity is outside the range defined in SR-PERF-02.	By using the range of A320neo as a constraint for the design of A320HACK. Investigate alternative streams of revenue to ensure that aircraft remains competitive with A320neo.
PR.9	Cargo capacity is considerably diminished with respect to A320neo.	Focus on options which do not integrate the fuel at the current cargo holds. Investigate alternative streams of revenue to ensure that aircraft remains competitive with A320neo.
PR.10	H_2 thermal control system fails.	Risk is in the tolerable zone.

[1] https://www.klmtakescare.com/en/content/-re-planting-trees-in-panama, accessed:29-Apr-2021

MR.1	The H_2 tanks presents leaks.	The tank is designed to have as few parts as possible. Ensure there is enough ventilation such that risk of explosion is minimised.
MR.2	Parts do not meet dimensional requirements.	Opt for high accuracy manufacturing processes. When designing allow for higher tolerances.
DR.1	The estimated structural weight is significantly off.	Use CAD software for the weight estimation of each part.
DR.2	The required fuel volume can not be integrated in the structure.	Opt for a lower percentage of H_2. Perform feasibility study of H_2 integration at the first stage of the design.
DR.3	The c.g. of the aircraft is difficult to estimate.	Adapt A320neo c.g. based on HACK design modifications. Design the empennage in such a way that a larger cg range is allowed.
DR.4	The structure becomes brittle due to the temperatures induced by the cryogenic tanks.	Account for tank thermal insulation inefficiency in the design. When designing, do not place primary structures in the close vicinity of the cryogenic tanks.
DR.5	Failure to accurately model the drag increase due to configuration change.	Risk is in the tolerable zone.
DR.6	Rupture of the hydrogen tanks.	Risk is in the tolerable zone.
DR.7	Valves and/or pressure relief discs fail.	Make use of redundancy during the design.
DR.8	The weight and placement of the propulsion system destabilises the aircraft.	Risk is in the tolerable zone.

The mitigation was performed only for the risks situated in the non-tolerable and highest risk zones. A mitigation plan, presented in Table 7.1, was developed for each of these risks. The risk map after the implementation of the mitigation strategy is illustrated in Figure 7.1.

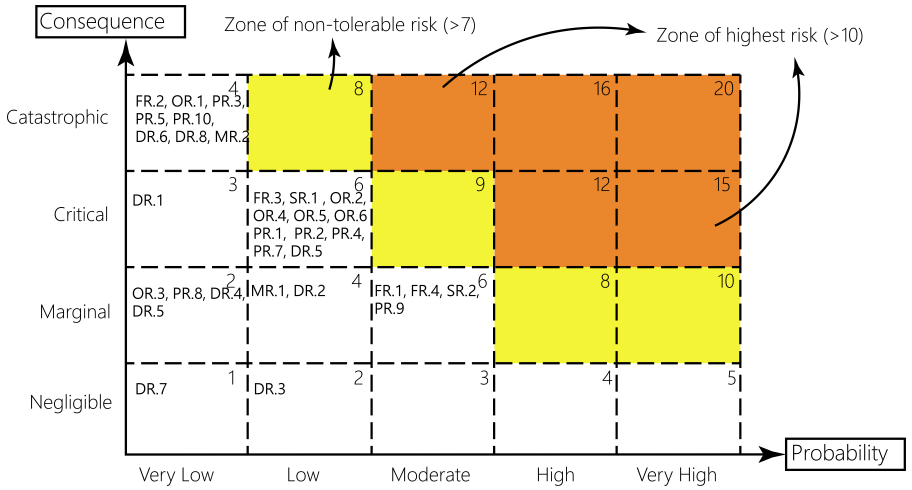

Figure 7.1: Technical risk map post-mitigation

8 | Design Choices

Following the market analysis, the sustainability development strategy, the functional analysis, and the evaluation of the technical risks, design choices were made. Section 8.1 elaborates on the choice of hydrogen storage state and Section 8.2 on that of the tank's location. The chosen engines' position is explained in Section 8.3 and the tail configuration in Section 8.4. Finally Section 8.5 summarises the details of the final configuration of the A320-HACK.

8.1 Hydrogen Storage State

Hydrogen as an energy carrier could be stored on-board in seven forms of varying physical and chemical nature. Five of them were ruled out early on and a trade-off was performed for the two remaining options. The motivation for discarding five forms of hydrogen is set out in Table 8.1.

Table 8.1: Rationale behind discarding several forms of hydrogen

Hydrogen state	Rationale
Ammonia	Unstable flame and narrow flammability which can be improved by 'cracking' hydrogen, a process that requires high temperatures and pressures. Emissions are improved only within a narrow range of equivalence ratios [12]
Metal hydrides	High temperature needed for de-hydrogenation and this system is too large and heavy to carry on-board
Liquid Organic Hydrogen Carriers	Development and practical usage are still in infancy [13]
Solid hydrogen	As absolute zero is approached, lowering the temperature becomes increasingly difficult and energy intensive [14]
Slush hydrogen	As absolute zero is approached, lowering the temperature becomes increasingly difficult and energy intensive [14]

Once the options of hydrogen form were narrowed down to GH_2 and LH_2, a trade off was performed using the Analytical Hierarchy Process (AHP) [15] with seven different criteria of varying weights. The results of the trade-off are summarised in Table 8.2, where a higher score means a better performance. It was concluded that LH_2 would be the best form to carry hydrogen on-board. More details on the scores awarded are found in [14].

Table 8.2: Hydrogen storage state trade-off summary table

Type H_2	Energy density	Handling safety	Structural weight	Energy required for storage	Cost	Re-fueling	Complexity	AHP Score
LH2	3	1	2	1	2	2	1	53%
GH2	1	2	1	2	1	1	2	47%

8.2 Hydrogen Tanks' Location

The size of the hydrogen tanks are constrained by their placement and location. Five design options for tank placement were explored and are laid out in Table 8.3.

Table 8.3: Description of the proposed design options for the positioning of the hydrogen tanks

Design option	Description
Design option I (Cargo-space)	Hydrogen tanks are stored in the unused cargo space and the space freed up by the redundancy of kerosene tank in the central wingbox. Requires no external modification.
Design option II (Extended fuselage)	The fuselage is extended to accommodate the hydrogen tanks, this places it between A320neo and A321neo in terms of length. This configuration allows to maintain the same passenger capacity without the need to decrease cargo capacity. Minimal and familiar exterior adaptations will be made to the aircraft layout.
Design option III (Flat Bottom)	In this option the fuel tanks are placed in the belly of the aircraft. This size of this region will therefore increase in size, partially resembling the Antonov An-22 lower fuselage design. Requires modifications to the aircraft's belly, the position and the length of landing gear.

Design option IV (Wing mounted)	Hydrogen tanks are mounted on the wings, akin to military jets. Requires modification to the wing assembly. Although it impacts the aircraft's topology and aerodynamic profile, it does not compromise cargo space and alleviates the bending loads imposed on the central wing box.
Design option V (Beluga)	In this option the hydrogen tanks on placed on top of the passenger cabin, implying the design of a new fuselage and making modification to the production lines. It will most likely resemble - although in an attenuated way - the shape of the Airbus Beluga.

The different design options were evaluated using four different trade-off criteria, being them, by order of increasing weight, the impact on the aerodynamic efficiency, the impact on weight, the feasible hydrogen storage capacity, and safety. Their weights were determined using the AHP method.

Table 8.4: Trade-off summary table for the tank's location

Criteria	**Weight**	**DO-I** Cargo Space	**DO-II** Extended fuselage	**DO-III** Flat bottom	**DO-IV** Wing podded	**DO-V** Beluga
Aerodynamic impact	9%	50%	31%	8%	8%	3%
Capacity of H2 storage	32%	6%	34%	3%	21%	36%
Weight increase	14%	24%	5%	46%	19%	7%
Safety	45%	16%	16%	21%	31%	15%
Total	100%	17%	22%	17%	24%	20%

Option IV - Wing podded - won and was chosen. Highlights are the wing bending relief it provides, together with storage capacity of 32.6 m^3 of LH_2, equivalent to 33% of the energy required for ferry flight. Their large distance from the passengers and the easiness of ventilation make it the safest option. Another aspects only considered after the trade-off process was that these modular tanks can reduce both the turnaround time and the downtime due to tank maintenance and inspection.

A sensitivity analysis was conducted to verify the robustness of the design by increasing/decreasing the weight of each criterion, eliminating the design option that scored the least, and removing each criterion at a time. Design option IV proved to be robust.

8.3 Main Engines' Location

Four possible locations for the main engines were considered, all with the same position for the hydrogen tanks, as discussed in Section 8.2.

Table 8.5: Advantages and disadvantages of different engine configurations

Configuration	**Advantages**	**Disadvantages**
1 - Two engines placed on an H-tail	Smaller vertical tail due to less yawing moment in one engine situations	Engines do not counteract the wing's bending and twist, requiring wing reinforcements, and increasing the structural weight
	Smaller landing gear due to clearance reasons	Fuselage reinforced: higher structural weight.
	Noise at the front of the cabin reduces	Large horizontal tail for stability reasons
	Lower risk of foreign debris damage	No significant fuel efficiency improvement
		Extra development and manufacturing costs due to unconventional lay-out

2 - Fuselage embedded engines at the back	Increased aircraft efficiency due to the use of boundary layer ingestion [16]	Engines do not counteract the wing's bending and twist, requiring wing reinforcements, and increasing the structural weight
	Smaller vertical tail due to less yawing moment in one engine situations	Fuselage enlarged and reinforced, increasing structural weight
	Smaller landing gear due to clearance reasons	Extra development and manufacturing costs due to unconventional lay-out
	Noise at the front of the cabin reduces	Increased complexity
	T-tail not affected by wake of the main wing	
	Lower risk of foreign debris damage	
3 - Quasi-distributed propulsion, with two or more engines on per wing	Small complexity increase	Negative aerodynamic impact compared to a conventional aircraft
	No negative stability impact	More material is needed when using several small engines[1] resulting in a higher structural weight
	Wing distributed engines contribute to the bending release of the main wings, allowing for less reinforcements and thus wing's structural weight	Smaller turbofan engines are less efficient than larger turbofans and thus the net thrust does not scale linearly with the increase in weight
		More engines: higher maintenance costs
4 - Conventional aircraft with one engine mounted on each wing	No negative stability impact	Efficiency not increased
	No added weight	
	Low complexity increase	
	Low cost increase	

Concepts 1 and 2 were ruled out as they could also pose a big challenge in terms of stability and of the requirements on development and production costs (UR-COST-01 and UR-COST-02). Configurations 3 and 4 are similar in terms of complexity, and costs but the former has an increased weight and reduced efficiency. Therefore, configuration 4 was chosen for the placement of the engines.

8.4 Tail Configuration

Three tail configurations were considered. Their advantages and disadvantages are seen on Table 8.6.

Table 8.6: Advantages and disadvantages of different tail configurations [17]

Configuration	Advantages	Disadvantages
Conventional	Most lightweight configuration	Horizontal stabilizer has down wash of wing
T-tail	Horizontal stabilizer does not experience down wash of wing and may be smaller	Vertical stabilizer heavier to support the horizontal stabilizer
	End-plate effect so no vortices produced at the tip of the vertical stabilizer: smaller vertical tail area	Susceptible to deep stall at high angles of attack
Cruciform	Combines advantages of conventional and T-tail configuration	Horizontal stabilizer reduces effective surface of vertical tail
		There is still some down wash

The conventional tail proved to be the best option. As described in Section 8.2, the hydrogen will be stored in wing podded tanks, thus the stability of the aircraft will not be affected as much as if for instance the tanks were placed at the back of the fuselage. Hence, the choice of a T-tail is not justified. Further, the cruciform tail was ruled out as it implies the reinforcement of the vertical tail. However, this choice

[1] Having a single engine as efficient as two or three small engines only requires the engine elements to be increased by a certain portion. In contrast, each small engine will have its own cowling, pylon, internal engine elements, and feeding pipes.

should be revisited later in the project, once the stability and controllability characteristics are analysed.

8.5 Final A320-HACK Configuration

The A320-HACK (depicted in **??**) has a rather conventional configuration, typical of such airliners. The engines are wing-podded and the tail has a standard configuration. The main topology change is represented by the hydrogen tanks, which are wing-mounted. This solution does not compromise cargo space; secondly, it is preferable for airworthiness reasons; then it allows to quickly remove the tanks for inspection and maintenance; and eventually swap them for refueling.

In terms of the on-board hydrogen/kerosene ratio, 1/3 of the total usable energy is stored as hydrogen, while the remaining in kerosene (in compliance with UR-PROP-01). This means that - assuming the A320-HACK carries the same energy of the A320neo, equivalent to 831,009 MJ - 277,003 MJ will be stored as hydrogen, while the remaining 554,006 MJ as kerosene. Liquid hydrogen was the chosen hydrogen storage state. Therefore, the A320-HACK carries a net volume of LH_2 of 32,462 L and 15,906 L of kerosene. Using the methodology described in the Midterm phase Sofia et al. [14], accounting for unusable space and fuel, the gross volume and mass of LH_2 to be stored are 33,542 L and 2,385 kg respectively, while the tanks will need to be designed for a total volume of 37,900 L.

The A320-HACK will idle and taxi fully powered by hydrogen, as these phases have a very low power requirement. This eliminates the CO and CO_2 emissions on ground. Then, during the flight phases, a mixture of kerosene and hydrogen is used with 14% mass of hydrogen and 86% of kerosene.

Lastly, the A320-HACK has a fuel cell module in place of a traditional auxiliary power unit, providing power to the electrical systems during the whole mission. This results in reduced emissions and improved engine efficiency.

Part III

Subsystems' Design

9 | Fuel System Design

This chapter focuses on the design of the fuel system for the hydrogen. Section 11.1 lists the relevant requirements for the fuel system. Section 9.2 investigates the hydrogen storage system, while Section 9.3 outlines the structure of the fuel delivery system. The chapter is concluded with Section 9.4 which draws out the limitations and recommendations.

9.1 Requirements

The requirements related to the fuel system design are listed below.

UR-SR-01 The LH_2 storage system shall store the fuel for 36 hours without boil-off at an ambient temperature of 45°C.

UG-SR-01 The issue of ground clearance and tail strike shall be considered

UR-PERF-02 The design shall satisfy the CS25 regulations:

CS 25.303 "Unless otherwise specified, a factor of safety of 1.5 must be applied to the prescribed limit load which are considered external loads on the structure." [6].
CS 25.631 "Aeroplane must be designed to assure capability of continued safe flight and landing of the aeroplane after impact with a 4 *lbs* bird when the velocity of the aeroplane (relative to the bird along the aeroplane's flight path) is equal to V_c at sea-level or 0.85 V_c at 8000 ft, whichever is the more critical" [6].

9.2 Hydrogen Fuel Tanks Design

Here, the tank placement, configuration, and thermal design are described. Besides, the fatigue is considered as well as the mechanical design and fuel tank dimensions. Safety is considered, and finally the pylon is designed.

9.2.1 Tank Placement

The first aspect that needed to be considered in terms of tank placement is upper or lower wing mounting. With a few exceptions, most aircraft opt for placing the engines underneath the wing. The main reasons for this are the structural load that the pylon would need to account for, and better aerodynamics. However, as the hydrogen tanks do not produce huge forces and moments compared to engines, an upper wing configuration can be examined.

For lower mounting, the scalability of the tanks is the most evident problem. The diameter is limited due to nacelle strike, while the length is limited by the scrape angle. Another limitation is the deployment of the high lift devices (HLD) during landing and take-off, which would hit the tanks when deployed. Placing tanks below would involve the removal of HLD for the section occupied by the tanks and then redesigning the remaining area of the HLD to account for the loss. Probably the most important consideration in this application is the heat induced by the exhaust of the engine. The LEAP1-A engine has an exhaust temperature of up to 1060 $°C$ which would pose a great threat to the cryogenic insulation[1].

For the upper mounting, speed brake deployment needs to be considered by adjusting the height of the pylon accordingly, to prevent an impact between the brake and the tank. The biggest concern of such a configuration is the alteration of the flow on top of the wing, which is critical in generating lift. However, the VFW Fokker 614 and the Hondajet prove that with a good design of the nacelle such a configuration is possible [18]. Considering from a qualitative point of view the challenges and complexity of the required solutions, the upper mounting of the tanks will be selected for the A320-HACK.

After selecting the mounting configuration, the exact placement of the tank needs to be determined. For the vertical placement, the speed brakes deployment constitutes the limiting factor. The surface area of

[1] https://tinyurl.com/erva7zkj, accessed: 03-Jun-2021

the spoilers[2], 8.35 m^2 and their placement between 35% and 95% of the span [19] are known variables. Thus, the length of the spoiler is estimated to be around 0.42 m. Assuming a maximum deflection angle of 65 deg [19], it is determined that the pylon height should be at least 0.38 m.

9.2.2 Tank Configuration

The tanks will have a cylindrical shape with hemispheric caps as depicted in Figure 9.1. As illustrated in Figure 9.2, the tank will have a double wall configuration, with the insulation system in between. Both walls are made from Al-2090-T1, while the insulation is a vacuum jacketed Multi-Layer Insulation (MLI). Please consult [14] for details regarding the material selection.

From the aerodynamic analysis in Chapter 14, it was noticed that the tank diameter is the main parameter influencing the drag of the tanks. Hence, in order to reduce the drag of the tank while not excessively increasing the length, a script for obtaining an optimal diameter was written. This diameter was identified as 2.1 m.

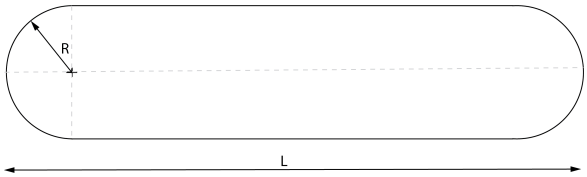

Figure 9.1: Tank Geometry

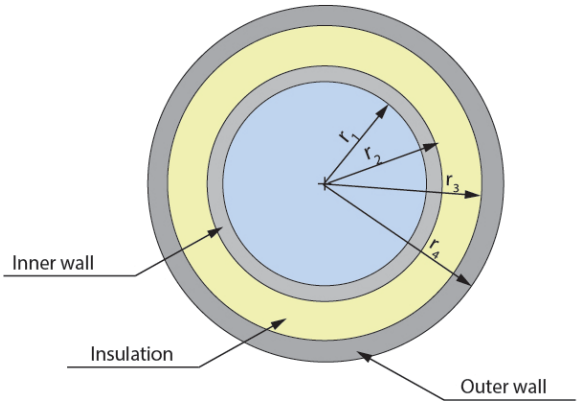

Figure 9.2: Tank Layers

9.2.3 Thermal Design

No matter how well insulated the tank is, some heat transfer will still exist, and has to be accounted for. Using the method presented in [20], it is assumed that that evaporation can be neglected under 20 K. In Equation 9.1, C_p represents the specific heat capacity of hydrogen, m_{H_2} the mass of hydrogen, ΔT is the allowable temperature difference and t is the time [20]. As hydrogen is assumed to begin boil-off at 20 K, the initial temperature of the tank must be lower. For this design a temperature, T_c, of 19.75 K was assumed, based on a previous space application where a temperature of 18 K was assumed for a zero boil-off storage period of 2 yrs [20].

$$Q_{req} = \frac{Cp \cdot m_{H_2} \cdot \Delta T}{t} \tag{9.1}$$

Knowing that each tank contains at most 1192.42 kg of LH_2 with C_p of 10,310 $J/kg \cdot K$, t of 129,600 s and ΔT of 0.25, it is possible to calculate that the maximum allowable heat transfer, to meet the US-SR-01 requirement, is 23.715 W.

In order to satisfy this requirement, it was chosen to use an MLI system. It comprises layers of perforated reflector films and insulating spacers between them [21], all placed in a hard vacuum with pressure lower than 13 mPa or $1.3e^{-7}$ bar [22]. The advantages of MLI compared to other insulation techniques, such as foams or aerogels, is the extremely low thermal and radiative conductivity, with an overall two orders of magnitude lower heat flow [22]. To design such systems, the Modified Lockheed Equation 9.2 is used, with C_s, C_R and C_G being the solid, radiation and gaseous conduction coefficients, N and $\bar{N}$ being the number and density of layers, p_{vac} the vacuum pressure (in $torr$), T_h and T_c the temperatures at the two boundaries and ϵ the emissivity coefficient defined by Equation 9.3 [23, 24].

$$q_{\text{total}} = \frac{C_R \varepsilon \left(T_h^{4.67} - T_c^{4.67}\right)}{N} + \frac{C_S \bar{N}^{2.63} \left(T_h - T_c\right)\left(T_h + T_c\right)}{2(N+1)} + \frac{C_G p_{vac} \left(T_h^{0.52} - T_c^{0.52}\right)}{N} \tag{9.2}$$

[2] https://tinyurl.com/fvhprkeb, accessed: 08-Jun-2021

$$\epsilon = 6.8 \cdot 10^{-4} \ \mathrm{T}^{0.67} = 6.8 \cdot 10^{-4} \cdot (T_h^{0.67} - T_c^{0.67}) \tag{9.3}$$

$$Q_{tot} = q_{tot} \cdot (4\pi r_4 + 2\pi r_4 \cdot (L - 2r_4)) \tag{9.4}$$

In a recent study performed by Singh et al. [24], it was demonstrated that the perforated Double Aluminized Mylar (DAM) reflector sheets with glass-tissue spacers outperform other reflector-spacer combinations. It was shown that the optimal density $\bar{N}$ for this MLI was 22.7 $layers/cm$, and hence this value was adopted. With $C_s = 7.3 \cdot 10^{-8}$, $C_R = 7.07 \cdot 10^{-10}$ and $C_G = 1.46 \cdot 10^{-4}$ [24], p_{vac} of $9.75 \cdot 10^{-05} torr$ (13 mPa) and $T_h = 318.15K$ (defined by UR-SR-01), using the equations 9.2 and 9.4 the number of layers was varied in order to be below the required heat flow. It was obtained that 40 layers of insulation would be needed, resulting in an insulation thickness, t_{insul}, of 17.62 mm. This result could be directly validated as the Singh et al. study investigated the heat load for this number of layers too. Finally, the DAM + glass-tissue combination was compared to other MLI solutions from the Fesmire and Johnson study [21] and was confirmed to be the optimal solution.

9.2.4 Fatigue Considerations

For fatigue considerations, the expected number of cycles was first established. The A320 family is expected to operate for 60,000 cycles [3]. Although there is no standard consensus, usually low cycle fatigue (LCF) is defined for up to 10^6 cycles [25]. The most used diagram for visualizing the fatigue life is the S-N diagram, which evaluates the nominal stress amplitude with respect to the number of cycles. The part corresponding to LCF can be estimated using the Basquin relation Equation 9.5.

$$\sigma = AN^b \tag{9.5}$$

Due to the lack of information on the coefficients of the selected Al-2090-T1, the extrapolated fatigue behaviour of another metal alloy was used. For Al-2024-T4, A is equal to 855 and b to -0.109 [26]. Thus, $\sigma_f = 257.1$ MPa after N = 60,000 cycles. Compared to the standard strength of 325 MPa, a decrease of 20.7% in strength is observed. This decrease will also be considered for Al-2090-T1. All calculations for the mechanical design will be performed using the fatigue/end-of-life strength value.

9.2.5 Mechanical Design

It was assumed that the inner wall will need to support the pressure stresses. The necessary wall thickness was calculated using Equation 9.6, where Δp is the pressure difference, σ_a is the allowable stress and e_w is the weld efficiency which is assumed to be equal to 0.8 [27]. The σ_a is equated to the yield strength of the material, and the pressure difference on the inner wall, Δp, was equated to $p_{tank} - p_{vac}$. The critical design case was used in order to obtain the thickness. Thus, the highest pressure that is experienced by the tank, being 3.5 [bar] and corresponding to the venting pressure, was assumed. As a conservative estimate, a safety factor of 1.5 was applied on both the loads and the determined thickness to meet the CS25.303 regulation and to account for model inaccuracies, resulting in a final t_{wall} of 1.96 mm. This value was used for both the inner and the outer walls.

$$t_{wall} = \frac{\Delta p \cdot d}{2\sigma_a e_w + 0.8 \cdot \Delta p} = 0.00196 \ m \tag{9.6}$$

9.2.6 Final Tank Dimensions

The data from previous sections are summarised in Table 9.1, where the inputs and the outputs of the tank design code are presented. The outputs refer to the characteristics of each tank.

[3] https://www.airbus.com/newsroom/news/en/2008/03/new-service-package-will-extend-a320-039-s-life.html, accessed: 01-Jun-2021

Table 9.1: Tank design inputs-outputs overview

Inputs		Outputs	
Diameter $[m]$	2.13	Wall thickness $[mm]$	1.96
MLI density $[kg/m^3]$	50	MLI thickness $[mm]$	17.62
Al-2090-T1 density $[kg/m^3]$	2590	Mass $[kg]$	421.63
Al-2090-T1 yield strength $[MPa]$	663	Length $[m]$	6.19
Hydrogen volume $[m^3]$	37.9	Tank Volume $[m^3]$	18.95

9.2.7 Safety Considerations

This subsection investigates the design of the tank from a safety perspective. The uncontained engine failure and bird strike will be discussed.

Engine Debris

For the wing mounted tanks, the location of the tanks with respect to the engine needs to be considered from a safety perspective. A turbine blade failure can lead to uncontained fragments bursting out. These fragments are charged with large amounts of energy due to the high rpm's they are exposed to and can penetrate through other structures, causing catastrophic damages.

The A320-HACK uses a turbofan, so for the engine debris the failure of the fan, the turbine and the compressor were considered. The AIR4003 and AIR4770 reports [4] offer data on the statistics of engine debris. Table 9.2 shows the most critical combination of velocity and mass for each type of failure. Based on these parameters, the kinetic energy of the debris could be computed.

Table 9.2: Uncontained engine failure statistics [4]

Failure Type	**Velocity $[m/s]$**	**Mass $[kg]$**	**Kinetic Energy $[KJ]$**	**Angle $[^\circ]$**
Compressor disk	120.70	2.88	20.98	-5
Compressor Blade	319.12	0.11	5.77	-30
Compressor Rim	156.97	3.17	39.12	0
Turbine Disk	158.49	37.01	464.9	-5
Turbine Blade	412.39	0.11	9.64	-45
Turbine Rim	216.10	9.07	211.83	-30
Fan Disk	88.08	32.20	124.95	-5
Fan Blade	317.90	1.36	68.76	-35

By knowing the kinetic energy of each type of failure, it can be determined if the hydrogen tank can resist the impact. A series of assumptions and simplifications were made for these estimations. It is assumed that the kinetic energy remain constant along the trajectory. The loss of kinetic energy due to the penetration of the engine or other surfaces such as the wing is neglected. It is assumed that the tank failed if the outer wall fails and the vacuum jacket is lost. The amount of kinetic energy that can be absorbed by the tank is estimated using the material toughness parameter G_c. The material charts presented in Ashby [28], show that for metal alloys, such as the one used for the outer wall, G_c has a value of around 10 kJ/m^2. Using the projected area of the tank that is exposed to an impact, $A = Ld$, and multiplying it by G_c it is determined that the tank should withstand 131847 J.

Regulations allow for kerosene tanks to be placed in the impact area of engine debris if some additional precautions are implemented [5]. However, the failure of a LH_2 tank is more critical than the failure

[4] http://www.tc.faa.gov/its/worldpac/techrpt/AR99-11.pdf, accessed: 03-Jun-2021

[5] https://www.faa.gov/regulations_policies/advisory_circulars/index.cfm/go/document.information/doc

of a kerosene tank. The main difference comes from the risk of embrittlement of the wing structure due to the LH_2 spill. Such an event can lead to the failure of the skin of the wing. The failure of a primary structure is completely unacceptable. Thus, the aim is to mitigate any potential failure of the tank. This can be done by removing the tanks from the critical spread angle. If the tanks are moved more aft, the likelihood of such an impact is reduced. Moreover, a more aft position is expected to lead to a better aerodynamic performance as a smaller area of the upper wing air flow is obstructed by the tank.

It can be seen that the critical failures for the currently designed tanks are the turbine disk and the turbine rim. Using the backward spread angle, the limiting most forward position of the tank can be determined. Due to time constraints and scarce data, the engine is modelled as a point, having all the types of engine debris originate at the same location.

The most critical angle of failure is -30 deg, corresponding to the failure of the turbine rim as shown in Figure 9.3. The distance from the nose to this critical line was measured to be 15.6 m, meaning that this is the most forward location where the tank can be placed.

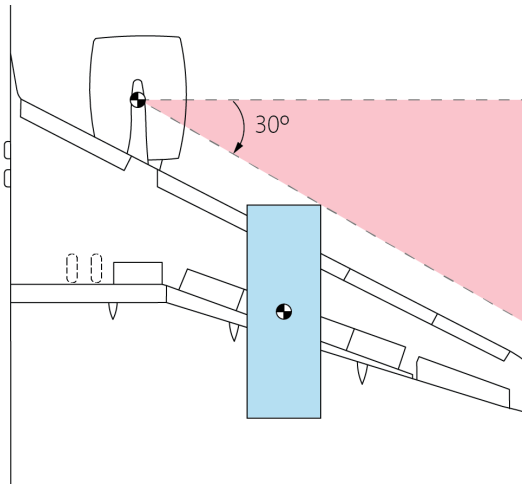

Figure 9.3: Lateral uncontained engine failure impact area

Bird Impact

The tanks require protection against potential bird impacts, as stipulated by the CS 25.631 regulation. For the A320-HACK, the take-off velocity is 85 m/s while the $0.85V_c$ at 8000 ft is 97.75 m/s. Hence, the latter is the critical case for which a 4 lbs (1.814 kg) bird impact structure should be designed. Using the kinetic energy formula, it is possible to determine that the strike energy, E_{strike}, is 8668.21 J. In order to determine the force of impact, several assumptions were made:

- Bird is a sphere that is 90% water and 10% air [29].
- Upon impact, the bird deforms by 50%[6].
- The velocity of the bird is neglected, and the impact is perfectly horizontal.

With the assumptions above, given the bird's mass of 1.814 kg and density of 900.1225 kg/m^3, the radius of the bird was determined to be 0.078 m using Equation 9.7. With this number, equating the E_{strike} with the force of impact (F_{impact}) times the radius of the bird ($E_{strike} = \frac{1}{2} \cdot m_{bird} \cdot V^2 = F_{impact} \cdot r_{bird}$), the bird impact force can be calculated using Equation 9.8.

$$r_{bird} = \sqrt[3]{\frac{3}{4} \cdot \frac{m_{bird}}{\rho \cdot \pi}} \tag{9.7}$$

$$F_{impact} = \frac{m_{bird} \cdot V^2}{2 \cdot r_{bird}} = 110615.9\ N \tag{9.8}$$

Finally, the total stress induced to the protective fairing structure is given by the Equation 9.9:

$$\sigma_{impact} = \frac{F_{impact}}{A_{impact}} = \frac{F_{impact}}{\pi \cdot r_{bird}^2} = 5.787\ MPa \tag{9.9}$$

In order to resist this bird impact, a foam-filled fairing was chosen. Foams offer high energy absorption characteristics for optimal density, and are widely used in automotive industry for impact absorption. In the study by M. Avalle [30], it was demonstrated that polyamide reinforced foam NORYL GTX 75 has an efficiency, η_{foam}, of around 40% at the stress of bird impact. The efficiency being defined as the absorbed energy per unit of volume, $E_{absorbed}$, over the given stress. Therefore, for NORYL GTX 75:

umentid/22187, accessed: 03-Jun-2021

[6] https://tc.canada.ca/en/aviation/publications/sharing-skies-guide-management-wildlife-hazards-tp-13549/appendix-121-bird-impact-forces-physics, accessed: 15-Jun-2021

$$E_{absorbed,NORYL} = \sigma_{impact} \cdot \eta_{foam} = 5.787 \cdot 10^6 \cdot 0.4 = 2,314,800 \ J/m^3 \tag{9.10}$$

Recalling that E_{impact} to be absorbed is equal to 8668.21 J, this results in a total volume of foam required, V_{foam}, of $3.744 \cdot 10^{-3} m^3$ (taking $E_{impact}/E_{absorbed,NORYL}$). Finally, to determine the required thickness of the foam fairing, it was decided to assume that only the foam right behind the impact area is absorbing the energy, as illustrated in Figure 9.4. The required thickness is given by:

$$t_{foam} = \frac{V_{foam}}{\pi \cdot r_{bird}^2} = 0.196 \ m \tag{9.11}$$

This thickness of 0.196 m is a conservative estimate as it does not take into account the energy absorbed by the foam surrounding the impact zone. NORYL GTX 75 has an apparent density of 75 kg/m^3 [30], resulting in a fairing weight of 0.281 kg.

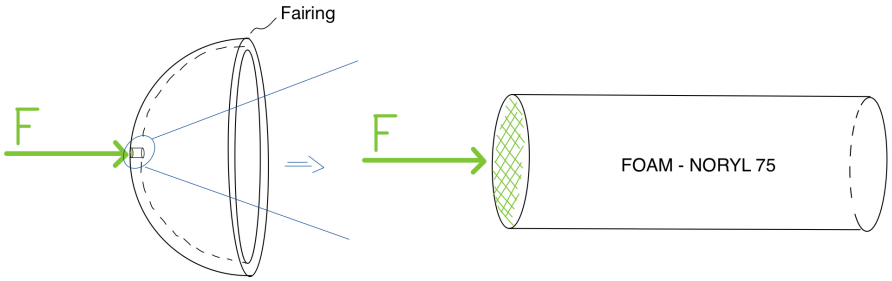

Figure 9.4: Bird strike and fairing representation

9.2.8 Pylon Design

The tanks will be attached to the wing using a pylon. Its design is inspired by the pylons that are used for the integration of the engine. The pylon will attach to the wing through the spars. The supports of the pylon shall withstand loads that can occur during an emergency landing, which are prescribed as 4.5 g (gravity) downward, 2.0 g upward, 9.0 g forward, and 1.5 g sideward [31].
The pylon is modelled as a hollow thin-walled beam. Its height is set to 0.38 m (Section 9.2.1) and its length to 1.5 m (distance between the spars). The pylon shall be wide enough to house all the required pipes and valves. Cryogenic valves can have diameter of up to around 13 cm [7]. A width of 20 cm is used for the pylon calculation, as it is deemed to offer enough storage space. The shear caused by the 9g load, combined with the moment created by the wight of the tank comprised the critical case, requiring a thickness of 5.12 mm. The total pylon mass was calculated as 22.6 kg.

9.3 Engine Fuel Delivery System

The fuel delivery system is responsible for transporting the hydrogen from the tanks to the engine. The main components that need to be considered for this trajectory are the fuel lines, the boost pump, the high-pressure pump and the heat exchanger. See Figure 9.5 for a schematic representation of the system. The boost pump is used to ensure the liquid hydrogen is able to flow through the fuel lines to the engine. Then the high-pressure pump increases the pressure of the (still) liquid hydrogen for injection into the combustion chamber. The hydrogen is then heated up to an injection temperature of 600 K by means of the engine-mounted heat exchangers.

[7] https://habonim.com/valves/cryogenic-valves/, accessed: 22-Jun-2021

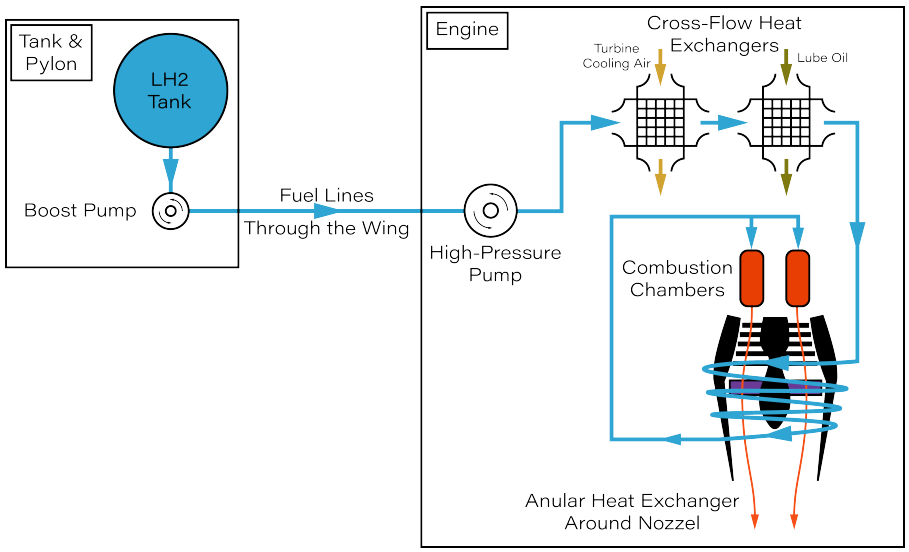

Figure 9.5: Sketched fuel delivery system from the tank to the combustion chamber

9.3.1 Fuel Lines

The fuel lines are mainly characterised by their diameter and their insulation, as they need to deliver the hydrogen in liquid form to the heat exchanger. For a fuel flow of 0.351 kg/s, a diameter of 1 in (2.54 cm) is used in Brewer [31]. Scaling this to the current fuel flow rate of 0.217 kg/s (Section 10.2.1), the diameter can be reduced by around a third. Thus, a fuel flow of 0.217 kg/s needs to be maintained by a pipe with a diameter of 1.7 cm. The rest of the design adheres to the one presented in Brewer and is illustrated in Figure 9.6.

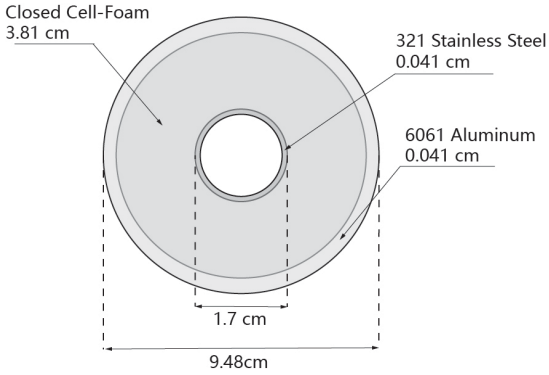

Figure 9.6: Fuel pipeline lay-out

9.3.2 Pump Type Selection

Multiple types of mechanical pumps, different performance characteristics, are available. The most suitable one for the A320-HACK applications must be selected. The current selection will apply to both the booster and the high-pressure pump. Three types of pumps were considered: centrifugal, vane and piston pumps. Both vane and piston pumps fall under the category of positive-displacement pumps(PD). One of the main operational characteristics of the pumps is the effective viscosity range. Centrifugal pumps have a better efficiency with lowering viscosity, while PD pumps are more efficient with increasing viscosity[8]. Vane pumps can operate extremely low viscosities, while the piston pumps can operate low viscosities. Liquid hydrogen has a viscosity of about $14 \cdot 10^{-6}$ $Pa \cdot s$ [32], being on the extremely low viscosity spectrum. Vane pumps are the most suitable choice for these criteria. Nevertheless, there are multiple successful records of using centrifugal pumps for LH_2 [31].

Centrifugal pumps offer a constant smooth flow, while PD pumps provide pulsating mass flows.

[8] https://www.michael-smith-engineers.co.uk/resources/useful-info/centrifugal-pumps, accessed: 11-Jun-2021

Considering the fact that the pulses should dampen out along the pipeline, the pulsing flow should not represent an issue for the engine. However, the pulsating flow, with the additional back-and-forth stroke motions of the PD pumps induce vibrations in the pipe system and possible cavitations. Considering the LH_2 applications, vibrations can accelerate the boil-off phenomena and create additional GH_2 in the pipeline system which will reduce considerably the efficiency of the pumps. The centrifugal pump offers an alternative with lower noise and vibrations. [9].

As opposed to PD pumps, centrifugal pumps have a high capacity, being able to deliver the required mass flows. Both piston and vane pumps can reach large weights due to the reduced operational speeds, requiring a larger pump to satisfy the required fuel flow [31]. In terms of operating pressure, centrifugal pumps perform the worst while the piston pumps support the highest pressures. Nevertheless, the pumps will operate with only LH_2, not GH_2, which does not require a high pressure. An overview of the aforementioned performance criteria is presented in Table 9.3.

Table 9.3: Overview operating performance of pumps

	Centrifugal	Vane	Piston
Operational viscosity	low	extremely low	low
Flow behaviour	smooth	pulsing	pulsing
Vibrations	low	high	high
Mass flow capacity	high	low	low
Operating pressure	low	high	extremely high

Brewer [31] highlights additional aspects related specifically to LH_2 applications. Piston pumps had incidents of leakage. Considering the A320-HACK application, the centrifugal pump looks like the best candidate. An additional consideration is the drive system of the pump. It can be either based on bleed-air, shaft drive or electrical power. Considering the general aim of electrifying the A320-HACK as discussed in Section 20.1, all the pumps that will be used in the hydrogen fuel system will be electrified.

9.3.3 Pump Characteristics

For the purpose of this report, the main concern was investigating the boost pump. The boost pump is responsible for delivering the fuel from the tanks to the engines, and is highly dependent on the fuel system lay-out. The high-pressure pump is mounted at the engine level, so it was considered that only the required mass flow would change its characteristics. Thus, it was decided to keep the same characteristics as the ones presented for the high pressure pump in Brewer [31].Using the inlet pressure of the high-pressure pump from Brewer, the outlet pressure of the boost pump can be computed. Using the mass flow Equation 9.12, the velocity of the LH_2 through the pipes can be computed. This allows p_1, the pressure at the outlet of the boost pump to be calculated.

$$\dot{m} = \rho v A \tag{9.12}$$

This velocity can be further used in Bernoulli's Equation 9.13 where the pressure losses are calculated using the Darcy-Weisbach Equation 9.14. As a turbulent regime is expected, the Swamee-Jain Equation 9.15 is used [10]. ϵ is the absolute roughness of the pipe and depends on the material that is used. For steel, the value is around 0.00015 ft [10].

$$p_1 + \frac{1}{2}\rho v_1^2 + \rho g h_1 = p_2 + \frac{1}{2}\rho v_2^2 + \rho g h_2 + p_{loss} \tag{9.13}$$

$$\frac{\Delta p}{L} = f\frac{\rho}{2}\frac{v^2}{D} \tag{9.14}$$

$$f = \frac{0.25}{\left(\log_{10}\left(\frac{\epsilon}{3.7D} + \frac{5.74}{R_e^{0.9}}\right)\right)^2} \tag{9.15}$$

[9] https://www.michael-smith-engineers.co.uk/resources/useful-info/positive-displacement-pumps, accessed: 11-Jun-2021

[10] https://tinyurl.com/ywzceaue, accessed: 14-Jun-2021

Based on the outlet pressure of the pump, and inlet pressure of pump (assumed equal to the pressure of the tank) the power required by the pump can be computed using Equation 9.16 [11]. q stands for the flow and is measured in m^3/h. The result is divided by the efficiency of the pump in order to obtain the total power that needs to be delivered to the pump.

$$P_{kW} = \frac{q\Delta p}{2.6 \cdot 10^6} \tag{9.16}$$

An overview of the used inputs is provided in Table 9.4. The height and the pipe length correspond to the path from a wing mounted tank to the engine. A required power of 1.19 kW was estimated for the boost pump.

Table 9.4: Boost pump calculations overview

Parameter	Value	Parameter	Value
High pressure pump inlet pressure [bar]	3.45 [31]	High-pressure pump height[m]	0
Fuel mass [kg/s]	0.251	Boost Pump Efficiency [-]	0.6 [12]
Pipe diameter[cm]	1.7	Boost pump inlet pressure [bar]	1.2
Pipe length [m]	5.1	Boost pump outlet pressure [bar]	3.55
Boost pump height[m]	0.38	Boost pump power[kW]	1.19

9.3.4 Heat Exchanger

Because most of the hydrogen is still liquid when it leaves the high-pressure pump, it needs to pass through a heat exchanger, which is able to vaporize and heat up the hydrogen. Based on the design from G. Daniel Brewer [31] and Cryoplane [33], three different heat exchangers are used to bring the hydrogen from 30 K to 600 K. This is because the lower the temperature of injected hydrogen, the more heat from combustion is wasted to heat up the fuel. The heat exchanger can be seen in Figure 9.5. Bleed air from the compressor, which is used to cool down the turbine vanes and blades, is passed through the first heat exchanger. Then, the lube oil from the engine is passed through the second heat exchanger. Finally, the third heat exchanger consists of an annular section surrounding the exhaust nozzle.

The design of the heat exchanger is performed by considering the most critical situation, namely the moment at which the mass flow of hydrogen into the combustion chamber is highest. This happens during take-off, therefore values of mass flow, temperature and pressure are obtained from Table 10.10 if not specified differently.

Bleed Air Heat Exchanger

A cross-flow heat exchanger is used to transfer the heat of bleed air at a temperature of 874 K ($= T_{0,3}$ from Table 10.10) to the LH_2. The ϵ-NTU method from the book of Ghoshdastidar is used to design this heat exchanger [34]. This method computes the required contact area (A) between both fluids.

The heat which is transferred from the bleed air to the hydrogen can be computed using Equation 9.17. Furthermore, the temperature of hydrogen at the outlet of the heat exchanger can be computed with the same equation. The effectiveness is then found using Equations 9.18 and 9.19. The Number of Transfer Units (NTU) is found using the chart from Figure 9.7, which is then used to compute the heat exchanger area with Equation 9.20.

[11] https://www.engineeringtoolbox.com/pumps-power-d_505.html, accessed: 14-Jun-2021
[12] https://www.pumpsandsystems.com/pump-efficiency-what-efficiency, accessed: 10-Jun-2021

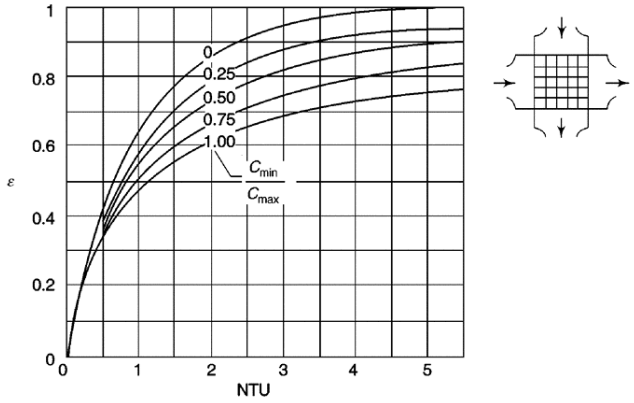

Figure 9.7: Effectiveness-NTU chart for a crossflow heat exchanger with both fluids unmixed [34]

$$q = \dot{m}_{air} cp_{air} \Delta T_{air} = \dot{m}_{H2} cp_{H2} \Delta T_{H2} \tag{9.17}$$

$$C_h = \dot{m}_{air} cp_{air} \tag{9.18a}$$

$$C_c = \dot{m}_{H2} cp_{H2} \tag{9.18b}$$

$$\text{if } C_h < C_c: \quad \epsilon = \epsilon_h = \frac{T_{h_1} - T_{h_2}}{T_{h_1} - T_{c_1}} \tag{9.19a}$$

$$\text{if } C_h > C_c: \quad \epsilon = \epsilon_c = \frac{T_{c_2} - T_{c_1}}{T_{h_1} - T_{c_1}} \tag{9.19b}$$

$$NTU = \frac{UA}{C_{min}} \tag{9.20}$$

The mass flow of bleed air and its temperature at the exit of the heat exchanger are obtained from Brewer [31], and the overall heat transfer coefficient (U) is based on Ghoshdastidar [34]. The specific heat of air is found by taking the average value between the inlet and outlet air temperatures [13]. The specific heat of hydrogen does vary with temperature, therefore Figure 9.8 was used to find the average cp of hydrogen in the heat exchanger [14]. The values mentioned are shown in Table 9.5.

Table 9.5: Inputs for the design of the bleed air heat exchanger

Inputs	Value	Unit
U	180	W/m^2K
cp_{air}	1100	J/kgK
cp_{H2}	15230	J/KgK
$\dot{m}_{air}$	0.83	kg/s
$\dot{m}_{H2}$	0.145	kg/s
$T_{h_1} (= T_{0,3})$	874	K
$T_{h_2} (= T_{turb})$	300	K
$T_{c_1} (= T_{H2_{in}})$	30	K

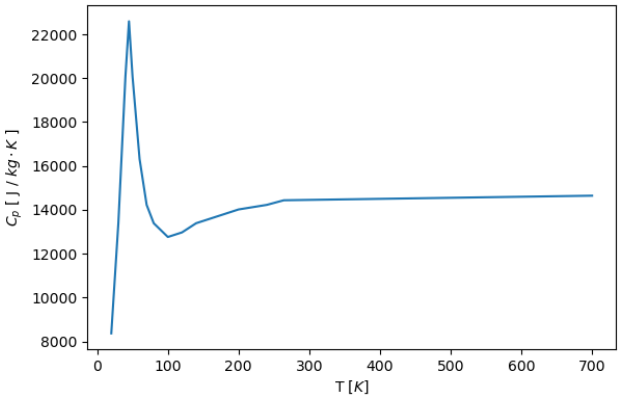

Figure 9.8: Specific heat of hydrogen from 20 K to 700 K

The outcome from the ϵ-NTU method is a hydrogen outlet temperature (T_{c_2}) of 275 K and a required heat exchanger area of 1.2 m^2. In terms of temperature, this means that the hydrogen has already reached a gaseous state, but it is desirable to increase the temperature further. Considering the heat exchanger area, if a compact heat exchanger is used, the surface area per unit of volume can be assumed to be 700 m^2/m^3 or greater. Using this lower limit, the heat exchanger requires a volume of less than 2 L. Such a small volume can be fit into the cowling of the engine.

The effect of having bleed air taken from the compressor has only been considered for the take-off phase, hence other phases require less bleed air. This is not addressed and is an item for further consideration. Using more bleed air than required during some phases could lead to hydrogen reaching its self ignition temperature. Also, because bleed air mass flow is only considered during take-off, the effects of bleed air have not been considered in the engine cycle computations from Chapter 10. This effect should also be taken into account in future design work to predict the engine cycle more accurately, because as was stated in Section 10.3, the bleed air can cause up to 8% thrust losses.

[13] https://www.engineeringtoolbox.com/air-specific-heat-capacity-d_705.html, accessed: 5-Jun-2021

[14] https://www.bnl.gov/magnets/Staff/Gupta/cryogenic-data-handbook/Section3.pdf, accessed: 5-Jun-2021

Lube Oil Heat Exchanger

To further heat up the hydrogen, the lube oil is used in a second cross-flow heat exchanger. Therefore, the method used to design the bleed air heat exchanger (Equations 9.17 to 9.20) is used again. The inlet and outlet temperatures of the lube oil, as well as its mass flow, are retrieved from Brewer [31]. The specific heat of oil is obtained from Ghoshdastidar [34], and that of hydrogen from Figure 9.8. All the required inputs to design this heat exchanger are given in Table 9.6.

Table 9.6: Inputs for the design of the bleed air heat exchanger

Inputs	Value	Unit	Inputs	Value	Unit
U	180	W/m^2K	cp_{oil}	2000	J/kgK
$T_{h_1}(=T_{oil_{in}})$	378	K	cp_{H2}	13810	J/KgK
$T_{h_2}(=T_{oil_{out}})$	343	K	$\dot{m}_{oil}$	0.96	kg/s
$T_{c_1}(=T_{H2_{in}})$	275	K	$\dot{m}_{H2}$	0.145	kg/s

This heat exchanger increases the temperature of hydrogen to 308.5 K using a surface area of 1.1 m^2. Assuming again that a compact heat exchanger is used with an area to volume ratio of 700 m^2/m^3, the required volume is of 1.5 L. This heat exchanger could therefore be stored within the engine cowling.

Exhaust Nozzle Heat Exchanger

In order to elevate the temperature to 600 K, the hydrogen is passed through a channel which is wrapped around the exhaust nozzle as shown in Figure 9.9. It consists of two concentric truncated cones, in between which the hydrogen flows to receive heat from the exhaust gases. But for simplicity they are assumed to be concentric cylinders which are separated by a distance equal to the difference between outer and inner radius.

To design this heat exchanger, heat transfer in Equation 9.21 is defined as a function of the Log-mean Temperature Difference (LMTD). The expression for LMTD is dependent on the temperature differences at the inlet and outlet of the heat exchanger, and is given by Equation 9.22. The overall heat transfer coefficient is computed using Equations 9.23 and 9.24, which are dependent on the properties of the fluid and the dimensions of the heat exchanger [34].

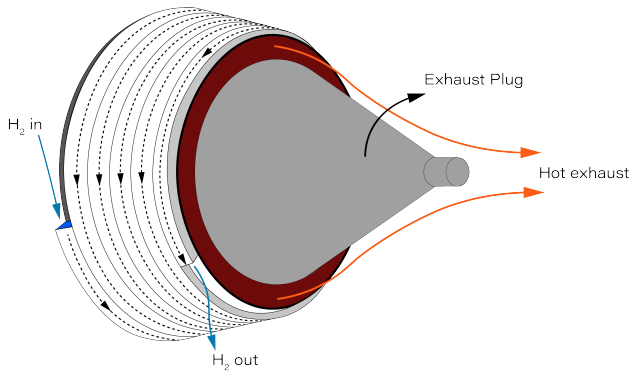

Figure 9.9: Heat exchanger around the exhaust nozzle of the engine

$$q = UA(\text{LMTD}) \tag{9.21}$$

$$\text{LMTD} = \frac{\Delta T_0 - \Delta T_L}{\ln\left(\frac{\Delta T_0}{\Delta T_L}\right)} \tag{9.22}$$

$$U = \frac{1}{\frac{1}{h_i} + \frac{1}{h_o}} \tag{9.23}$$

$$\frac{hD_h}{k_f} = 0.023\,(\text{Re})^{0.8}\,(\text{Pr})^n \tag{9.24}$$

Heat transfer is computed using Equation 9.17, which allows to also find the end temperature of the exhaust gas. Furthermore, the way this design problem is solved is by iterating the dimensions of the inner and outer cylinders. The values of inner and outer diameter (D_i is the nozzle diameter and D_o is the nozzle diameter plus the thickness of the hydrogen conduct) are changed until a feasible design is found. The length required for the heat exchanger is found from the contact area $A(=\pi D_{nozzle} L_{nozzle})$, and is also checked after each iteration to confirm that the heat exchanger fits on the nozzle.

The fixed inputs used to perform the iterations are given in Table 9.7. Then by varying the dimensions of the nozzle, plug and hydrogen conduct it was possible to find a feasible design. The resulting nozzle

with heat exchanger dimensions can also be found in Table 9.7.

Table 9.7: Fixed inputs and outputs of the nozzle heat exchanger design

Fixed Inputs						Outputs		
Inner Section			Outer Section					
Parameter	Value	Unit	Parameter	Value	Unit	Parameter	Value	Unit
$T_{air_{in}}$	752	K	$T_{H2_{in}}$	308.5	K	D_{nozzle}	0.9	m
			$T_{H2_{out}}$	600	K	D_{plug}	0.8	m
$\dot{m}_{air}$	35	kg/s	$\dot{m}_{H2}$	0.145	kg/s	$t_{H2\ conduct}$	5	mm
μ_{air}	$4.25 \cdot 10^{-5}$	Ns/m^2	μ_{H2}	$1.13 \cdot 10^{-5}$	Ns/m^2	U	1130	W/m^2K
$k_{f_{air}}$	0.075	W/mK	$k_{f_{H2}}$	0.377	W/mK	$T_{air_{out}}$	736	K
cp_{air}	1150	J/kgK	cp_{H2}	14650	J/KgK	L_{nozzle}	0.5	m

9.3.5 Fuel Block Diagram

The fuel block diagram Figure 9.10 depicts the system securing the flow of the fuel from the tanks to the turbofan engines and the DPU. Since the fuel system for the kerosene will closely resemble the original fuel system of the A320neo, the focus of this section is the hydrogen fuel system. Figure 9.10 is a combination of the A320 [35] and the Cryogenic Plane fuel block diagrams [36].

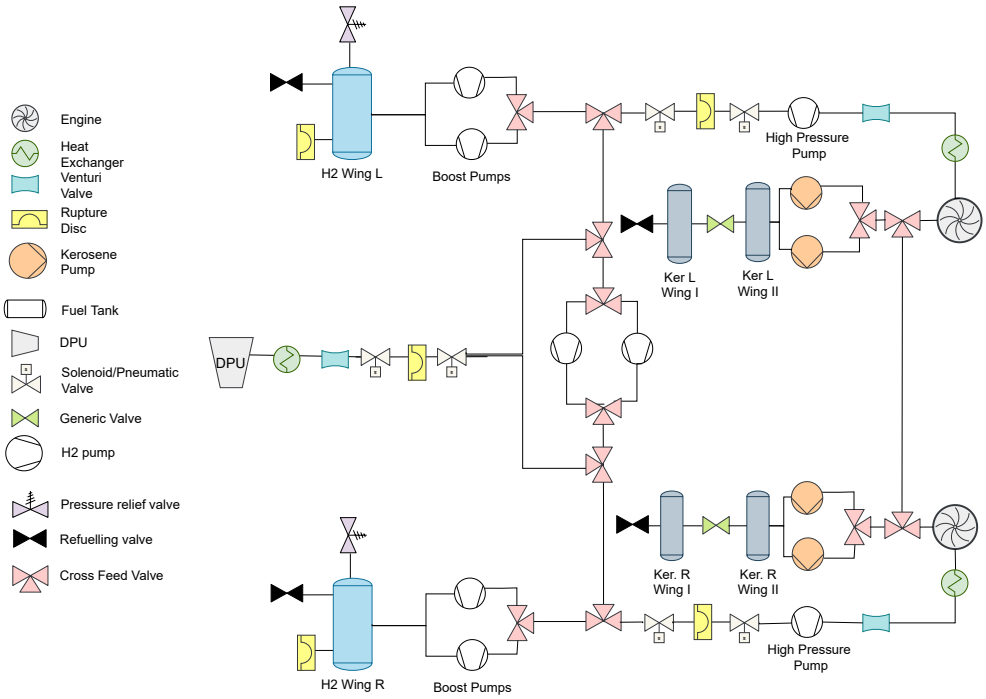

Figure 9.10: Fuel block diagram A320-HACK

The hydrogen fuel tanks are filled through the refuelling valves, which shall provide proper sealing to prevent hydrogen leakage. The safety is ensured by two components per tank, namely a pressure relief valve and a rupture disc. As mentioned in Section 9.3.3, two boost pumps are present at the tank level. The flow of the hydrogen is controlled by solenoid valves, which come in pairs for redundancy. The hydrogen is then passed through the high-pressure pump and a Venturi valve for a more strict mass flow management. Lastly, the hydrogen is passed through a heat exchanger as the temperature needs to be increased to a certain level before it enters the engine. The hydrogen goes through the same type of components for reaching the DPU.

The kerosene tanks have a refuelling valve for filling the tanks. Further, similarly to the hydrogen system, the kerosene fuel system is interconnected with a set of pipes and valves, guaranteeing that each engine can draw fuel from any of the tanks. Besides, the flow of the fuel is ensured by a set of pumps, where 2 pumps are present for each tank.

9.4 Limitations & Recommendations

Being only the preliminary design of the fuel system, several recommendations can be made for further development. Additional phenomena could be considered for the insulation of the tank. One of them is sloshing, caused by the liquid dynamics due to plane movement. These movements can increase the boil-off rate, requiring better insulation. Another aspect that could be considered is the effect of the aerodynamic friction on the tank and whether the critical storage condition of the tank is changed. Additionally, looking into separated vacuum jackets instead of a continuous one is recommended for ensuring redundancy of the insulation system. For the mechanical design of the tank, additional investigations on the stress concentrations, induced by the cut-outs for the inlet and the outlet, should be performed. Moreover, the interaction between the layers and the shear stresses induced by them could be analysed.

10 | Main Engines Design

The performance and climate impact of an aircraft heavily depend on engines. One of the engine options of the A320neo, LEAP-1A[1], was redesigned to account for the engine improvements in the coming years and to accommodate the Hydrogen Assisted Combustion of Kerosene system. Section 10.1 states the most relevant engine requirements. In Section 10.2 the hydrogen to kerosene energy split is made, as well as the thrust, speed and altitude analysis. The A320-HACK engine is then designed with a cycle analysis in Section 10.3. The emissions related to the combustion process are evaluated in Section 10.4.

10.1 Requirements

The most relevant main engine system requirements are as follows.

UR-PROP-01 The amount of usable energy stored in H2 shall not exceed 1/2 of the energy content in kerosene.

SR-PROP-30 The main engines shall provide backup power to essential subsystems.

SR-PROP-31 The main engines shall be able to run on hydrogen, kerosene, or a mixture of the two.

SR-SUST-01 The cruise emissions of NO_x, CO, unburnt hydrocarbon and soot emission shall be at least 30% lower than A320neo.

SR-SUST-02 The NO_x, CO, unburnt hydrocarbon and soot emission for the Landing and Take-Off (LTO) cycle shall be reduced by at least 50% when compared to the A320neo.

10.2 Mission Analysis

Section 10.2.1 describes the energy and mass split between hydrogen and kerosene during a mission with the maximum fuel capacity on-board. Then, the thrust, speed, and altitude for each phase of a sample mission are described in Section 10.2.2.

10.2.1 Energy & Mass Split

To minimise the environmental impact of the A320-HACK, only hydrogen is used on ground and for the dedicated power unit (DPU). Hydrogen mixed with kerosene is used in all flight phases, for which the hydrogen to kerosene ratio was computed by firstly finding the hydrogen allocated to the DPU and ground.

[1] https://www.safran-aircraft-engines.com/commercial-engines/single-aisle-commercial-jets/leap/leap-1a, accessed:05-May-2021

The A320neo has at most 23,859 L of usable kerosene on-board. Assuming that the A320-HACK carries the same amount of energy, and knowing that at most 1/3 of that should be stored as hydrogen, the volume, mass, and energy split between hydrogen and kerosene for the A320-HACK was summarised in Table 10.1. The lower heating value and density of kerosene and hydrogen, needed for the conversions from volume to energy and mass are in Table 10.2.

Table 10.1: Maximum fuel volume, mass, and energy available for the A320neo and the A320-HACK

Aircraft	**A320neo**	**A320-HACK**	
Fuel type	Kerosene	Hydrogen	Kerosene
Volume $[L]$	23,859	32,462	15,906
Mass $[kg]$	19,326	2,308	12,884
Energy $[MJ]$	831,009	277,003	554,006

Table 10.2: Lower heating value (LHV) and density (in liquid form) of kerosene and hydrogen

Fuel type	**Kerosene**	**Hydrogen**
LHV $[MJ/kg]$	43	120
Density[a] $[kg/L]$	0.81	0.071

For a maximum range mission, the DPU needs 140.7 kg of hydrogen. From the engine cycle analysis, explained in Section 10.3, the fuel flow of hydrogen in idle and taxi is 0.017 and 0.067 kg/s, respectively. Taking an average idling and taxiing time of 5 and 15.5 minutes[2]. The mass required for these phases is presented in Table 10.3, with the mass and energy percentages of hydrogen and kerosene during the flight phases added. In case one or more tanks are not completely full, the values in Table 10.1 change, but the analysis that followed sits upon the same logic.

Table 10.3: Fuel mass and energy usage for the A320-HACK

Fuel Usage	**Hydrogen**				**Kerosene**
	DPU	Idle	Taxi	Flight phases	Flight phases
Mass $[kg]$	141	5.1	62.3	2,100 (14.02%)	12,884 (85.98%)
Energy $[MJ]$	16,884	612	7,477	252,030 (31.27%)	554,006 (68.73%)

10.2.2 Thrust Required

The thrust required for a sample mission with a range of 3200 km, a starting weight equal to the maximum ramp weight and a maximum cruise altitude of 11600 m was calculated, as detailed in this section. The duration of the various flight phases of the mission are shown in Table 10.4, which also shows the contributions to the required thrust for each phase. There, x means the contribution is accounted for in that phase and the $(-)$ indicates that it has a negative contribution

Table 10.4: Duration and thrust contributions for each mission phase

Phase	Taxi-out	Take-off	Climb	Cruise	Descent	Landing & Taxi-in
Duration $[min]$	7.5	1	20	217	18	8
Thrust to overcome drag	x	x	x	x	x	x
Thrust to accelerate		x	x		x (-)	x (-)
Thrust to overcome static friction	x	x				
Thrust to overcome dynamic friction	x	x				x
Thrust to climb			x		x (-)	

[2]The total 15.5 min of taxi includes 7.5 min of taxi-out and 8 min of taxi-in, from a sample mission

The thrust to overcome drag was calculated using the sum of forces in the X_b body axis[3], using Equation 10.2 and assuming the thrust acts along X_b. In turn, C_D is found via Equation 10.1.

$$T = D = C_D \frac{1}{2} \rho V^2 \quad (10.1) \qquad C_D = C_{D_0} + \frac{C_L}{\pi A e} \quad (10.2)$$

In Equation 10.1, C_{D_0}, A, and e are taken from the aerodynamic analysis in Chapter 14. The C_L was estimated to be 1.3 in take-off by using Equation 10.3, where $(C_{L_{max}})_{TO} = 1.6$ was estimated from the average range of $1.6 - 2.2$ [37]. During taxiing, C_L is assumed to be 0.1, the average C_L at zero angle of attack for four supercritical airfoils [38], while for climb, cruise, and descent phases, C_L is calculated using Equation 10.4. The velocity at these stages, given in Table 10.5, was available from the same sample mission data from which the phases' duration were taken from.

$$C_{L_{TO}} = \frac{(C_{L_{max}})_{TO}}{1.1^2} \quad (10.3)$$

$$C_L = \frac{2W}{\rho V^2 S} \quad (10.4)$$

Table 10.5: Velocity for taxi, lift-off, cruise and touch down for a sample mission

Phase	Taxiing	Lift-off	Cruise	Touchdown
Velocity [m/s]	13	85	230	68
Mach [m/s]	0.038	0.25	0.78	0.2

Using the climb/descent rates and the acceleration/deceleration, the velocity at any point during the mission could be calculated. This velocity was corrected for the compressibility of air, when necessary, using Equation 10.5 where V_{TAS} is true airspeed (corrected for compressibility), V_{EAS} and ρ the air speed and density at that altitude, respectively, and ρ_0 the sea-level air density. The accelerations were assumed constant during take-off, climb, and descent, and calculated using Equation 10.6. For the take-off procedure, an acceleration of 1.42 m/s^2 was obtained. The thrust required to accelerate during these phases was calculated using $T_{acc} = m \cdot a$.

$$V_{TAS} = V_{EAS} \sqrt{\frac{\rho_0}{\rho}} \quad (10.5) \qquad a = \frac{dv}{dt} \quad (10.6)$$

For the weight of A320-HACK throughout the flight analysis, the maximum ramp weight MRW was taken as the initial weight input. Depending on the fuel flows during the phases and their duration, the weight decrease due to the consumed fuel was computed and subtracted from the weight at the start of each specific phase. For the first iteration, the fuel flows of the A320neo were taken. Then, the fuel flows determined from the engine cycle analysis (see Section 10.3), such that the required engine thrust was met, were used. This iteration was performed until the results converged. The final fuel flows are presented in Table 10.10 and Section A.2.

Next, the thrust to overcome the dynamic and static friction was calculated using Equation 10.7 and 10.8, where μ is the dynamic friction coefficient, equal to 0.04 [37]. For the touchdown to the stop-time, this is the braking friction coefficient. The static friction coefficient required to overcome the static friction of the tires against the runway is taken as 4 times the rolling friction coefficient.

$$(T_{friction})_{dyn} = \mu_{dyn}(W - L) \quad (10.7) \qquad (T_{fric})_{stat} = 4\mu_{dyn}(W - L) \quad (10.8)$$

Finally, the thrust required to climb and descend was calculated using Equation 10.11, where ROC and P_{req} were found through Equation 10.9 and 10.10.

$$ROC = \frac{altitude\ change}{duration} = \frac{P_{req}}{W} \quad (10.9) \qquad P_{req} = T_{ROC} \cdot V \quad (10.10) \qquad T_{ROC} = \frac{ROC \cdot W}{V} \quad (10.11)$$

For climb, ROC was found to be 9.67 m/s and for the descent phase $ROD = 10.74$ m/s is the rate of descent. The total thrust required at various phases of the flight, from both engines combined, is presented in Table 10.6. The touchdown value is the 'reverse thrust'.

[3] https://dodlithr.blogspot.com/2011/09/airplanes-stability-axis.html, accessed:21-Jun-2021

Table 10.6: Thrust required during the mission

Phase	Taxi out	Start of take-off	Lift-off	Mid-climb	Cruise	Start of descent	Mid-descent	Touchdown	Taxi in
Thrust required [*kN*]	29.6	231.8	160.3	93.9	42.0	102.6	67.4	230 (-)	30.0

10.3 Engine Cycle Analysis & Design

An engine cycle analysis was performed to design the A320-HACK's engine and evaluate its performance. In Section 10.3.1, the method used in the engine cycle analysis is briefly explained, after which HACK's engine parameters are estimated in Section 10.3.2. Then, Section 10.3.3 presents the main results of the engine cycle analysis, while Section 10.3.4 discusses how the new engine parameters can be attained.

10.3.1 Engine Cycle Analysis Method

The engine cycle analysis calculations followed the TU Delft approach. In this subsection, only the equations derived are described, with the station numbering corresponding to that in Figure 10.1. Firstly, the mass flow of air going through the fan was computed using $\dot{m}_{air} = \rho_0 A_0 v_0$. Here, ρ_0 is the air density and v_0 the speed of the aircraft. A_0 was obtained using Figure 10.2. For take-off and cruise, an M_2 of 0.425 and 0.55 were used to have an $\dot{m}_{air}$ as close as possible to the one in the tutor's data. For the remaining flight phases, $M_2 = 0.5$ was taken. For taxi and idle, in which $M_0 < 0.1$, the value at $M_0 = 0.1$ was still used, but for $M_2 = 0.4$. This was assumed to represent A_0/A_2 for a $M_0 < 0.05$ and $M_2 < 0.4$.

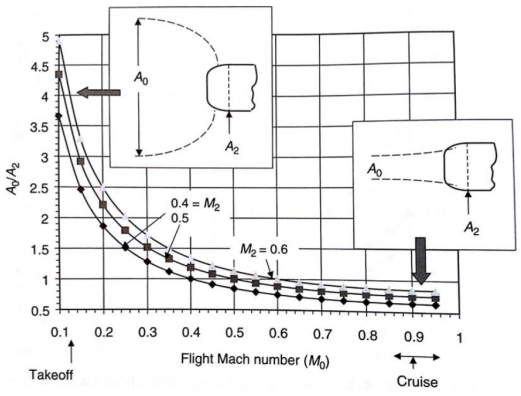

Figure 10.1: Schematic of a turbofan engine [39]

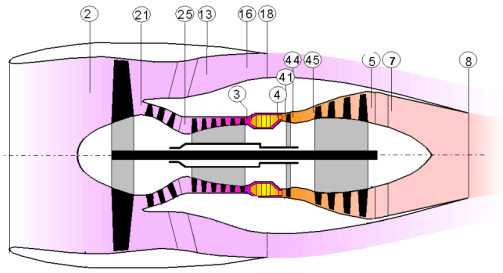

Figure 10.2: Variation of capture area with Mach number from take-off to cruise [40]

Further, the thrust specific fuel consumption (TSFC) was found using Equation 10.12 and 10.13, where T_{total} is the total net thrust produced.

$$TSFC\ [g/kN/s] = \frac{\dot{m}_{fuel}}{T_{total}} \qquad (10.12)$$

$$TSFC\ [MJ/kN/s] = \frac{\dot{m}_{fuel} \cdot LHV_f}{T_{total}} \qquad (10.13)$$

The equivalence ratio, ϕ, was computed using Equation 10.14. The stoichiometric ratio depends on the amount of hydrogen and kerosene being burned since they impact the combustion's chemical equation. For every mole of kerosene burned, Table 10.7 gives the number of moles of hydrogen, oxygen and nitrogen needed for a complete combustion. Z is found with Equation 10.15, where M stands for molar mass. Kerosene was assumed to be composed of 74% decane, $C_{10}H_{22}$, 15% n-propylbenzene, C_9H_{12}, and 11% cyclononane, C_9H_{18}, and its molar mass was obtained accordingly.

$$\phi = \frac{\dot{m}_{fuel}/\dot{m}_{air}}{(\dot{m}_{fuel}/\dot{m}_{air})_{stoic}} \quad (10.14)$$

$$Z = \frac{\dot{m}_{H2}}{\dot{m}_{ker}} \cdot \frac{M_{ker}}{M_{H2}} \quad (10.15)$$

Table 10.7: Number of moles of H_2, O_2 and N_2 needed for a complete combustion

Reactant	Fuel		Oxidizer	
	Kerosene	H_2	O_2	N_2
# Moles	1	Z	$14.76 + Z/2$	$55.45 + 1.88Z$

Equation 10.16 gives the stoichiometric fuel to air ratio, where n is number of moles of each species.

$$(\dot{m}_{fuel}/\dot{m}_{air})_{stoic} = \frac{n_{ker}M_{ker} + n_{H_2}M_{H_2}}{n_{O_2}M_{O_2} + n_{N_2}M_{N_2}} \quad (10.16)$$

To estimate the produced emissions, topic discussed in Section 10.4, the equivalence ratio in the primary zone of the combustion chamber was needed. The combustion chamber was simplified to consist of only a primary (PZ) and a dilution zone (DZ), as shown in Figure 10.3, and it was assumed that all fuel is burned in the PZ. Note that the schematic shows only half of the upper/bottom part of the cross-section of the LEAP-1A annular combustion chamber (see Figure 10.4). In Figure 10.3, $X\%$ is the amount of air entering the PZ while $Y\%$ that injected in the DZ in order to cool the air before it enters the turbine, with $X + Y = 100\%$. The equivalence ratio in the OZ is calculated with Equation 10.14, by taking $\dot{m}_{air} = \dot{m}_{core} \cdot X$. The percentage X and Y are different depending on which fuel type or mixture is being burned, such that a certain minimum equivalence ratio is assured. The values used are presented in Table 10.8. To accommodate the different values of X, a flap system is used on the inlet of the combustion chamber, as discussed in Section 10.3.4.

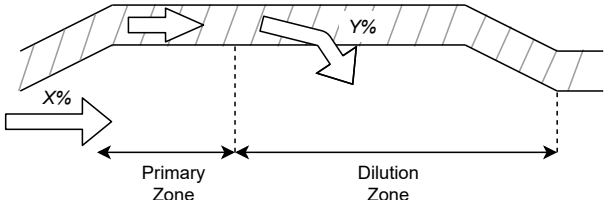

Figure 10.3: Schematic of a simplified combustion chamber

Figure 10.4: Twin-Annular, Pre-Mixing Swirler Combustor of the LEAP-1A engine[4]

Table 10.8: Percentage of air injected to primary zone, X, and resulting primary zone's minimum equivalence ratio, ϕ

Fuel used	X [%]	Minimum ϕ
H_2	73	0.25
H_2 & Kerosene	50	0.45
Kerosene	32	0.6

Through an enthalpy balance, the temperature at the end of the PZ was estimated. Assuming an adiabatic reaction at constant pressure, the equation $\Delta h_{reactants} = \Delta h_{products}$ applies [41], from which Equation 10.17 and 10.18 were derived. The former corresponds to the enthalpy balance between the combustion chamber's entrance and the end of the PZ, while the latter to that between the end of the PZ and the combustion chamber's exit. It was assumed that the specific heat capacity, c_p, was constant due to the difficulty of finding c_p values for kerosene at different temperatures. A value of $c_{p_{gas}} = 1150\ J/kg/K$ and $c_{p_{air}} = 1000\ J/kg/K$ was used. This simplification means Equation 10.17 and 10.18 are not fully accurate, and each gives a slightly different value for T_{PZ}. This variable was thus estimated by taking an average of the two computed values. The highest error found was for the climb

[4] https://www.cfmaeroengines.com/engines/leap/, accessed:21-Jun-2021

phase and equaled 3.79% for the analysis of A320neo and 1.49% for that of A320-HACK.

$$\dot{m}_{fuel} LHV_f = (X\dot{m}_{core} + \dot{m}_{fuel}) c_{p_{gas}} (T_{PZ} - T_{0,3}) \tag{10.17}$$

$$(X\dot{m}_{core} + \dot{m}_{fuel}) c_{p_{gas}} (T_{0,4} - T_{PZ}) = (Y\dot{m}_{core}) c_{p_{air}} (T_{0,3} - T_{0,4}) \tag{10.18}$$

Finally, in the A320-HACK, unlike the A320neo, the DPU is responsible for the compressed air, e.g. for the cabin air, and for the power for the electrical systems. The engines work as a backup for these tasks. A very small percentage of bleed is still removed from the compressor stage of the engine, after which it is cooled by being in contact with the liquid hydrogen pipes and used to cool the turbine blades[5]. Nonetheless this air is at most 1.7% of the engine's core air. Besides, it joins the latter at the turbine stage, meaning that all the initial core air is still expelled by the exhaust nozzle. This air to cool the turbine stage has hence a negligible effect on the engine's performance and that the main engines are practically solely used to provide thrust. This results in an improved engine efficiency: according to [42], providing bleed air can reduce the engine's thrust by 8% in the worst case scenario. The engine of A320-HACK is a geared turbofan with a variable exit nozzle[6]. The engine cycle analysis does not account for neither of these factors. Therefore, the results presented in Section 10.3.3 are a conservative estimates of the actual results.

Verification & Validation

The Python code for engine cycle analysis was verified by hand calculations as well as by cross-checking the outputs with those from two exercises present in the *Aero Engine Technology* course. Concerning validation, only cruise TSFC was found to be publicly available. The Python model computed $TSFC = 12.76\ g/kN/s$, compared to a $TSFC = 14.40\ g/kN/s$[7]. This gives an error of 11.39%. Total range, determined in Chapter 15, using the estimated fuel flows was also validated.

10.3.2 Engine Parameters

Due to the entrance into service gap, engine of A320-HACK will be technologically more advanced than LEAP-1A and improved engine parameters and turbomachinery were analysed. The take-off and cruise parameters of LEAP-1A were estimated from data from directly or by retrofitting, and on SAFRAN's available data[8]. The main difference in engine parameters for different phases stems from the operating altitude. Thus, for the ground phases, the same parameters as for take-off were considered. For climb and approach, average between the take-off and cruise value was taken.

An analysis was performed for cruise condition to determine which parameters had the largest impact on the thrust specific fuel consumption (TSFC), as these are likely the ones to be improved in the coming years. Figure 10.5a shows how changing each efficiency impacts the TSFC. As shown, improving the efficiency of the mechanical components and the duct's nozzle results in the highest reduction TSFC. Therefore, these were increased to 0.995 for the A320-HACK's engine. Figure 10.5b zooms in on the efficiency parameters with a lower impact on the TSFC. Out of these, the inlet, combustion chamber (cc), fan, and LPT reduce the TSFC the most. The efficiency of the inlet and cc were increased to 0.995 and 0.9995 as they were already 0.99 and 0.995, respectively. Those of the fan and LPT were increased by 2 percentage points. As for the pressure loss in the combustion chamber, a similar plot of TSFC Vs. pressure loss was obtained, for $0.9 \leq \Pi_{cc} \leq 0.1$. The TSFC reduced approximately the same as for the HPT curve in Figure 10.5b and thus Π_{cc} was increased by 1 percentage point as well.

For the pressure ratios of the fan and compressor stages, either the bypass ratio (BPR) or the overall pressure ratio (OPR) had to be known. The OPR and BPR were determined by looking at the trend

[5] More details are found in Section 9.3.4.

[6] These concepts are discussed in Section 10.3.4.

[7] https://www.ainonline.com/aviation-news/air-transport/2019-08-19/aviadvigatel-mulls-higher-thrust-pd-14s-replace-ps-90a, accessed:05-May-2021

[8] https://www.safran-aircraft-engines.com/commercial-engines/single-aisle-commercial-jets/leap/leap-1a, accessed:05-May-2021

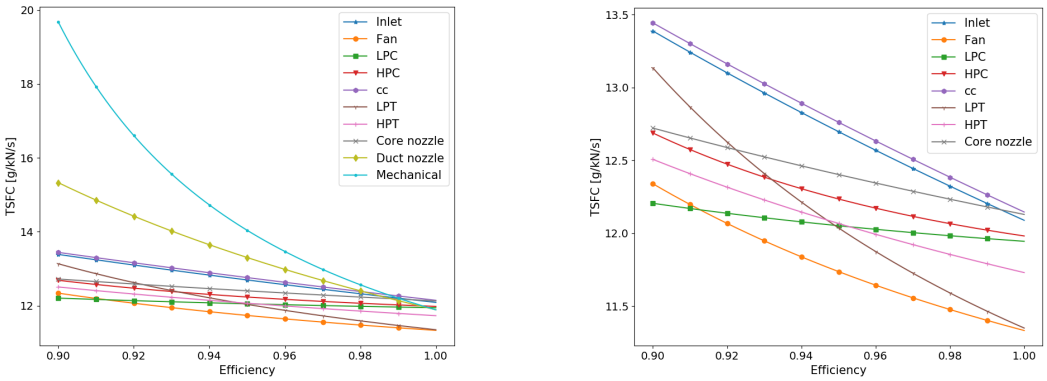

(a) Full graph **(b)** Zoomed in

Figure 10.5: Change in thrust specific fuel consumption with increased efficiency for cruise

of these parameters since 1985 for 13 turbofan engines with a thrust setting similar to the A320-HACK. This is seen in Figure 10.6 and 10.6. These parameters were estimated for 2030 as the A320-HACK shall be delivered in 2035. The OPR was estimated to be 49.87 and the BPR 15.81 for cruise. The errors correspond to the average error between the available data and the trend lines. The new values for the OPR and BPR are 33.81% and 40.59% higher than the ones estimated for LEAP-1A and the same percentage increase was applied to the remaining flight phases. In order to cope with the increased BPR, the engine diameter was increased from 1.89 m to 2.06 m.

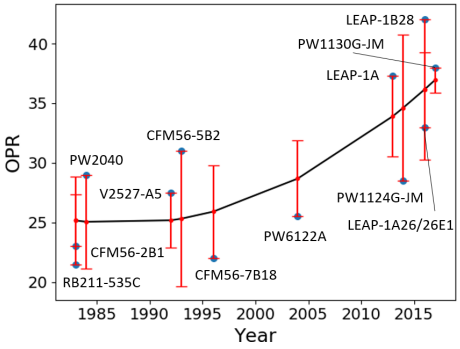

Figure 10.6: Overall pressure ratio as a function of time for 13 turbofan engines for cruise. $R^2 = 0.824$, $RMSE = 1.312$, using a 2nd degree polynomial [43]

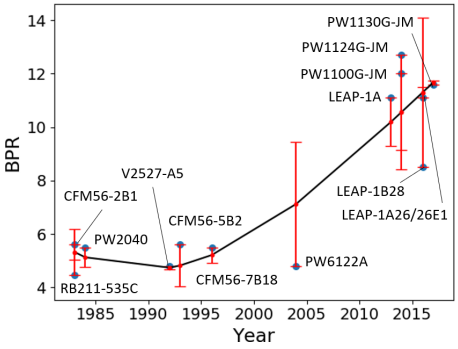

Figure 10.7: By-pass ratio as a function of time for 13 turbofan engines for cruise. $R^2 = 0.607$, $RMSE = 3.987$, using a 3rd degree polynomial [43]

The impact of the high pressure compressor (HPC) pressure ratio on the TSFC on the turbine inlet (TIT). This dependency is visualised in Figure 10.8 for cruise. The green circle is the design point of LEAP-1A, for which $TIT = 1298\ K$ and $\Pi_{HPC} = 9.74$. According to [44] the TIT has been increasing $10K$/year. Assuming that changing the Π_{HPC} increases the TIT by $3K$/year, the new TIT equals 1350 K. To provide the same thrust as LEAP-1A this new temperature, the new design point is at $\Pi_{HPC} = 14.82$, for which a TSFC reduction of 5% resulted. With the estimated $OPR = 49.87$, the low pressure compressor (LPC) pressure ratio becomes $\Pi_{LPC} = 2.37$, compared to the LEAP-1A's 2.69.

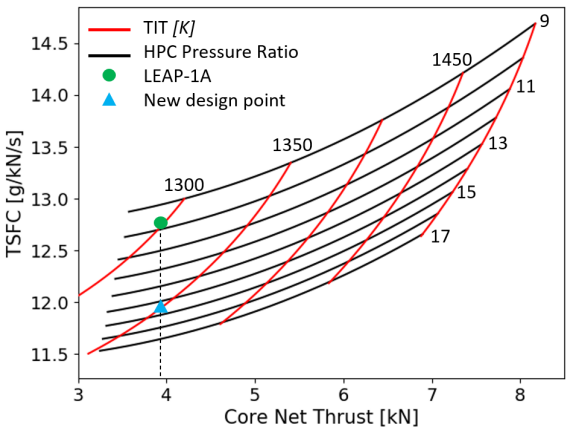

Figure 10.8: TSFC against core's net thrust for several HPC pressure ratios and turbine inlet temperatures for cruise

The fan pressure ratio was then estimated. The LEAP-1A was modified to geared turbofan engine[9]. Geared turbofans allow for a lower fan rotational speed and lower Π_{fan}. It was assumed that this parameter could be reduced by 0.05 in all phases. For instance, for cruise, $\Pi_{fan} = 1.37$ for the new engine compared to $\Pi_{fan} = 1.42$ for LEAP-1A. Having a Π_{fan} lower than 1.4 means that an adjustable duct nozzle is needed [45], topic discussed in Section 10.3.4. The new engine parameters for cruise, alongside their percentage change compared to those of LEAP-1A are given in Table 10.9. The new parameters for the take-off phase are given in Table A.1.

Table 10.9: A320-HACK's engine parameters for cruise

Parameter	η_{inlet}	η_{LPC}	η_{HPC}	η_{mech}	η_{cc}	η_{HPT}	η_{LPT}	$(\eta_{noz})_{core}$	$(\eta_{noz})_{fan}$
HACK's value	0.995	0.91	0.96	0.995	0.9995	0.94	0.96	0.99	0.995
Relative difference	0.51	1.11	1.05	0.51	0.45	1.07	2.13	0.46	0.77
Parameter	η_{fan}	Π_{fan}	Π_{LPC}	Π_{HPC}	Π_{cc}	BPR	OPR	TIT $[K]$	
HACK's value	0.93	1.37	2.37	14.82	0.954	15.81	49.87	1546.08	
Relative difference	2.20	-3.52	-12.05	52.15	1.60	40.59	33.81	17.66	

10.3.3 Engine Cycle Analysis Results

The most relevant outputs for lift-off and cruise are summarised in Table 10.10. Similar tables for the remaining phases are listed in Section A.2.

Table 10.10: Engine cycle analysis for list-off and cruise for the A320-HACK. Temperatures are given in K and pressures in bar. Altitude is in m, mass flows are in kg/s, and thrust, F_N, in kN. TSFC is given in $g/kN/s$

Lift-off						**Cruise**					
M_0	0.249	h	0			M_0	0.78	h	11,600		
$T_{0,3}$	873.89	$p_{0,3}$	45.59	$\dot{m}_{air}$	510.07	$T_{0,3}$	770.60	$p_{0,3}$	14.77	$\dot{m}_{air}$	200.09
$\dot{m}_{fuel}$	0.377	$\dot{m}_{H_2}$	0.118	$\dot{m}_{ker}$	0.259	$\dot{m}_{fuel}$	0.163	$\dot{m}_{H_2}$	0.051	$\dot{m}_{ker}$	0.112
T_{PZ}	1,815	$T_{0,4}$	1,571	$p_{0,4}$	43.54	T_{PZ}	1,817	$T_{0,4}$	1,547	$p_{0,4}$	14.10
F_N	82.27	$F_{N,fan}$	73.09	$F_{N,core}$	9.18	F_N	20.98	$F_{N,fan}$	15.70	$F_{N,core}$	5.28
$TSFC$	4.59	ϕ_{PZ}	0.350	$\phi_{overall}$	0.256	$TSFC$	7.76	ϕ_{PZ}	0.390	$\phi_{overall}$	0.284

Figure 10.9 presents the thrust specific fuel consumption against the net total thrust for both A320neo and A320-HACK, for lift-off and cruise. A320-HACK proved to be more fuel efficient than A320neo both in terms of mass and energy. The exact relative percentage difference between the two aircraft for these phases is presented in Table 10.11. The results for taxi-out, lift-off and cruise while using only kerosene or only hydrogen are given in Table A.6.

[9] The changes to the turbomachinery of the engine and their advantages are elaborated upon in Section 10.3.4

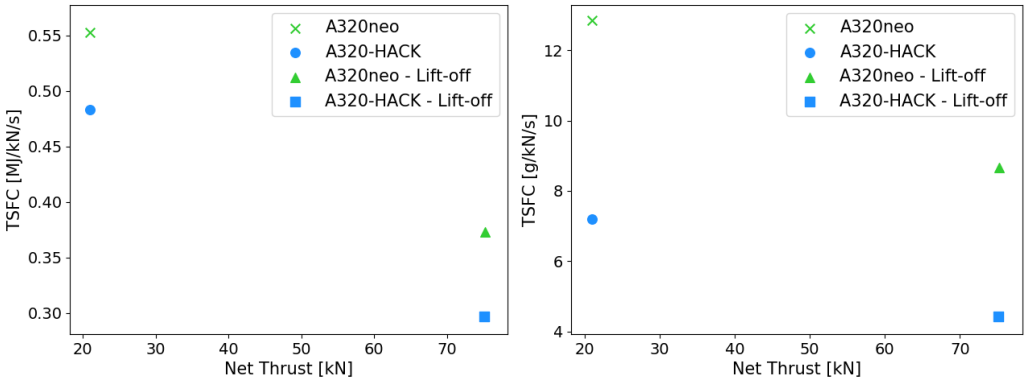

(a) With respect to mass **(b)** With respect to energy

Figure 10.9: Thrust specific fuel consumption (TSFC) for the A320neo and A320-HACK for cruise and lift-off

Table 10.11: Relative percentage different of TSFC for A320-HACK with respect to A320neo

Phase	Relative Difference	
	Mass TSFC	Energy TSFC
Lift-off	-48.96%	-20.39%
Cruise	-44.02%	-12.68%

The temperature versus entropy for A320neo and HACK are compared in Figure 10.10, where the station numbering is found in Figure 10.1. The change in entropy was found with Equation 10.19.
In Figure 10.10, the area enclosed by the green lines corresponds to the work performed by the system. The area below this is the energy lost as heat. Therefore, the T-s diagram allows the evaluation of the thermal efficiency of a cycle. Figure 10.11 shows a simplified version of the T-s diagram, the one used to estimate the thermal efficiency of the two engines. It was assumed that points 0 and 2 coincided since $T_{0,2} = T_{0,0}$ and $p_{0,2}$ is smaller than $p_{0,0}$. Besides, linear relations were assumed from points 2 to 25, 3 to 4, 4 to 8, and 8 to 0. In the figure, W and H are the work done, W, and energy lost, $\dot{Q}_{heat}$, where each corresponds to the area enclosed above or below the diagonal dotted line. The thermal efficiency of the cycle is found with Equation 10.20. Table 10.12 presents the results for the thermal efficiency of A320neo and HACK. The percentage difference for taxi-out, lift-off and cruise are given in Table A.6, for when only kerosene and only hydrogen are used.

$$\Delta s = c_p \ln\left(\frac{T_2}{T_1}\right) - R \ln\left(\frac{p_2}{p_1}\right) \tag{10.19}$$

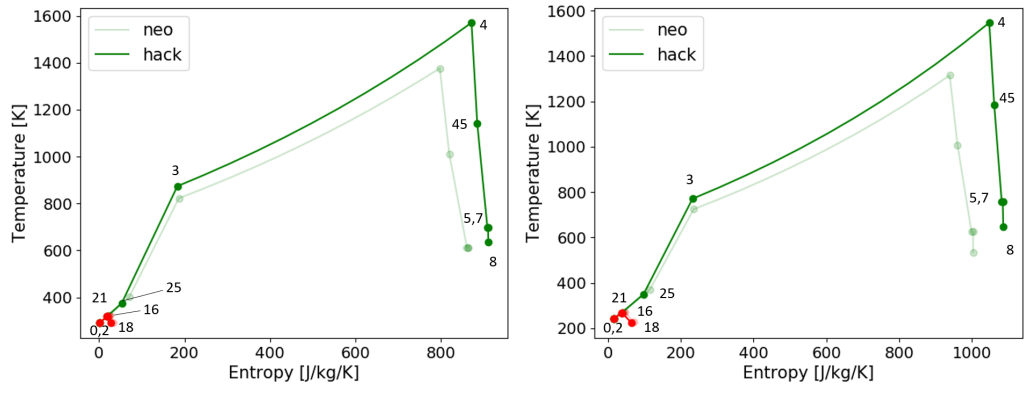

(a) Lift-off **(b)** Cruise

Figure 10.10: Temperature against entropy diagram for the A320neo and A320-HACK

$$\eta_{thermal} = \frac{W}{W + \dot{Q}_{heat}} \tag{10.20}$$

Table 10.12: Thermal efficiency and relative percentage difference for A320neo and A320-HACK

Phase	Lift-off	Cruise
A320neo	54.08%	56.95%
A320-HACK	57.69%	56.88%
Relative difference	3.61%	-0.07%

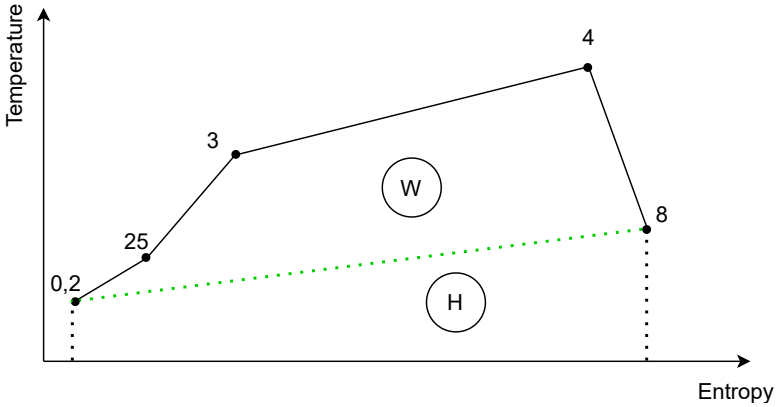

Figure 10.11: Simplified T-s diagram used for thermal efficiency calculation

The propulsive efficiency was computed using Equation 10.21, where $v_{j_{avg}}$, the average exhaust velocity, was found with Equation 10.22. The engine station numbering can be found in Figure 10.1. The total efficiency was found according to $\eta_{tot} = \eta_{th} \cdot \eta_{prop}$. The outcomes for the propulsive and total efficiencies are given in Table 10.13 and Table 10.14, respectively, for the lift-off and cruise phases of the A320neo and A320-HACK. The total efficiency is here overestimated due to the previous overestimation of the thermal efficiency, due to the simplified method used. However, the percentage difference between A320neo and HACK should still be valuable. The aircraft's percentage difference for the propulsive and total efficiencies for taxi-out, lift-off and cruise while using only kerosene or only hydrogen are given in Table A.6.

$$\eta_{prop} = \frac{2}{1 + v_{j_{avg}}/v_0} \tag{10.21}$$

$$v_{j_{avg}} = \frac{\dot{m}_{duct} v_{18} + \dot{m}_{core} v_8}{\dot{m}_{duct} + \dot{m}_{core}} \tag{10.22}$$

Table 10.13: Propulsive efficiency and relative percentage difference for A320neo and A320-HACK

Phase	Lift-off	Cruise
A320neo	51.904%	84.630%
A320-HACK	51.899%	85.384%
Relative difference	-0.005%	0.008%

Table 10.14: Total efficiency and relative percentage difference for A320neo and A320-HACK

Phase	Lift-off	Cruise
A320neo	28.12%	48.19%
A320-HACK	29.89%	50.65%
Relative difference	1.77%	2.46%

10.3.4 Engine's Turbomachinery

Below, the changes needed to achieve the compressor and turbine aimed performance and the OPR, TIT, and BPR higher values are elaborated upon. The consequences of these on the combustion chamber are described. The analyses made here are qualitative.

Compressor & Turbine

To increase the efficiency and pressure ratios of the compressor and turbine aerodynamics, materials and manufacturing should improve. Besides, tighter tolerances and lower tip leakage losses should be sought. To increase these efficiency and pressure ratios even further, LEAP-1A will be transformed into a geared turbofan (GTF), where a reduction gearbox is added. This way, the fan rotates at a different RPM than the low speed spool, meaning that the RPM of the spool is no longer limited by the tip speed of the blades of the fan. The compressor and turbine can rotate at their optimal speed and their efficiency increases. The number of compressor and turbine stages reduces, and thus the engine can be made shorter.

A triple spool turbofan was also considered as it allows for a better performance than a twin spool too. However, a triple spool does not allow for a complete decoupling of the fan and the low speed spool. Besides, at by-pass ratios above 10, a GTF is more fuel efficient [46]. Another alternative, or addition, to the GTF concept is the use of counter-rotating fans. Nevertheless, even though implementing it allows for a further reduction in fuel consumption, weight is added and the concept's technical readiness level

is still complex[10].

Bypass Ratio
To achieve a higher bypass ratio (BPR), the fan should become more efficient, which is already the case for a GTF. Improved and lighter materials should be used, the tolerances should decrease, and wide fan chord blades should be opted for.

Fan & Duct
To accommodate the rise in BPR, the fan diameter was increased from 78 to 81 *in*. "A variable area nozzle on the bypass stream of a turbofan engine may prove to be necessary for a sufficient surge margin on an ultra-high bypass ratio fan" [45], according to whom results in noise and fuel consumption benefits. The A320-HACK's engine has then a variable duct exit. However, this factor was not included in the engine cycle analysis in this stage.

Overall Pressure Ratio
For one, a GTF already contributes to a higher overall pressure ratio (OPR) since it allows for a higher LPC rotational speed. However, the latter requires lighter materials. Additionally, to achieve a higher OPR, better aerodynamics are required, which translates in a higher compressor efficiency and stage loading. Finally, better manufacturing processes contribute to tighter tolerances and lower tip leakage losses, resulting in higher OPR.

Turbine Inlet Temperature
To increase the turbine inlet temperature (TIT), the effectiveness of cooling shall rise, as well as the quality and performance of the materials used. In terms of manufacturing, tighter tolerances and better cooling channels should be explored. The blade coatings should also be improved to attain a higher temperature resistance and durability.

Combustor
A flap system was added to the combustion chamber's inlet to allow for the different ratios of air injected into the primary zone (PZ), as described in Section 10.3.1. These flaps rotate, as shown in Figure 10.12, changing the area ratio between the combustor's inlet and the air film's entrance. In a nominal flight, the flaps change position at the beginning of take-off (where a mixture of H_2 and kerosene starts being used) and taxi-in (where only hydrogen is used again). If the engine runs only on kerosene, less air than in the previous scenarios is allowed to go into the PZ and the flaps are at their maximum deflection - in the direction of the green arrows in Figure 10.12.

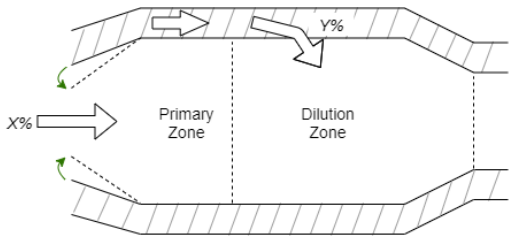

Figure 10.12: Flap system at the inlet of the combustion chamber

Besides, higher OPR, TIT and BPR lead to changes needed to the combustor, namely in terms of air distribution and cooling. There should be an improved fuel to air mixing and a lower equivalence ratio.

10.4 Combustion Emissions and Design

This section will discuss the emissions of the A320neo and the A320-HACK engine systems. First, the method used to evaluate and compare the emissions of the two aircraft is presented in Section 10.4.1. Subsequently, the results are discussed in Section 10.4.2

[10] https://www.safran-group.com/media/what-does-future-hold-store-open-rotor-20190328, accessed:22-Jun-2021

The advantage of a hydrogen assisted combustion is that the equivalence ratio can be reduced. The equivalence ratio limit for stable hydrogen combustion is lower than for kerosene[11]. So, hydrogen can act as a catalyst for the kerosene combustion at low equivalence ratios, which allows for a leaner combustion. As seen in Figure 10.13, this means that the *NOx* and *CO* emissions can be further reduced. Therefore, this section will be concluded with the suggestions for the reduction in equivalence ratios, such that the requirements regarding the reduction in emissions can be met. Finally, in Section 10.4.2 a new combustor design will be proposed to accommodate the A320-HACK engine for the leaner combustion.

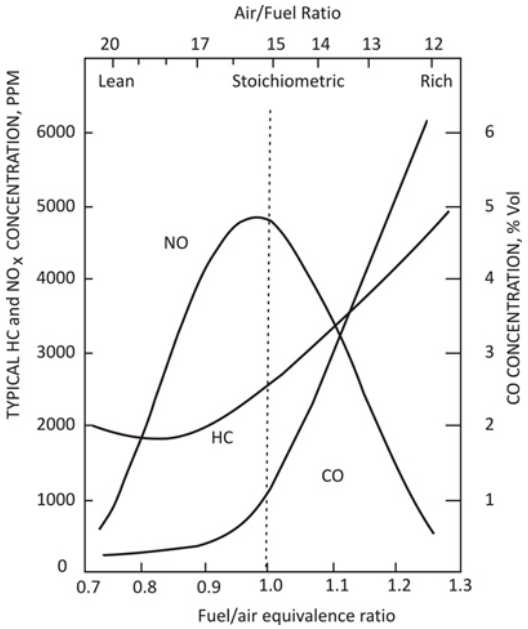

Figure 10.13: Example of emissions breakdown for various equivalence ratios[12]

The emissions produced by combustion were approached with the help of Cantera[13]; an open-source tool suitable to analyse problems involving chemical kinetics and thermodynamics. Furthermore, the ICAO Aircraft Engine Emissions Databank[14] was used to both compare the results of the analysis with the real test data and to optimize the input parameters for Cantera. Finally, the input parameters, such as the static pressure, temperature, and the air and fuel flows were retrieved from the engine cycle analysis ran in the Gas turbine Simulation Program 11 (GSP11) or from the results from the engine cycle analysis in Section 10.3.3.

The ICAO databank provides data only for the take-off, climb-out, approach and idle phases, therefore the analysis was performed only for these stages of the mission. The step-by-step procedure will be shown for the take-off stage only, since it was equal for all stages considered.

10.4.1 Method

First, the combustion reaction of the A320neo was modelled in Cantera. Cantera requires several inputs, such as the combustor inlet static pressure and temperature, and the equivalence ratio in the primary zone. It then outputs the break-down of the chemical compounds in the reaction with respect to the time. The input parameters to the program were optimized such that the error between the Cantera outputs and the ICAO data was minimized. With the already mentioned parameters, the residence time

[11] https://www.sciencedirect.com/science/article/abs/pii/S1540748910002506, accessed:27-Jun-2021
[12] https://nptel.ac.in/content/storage2/courses/112104033/lecture3/3_3.html, accessed:18-Jun-2021
[13] https://cantera.org/, accessed:25-Jun-2021
[14] https://www.easa.europa.eu/domains/environment/icao-aircraft-engine-emissions-databank, accessed:22-Jun-2021

was also optimized. The emissions were then measured at the end point of this residence time. As will be shown later, a minor shift in the residence time may cause large changes in the NO_x and CO emissions.

Two rules were followed for the evaluation of the residence time. First, the residence time was measured from the point where the temperature reaches the value given by Equation 10.23. Second, the final point of the residence time was not allowed to be before the point where the temperature reached 99.99% of its final value. The second condition was checked after each optimization. Both rules are visualized in Figure 10.14.

$$T_{10\%} = T_{initial} + 0.1(T_{final} - T_{initial}) \quad (10.23)$$

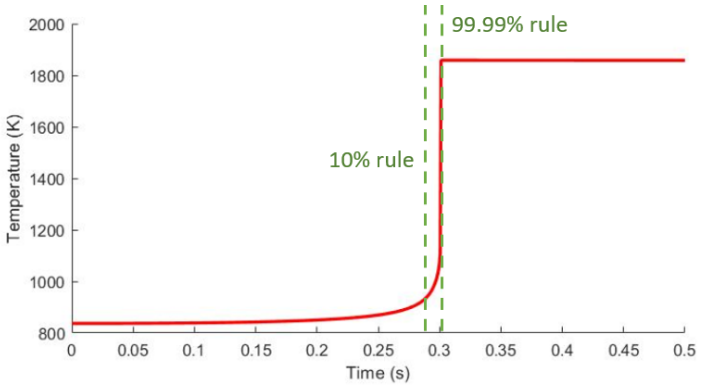

Figure 10.14: Residence times rules

The emissions provided by ICAO are in terms of grams per kg of fuel, but Cantera outputs the emissions as the mass ratio with respect to the products' mass (which equals the reactants' mass). Therefore, the ICAO values had to be first converted to the Cantera output form, using Equation 10.24, for a certain primary zone equivalence ratios. EF stands for "Emission fraction".

$$EF_{(kg/kg\ \text{all products})} = EF_{(kg/kg\ \text{fuel})} + \dot{m}_{air} \quad (10.24)$$

$$\dot{m}_{air} = \frac{AF_{stoich}}{\phi} \cdot \dot{m}_{fuel} \quad (10.25)$$

$$EF_{(kg/kg\ \text{all products})} = \frac{EF_{(kg/kg\ \text{fuel})}}{1 + \frac{AF_{stoich}}{\phi}} \quad (10.26)$$

The temperature, pressure, the air flow and the fuel flow for the A320neo in the take-off are taken from GSP11 and are presented in Table 10.15. Only the total temperature and pressure are output by GSP11, yet the static value should be input to Cantera. Therefore, the temperature and pressure were converted to static values using Equation 10.27 and 10.28. As the Mach number at the combustion chamber inlet is not known, a common value of 0.15 was assumed.

$$T_s = T_t \left(1 + \frac{\gamma - 1}{2} M^2\right)^{-1} \quad (10.27)$$

$$p_s = p_t \left(\frac{T_s}{T_t}\right)^{\frac{\gamma}{\gamma-1}} \quad (10.28)$$

Table 10.15: GSP 11 estimates for the stage 3 of the A320neo engine in take-off

Parameter	Temperature	Pressure	Air flow	Fuel Flow
Value	805	3283120	34.06	0.855
Unit	$[K]$	$[Pa]$	$[kg/s]$	$[kg/s]$

Since GSP11 is a validated software, the values in Table 10.15 were trusted and used directly. The unknowns, such as the equivalence ratio and the residence time, were optimized such that the error between the emission levels output by Cantera and the data provided by the ICAO databank were minimized. Specifically, the Cantera simulation was ran to output the emission mass fractions at the end of a certain residence time for the equivalence ratios in the range of 0.4 to 0.9. Simultaneously, the mass

[14] The residence time characterizes the average time the reaction reactants and products stay in the primary zone of the combustion chamber.

fractions given by ICAO were translated to the Cantera form using Equation 10.24 for each equivalence ratio in the chosen range, as discussed earlier. Then, the absolute ratio of the Cantera output and the ICAO value was computed using Equation 10.29. This was done for both NO_x and CO and the sum of these two ratios was then minimized. This procedure was iterated for multiple residence times, until the minimum was found.

$$Absolute\ Ratio = \left| \frac{EF_{Cantera}}{EF_{ICAO}} \right| \tag{10.29}$$

The results of the optimization for the take-off are presented in Figure 10.15. The top graph shows the comparison of the CO mass fraction as estimated by Cantera and as given by ICAO, the middle graph shows the same comparison for NO_x , while the bottom one presents the absolute ratio for each of these emissions and their sum. As can be seen, the ratios (and hence the errors) are at minimum for a primary zone (PZ) equivalence ratio of about 0.55. The complete set of the optimized parameters is presented in Table 10.16.

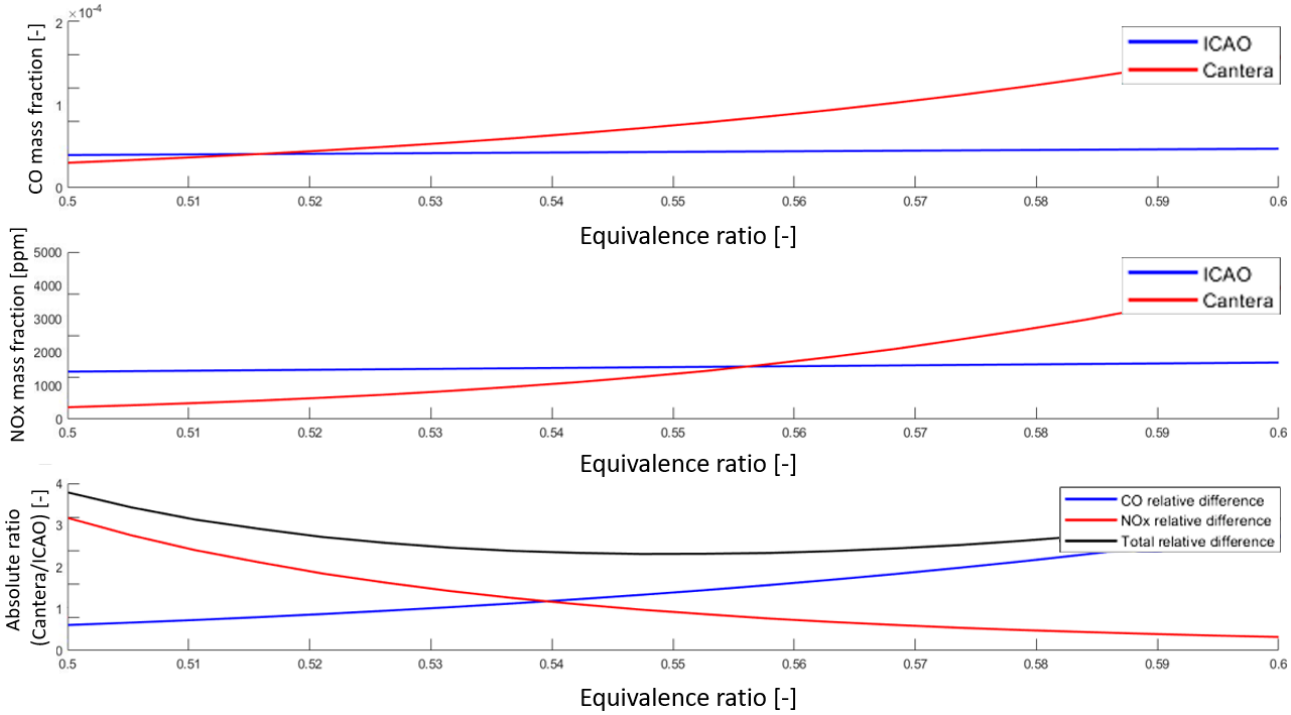

Figure 10.15: Evaluation of the equivalence ratio of A320neo in take-off. The top two graphs display the comparison of the CO respectively NO_x mass fractions at the end of the combustion chamber primary zone (for various equivalence ratios) as estimated by Cantera and as given by ICAO data. The bottom graph presents the (sum of) absolute errors, the minimum of which was used to estimate the equivalence ratio and the residence time

Table 10.16: Results from the optimization of the parameters for the A320neo in take-off

Parameter	Temperature	Pressure	PZ ϕ	Residence time
Value	805	3283120	0.55	24.3 $\pm$ 0.5
Unit	$[K]$	$[Pa]$	$[-]$	$[ms]$

To validate the resulting equivalence ratio, the combustion chamber of the LEAP-1A engine was investigated. The A320neo engine uses a Twin-Annular, Pre-Mixing Swirler (TAPS) combustor, which is shown in Figure 10.4. This combustor was designed for a very lean combustion to minimize the NO_x emissions. In fact, the Federal Aviation Administration (FAA) claims that 70% of the air flow at stage 3 enters the PZ[15]. Knowing the air flow and the fuel flow, while the air-to-fuel (AF) stoichiometric ratio was

[14] https://www.aerocontact.com/en/videos/496-taps-it-takes-nothing-away-but-nox-emissions, accessed:20-Jun-2021

[15] https://www.faa.gov/about/office_org/headquarters_offices/apl/research/aircraft_technology/cleen/

calculated to be 14.79, the take-off equivalence ratio can be estimated via Equation 10.30, using the $\dot{m}_{air}$ and $\dot{m}_{fuel}$ of Table 10.15.

$$\phi = \frac{AF_{stoi}}{0.7\dot{m}_{air}/\dot{m}_{fuel}} \tag{10.30}$$

This calculation resulted in a value for the equivalence ratio of 0.534. This value is only 3% lower than the ϕ estimated with the optimization, therefore the optimisation result is considered valid. As the error in the emissions' estimation is known for each species, the error in residence time can be estimated. This was performed for each species by evaluating how much the residence time needs to be increased or decreased to reach the ICAO value. Subsequently, the higher value was taken as the uncertainty.
Finally, before the emissions for the combination of hydrogen and kerosene could be addressed, the time point in the combustion reaction (for the combination of hydrogen and kerosene) for which the emissions should be considered was determined. This was done by linearising the residence time based on the speed of the combustion reaction for hydrogen and for kerosene. The Cantera simulation was ran individually for only kerosene and then for only hydrogen at the same conditions (pressure, temperature and ϕ as determined in Table 10.16). The speed of the reaction for each fuel was then determined by evaluating the time the temperature requires to rise from $T_1 = T_{init} + 0.1(T_{final} - T_{init})$ to 99.99% of the final value, T_{final}. The residence time for the combination of the two fuels was then estimated with Equation 10.31.

$$t_{res,HACK} = t_{res,neo}\left[r \cdot \frac{t_{reaction,H2}}{t_{reaction,ker}} + (1-r)\right] \tag{10.31}$$

In Equation 10.31, r is the fuel mass ratio of hydrogen. This was chosen for the flight phases to be 0.1402, as discussed in Section 10.2.1. Inserting the estimated reaction times, $t_{res,HACK} = 21.7 \pm 0.5$ ms was obtained. This estimation is very rough as it assumes that the recirculation region of the combustion chamber is not affected too much when different fuels are injected.

The emission mass fractions were then evaluated at the end of the residence time. The breakdown of the emissions for the combination of hydrogen and kerosene is visualized in Figure 10.16, where the vertical dotted line characterizes the end point of the calculated residence time. Note that the time ranges for the bottom two graphs are different as the graphs were zoomed for a clearer depiction.

The estimated CO and NO_x emissions of the A320-HACK including the uncertainty (due to the uncertainty in the residence time) were then compared with the ICAO data for A320neo. For CO_2 and H_2O, the emission mass fractions of A320-HACK were compared with the A320neo values output by the Cantera simulation, since no ICAO data exist for these species. This is summarized in Table 10.17, where also the percentage difference is included. Due to the lack of ICAO data for CO_2 and H_2O fractions, the uncertainty for these values could not be easily estimated. Nevertheless, the Cantera results are presented in the table to offer an idea of how these emissions change between the two engine configurations.

Table 10.17: Combustion emission mass fractions comparison for A320-HACK vs A320neo; ϕ_{HACK} = 0.55 and ϕ_{neo} = 0.55

Species	A320neo	A320-HACK	Difference
CO [-]	$5.38 \cdot 10^{-5}$	$(3.930 \pm 0.003) \cdot 10^{-5}$	-27.0 ± 0.1%
NOx [ppm]	624	780 ± 50	25 ± 8%
CO2 [-]	0.112	0.0629	-44%
H2O [-]	0.047	0.056630	10%

As can be observed in the table, the NO_x emissions increased, which was expected as the addition of the hydrogen increases the temperature of the reaction. The CO_2 and CO emissions, on the other hand, decreased, however, the reduction is not sufficient to satisfy the $SR - SUST - 02$ requirement. Therefore, it was investigated to what extent the equivalence ratio, ϕ, needs to be reduced, so that the requirement is met. It was evaluated that the equivalence ratio needs to be decreased to 0.51, which

reports/media/taps_ii_public_final_report.pdf, accessed:20-Jun-2021

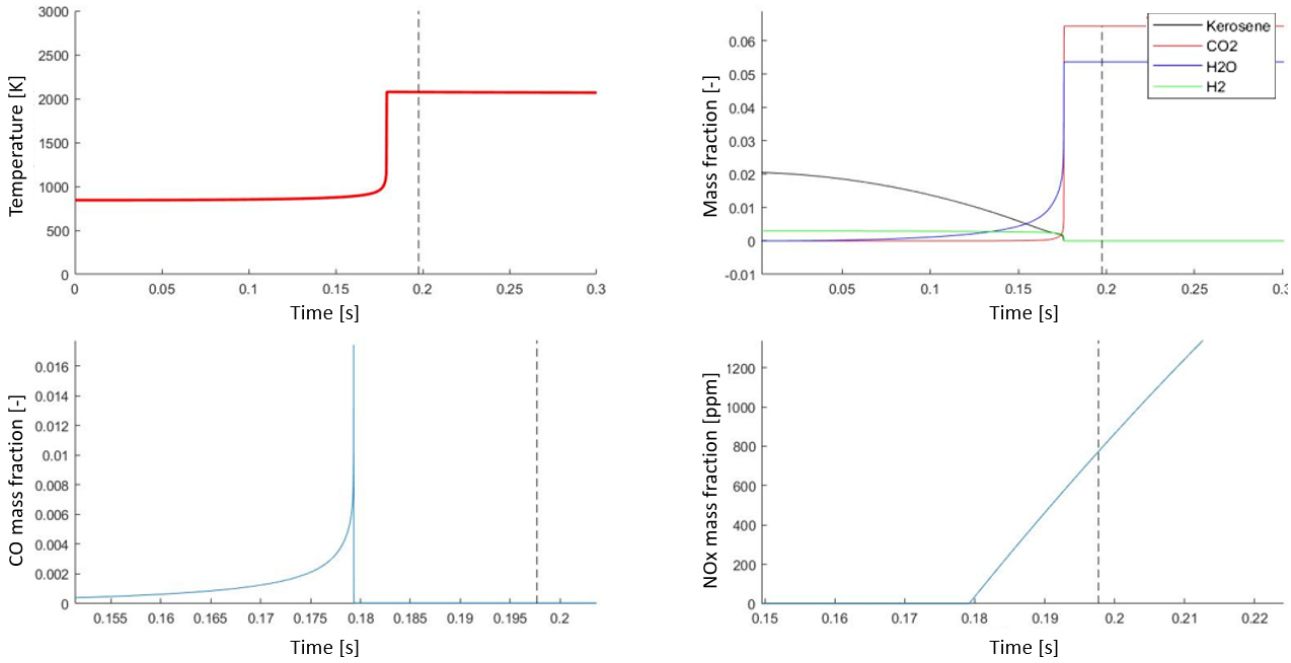

Figure 10.16: Emissions mass fractions for the A320-HACK in take-off. The top left graph represents the development of the temperature over the time in the reaction while the other graphs depict a similar development for the emission mass fractions. The dashed line symbolizes the time point where the emission mass fractions were retrieved from for the analysis.

would need a reduction by around 7%. The emissions results using this equivalence ratio are presented in Table 10.18.

Table 10.18: Emission mass fractions at the end of the primary zone of the combustion chamber for the A320-HACK in take-off for the equivalence ratio of ϕ = 0.51

Species	New value	Difference with respect to A320neo
CO [-]	$(1.962 \pm 0.004) \cdot 10^{-5}$	- (63.5 ± 0.1)%
NOx [ppm]	250 ± 50	-(60 ± 8)%
CO2 [-]	0.05537	-51%
H2O [-]	0.05083	+8%

This is the minimum reduction in the equivalence ratio required to decrease the emissions and meet the requirement. Considering all the assumptions and inaccuracies presented in this method, it is difficult to guarantee that the combustion will be stable or feasible once the equivalence ratio is reduced, despite the inclusion of hydrogen. The values presented in this chapter thus represent the "safe" design option, at which a stable combustion should still be achieved. However, the equivalence ratio can be lowered further in the design to improve the emissions' performance even more, although investigating the stability of such a combustion is beyond the scope of this project. For the analysis of the environmental impact of the combustion with lower equivalence ratios (as suggested in Section 10.3.3), the average temperature response analysis was performed and is discussed in Section 16.2.

10.4.2 Results

For the idle phase, no information was available for the conditions in the inlet of the combustion chamber, but the emissions can be discussed qualitatively. Since no kerosene is used during idling, the percentage mass fraction of CO and CO_2 is expected to be 0%. Furthermore, the engines at idle are ran at low thrust and hence the temperature and pressure at the inlet of the combustion chamber is expected to be low, hence resulting in low NO_x emissions. Nevertheless, the NO_x emissions for A320-HACK at idle are expected to be higher than for A320neo for the same combustion chamber inlet temperature, pressure and equivalence ratio, because the temperature in the combustion chamber of the engine is higher for the HACK's engine due to the sole use of hydrogen. However, as no specific data is available, the necessary reduction in equivalence ratio to reduce the NO_x emissions was not estimated. The results

for the remaining flight phases are presented in Table 10.19 and the combustion chamber inlet data of A320neo, which was used for optimization of the parameters, are given in Table 10.20. As can be seen, the largest decrease in the equivalence ratio to meet the A320-HACK $SR-SUST-02$ requirement is necessary for the Climb-Out phase, where a decrease of 9% is needed.

With these changes to the equivalence ratio in the primary zone of the combustion chamber, the NO_x and CO emissions requirements can be met. However, $SR-SUST-02$ cannot be claimed to be fully fulfilled, because the unburnt hydrocarbon and soot emissions were not investigated due to the limited time allocated to the project. Nevertheless, they are expected to follow a behaviour similar to the CO emissions, so they would reduce in a comparable way.

Table 10.19: The equivalence ratios and the emission mass fractions (at the end of the combustor primary zone) of A320-HACK and A320neo for take-off, climb-out and approach flight phases

	ϕ [-]	CO [-]	NO_x [ppm]	CO_2 [-]	H_2O [-]
A320neo Take-Off	0.55	$5.38{\cdot}10^{-5}$	624	0.112	0.047
A320-HACK Take-Off	0.51	$(1.962\pm0.004){\cdot}10^{-5}$	250±50	0.055	0.051
Difference	-7%	- (63.5±0.1)%	-(60±8)%	-51%	8%
A320neo Climb-Out	0.54	$4.18{\cdot}10^{-5}$	392	0.111	0.046
A320-HACK Climb-Out	0.49	$(1.505\pm0.007){\cdot}10^{-5}$	160±25	0.054	0.050
Difference	-9%	-(64.0±0.2) %	-(60±7)%	-52%	8%
A320neo Approach	0.5	$8.06{\cdot}10^{-5}$	212	0.104	0.039
A320-HACK Approach	0.47	$(2.98\pm0.01){\cdot}10^{-5}$	90 ± 15	0.051	0.043
Difference	-6%	-(63.0±0.1)%	-(58±7)%	-51%	11%

Table 10.20: Conditions at the stage 3 of the LEAP 1-A engine for different phases

	Temperature [K]	Pressure [bar]	Air mass flow [kg/s]	Fuel flow [kg/s]
Take-Off	805	32.8	34.06	0.855
Climb-Out	764	20.4	26.88	0.606
Approach	761	20.1	27.96	0.420

10.4.3 Proposed Combustor Design

As concluded in Section 10.4.2, a leaner combustion is required (and hence a lower equivalence ratio) to lower the NO_x emissions and meet the $SR-SUST-02$ requirement. Using only kerosene, the decrease in equivalence ratio would result in a deterioration of the flame stability. However, due to the presence of hydrogen, the flame can be stable at even lower equivalence ratios[16], therefore a leaner combustion is possible. For this reason, this section will be concluded by proposing the changes to the combustion chamber to allow for leaner combustion.

The most promising solution appears to be the Lean Direct Injection (LDI) concept, which is being developed as an ultra-low NO_x combustion scheme. In such a combustor, the fuel and air are directly injected into the primary zone with no prior premixing, all the combustion air enters the front entry of the combustor and there is no dilution zone present[17]. With this, the peak temperature in the combustor and the flow residence time can be decreased, which results in a reduction in NO_x emissions[18].

[16] https://www.sciencedirect.com/science/article/abs/pii/S1540748910002506, accessed:27-Jun-2021

[17] https://repository.tudelft.nl/islandora/object/uuid:916b027f-4d60-459d-8eb2-d5bea69910ce/datastream/OBJ/download, retrieved 27-Jun-2021

[18] https://repository.tudelft.nl/islandora/object/uuid:916b027f-4d60-459d-8eb2-d5bea69910ce/datastream/OBJ/download, retrieved 27-Jun-2021

The LDI was adapted to the needs of the A320-HACK. To inject the fuel into the combustion chamber, a swirler injector system will be used. The system will consist of an arrangement of co-rotating swirlers, as shown in Figure 10.17. The central swirler is used for the injection of hydrogen, while the rest is used for kerosene. Such a configuration of swirlers results in high shear between the air flows leaving individual swirlers, which results in reduction of the peak temperature in the flame and hence in the reduction of the NO_x emissions [11].

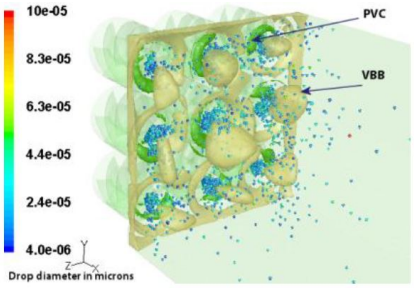

Figure 10.17: Swirler injection system arrangement [11]

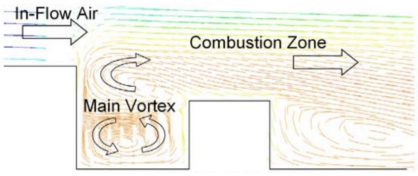

Figure 10.18: The Trapped Vortex Combustor principle[19]

Another concept, that could be considered, is the trapped vortex combustion (TVC). This concept is based on the mixing of hot combustion products with reactants at a high rate[20]. This is performed by "trapping" the turbulence in a cavity, where the reactants are efficiently mixed[21]. A simplified visualization of this principle is presented in Figure 10.18. The TVC has a potential to reduce the NO_x emissions by 10-40%, it extends the flammability limits (allowing for lower equivalence ratios) and reduces the pressure drop in the combustor[22].

10.5 Engine Mass Estimation

As described in Section 10.3.4, several changes were applied to the LEAP-1A to represent the engine of the A320-HACK. To account for the increased fan diameter, the dry engine mass of 19 turbofan engines with a similar thrust setting was considered, as a function of the fan diameter [47]. The data is plotted in Figure 10.19. Due to the time-wise spread of these engines, the effect of the improvements in the materials used is also taken into account. Knowing that the engine of the A320-HACK has a $D_{fan} = 2.06\ m$, Figure 10.19 was used to find $M_{eng} = 3144.27\ kg$. This contrasts with the 2780 kg for LEAP-1A, with a $D_{fan} = 1.98\ m$.

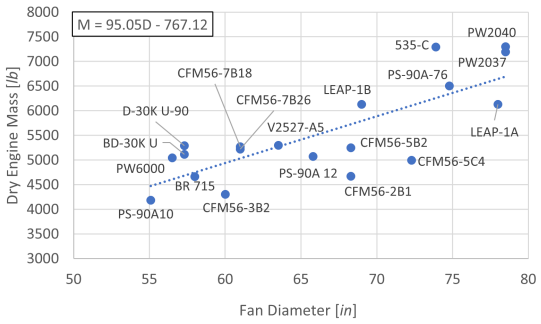

Figure 10.19: Engine dry mass against fan diameter for 19 turbofan engines.

However, the fact that a gearbox is added to the engine is not taken into account in this estimated value.

[20] https://www.intechopen.com/books/progress-in-gas-turbine-performance/review-of-the-new-combustion-technologies-in-modern-gas-turbines, accessed:27-Jun-2021

[21] https://www.intechopen.com/books/progress-in-gas-turbine-performance/review-of-the-new-combustion-technologies-in-modern-gas-turbines, accessed:27-Jun-2021

[22] https://www.intechopen.com/books/progress-in-gas-turbine-performance/review-of-the-new-combustion-technologies-in-modern-gas-turbines, accessed:27-Jun-2021

[22] https://netl.doe.gov/sites/default/files/gas-turbine-handbook/3-2-1-4-1.pdf, accessed:27-Jun-2021

The A320neo has two engine options, the LEAP-1A and the PW1100G, with the latter being geared unlike the former. These engines have similar by-pass ratios, and power the same aircraft. Therefore, to analyse the impact of a geared engine on the engine's dry mass, these engines were compared: the dry weight of PW110G is 1.028 that of LEAP-1A. Hence, the final dry mass of the A320-HACK's engine was estimated as $M_{eng} = 3144.27 \cdot 1.028 = 3232.04\ kg$, 16.26% higher than LEAP-1A.

11 | Dedicated Power Unit Design

To further reduce the environmental impact of the A320-HACK, running the Auxiliary Power Unit (APU) also on hydrogen was explored. According to the Eurocontrol, "APUs contribute 5-10% of the overall aircraft pollution at airports"[1], hence mitigating these emissions was considered worth. Furthermore, as explained in Chapter 10 and further in this chapter, the A320-HACK APU was re-designed as a primary power source for all flight phases, besides being responsible for starting the engines and providing power for on-ground operations. Therefore, this component was renamed into Dedicated Power Unit (DPU).

In this chapter, Section 11.1 states the DPU requirements and Section 11.2 discusses the trade-off between a gas generator and a fuel cell. Then, a more in-depth trade-off between the options of the chosen DPU type is found in Section 11.3. A layout of the system is reported in Section 11.4. The DPU fuel cell model, the required power and sizing of the DPU are explained in Section 11.5, 11.6 and 11.7, respectively. The water production and cooling system are described in Section 11.8 and 11.9. Lastly, verification and validation is presented in Section 11.10 and the results with the limitations and recommendations are treated in Section 11.11.

11.1 Requirements

The new DPU shall comply with the following requirements:

SR-DPU-01 The DPU shall provide the on-board power of the A320-HACK.

SR-DPU-02 The DPU shall aid with the start-up of the engines.

SR-DPU-03 The DPU shall run on hydrogen.

11.2 Gas Generator vs. Fuel Cell

Currently, the Airbus A320neo employs Honeywell 131-9A, a conventional gas generator Auxiliary Power Unit (APU). When replacing this engine by a hydrogen alternative, one option was to redesign the gas generator similarly to the main engines, to accommodate hydrogen combustion. The other option was to use a fuel cell. These two options were considered and are here compared. When comparing the gas generator and the fuel cell the efficiency, noise, weight, volume, cost and fuel flexibility were considered. The results of this comparison arepresented in Table 11.1.

The efficiency was included as a measure of sustainability, as higher efficiency implies less burnt fuel. For the fuel cells, the conversion from chemical energy to electrical takes place with no combustion, which makes the process highly efficient, clean and quiet[2], which is reflected in Table 11.1. Since the efficiency differs between the fuel cell types, a general range of values was considered[3].

When it comes to noise, the absence of combustion makes the fuel cells quieter than a typical human conversation (60 dB[4]). For the gas generator, the data from C130H Hercules aircraft APU were

[1] https://www.eurocontrol.int/sites/default/files/library/034_Benefits_of_Fuel_Cell_Usage.pdf, accessed:31-May-2021

[2] https://www.eurocontrol.int/sites/default/files/library/034_Benefits_of_Fuel_Cell_Usage.pdf, accessed:31-May-2021

[3] https://www1.eere.energy.gov/hydrogenandfuelcells/fuelcells/pdfs/fc_comparison_chart.pdf, accessed:31-May-2021

[4] https://www.uofmhealth.org/health-library/tf4173, accessed:26-Jun-2021

considered. This APU is also produced by Honeywell and bears similar parameters to the A320neo's Honeywell 131-9A, which is why it was regarded as a reasonable indication for the comparison.

The mass of the Honeywell 131-9A is known, but the volume had to be estimated. The specific power of a gas turbine APU was found to be around 200 hp/ft^3[5] (= 5.4 kW/L). The Honeywell 131-9A can produce power up to 400 kW, which corresponds to the volume of roughly 75 L. The average gravimetric power of liquid cooled fuel cells (including all the supporting systems, such as cooling) is around 0.443 kW/kg with the current technology and the average volumetric power density is about 0.540 kW/L, according to estimates from 2017[6]. A fuel cell also producing 400 kW, would thus weight about 900 kg and take 740 L of space. Similarly, the specific cost of a fuel cell was estimated to be 40 $\$/kW$[7], therefore a 400 kW fuel cell would cost 16,000$.

Finally, the fuel flexibility was addressed since a mechanism able to operate on both hydrogen and kerosene is advantageous in case of absence of hydrogen. The gas turbine APU can be designed in a similar way as the main engines to operate on both fuels. In contrast, some fuel cells must be operated on pure hydrogen[8]. However, even for those, a reformer can be included in the system to obtain hydrogen from the carbohydrates contained in kerosene, although the efficiency of the fuel cell would decrease[9].

The advantages of the fuel cell for emissions and noise out-weight its disadvantages, as they correspond to the main goals of the A320-HACK project. Therefore, the fuel cell was selected. Furthermore, the fuel cell was decided to provide power during the entire mission. This is different from a conventional APU, where it is only used to start the engine and to provide power on ground (or in-flight as a back-up). In this way, the gas generators in the main engines can be deactivated during the mission and serve merely as a back-up, thereby providing redundancy to the fuel cells. Consequently, the efficiency of the main engines can be improved.

Table 11.1: Trade-off between a gas generator and a fuel cell

Physical properties	Units	Fuel Cell	Gas Generator
Efficiency	[-]	40 - 60%[3]	15%[2]
Noise at 1 m distance	[dB]	40-50[10]	127[11]
Mass	[kg]	900[6]	145[12]
Volume	[L]	740[6]	50-75
Cost	[$]	16,000	250,000-350,000[13]
Fuel flexibility	[-]	Yes	Yes

Finally, the fuel cell mass and volume estimates presented in Table 11.1 are based on the current technology. However, with increasing development in the fuel cell technology, the specific weight and volume of

[5] https://asmedigitalcollection.asme.org/GT/proceedings-pdf/GT1985/79382/V001T04A002/4456412/v001t04a002-85-gt-124.pdf, accessed: 14-Jun-2021

[6] https://repository.lboro.ac.uk/articles/conference_contribution/A_fuel_cell_system_sizing_tool_based_on_current_production_aircraft/9221111, accessed:01-Jun-2021

[7] https://www.energy.gov/sites/prod/files/2016/10/f33/fcto_myrdd_fuel_cells.pdf, accessed:02-Jun-2021

[8] https://fuelcellsworks.com/knowledge/technologies/pemfc/, accessed:02-Jun-2021

[9] https://www.fuelcellstore.com/blog-section/processing-alternative-fuels-for-fuel-cells, accessed:02-Jun-2021

[10] https://energies.airliquide.com/resources-planet-hydrogen/fuel-cell#:~:text=The%20fuel%20cell%20is%20very%20quiet.&text=Overall%2C%20the%20fuel%20cell%20emits,conversation%20(around%2060%20dB)., retrieved on 31-May-2021

[11] http://wprim.whocc.org.cn/admin/article/articleDetail?WPRIMID=627259&articleId=627259, accessed:16-Jun-2021

[12] https://www.fzt.haw-hamburg.de/pers/Scholz/Airport2030/Airport2030_PUB_CEAS_15-09-07_Scholz.pdf, accessed: 01-Jun-2021

[13] https://www.skylinkintl.com/blog/fleets-need-4059422121-worth-of-aircraft-apus-heres-how-to-buy-your-next-one#:~:text=We've%20seen%20these%20APUs,the%20supply%20and%20demand%20environments., accessed: 03-Jun-2021

fuel cells rapidly improve. In 2016, the US Department of Energy has set targets to increase the specific weight ultimately to 0.85 kW/kg and 0.85 kW/L[14]. For the A320-HACK, it was hence predicted that these values will rise to 0.8 kW/kg and 0.8 kW/L by 2035. Lastly, the specific cost was predicted to decrease to 30 $\$/kW$[14]. These values will be used for the estimations from now on.

11.3 Proton-Exchange Membrane vs. Solid Oxide Fuel Cells

A trade-off between the two most promising fuel cell (FC) types[15], the Proton-Exchange Membrane Fuel Cell (PEMFC) and Solid Oxide Fuel Cell (SOFC), was conducted, as listed in Table 11.2.

Table 11.2: PEMFC vs. SOFC

Physical properties	**PEMFC**	**SOFC**
Electrolyte [48]	Ion exchange membrane	Ceramic
Operating temperature ($°C$)[16] [49, 48, 50, 51]	30-100	500-1000
Fuel [49, 52]	Hydrogen	Kerosene, hydrogen
Mass[17]	Relatively lighter	19x heavier than PEMFC
Volume[18]	Relatively smaller	Large
Purity of H_2[16] [49]	Very high	Low
Efficiency[16] [49, 53, 50]	40-60%	60%
Dynamic response[16]	Fast	Slow

The PEMFC uses air directly from the environment. However at 10 km altitude, the atmospheric pressure and temperature are 0.227 bar and -56 $°C$, respectively [49]. As stated in Table 11.2, the PEMFC cannot operate in these conditions. A solution would be compressing and heating the air before the entry to the PEMFC. Using the preheated air avoids excessive stack cooling and thermal stress caused by the cold air from the environment [54].

The SOFC DPU is possible with some adaptations to the system, namely a heat-exchanger to heat-up the air and H_2, along with pumps and blowers. In case of using kerosene, a reformer to extract H_2 from kerosene and desulfuriser [55] are also needed. SOFCs have a higher power density and greater efficiency than PEMFCs, however it has not been experimentally tested on board of an aircraft [48]. Besides, the start-up and shut-down cycles become slower [48], which is not favourable. Eelman et al. and Fernandes et al. concluded that, when pure hydrogen is used, the PEMFC is the best option and that the maturity level of the PEMFC might outweigh the SOFC [48, 55].

Finally, in 2003, Boeing discussed the used of fuel cell APUs to reduce emissions and fuel use. They estimated that the required power delivered by a SOFC would equal 440 kW. The identified drawbacks of the SOFC were the weight and start-up time [56].

To conclude, the PEMFC is the most optimal choice for the A320-HACK's DPU design due to its fast dynamic responses, short start-up time and comparatively lower mass and volume. These advantages make the PEMFC suitable for transportation applications[19] and hence for A320-HACK.

11.4 Fuel Cell System

The layout of the fuel cell system that was chosen for the A320-HACK is depicted in Figure 11.1.

[14] https://www.energy.gov/sites/prod/files/2016/10/f33/fcto_myrdd_fuel_cells.pdf, accessed: 01-Jun-2021
[15] https://www.sciencedirect.com/topics/engineering/fuel-cells-for-transportation,accessed:26-Jun-2021
[16] https://www.energy.gov/sites/default/files/2016/06/f32/fcto_fuel_cells_comparison_chart_apr2016.pdf, accessed:14-Jun-2021
[17] https://www.mdpi.com/2076-3417/8/12/2474/pdf, accessed:26-Jun-2021
[18] https://odr.chalmers.se/bitstream/20.500.12380/301883/1/A%20Proton%20Exchange%20Membrane%20%20Solid%20Oxide%20Fuel%20Cell%20comparison.pdf, accessed:26-Jun-2021
[19] https://www.researchgate.net/publication/320250245_Proton_exchange_membrane_PEM_and_solid_oxide_S

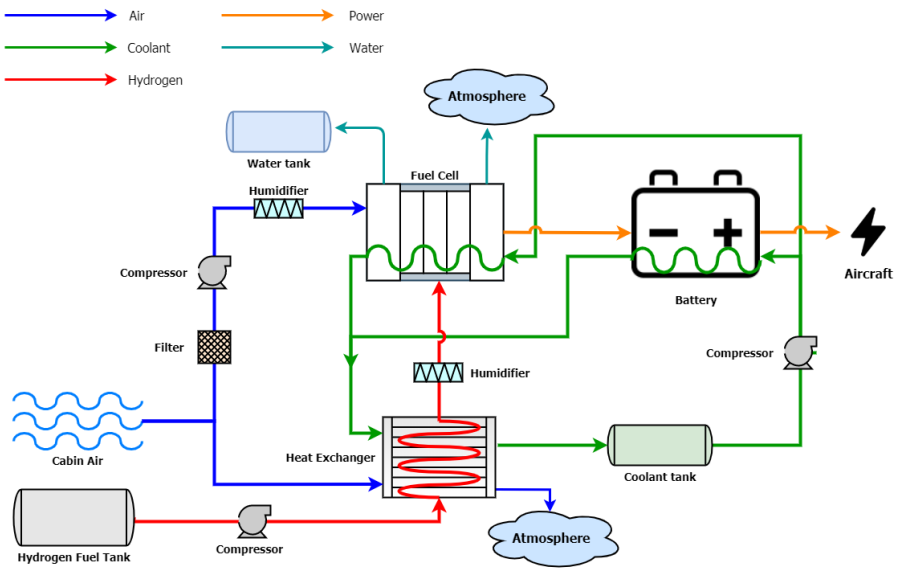

Figure 11.1: Fuel cell system

The dark blue line represents the flow of the cabin air, which is used for both the chemical reactions in the fuel cell and for cooling the heat-exchanger. A certain level of flow rate, purity, pressure and temperature is required from the air incoming to the PEMFC for it to operate optimally. Thus, components such as a filter, compressor and humidifier are used to adjust the air before it enters the fuel cell.

The cabin air was chosen instead of the air from the outside of the aircraft as it will simplify the design of the fuel cell system. The cabin air is kept at the temperatures of 20-27 $°C$[20], which is sufficient for satisfactory performance of the fuel cell[20]. Therefore, no cooling or heating elements need to be added. Furthermore, the air is already compressed to 0.8 atm [21], which significantly reduces the power consumption of the compressor (see Section 11.6). Also, the PEMFCs can be operated at the pressures between 1-6 atm[22]. The lower limit of this range was chosen for this project to reduce the required power of the compressor further and hence reduce the power requirements (and consequently the mass and volume) of the fuel cell and the battery. Finally, the cabin air is used for cooling of the heat-exchanger. The advantage of this solution is that no external heat-exchanger is needed and thus it does not introduce any additional aerodynamic drag.

The red line displays the flow of hydrogen. It is still a cryogenic liquid when it is pumped from the tank. Therefore, it is first heated at the heat-exchanger, where it contributes to the cooling of the coolant. Before entering the FC, it is also humidified.

The green line represents the flow of the coolant, which is used to cool the fuel cell and the battery. Afterwards, it is cooled itself in the heat-exchanger. Moreover, a coolant tank is included to increase the flexibility of the system in case of rapid changes in the coolant mass flow and to compensate for the loss of coolant due to evaporation and leakage during the mission.

The turquoise line is used to indicate the produced water vapour of the PEMFC. Part of it is captured and stored in the water tank and used on board of the aircraft. The excess water is vented out via the drain masts to the atmosphere.

Finally, the orange line represents the flow of electrical power. A battery is added as a buffer: it is charged when the fuel cell provides excessive power and discharged when extra power is needed. This allows the DPU to deliver constant power, which increases the fuel cell's performance and lifetime.

OFC_fuel_cell_based_vehicles-a_review, accessed:26-Jun-2021

[20] https://www.sciencedirect.com/science/article/pii/S1000936114000314, accessed: 03-Jun-2021

[21] https://www.businessinsider.com/boeing-787-dreamliner-777x-cabin-pressure-jetlag-2016-9?international=true&r=US&IR=T, accessed: 14-Jun-2021

[22] https://www.researchgate.net/publication/266053721_Optimal_operating_temperature_and_pressure_of_PEM_fuel_cell_systems_in_automotive_applications,accessed:20-Jun-2021

11.5 Fuel Cell Model

This section discusses the fuel cell model. Section 11.5.1 elaborates on the chosen membrane and the power provided. Section 11.5.2 gives more information about the chosen design point.

11.5.1 Membrane Calculations

A proton-exchange membrane fuel cell (PEMFC) uses hydrogen (H_2) and oxygen (O_2) to produce water (H_2O) as an end product. The chemical half reactions are given in Equation 11.1 and 11.2. The Nafion 117 membrane is widely used in PEMFCs operating below 100 $°C$. The Hyflon membrane is another membrane which can be considered. Shamine et al. states that the Hyflon membrane has a higher glass-transition temperature compared to the Nafion, which makes operation at higher temperatures possible [57]. However, the operating temperature of the PEMFC was decided to be around 90$°C$, therefore the Nafion 117 membrane was selected instead of the Hyflon.

Oxidation half reaction (anode side) [51]:

$$H_2 \longrightarrow 2H^+ + 2e^- \tag{11.1}$$

Reduction half reaction (cathode side) [51]:

$$O_2 + 4H^+ + 4e^- \longrightarrow 2H_2O \tag{11.2}$$

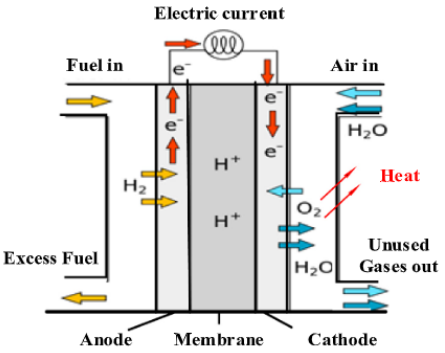

Figure 11.2: PEMFC membrane chemical reactions [58]

Table 11.3: Known physical properties of PEMFC [59]

Physical properties	Symbol	Values	Unit
Thermodynamic voltage	E_{thermo}	1	$[V]$
Operating current density	j	0.5	$[A/cm^2]$
Temperature[23]	T	363	[K]
Hydrogen mole fraction	x_{H_2}	0.9	[-]
Oxygen mole fraction	x_{O_2}	0.19	[-]
Cathode water mole fraction	x_{H_2O}	0.1	[-]
Cathode pressure[23]	p^C	1	$[atm]$
Anode pressure[23]	p^A	1	$[atm]$
Transfer coefficient	α	0.5	[-]
Exchange current density	j_0	0.0001	$[A/cm^2]$
Electrolyte thickness[23]	t^M	183	$[\mu m]$
Anode thickness	t^A	350	$[\mu m]$
Cathode thickness	t^C	350	$[\mu m]$
Dry density of Nafion 117	ρ_{dry}	0.0021	$[kg/cm^3]$
Nafion equivalent weight	M_m	1	$[kg/mol]$
Electro-osmothic drag coefficient saturated Nafion	n_{drag}^{SAT}	2.5	[-]
Gas constant	R	8.314	$[J/molK]$
Faraday constant	F	96,485	$[C/mol]$

Table 11.4: Calculated physical properties of PEMFC using Appendix B

Physical properties	Symbol	Values	Unit
Vapor saturation pressure	p_{SAT}	0.691	$[atm]$
Mole fraction water in fully humidified air	$x_{H_2O,SAT}$	0.227	[-]
Water diffusivity	D_λ	$5.135 \cdot 10^{-6}$	$[A/cm^2]$
Effective hydrogen (or water) diffusivity	$D^{eff}_{H_2,H_2O}$	0.509	$[cm^2/s]$
Effective oxygen (or water) diffusivity	$D^{eff}_{O_2,H_2O}$	0.100	$[cm^2/s]$
Effective oxygen (or nitrogen) diffusivity	$D^{eff}_{O_2,N_2}$	0.075	$[cm^2/s]$
Constant C	C	4.974	[-]
Constant α^*	α^*	-0.654	[-]
Total area-specific resistance of membrane	ASR_m	0.204	$[cm^2/A]$
Ohmic overvoltage	η_{ohmic}	0.102	$[V]$
Cathodic overvoltage	$\eta_{cathodic}$	0.161	$[V]$
Operating cell voltage	V	0.737	$[V]$

The operating cell voltage (V) is of the Nafion 117 membrane is given in Equation 11.3 [59].

$$V = E_{thermo} - \eta_{ohmic} - \eta_{cathode} \tag{11.3}$$

The cathodic and ohmic overpotentials are calculated by using 11.4 and Equation 11.5. These equations depend on several different parameters. Table 11.3 contains the known physical properties of the PEMFC and Table 11.4 lists the calculated parameters (see Appendix B for more information) needed to calculate the overpotentials.

The cathodic and ohmic overpotentials can be found using Equation 11.4 and 11.5 [59]:

$$\eta_{cathode} = \frac{RT}{4\alpha F} \cdot \ln\left(\frac{j}{j_0 p^C \cdot \left[x_{O_2}\big|_d - \frac{t^C j RT}{4Fp^C D^{eff}_{O_2,N_2}}\right]}\right) = 0.161\ V \tag{11.4}$$

$$\eta_{ohmic} = j \cdot ASR_m = 0.102\ V \tag{11.5}$$

All the required parameters are listed in Table 11.3 and 11.4. The fuel cell voltage in the Nafion 117 membrane operating at 90 °C and 1 atm is then $V = 1 - \eta_{cathode} - \eta_{ohmic} = 1 - 0.102 - 0.161 = 0.73V$.

11.5.2 Design point

Finally, using the analysis discussed in Section 11.5.1, the A320-HACK PEMFC was customized and modelled. A polarization curve was derived by calculating the fuel cell voltage for different current

[23] Adapted to the A320-HACK

densities, which could be then used to choose a design point and predict the performance of the fuel cell. The polarization curve gives the dependency of the cell voltage on the current density and is presented in Figure 11.3. From this, the power density of the fuel cell can be estimated, which is given as $P = i \cdot V_c$, where i represents the current density and V_c the fuel voltage. This is visualized in Figure 11.4.

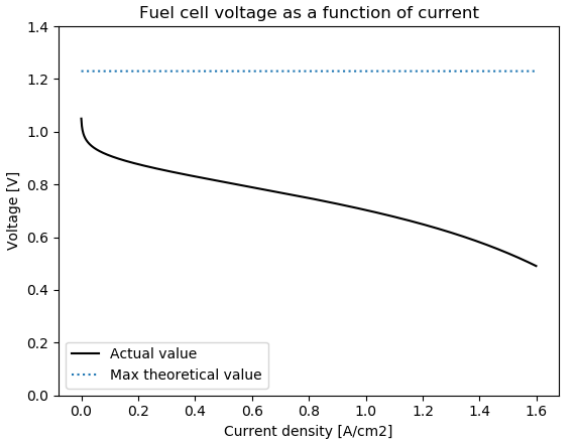

Figure 11.3: Polarization Curve

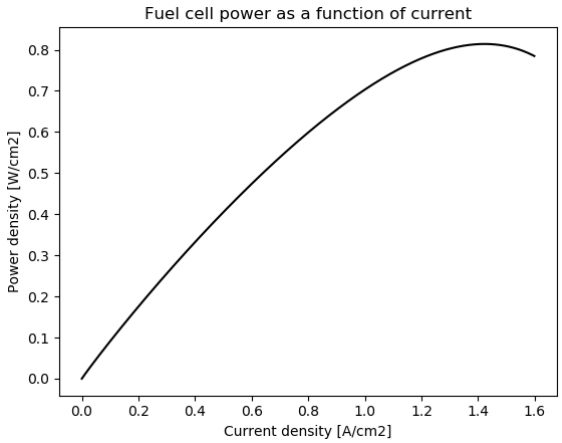

Figure 11.4: Fuel curve power density

Finally, the efficiency was calculated using Equation 11.6 [60], Where a value of 0.85 is assumed for the fuel utilization coefficient μ_f. Plotting the efficiency against the current, we obtain Figure 11.5.

$$\eta = \mu_f \frac{V_c}{1.25} \cdot 100\% = \mu_f \frac{P}{1.25i} \cdot 100\% \quad (11.6)$$

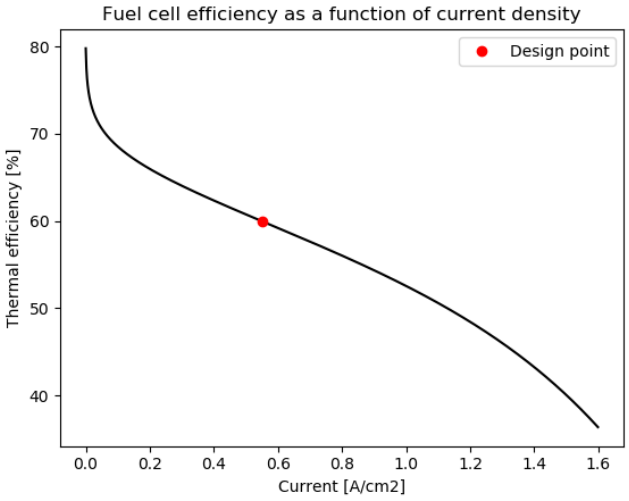

Figure 11.5: Fuel cell efficiency as a function of current density

From these graphs, the design point was chosen. The PEMFC efficiency ranges between 40-60%[24]. Due to the intensive research in the fuel cell technology, it is expected that this efficiency will rise by the time the A320-HACK is deployed. Therefore, for this analysis, the upper limit of 60% FC efficiency was assumed, highlighted in Figure 11.5 by a red point. This corresponds to a current density of $i = 0.55\ A/cm^2$ and a cell voltage $V_c = 0.8\ V$.

11.6 Required Power

The electrical power required by the aircraft systems and the power needed by the fuel cell itself are analysed in this section.

11.6.1 Power Required by the Aircraft Subsystems

The power estimates during each mission phase were based on X. Xia thesis, who evaluated the power requirements for a future aircraft concept with 150 seats, utilising electrical power instead of the con-

[24] https://www1.eere.energy.gov/hydrogenandfuelcells/fuelcells/pdfs/fc_comparison_chart.pdf, accessed:18-Jun-2021

ventional pneumatic and hydraulic systems [61]. These values were then scaled by a factor 180/150 to estimate the power requirements of the A320-HACK (with 180 seats), which are presented in Table 11.5. The last row represents the time per phase, as determined in the previous work [14].

Table 11.5: Power requirement during mission phases

	Ground	Take-Off	Climb	Cruise	Descend	Landing
X. Xia estimate [kW] [61]	195.4	90.1	223.5	275.6	233.5	96.35
A320-HACK [kW]	233.9	108.1	268.2	330.7	280.2	115.62
Time [min] [61]	20	1	20	430	18	3

11.6.2 Hydrogen and Air Mass Flows

For the first iteration, the fuel cell was assumed to constantly deliver the average of the powers derived from the values in Table 11.5. Knowing the fuel cell power requirements, the mass flow of H_2 and O_2 were estimated usingEquation 11.7 and 11.8[25].

$$\dot{m}_{H_2} = \frac{M_{H_2} P_{elec}}{2 V_c F} \tag{11.7}$$

$$\dot{m}_{O_2} = \frac{M_{O_2} P_{elec} \lambda}{4 V_c F} \tag{11.8}$$

The molar masses, M_{H_2} and M_{O_2}, were set to 2.016 g/mol and 31.998 g/mol, respectively, and the Faraday's constant, F, equals 96,485 C/mol. The P_{elec} is the average power as determined from Table 11.5 and V_c comes from Section 11.5. For the stoichiometric ratio, λ, a usual value of 2 was chosen [60].

The oxygen is retrieved from the atmosphere so no additional oxidiser tank is required. The oxygen mass flow was translated to the air flow. The atmosphere consists of roughly 21% oxygen and 78% nitrogen by volume, while the remaining 1% of other gases was neglected. For N_2, a molar mass of 28.0134 g/mol was taken, and Equation 11.9 and 11.10 were used to find the mass ratio of O_2 in the air and the air's mass flow rate, respectively.

$$O_2 \text{ mass proportion} = \frac{0.21 M_{O_2}}{0.21 M_{O_2} + 0.78 M_{N_2}} \tag{11.9}$$

$$\dot{m}_{air} = \frac{\dot{m}_{O_2}}{O_2 \text{ mass proportion}} \tag{11.10}$$

11.6.3 Power Required by the Fuel Cell System

The fuel cell is required to provide power to its auxiliary components such as the compressor, pumps and humidifiers. Furthermore, the fuel cell and the battery dissipate power, due to their limited efficiency. First, the compressor was modelled, assuming the compression is isotropic. The power required for such a compressor is found with Equation 11.11 [60].

$$P = c_p \frac{T_1}{\eta_c} \left[\left(\frac{P_2}{P_1} \right)^{(\gamma-1)/\gamma} - 1 \right] \dot{m} \tag{11.11}$$

For the air, c_p and γ are equal to 1004 $J/(kgK)$ and 1.4, respectively, and the mass flow of the air was determined in Section 11.6.2. A common value of 0.7 was taken for the compressor efficiency η_c [59]. Assuming that the air is taken out of the atmosphere, the temperature T_1 and pressure P_1 for the troposphere can be estimated using the International Standard Atmosphere model. With this information, the compressor required power can be plotted as a function of altitude, as displayed in Figure 11.6, where the power curve is plotted for different output pressures p_2.

As can be seen in Figure 11.6, power can be saved when compressing the air to only 1 atm, which is within the limits of the operating pressures for PEMFC[26] and hence it was chosen for the design.

[25] https://repository.lboro.ac.uk/articles/conference_contribution/A_fuel_cell_system_sizing_tool_based_on_current_production_aircraft/9221111, accessed:15-Jun-2021

[26] https://www.researchgate.net/publication/266053721_Optimal_operating_temperature_and_pressure_of_PEM_fuel_cell_systems_in_automotive_applications, accessed:20-Jun-2021

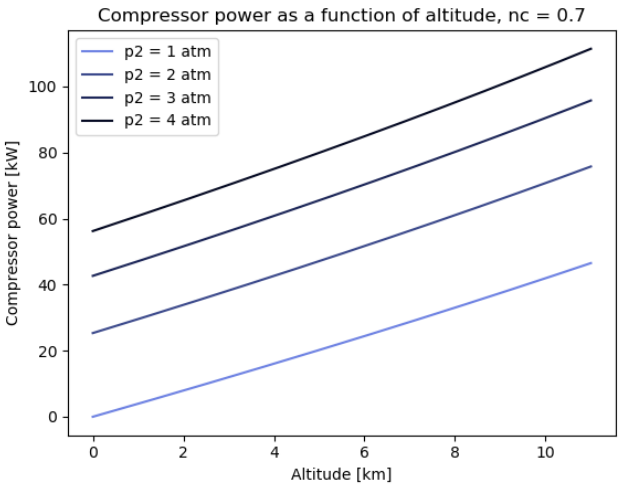

Figure 11.6: Compressor power as a function of altitude

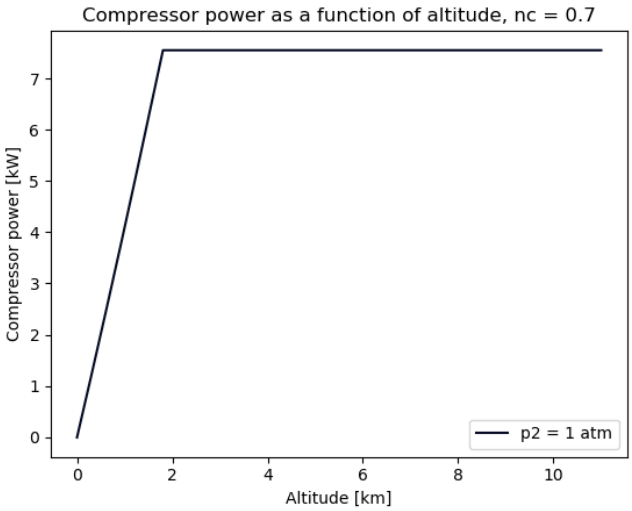

Figure 11.7: Power curve of a compressor using cabin air

To further reduce the power, cabin air is used, which is compressed to 0.8 atm at high altitudes. This way, the pressure increase over the compressor is minimized to 0.2 atm. Knowing that the temperature of the cabin air is kept at around 20 $°C$, the required power was recalculated, and the final compressor power curve as a function of altitude is presented in Figure 11.7. Based on the corresponding altitudes, this power was added to the previously computed required power by the aircraft systems.

Finally, the first order estimation for the power of other components, such as the hydrogen fuel and coolant pumps, was made using the methods presented in Section 9.3.3. These were found to have only marginal effects on the power estimation. Hence, a safety factor of 1.2 was applied to each phase, as suggested by A. Thirkell[27] to account for these other power requirements, but also to account for the degradation of the fuel cell over time and to increase the flexibility for peak loads. Subsequently, the new power levels could be estimated for each flight phase, resulting in a new average power, which will be provided by the fuel cell.

Since there is a circular dependency between the fuel cell power and the required compressor power, these calculations were iterated until the results did not change by more than 2%. From this analysis, it was evaluated that the PEM fuel cell system has to provide the power of 394 kW, which was rounded up to 400 kW. This fuel cell will also have a hydrogen consumption of 5.2 g/s and will require the cabin air inflow of around 350 g/s.

11.7 Fuel Cell and Battery Sizing

Once the power requirements for each stage are determined, the fuel cell and the battery can be sized. This section will discuss the fuel cell sizing in Section 11.7.1 and the battery sizing in Section 11.7.2.

11.7.1 Fuel Cell Sizing

The fuel cell shall provide an output power of 400 kW (see Section 11.6). Based on this requirement, the connection of the individual cells can be determined. For that, the requirements on the voltage and the current have to be set. The APU of A320neo delivers the power at a voltage of 115 V. Designing the fuel cell for this output would, however, correspond to a current of

$$I = \frac{P}{V} = \frac{400 \cdot 10^3}{115} \approx 3500\ A \tag{11.12}$$

The drawback of such a large current are high power losses resulting in high production of heat, reducing the efficiency and requiring additional cable cooling. Therefore, it was decided to design the fuel cell with higher voltage and lower current output. To determine the optimum current which would not require cooling, the cable heat loss was modelled. The power dissipated per length in a cable hence equals:

[27] https://repository.lboro.ac.uk/articles/conference_contribution/A_fuel_cell_system_sizing_tool_based_on_current_production_aircraft/9221111, accessed:08-Jun-2021

$$P' = I^2 R' \qquad (11.13) \qquad \text{where} \qquad R' = \frac{\rho}{A} \qquad (11.14)$$

with ρ being the resistivity of the wire, L its length and A its area. The power dissipated per length must equal the heat flow from the conductor per length as given in Equation 11.15 with R_{th} the thermal resistance measured in Km/W.

$$\frac{I^2 \rho}{A} = \frac{T_{cable} - T_{outside}}{R_{th}} \qquad (11.15) \qquad A = \frac{I^2 \rho R_{th}}{T_{cable} - T_{outside}} \qquad (11.16)$$

The resistivity of a wire depends on the temperature, but a linear relationship can be assumed. Hence, the resistivity can be modelled by Equation 11.17, where ρ_0 and T_0 correspond to the resistivity and temperature at a known point, and α is the temperature coefficient of resistance. With the circular cross-section of the wire, Equation 11.16 can be rewritten to:

$$\rho = \rho_0 \left(1 + \alpha (T - T_0)\right) \qquad (11.17) \qquad r = \sqrt{\frac{I^2 \rho_0 (1 + \alpha (T - T_0)) R_{th}}{\pi (T_{cable} - T_{outside})}} \qquad (11.18)$$

For the model, the values in Table 11.6 were considered.

Table 11.6: Wires thermal assessment overview

Parameter	Value	Unit	Note
ρ_0	$1.68 \cdot 10^8$[28]	$[\Omega m]$	Copper wire was assumed
α	0.00386	[1/K]	Copper wire was assumed
T_0	293	[K]	20 °C
$R_{th_{XPLE}}$	3.5[29]	[Km/W]	XLPE insulation was assumed
$R_{th_{air}}$	36.075[30]	[Km/W]	Taken at 45 °C
R_{th}	39.575	[Km/W]	$R_{th_{XPLE}}$ + $R_{th_{air}}$
$T_{outside}$	313	$[K]$	The temperature inside the aircraft is assumed to not exceed this value; 40 °C

With this analysis, the dependency of the required diameter of the wire with respect to the equilibrium temperature in the wire was modelled. Figure 11.8 displays this relationship for various currents. The red vertical line sets the temperature limit to 90 °C corresponding to the maximum allowable temperature for the XLPE insulation[31], which is commonly used with these wires.

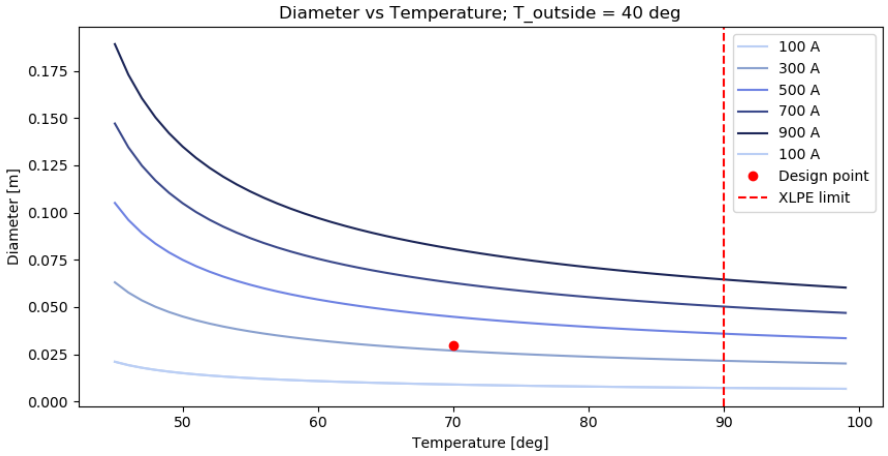

Figure 11.8: Cable diameter as a function of cable temperature

[28] http://hyperphysics.phy-astr.gsu.edu/hbase/Tables/rstiv.html, accessed: 08-Jun-2021

[29] https://wire.buyawg.com/viewitems/tegories-appendix-thermal-resistivity-of-materials/vity-of-materials-thermal-resistivity-of-materials, accessed:09-Jun-2021

[30] https://www.engineeringtoolbox.com/air-properties-viscosity-conductivity-heat-capacity-d_1509.html, accessed:09-Jun-2021

[31] https://mycableengineering.com/knowledge-base/iec-60287-current-capacity-of-cables-introduction, accessed:08-Jun-2021

To keep sufficient margin from 90 °C limit, it was decided to maintain the temperature inside the wire at 70 °C. Next, the current had to be selected. Too high currents will result in too thick wires connected to the fuel cell and hence too heavy harness system. However, decreasing the current too much will result in excessively high voltage. The voltage of 1200 V was evaluated as feasible since there already exist fuel cells operating at 1000 V[32]. This would correspond to a current of 333 A and the diameter of a wire of around 2.9 cm, shown by a red point in Figure 11.8.

Knowing the cells voltage and the current, it can be determined how many cells can be placed in parallel and in series. As modelled in Section 11.5, one cell in A320-HACK FC system design is assumed to produce 0.8 V of voltage with the current density of 0.55 A/cm^2. The number of cells in series can be determined as:

$$n_{series} = \frac{V}{V_c} = \frac{1200}{0.8} = 1500 \tag{11.19}$$

To estimate the number of cells in parallel, the total number of required cells was evaluated first. The Toyota Mirai fuel cell uses 370 cells to produce 114 kW of power, which gives the ratio of 0.308 $kW/cell$. Similarly, BOSCH claims that roughly 400 cells are needed to produce 120 kW, giving 0.3 $kW/cell$[33]. Assuming the BOSCH value, the number of cells required to produce 400 kW of power on board of A320-HACK is roughly 1334. However, 1500 cells are already placed in series, which means that only 1 row of these cells is required and none will be placed in parallel.

The data from Toyota Mirai were used also to determine the volume and mass of the stack. The Mirai stack takes up 37 L and weights 56 kg. This gives 0.1 $L/cell$ and 0.15 $kg/cell$. The A320-HACK would hence result in a mass and volume of 225 kg and 150 L, respectively.

Next, specific dimensions were determined. The fuel cell is required to produce 333 A as evaluated previously. With the current density, i, determined in Section 11.5, the dimensions were determined as follows:

$$A = \frac{I}{i} = \frac{333}{0.55} \approx 606\ cm^2 \tag{11.20}$$

$$\text{length} = \frac{V}{A} = \frac{150 \cdot 10^3}{606} \approx 248\ cm \tag{11.21}$$

This gives a thickness of about 1.65 mm for one single cell. This was validated by the Mirai stack, where 1 cell has a thickness of 1.34 mm[34] (which is 20% lower).

Finally, to prevent the cell from being too long, it was decided to divide it into 5 stacks placed on top of each other and connect them with wires. Each stack thus has about 50 cm in length. The width was chosen to be 60 cm, which gives the height of one stack of 606/60 = 10.1 cm. All of these dimensions are summarized in Figure 11.9.

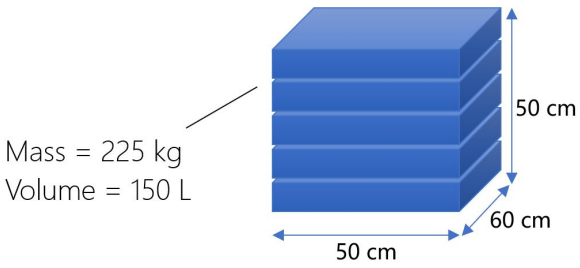

Figure 11.9: Fuel cell dimensions

11.7.2 Battery Sizing

The sizing of the battery will depend on the difference of the power required by the aircraft systems (including the fuel cell auxiliary components) for each phase and the (constant) power provided by the fuel cell. These two components were determined as described in Section 11.6 and the differences in the values is provided in Table 11.7. The negative value signifies that the battery outputs power, while the positive values signify charging of the battery.

Table 11.7: Power required by the battery

[32] https://nedstack.com/en/pemgen-solutions/stationary-fuel-cell-power-systems/pemgen-chp-fcps-1000, accessed:10-Jun-2021

[33] https://www.bosch.com/stories/fuel-cell-stack/, accessed:12-Jun-2021

[34] https://www.toyota-europe.com/download/cms/euen/Toyota%20Mirai%20FCV_Posters_LR_tcm-11-564265.pdf, accessed:07-Jun-2021

Year	Ground	Take-Off	Climb	Cruise	Descend	Landing
Power difference [kW]	93.45	219.8	53.3	-9.8	41.3	212.3
Time [min]	20	1	20	430	18	3

The state of the battery during each phase of the mission was determined by multiplying the power differences presented in Table 11.7 with corresponding times. This is graphically depicted in Figure 11.10.

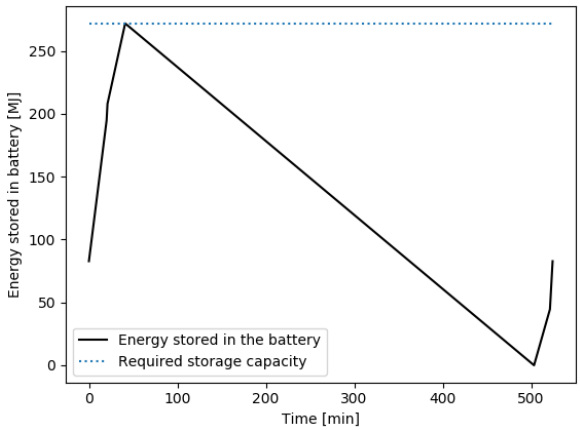

Figure 11.10: Energy stored in the battery during the mission

As can be seen in Figure 11.10, the battery requires the capacity of around 267 MJ. To account for the depth of discharge and degradation of the battery, a 1.2 factor was added resulting in a capacity of 320 MJ. The battery will be charged during all the flight phases, excluding the cruise phase. The A320-HACK will draw power from the battery during cruise to support the fuel cell. Furthermore, the battery might require on-ground charging during before the flight, as suggested by Figure 11.10, but it is not strictly necessary as the battery is also being charged on-board during the final phases of the mission, which means it is already charged to a certain extent at the end of the mission.
The battery was sized based on the capacity requirement. A stack of lithium-ion cells were chosen due to their high energy density, high voltage capabilities and low maintenance required[35]. A cell with the nominal voltage of 3.7 V and the capacity of 2550 mAh was considered.

The battery was designed to provide the same voltage as the fuel cell to simplify the circuit. The required number of batteries in series and in parallel was determined as follows:

$$C_{bat} = \frac{E_{bat}}{V_{bat}} = \frac{320\ MJ}{1200\ V} = \frac{88900}{1200} = 74\ Ah \tag{11.22}$$

$$\text{Cells in series} = \frac{V_{bat}}{V_{cell}} = \frac{1200}{3.7} = 324.32 \rightarrow 325 \tag{11.24}$$

$$\text{Cells in parallel} = \frac{C_{bat}}{C_{cell}} = \frac{74}{2.55} = 29.02 \rightarrow 30 \tag{11.23}$$

$$\text{Total number of cells} = \text{Cells in series} \cdot \text{Cells in parallel} = 9750 \tag{11.25}$$

The batteries connected in series will be connected in their vertical position, as shown in Figure 11.12. The rows in parallel will be placed next to each other. Similarly to the fuel cells, it was decided to group the Li-ion cells into 5 stacks placed on top of each other. One stack will contain a row of 65 cells in series and 30 rows in parallel.

A typical Li-ion cell with the height of 6.4 cm and diameter of 1.8 cm was assumed. This would give a stack size of 1.8·65 = 117 cm in length, $1.8 \cdot 30 = 54\ cm$ in width and 6.4·5 = 32 cm in height. This would give a volume of approximately 202 L. However, this analysis assumed that the cells are placed perfectly next to each other and no extra space is left for cooling, wiring and other mechanisms. In fact, Hossain S. et al. estimate the Li-ion stack energy density of 280 Wh/L[36] , which would result in a

[35] https://www.electronics-notes.com/articles/electronic_components/battery-technology/li-ion-lithium-ion-advantages-disadvantages.php, accessed:09-Jun-2021
[36] https://ieeexplore.ieee.org/document/659154, accessed:15-Jun-2021

volume of about 330 L. As a conservative estimate, the higher value will be considered. Furthermore, the specific energy was estimated to be 300 Wh/kg. This value considers the expected rapid development in the battery technology. As shown in Figure 11.13, Airbus expects the battery energy density to rise to 600 Wh/kg by 2030, but a more conservative value was considered in this analysis, which gives the battery mass of about 296 kg. All these dimensions are summarized in Figure 11.11.

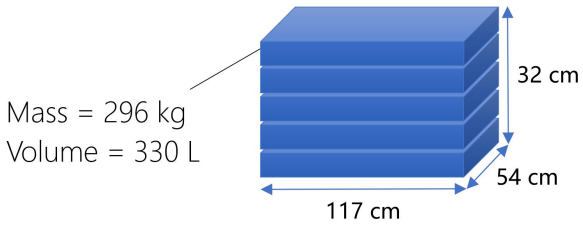

Figure 11.11: Battery dimensions

Next, the cost was estimated using the specific costs of Li-ion stacks for the last 10 years[37]. A best fit line was used to predict the cost in future and the results are shown in Figure 11.13. As seen, the battery cost reduces rapidly and is expected to fall below 100 USD/kWh by 2022. However, 100 USD/kWh was considered as a conservative estimate, which would result in the total cost of around 7600 €.

Finally, it is highlighted that the FC system provides the power at the voltage of 1200 V DC. Therefore, the system has to be connected in circuit first to the power inverter and subsequently to a transformer, so that the power is delivered in the AC form and at the voltage required by the A320-HACK system.

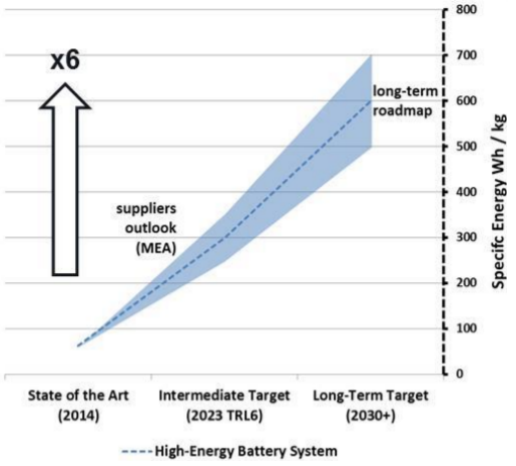

Figure 11.12: Battery specific energy predictions[38]

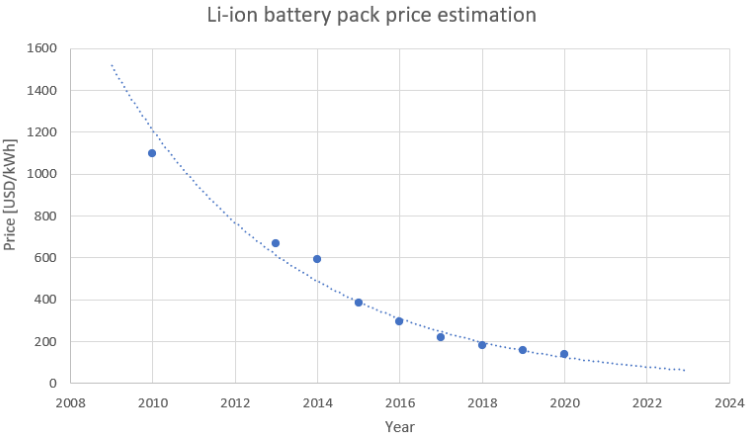

Figure 11.13: Battery specific cost[39]

11.8 Water Production

A proton-exchange membrane fuel cell (PEMFC) lets hydrogen (H_2) and oxygen (O_2) react with each other to produce water (H_2O). The chemical reaction can be found in Section 11.5.1. The water produced by the fuel cell can be recovered and reused for the lavatories on board. Therefore, the amount of produced H_2O needs to be calculated. This can be done using Equation 11.26 [60].

$$\text{Water produced} = 9.34 \cdot 10^{-8} \cdot \frac{P_e}{V_c} \quad [kg/s] \tag{11.26}$$

[37] https://www.renewableenergyworld.com/storage/annual-survey-finds-battery-prices-dropped-13-in-2020/#gref, accessed:17-Jun-2021

[38] https://www.renewableenergyworld.com/storage/annual-survey-finds-battery-prices-dropped-13-in-2020/#:~:text=Lithium%2Dion%20battery%20pack%20prices,forecast%20from%20BloombergNEF%20(BNEF)., accessed:10-Jun-2021

[39] https://sunjet-project.eu/sites/default/files/Airbus%20-%20Delhaye.pdf, accessed:10-Jun-2021

Where P_e is the required power of the fuel cell and V_c the voltage per cell (0.8 V). The water production of our PEMFC will be equal to 0.0374 kg/s, which can be translated to 134.5 L/hr.

The water collection system is based on a fuel cell system for a car by Mann & Hummel[40]. This system includes a water separator before the fuel cell to drain the excess water to prevent the fuel cell membrane from drowning. The exhaust air system, located after the FC, has a turbine water separator. A similar system could be implemented in the A320-HACK to separate the water and connect it to the already existing water tank.

The A320neo water tank contains 200 L [62]. This means that the water produced by the PEMFC can be recovered and stored in this tank. When the tank is completely full, the excess water will be vented out of the A320-HACK, using the drain masts at the back of the aircraft [63]. Using a system to recover the water from the PEMFC will reduce the amount of water needed to be pumped into the A320-HACK at the airport, thus potentially reducing turn-around time and cost.

11.9 Water Cooling

A fuel cell and battery produce heat due to their efficiency limitations, therefore they require cooling. This section will elaborate on the cooling mechanism of the fuel cell system and the battery. There are two widely used types of cooling, air and water cooling. Air cooling is usually used to cool down systems generating low power. On the other hand, [51, 60] mentions that water cooling should be used when more than 1 kW of power is required, while [58] suggests >10 kW. The A320-HACK FC system produces 400 kW of power, thus water cooling is required.

Water cooling will use a mixture of water and antifreeze (usually glycol [58]). However, after a while, the coolant can become electrically conductive due to the ionising nature of glycol [58]. Therefore, the A320-HACK system will use R134a instead of glycol. The characteristics of water, R134a and the coolant mixture are summarized in Table 11.8.

Table 11.8: Physical properties of coolant

Physical properties	Water	R134a	Coolant mixture
Freezing point [K]	273.15	176.5[41]	244.2
Density at 293 K [kg/m^3]	998.21[42]	1225.5 [43]	1066.4
Specific heat capacity [$J/(kgK)$]	4180[44]	827.7 [64]	3174.3

For the first order estimate, the physical properties of the mixture of water and R134a were determined by linearising the properties of each compound based on the water-R134a ratio. For example, the freezing point of the mixture was determined as:

$$T_{freeze,mix} = r \cdot T_{freeze,water} + (1 - r) \cdot T_{freeze,R134a} \tag{11.27}$$

where r is the proportion of water in the mixture and the temperatures are in Kelvins. The density and specific heat can be found in a similar way. It was decided to use a 70/30 water-R134a ratio instead of a conventional 50/50 ratio. The reason for this is that the heat efficiency of heat conduction of the coolant can be increased, resulting in a lower requirement for the fuel flow and pump power. Furthermore, according to the estimates presented in Table 11.8, the freezing point of 70/30 mixture is estimated to be around -30 °C, which is more than sufficient if the fuel cell system will be kept at a temperature similar to the cargo compartment (kept above 7 °C[45]). The other physical properties of the coolant mixture are

[40] https://www.mann-hummel.com/en/oe-products/applications/fuel-cells/, accessed:21-Jun-2021
[41] https://www.engineeringtoolbox.com/refrigerants-d_902.html, accessed: 11-May-2021
[42] https://www.engineeringtoolbox.com/water-density-specific-weight-d_595.html, accessed: 11-May-2021
[43] https://www.engineeringtoolbox.com/r134a-properties-d_1682.html, accessed: 11-May-2021
[44] https://www.engineeringtoolbox.com/specific-heat-capacity-water-d_660.html, accessed: 11-May-2021
[45] https://enroute.aircanada.com/en/aviation/what-temperature-is-it-in-the-baggage-hold/, accessed:12-May-2021

also stated in Table 11.8. The cooling will be analysed for both the PEMFC and battery in Section 11.9.1 and in 11.9.2, respectively.

11.9.1 Fuel Cell Liquid Cooling

To estimate the coolant mass flow needed to cool the PEMFC, the heat produced by the PEMFC needs to be estimated. The fuel cell was assumed to have an efficiency of 60%. The remaining 40% can be assumed to be wasted in the form of heat. To estimate the required mass flow, Equation 11.28 was used.

$$(1-\eta)\dot{m}_{H_2} LHV = \dot{m}_{coolant} c_{p,coolant} \Delta T \qquad (11.28)$$

$$\dot{m}_{coolant} = \frac{(1-\eta)\dot{m}_{H_2} LHV}{c_{p,coolant}\Delta T} \qquad (11.29)$$

The efficiency η was set to 0.6, the lower heating value of hydrogen LHV was taken to be 120 MJ/kg, the hydrogen mass flow was determined in Section 11.6.2 and $c_{p,coolant}$ was taken from Table 11.8. Finally, the fuel cell was decided to be operated at 90°C, which is still within the operating limit (see Table 11.2), and the coolant was assumed to leave the heat-exchanger at a temperature of no more than 30°C. This gives a temperature difference of 60°C. Inserting these values into the equation, the required mass flow was calculated to be 1.05 kg/s.

Bipolar plates will be used for cooling the PEMFC as they are commonly used for this application [65]. A bipolar plate is a plate that is conductive, hence it also serves as the electrical connection between the different cells in the PEMFC [66]. It has a cathode on one side and an anode on the other and it typically has internal cooling channels. These thin plates are inserted between the individual cells, as shown in Figure 11.14. Some typical flow patterns of these channels can be seen in Figure 11.15. These flow patterns are all classified as serpentines [67]. The advantage of serpentine flow fields is that they have a stable performance and smooth temperature distribution [67]. The actual layout of the flow pattern is out of the scope of this project. However, an estimation of the amount of coolant needed for a serpentine flow patterns will be discussed.

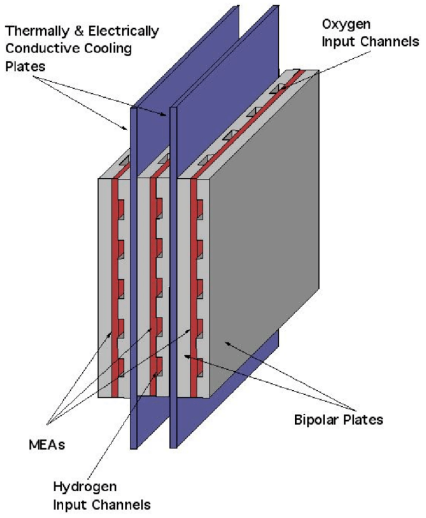

Figure 11.14: Cooling plate assembly for PEMFC

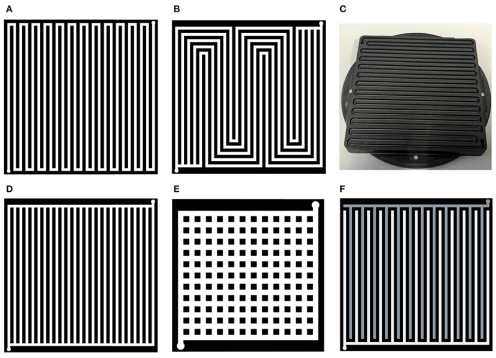

Figure 11.15: PEMFC water cooling flow patterns [67]

Assuming that the thickness of a cooling plate is 1.5 mm[46], the volume of the coolant needed can be estimated as

$$V_{coolant} = (n+5) \cdot A \cdot t_{plate} \cdot f \qquad (11.30)$$

where n is the number of single fuel cells (5 is added to account for the plates at the end of the 5 fuel cell stacks), A is the area of the fuel cell as determined in Section 11.7.1, t_{plate} is the plate thickness and f the fraction of the volume filled with the coolant. This fraction was estimated to be 50% based on Figure 11.15.

[46] https://www.researchgate.net/publication/326322053_Numerical_simulation_based_design_for_an_innovative_PEMFC_cooling_flow_field_with_metallic_bipolar_plates, accessed:09-Jun-2021

The required coolant volume for the fuel cell was determined to be approximately 68 litres. Furthermore, assuming the plates are made out of aluminium, a commonly used material for this application[47], the mass added by the cooling plates can be evaluated. As 50% of the plate volume was assumed to be occupied by the coolant, the volume of the aluminium is estimated to be approximately also 50%. Using the density of 2640 kg/m^3 [48], the additional mass of 180 kg was estimated.

11.9.2 Battery Liquid Cooling

The cooling design for the battery is similar as for the fuel cell. First, the dissipated heat was evaluated, which was estimated using equation Equation 11.31

$$P = RI^2 \tag{11.31}$$

Therefore, the resistance in the battery and the maximum current needs to be estimated.

The resistance of one Li-ion cell R_c was assumed to be 50 $m\Omega$[49]. As discussed in Section 11.7.2, 325 of these cells are connected in series, which results in a resistance per one series of cells of

$$R_{ser} = \sum^{n_{series}} R_{cell} = 325 \cdot 50 = 16.25\ \Omega \tag{11.32}$$

Since 30 of these series are connected in parallel, the total resistance is

$$\frac{1}{R_{tot}} = \sum^{n_{paral}} \frac{1}{R_{ser}} \tag{11.33}$$

$$R_{tot} = \frac{R_{ser}}{30} = 0.54\Omega \tag{11.34}$$

Next, the required current was determined. The powers at which the battery will be charged or discharged were determined in Section 11.7.2. During all this charging or discharging processes, the battery will be kept at 1200 V, which allows to calculate the batteries current as

$$I_{bat} = \frac{P_{bat}}{V_{bat}} = \frac{P_{bat}}{1200} \tag{11.35}$$

Now, the highest of the powers shall be selected to estimate the maximum current experienced by the battery. The battery is fed with the highest power at the take-off and landing stages. However, these stages last only a very small fraction of the mission and sizing for them would result in an overdesigned system. Therefore, it was decided to allow the battery to operate sub-optimally during these short phases, and the third highest power was taken for the calculation, which corresponds to the on-ground operations. Using Equation 11.35, the current of 78 A was estimated and hence using Equation 11.31, the heat dissipated $\dot{Q}$ was evaluated to be 3285 W.

Similarly to the fuel cell, the mass flow was evaluated as

$$\dot{m_{coolant}} = \frac{\dot{Q}}{c_{p,coolant}\Delta T} \tag{11.36}$$

Again, the coolant was assumed to be at 30°C and the battery was decided to be maintained at 50°C, which is still within the optimum operating range for the Li-ion cells[50]. Performing the calculation, the coolant mass flow of 0.052 kg/s was found.

[47] https://core.ac.uk/download/pdf/289993394.pdf, accessed:18-Jun-2020

[48] https://www.engineeringtoolbox.com/metal-alloys-densities-d_50.html, accessed:11-Jun-2021

[49] https://www.element14.com/community/groups/roadtest/blog/2021/02/16/battery-discharge-testing-with-the-bt3554, accessed:12-Jun-2021

[50] https://pubs.acs.org/doi/10.1021/acsenergylett.9b00663, accessed:06-Jun-2021

The design for the battery cooling was inspired by the fuel cell cooling - thin plates will be positioned between the battery rows. A plate will be placed between every second row in a configuration similar to Tesla Model S, as depicted in Figure 11.16. Again, the plate thickness of 1.5 mm was considered with channels covering 50% of the volume. As 65 cells are placed in series in the stack, 65/2 + 1 = 34 plates are needed. The area of the plate is assumed to be the same as the frontal area of the battery, which was specified in Section 11.7.2. Performing a similar calculation as for the fuel cell, the volume of the coolant for the battery was estimated to equal 4.5 L, and the plates would add 11 kg to the weight.

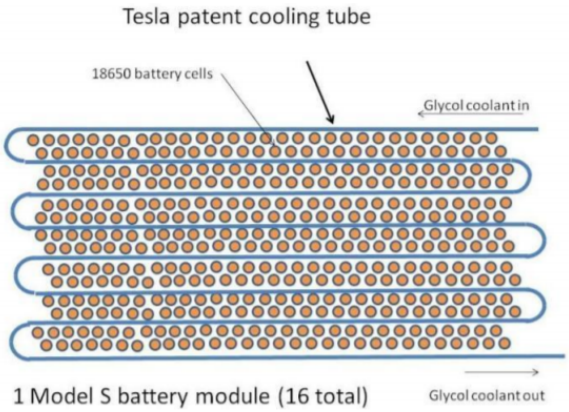

Figure 11.16: Tesla model S cooling system [68]

11.9.3 Coolant Heat-Exchanger

The coolant used inside the fuel cell also needs to be lowered in temperature before entering the fuel cell system. To do so, a heat-exchanger is used, which uses cabin air to bring the coolant from 90°C (assumed coolant temperature at the inlet to the heat-exchanger) to 30°C. The heat-exchanger is designed using the ϵ-NTU method explained in Section 9.3.4. The chosen design is a tinned-tube cross-flow heat-exchanger. The values which are used to design this heat-exchanger are given in Table 11.9.

Table 11.9: Inputs to the design of the coolant heat-exchanger

Parameter	Value	Unit	Parameter	Value	Unit
$T_{air_{in}}$	20	°C	$\dot{m}_{coolant}$	1.15	kg/s
$T_{coolant_{in}}$	90	°C	$c_{p_{air}}$	1000	$J/kg°C$
$T_{air_{out}}$	30	°C	$c_{p_{coolant}}$	3174.3	$J/kg°C$
$T_{coolant_{out}}$	30	°C	U	180	$W/m^2°C$

The resulting size of the heat-exchanger, assuming it had an area to volume fraction of 700 m^2/m^3 (see Section 9.3.4 for more detail), is of approximately 4 L. Such a heat-exchanger would weight around 20 kg by interpolating with the design from Brewer [31].

To complete the cooling design, the coolant tank has to be added, so that the losses due to leakage and evaporation are addressed and so that the cooling mechanism is flexible in case the coolant fuel flows need to be changed abruptly. The volume of the coolant tank was decided to be designed to 50% of the volume in the system. As determined previously, the fuel cell requires 68 L, the battery 4.5 L and the heat-exchanger 4 L of the coolant. 50% of the sum equals 38 L, which means that total volume of the coolant in the system sums up to 114 L. The liquid thus adds about 145 kg, using the values from Table 11.8.

11.10 Verification & Validation

The verification of the battery and fuel cell design are discussed in Section 11.10.1 and 11.10.2, respectively.

11.10.1 Battery Verification & Validation

The battery of the DPU will be able to store 320 MJ (88.9 kWh), have a mass of 296 kg, a voltage and current equal to 1200 V and 77 A, respectively. Finally, the battery will cost 7558€, as previously explained in Section 11.7.2. These values will need to be verified and validated with existing batteries currently on the market. The DPU battery will be compared with electric car batteries that have similar

specifications. They can be found in Table 11.10. The validation analysis will compare the energy capacity kWh, mass kg, voltage V, nominal capacity Ah and price €.

Table 11.10: Comparable car batteries

Car type	Energy capacity [kWh]	Mass [kg]	Max voltage [V]	Nominal capacity [Ah]	Price [€]
Ford Mustang Mach-E [51]	98.8	960	-	-	18,666-24360[52] [53]
Mercedes-Benz EQC	80	650[54]	405 [55]	230[55]	-
Jaguar-I-PACE [69]	90.2	606	389	232	32,650-34,491[56][57]
Tesla model S [70]	85	404.96[58]	21.6[58]	230	11,380[59]
Tesla model X	90	603[60]	400 [71]	400[61]	24,000[61]

As can be seen in Table 11.10, all the selected batteries are heavier and more expensive than the one from the DPU. This can be justified because the DPU battery mass and cost were predicted by using forecasts, which predict a reduction in price and mass for the future.

The nominal capacity of the A320-HACK fuel cell battery is equal to 74 Ah (see Section 11.7.2). This is three times lower than the ones stated in Table 11.10. However, this can be justified by Equation 11.22. The calculated nominal capacity depends on the chosen voltage. The A320-HACK battery operates at a voltage of 1200 V, which is three times higher than that of the batteries listed in Table 11.10. Thus, it can be assumed that the chosen voltage and nominal capacity are valid.

11.10.2 Fuel Cell Verification & Validation

The DPU fuel cell is specifically designed to deliver a power of 400 kW to the A320-HACK to comply with requirement *SR-DPU-01*. When designing this fuel cell, some assumptions were taken into account. This section will compare the DPU fuel cell to fuel cells that are currently on the market. If the DPU is very similar to the ones currently available on the market, then the DPU is validated.

Many fuel cells, which provide large amounts of power, are a combination of different smaller ones. For example, the CHP-FCP-1000 fuel cell consists of 120 Nedstack FCS 13-XXL fuel cells. Each Nedstack FCS 13-XXL provides a power of 13.6 kWe at 230 A[62]. PowerCell states that, when combining 12 S3-455C fuel cells, the power output will be equal to 1.14 MW. All the specifications of the considered fuel cells are stated in Table 11.11.

[51] https://www.ford.com/cmslibs/content/dam/brand_ford/en_us/brand/suvs-crossovers/mache/3-2/pdf/seo-pdfs/Mustang-Mach-E-Tech-Specs.pdf, accessed:18-Jun-2021

[52] Depending on the type of battery: 22,142.90 - 28.899.00 USD

[53] https://parts.ford.com/shop/en/us/electrical/battery-and-related-components/100/1#list, accessed:18-Jun-2021

[54] https://media.daimler.com/marsMediaSite/en/instance/ko/The-new-Mercedes-Benz-EQC-The-Mercedes-Benz-among-electric-vehicles.xhtml?oid=40995157, accessed:18-Jun-2021

[55] https://www.daimler.com/documents/sustainability/product/daimler-environmental-check-mb-eqc-class-org.pdf, accessed:18-Jun-2021

[56] Price for battery replacement.

[57] https://insideevs.com/news/491369/damage-jaguar-ipace-battery-enclosure-repair-cost/, accessed:19-Jun-2021

[58] Per module; a Tesla model S has 16 modules.

[59] https://www.currentautomotive.com/how-much-does-a-tesla-model-3-battery-replacement-cost/, accessed:18-Jun-2021

[60] https://teslatap.com/undocumented/, accessed: 19-Jun-2021

[61] https://stealthev.com/product/tesla-module/, accessed:19-Jun-2021

[62] https://nedstack.com/en/pemgen-solutions/stationary-fuel-cell-power-systems/pemgen-chp-fcps-1000, accessed:19-Jun-2021

Table 11.11: Comparable fuel cells

Fuel cell	Power [kW]	Max voltage [V]	Current [A]	Weight [kg]	Calculated power [kW]	Power-to-weight ratio [kg/kW]
VLS-II-150[63] [64]	150	$\geq$ 300	500	375	150	2.5
Nedstack FCS 13-XXL[65]	13.6	-	230	41	-	3
PureMotion Model 120[66]	120	-	-	900	-	7.5
FCM 120[67]	120	-	-	930	-	7.75
submarine[68]	120	215	-	900	-	7.5
HySeas III[69]	600	-	-	153.6	-	0.256
Ballard FCveloCity HD60[70]	60	220-350	288	244	63-100	4.1
Ballard FCveloCity HD85[70]	85	280-420	288	256	80.6-121	3
Ballard FCveloCity HD100[70]	100	200-580	288	285	57.6-167	2.85
S3-455C[71]	130	280-440	-	43	-	0.33

The power is related to the voltage and current by Equation 11.37

$$\text{Power} = \text{Voltage} \cdot \text{Current} \tag{11.37}$$

The power could be calculated for the Ballard FCveloCity-HD fuel cells. The lower limit of the power range for the HD60 and HD80 is very close to the advertised power. The Ballard FCveloCity-HD100 advertised power lies in the middle of the calculated range. This has everything to do with the operation conditions of the fuel cell, as it cannot operate at maximum conditions for a long period of time.

The power-to-weight ratio of the listed fuel cells is about 3.5 kg/kW. However, our fuel cell used a power-to-weight ration of 0.8 kg/kW. As can be seen in Table 11.11, the HySea III and S3-455C have a power-to-weight ratio is much lower and is equal to 0.256 and 0.33, respectively. Note, that these values are only for the fuel cell stack and not for the whole system including, for example, the cooling system. Therefore, it can be assumed that the chosen 0.8 kg/kW power-to-weight ratio is a reasonable value. Thus, the fuel cell design was done in a correct way, given these reasonable values.

11.11 Discussion, Limitations & Recommendations

The fuel cell was designed to provide power up of to 400 kW. The results of the fuel cell system design are summarized and compared with the current Honeywell 131-9A APU in Table 11.12.

[63] https://fuelcellsworks.com/news/horizon-automotive-pem-fuel-cells-to-set-300kw-benchmark/, accessed: 20-Jun-2021

[64] https://nedstack.com/sites/default/files/2019-11/20191105_nedstack_fcs_13-xxl.pdf, accessed:19-Jun-2021

[65] https://nedstack.com/en/pemgen-solutions/stationary-fuel-cell-power-systems/pemgen-chp-fcps-1000, accessed:19-Jun-2021

[66] https://ushybrid.com/wp-content/uploads/2017/11/DS0123_PureMotion120_080312.pdf, accessed:19-Jun-2021

[67] https://assets.new.siemens.com/siemens/assets/public.1535009488.28615cde70250d0e81b68ba466bd77d7f5c68c73.sinavy-pem-fuel-cells.pdf, accessed:20-Jun-2021

[68] https://www.slideshare.net/jornw1/u6000-power-73385-fuel-cellsversion1e, accessed:19-Jun-2021

[69] https://elib.dlr.de/132926/1/ELMAR-REGWA%20Paper_v6.pdf, accessed:20-Jun-2021

[70] https://www.ballard.com/docs/default-source/motive-modules-documents/fcvelocity_hd_family_of_products_low_res.pdf, accessed:20-Jun-2021

[71] https://www.fch.europa.eu/sites/default/files/Per%20Erkunge-PowerCell.pdf, accessed:20-Jun-2021

Table 11.12: A320-HACK DPU vs A320neo APU

Physical properties	**HACK DPU**	**neo APU**	Net Change
Efficiency [%]	60	15	+300%
Noise [dB]	40	127	-70%
Mass [kg]	788	145	+440%
Volume [L]	810	75	+980%
Cost [$]	19,300	350,000	-95%

As the results in Table 11.12 suggest, the use of fuel cells introduces a significant improvement in terms of the efficiency, noise and the cost. On the other hand, although rather optimistic predictions were considered for the mass and volume, these two parameters might still remain the problem.

The increase in mass means that the amount of payload or the amount of fuel might need to be compromised, neither of which is profitable for an airline. Therefore, the actual benefit of the inclusion of the fuel cell should be analysed in further detail.

Next, the fuel flexibility of the fuel cell system shall be evaluated. The DPU fuel cell is designed to work on hydrogen. However, not all airports will be able to offer hydrogen. This would mean that the DPU cannot start up and power the aircraft and thus not comply with the requirement *SR-DPU-01*. A solution could be to use a reformer on-board of the aircraft, which can extract hydrogen from hydrocarbons, such as kerosene. To this day, there are multiple projects investigating this solution[72]. Additionally, the power generators placed in the main engines should be used as a back-up power source in case the hydrogen is not available on board.

Finally, the durability of the fuel cells should be discussed, as it is known as the major obstacle of their commercialization in transportation applications[73]. The current PEM fuel cell lifetime amount to 3000 hours[74], although large improvements are expected in future. Assuming 4 flights per day, each taking 1.5 hour, such a fuel cell would not last more than 2 years in operation, which is a very short period considering the much longer operation lifespan of an aircraft. Regular replacements of the fuel cell would be required, which would result in additional high maintenance costs for the airline. In conclusion, the fuel cells still require further development before their mass, volume and durability can be considered acceptable for the use in aviation.

12 | Wing System Design

The main structural modifications to the A320neo that are needed to conceive A320-HACK stem from the wing, particularly from the wing and hydrogen tank interface. These modifications together with a brief structural analysis of the A320-HACK's wing is discussed in this chapter. In Section 12.1 loads acting on the wing are computed and in Section 12.2 stresses acting on the wingbox are analyses.

12.1 Load Analysis

The loads which act on the wingbox at each point along the span can be determined using the principle of static equilibrium. The external loads are first depicted by means of a free body diagrams, and using

[72] https://trimis.ec.europa.eu/project/generation-hydrogen-kerosene-reforming-efficient-and-low-emission-new-alternative-innovative, accessed: 22-Jun-2021

[73] https://www.hydrogen.energy.gov/pdfs/progress05/vii_i_3_borup.pdf, accessed:27-Jun-2021

[74] https://hal.archives-ouvertes.fr/hal-02380401/document, accessed:27-Jun-2021

these, the internal loads can be modelled and computed.

12.1.1 Free Body Diagram

The structural element which carries the load acting on the wing is the wingbox. The wingbox will be designed for the exposed wing and not for the centre section, meaning that the loads start acting on the wing at the point where the fuselage ends. The wingbox can be seen in Figure 12.1, as well as the three elements which induce point loads onto the structure: the engine, the tank and the winglet. The coordinate system used throughout the wing structural analysis is the one presented in Figures 12.2 to 12.4. The loads which act on the wing are divided in three types:

- Point loads acting on the sharklet, tank and engine. It is assumed that the sharklets carry all the induced drag at their tips. The other point forces are the weight of the tank, engine and sharklet; the drag of the engine and the tank; and the thrust of the engine.
- Distributed loads acting along the entire exposed wing: lift, zero lift drag and the weight of the wing surface.
- Reaction forces and reaction moments. Located at the Along each axis there is one reaction force and one reaction moment

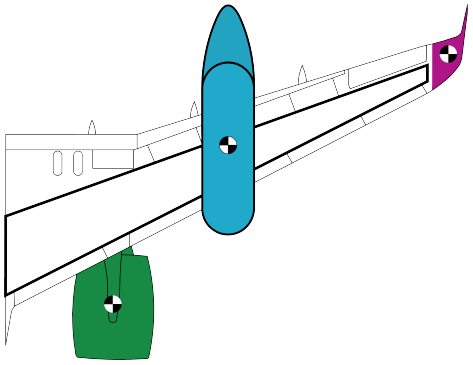

Figure 12.1: Components of the wing group

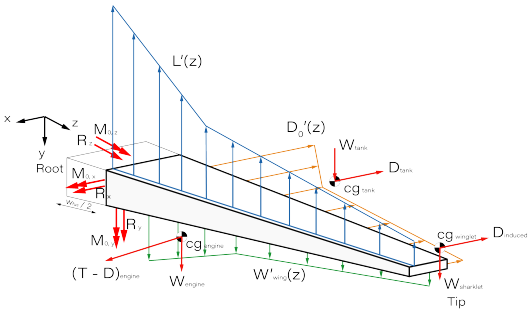

Figure 12.2: Free body diagram of the wing loading

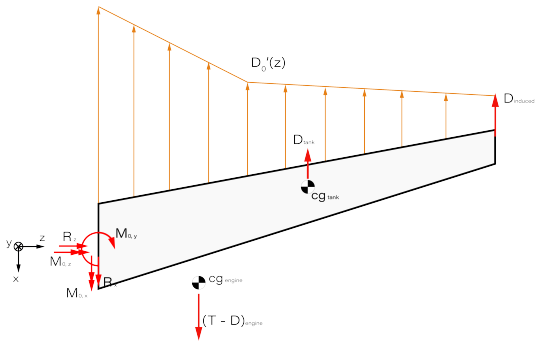

Figure 12.3: Top view of the free body diagram

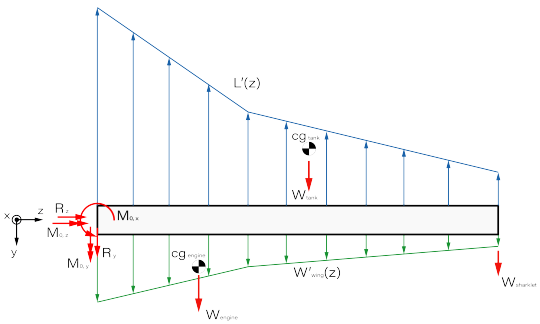

Figure 12.4: Front view of the free body diagram

12.1.2 Distribution of the Chord

The wing does not have a constant chord along its span, meaning that the aerodynamic loads and the cross section of the wingbox do change along the span and are therefore a function of z. A function for the chord is defined for further use throughout this chapter, and is given by Equation 12.1.

$$c(z) = \begin{cases} \frac{c_k - c_r}{z_k} z + c_r = m_1 z + c_r = -0.52z + 7.05 & \text{if } z < z_k \\ \frac{c_t - c_k}{b/2 - z_k}(z - z_k) + c_k = m_2 z + n_2 = -0.21z + 5.07 & \text{if } z \geq z_k \end{cases} \tag{12.1}$$

12.1.3 Individual Loads

Lift

In order to derive the lift load which act on the wingbox, it is necessary to see at which flight conditions the load is the highest. This was done by checking all possible combinations of weight and altitude until the highest lift ($L = n \cdot W$) was found. The load factor is found by means of a manoeuvre and gust envelope (see Figure 12.5) and the results are given in Table 12.1.

The distributed lift is a function of chord length, such that when integrated over the span, one is able to obtain the total lift. Using this equality, it is possible to derive the expression of distributed lift Equation 12.2.

$$\frac{1}{2}L_{max} = \int_{w_f/s}^{b/2} k_L c(z)\mathrm{d}z = k_L \frac{S_{exp}}{2} \qquad L'(z) = k_L c(z)\ , \quad \text{where } k_L = \frac{L_{max}}{S_{exp}} \tag{12.2}$$

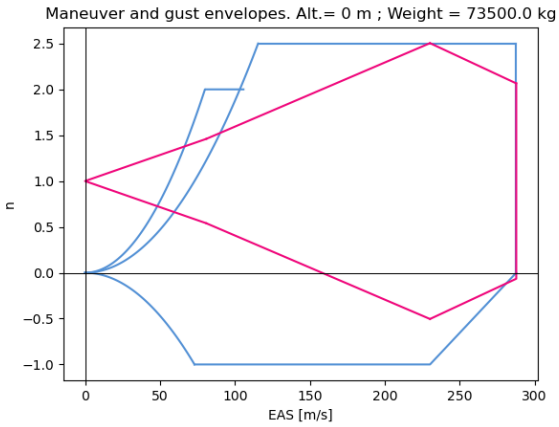

Figure 12.5: Manoeuvre and gust envelopes for the case of highest lift load based on CS25 regulations [6]

Table 12.1: Results for the highest lift case

Parameter	Value	Unit
h	0.0	m
W_{des}	73500	kg
n_{max}	2.51	-
$V_{des}(=V_c)$	230	m/s
$q(=\frac{1}{2}\rho V_{des}^2)$	32400	Pa
L_{max}	721	kN

Zero Lift Drag

In order to model a distributed zero lift drag of the wing, the equality between the integrated distributed drag and total drag is used. The zero-lift drag coefficient is in this case that of the wing only. The resulting distributed drag is given by Equation 12.3.

$$\frac{1}{2}D_{0_w} = \frac{1}{2}C_{D_{0_w}} qS = \frac{1}{2}C_{D_{0_w}} qS \frac{2}{S_{exp}} \int_{w_f/s}^{b/2} c(z)\mathrm{d}z = \int_{w_f/s}^{b/2} D_0'(z)\mathrm{d}z$$

$$D_0' = C_{D_{0_w}} q \frac{S}{S_{exp}} c(z) = k_D c(z) \tag{12.3}$$

Induced Drag

For the induced drag, the actual lift coefficient needs to be found. Then the simple quadratic relation between induced drag coefficient and lift coefficient, given by Equation 12.4, is used. The induced drag acting on one of the sharklets is then found using Equation 12.5

$$C_{D_i} = \left(\frac{L_{max}}{qS}\right)^2 \frac{1}{\pi \mathrm{AR} e} \tag{12.4} \qquad D_i = \frac{1}{2}C_{D_i} qS \tag{12.5}$$

Wing Weight

The weight of the wing is assumed to be a function of the chord, increasing proportionally with the chord length. Again, using the integral of the distributed weight, Equation 12.6 can be derived.

$$\frac{1}{2}W_w = \int_{w_f/s}^{b/2} k_w c(z)\mathrm{d}z = k_w \frac{S_{exp}}{2} \qquad W_w'(z) = k_w c(z)\ , \quad \text{where } k_w = \frac{W_w}{S_{exp}} \tag{12.6}$$

Engine and Tank Loads

The drag of the tank and the engine are derived using the zero-lift drag coefficients only, and are given by Equations 12.7 and 12.8. These coefficients were derived using the method proposed by Roskam [72], resulting in $C_{D_{0_{eng}}} = 0.0034$ and $C_{D_{0_{tk}}} = 0.00135$. The drag induced due to lift of these elements is negligible and therefore not included. The thrust of the engine is set as the maximum take off thrust to account for the highest load case.

$$D_{eng} = C_{D_{0_{eng}}} qS \tag{12.7}$$

$$D_{tk} = C_{D_{0_{tk}}} qS \tag{12.8}$$

12.1.4 Internal Loads

The internal loads are computed as a distribution along the span in order to compute the stress at every point of the wingbox. The convention used is that presented in Figure 12.6, where S is shear force, M a bending moment, T_z is torque and N_z is the normal force. Note that in the free body diagram from Figure 12.2 there are no forces acting in the z direction, hence N_z is neglected. The shear forces in y and x are given by Equation 12.9 and Equation 12.10 respectively. They make use of the Macauly step functions for the point loads and integrals of the chord for the distributed loads. The reaction forces R_x and R_y are found by setting the shear forces to zero at the tip of the wing. The integrals over the chord are solved analytically, but are not shown for conciseness.

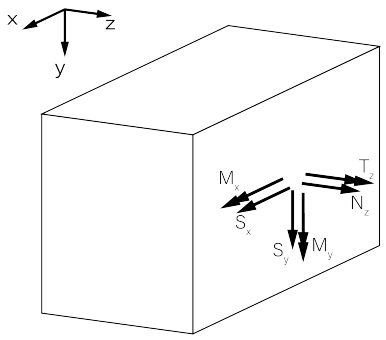

Figure 12.6: Internal load convention

$$S_y = -R_y \left[z - \frac{w_f}{2}\right]^0 - W_{eng}\left[z - z_{eng}\right]^0 - W_{tk}\left[z - z_{tk}\right]^0 - W_{shrk}\left[z - \frac{b}{2}\right]^0 + (k_L - k_w)\int_{\frac{w_f}{2}}^{z} c(z_a)\mathrm{d}z_a \tag{12.9}$$

$$S_x = -R_x \left[z - \frac{w_f}{2}\right]^0 + (D_{eng} - T_{max})[z - z_{eng}]^0 + D_{tk}[z - z_{tk}]^0 + D_i\left[z - \frac{b}{2}\right]^0 + k_D\int_{\frac{w_f}{2}}^{z} c(z_a)\mathrm{d}z_a \tag{12.10}$$

The internal moments around x and y are given by Equation 12.11 and Equation 12.12 respectively. In order to solve for the reaction moments in these equations, the internal moments are set to zero at the tip of the wing.

$$M_x = -M_{0,x}\left[z - \frac{w_f}{2}\right]^0 - R_y\left[z - \frac{w_f}{2}\right]^1 - W_{eng}[z - z_{eng}]^1 - W_{tk}[z - z_{tk}]^1 - W_{shrk}\left[z - \frac{b}{2}\right]^1 + (k_L - k_w)\int_{\frac{w_f}{2}}^{z}\int_{\frac{w_f}{2}}^{z_a} c(z_b)\mathrm{d}z_b\mathrm{d}z_a \tag{12.11}$$

$$M_y = -M_{0,y}\left[z - \frac{w_f}{2}\right]^0 - R_x\left[z - \frac{w_f}{2}\right]^1 + (D_{eng} - T_{max})\left[z - z_{eng}\right]^1 + D_{tk}[z - z_{tk}]^1 + D_i\left[z - \frac{b}{2}\right]^1 + k_D\int_{\frac{w_f}{2}}^{z}\int_{\frac{w_f}{2}}^{z_a} c(z_b)\mathrm{d}z_b\mathrm{d}z_a \tag{12.12}$$

Finally, the internal torque is computed using a combination of equations. The main expression is given by Equation 12.13, and the individual expressions for the torque arm (Δr) of each point load are given by Equations 12.14 to 12.18. The reaction torque $M_{0,z}$ is computed by setting the internal torque to zero at the tip.

$$\begin{aligned} T_z = &- M_{0,z}\left[z - \frac{w_f}{2}\right]^0 - R_y\Delta r_{R_y}\left[z - \frac{w_f}{2}\right]^0 - W_{eng}\Delta r_{W_{eng}}\left[z - z_{eng}\right]^0 - (D_{eng} - T_{max})\Delta r_{D_{eng}}\left[z - z_{eng}\right]^0 \\ &+ k_L\int_{\frac{w_f}{2}}^{z}\left(c(x_a)\left[\tan(\Lambda_{LE})(x - x_a) + x_c - 0.25c(x_a)\right]\right)\mathrm{d}z_a + k_w\int_{\frac{w_f}{2}}^{z}\left(c(x_a)\left[\tan(\Lambda_{LE})(x - x_a) + x_c - 0.5c(x_a)\right]\right)\mathrm{d}z_a \\ &+ D_{tk}\Delta r_{D_{tk}}\left[z - z_{tk}\right]^0 + W_{shrk}\Delta r_{shrk}\left[z - \frac{b}{2}\right]^0 + D_i\Delta h_{shrk}\left[z - \frac{b}{2}\right]^0 \end{aligned} \tag{12.13}$$

$$\Delta r_{R_y} = -x_{c,f} + \tan\Lambda_{LE}\left(z - \frac{w_f}{2}\right) + x_c \tag{12.14}$$

$$\Delta r_{W_{eng}} = 1.6 + \tan\Lambda_{LE}\left(z - z_{eng}\right) + x_c \tag{12.15}$$

$$\Delta r_{D_{eng}} = 1.5 + \tan\Gamma\,(z - z_{eng}) \tag{12.16}$$

$$\Delta r_{D_{tk}} = 1.6 - \tan\Gamma\,(z - z_{tk}) \tag{12.17}$$

$$\Delta r_{W_{tk}} = 6.8 - \tan\Lambda_{LE}\,(z) - x_c \tag{12.18}$$

12.1.5 Resulting Loading Diagrams

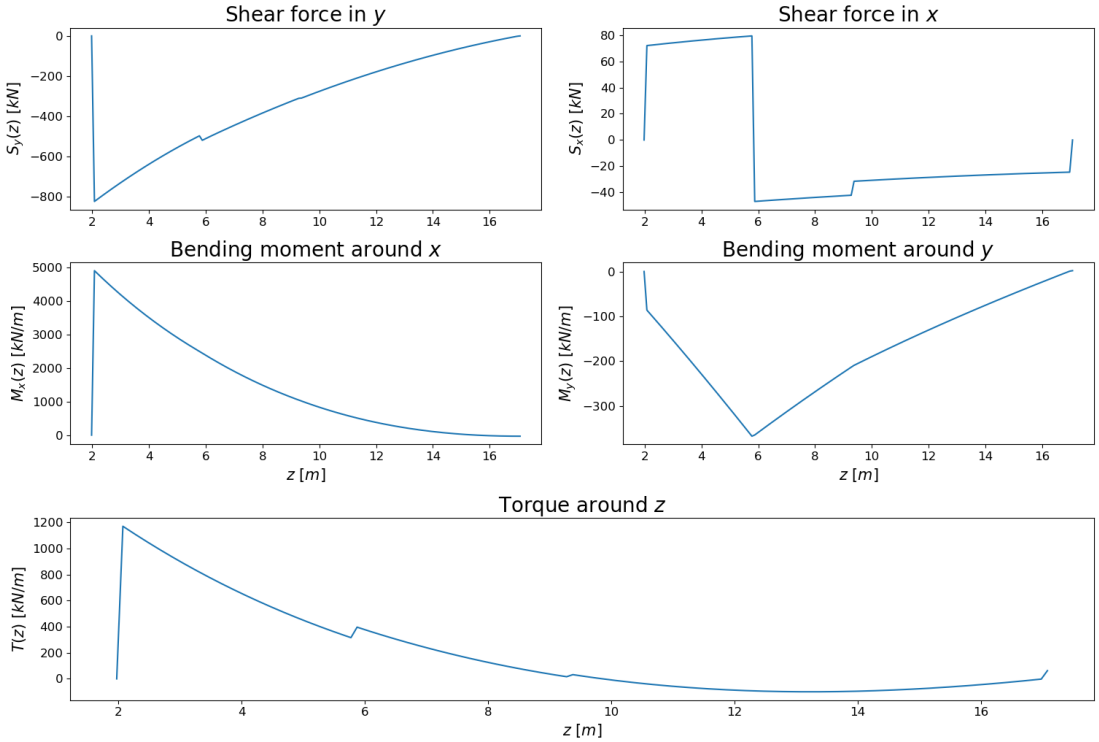

Figure 12.7: Internal loads along the half span of the wing

12.2 Stress Analysis

Based on the loads generated in Section 12.1, a script for computing the stresses experienced by the wing could be developed. Before being inputted in the stresses calculations, all the loads were multiplied by a factor of 1.5 as prescribed by CS 25.303 regulation.

12.2.1 Wing Box Configuration

The overall tendency in the aviation industry is switching to composites. Compared to metals, they offer considerable weight savings, corrosion resistance, fatigue resistance and more design tailoring freedom due to their anisotropic nature. The percentage of composites in Airbus aircraft has seen an exponential increase, reaching about 40% in their A350 model launched in 2010 [1]. It is safe to assume that this trend will continue and for EIS year of 2035, the A320-HACK shall incorporate more composite structures in order to remain competitive with future narrow body models. Thus, it was decided to investigate a carbon fiber composite wing box for the A320-HACK.

Composites offer a wide range of options and only the design of a composite material is a long process which is outside the scope of this project. Thus, only a simplified qualitative material selection was performed. One of the most promising manufacturing processes for large parts is automated tape laying (ATL) which offers a high level of precision and fast manufacturing times [2]. It was decided to go with an off-the-shelf tape option such as the ones offered by TORAY, leader in composites materials and processes. Both thermoset and thermoplastic based tapes are offered. Due to the better recyclability properties which align with the aim of the project, it was opted for thermoplastics. The Toray Cetexő TC1225 [3] was selected for this application. Its properties are displayed in Table 12.2.

[1] https://tinyurl.com/f2v2y6ak, accessed: 21-Jun-2021
[2] https://www.compositesworld.com/articles/fiber-placement-and-tape-laying, accessed:21-Jun-2021
[3] https://tinyurl.com/mzuh3bbd, accessed:21-Jun-2021

Table 12.2: Unidirectional tape material characteristics [3]

Tensile Strength [MPa]	Compression Strength [MPa]	Shear Strength[MPa]	Ply thickness [mm]	Weight per ply [g/m^2]
2410	1300	152	0.14	221

For the stress calculations in Section 12.2, it is assumed that only the fibers oriented at 0 °, along the direction of the span, will have to resists the stresses. This is a conservative assumption, as also the polymer and the fibers situated at different inclinations take up some of the loads. In composite design, three orientations adhering to the 10% rule should always be accounted for. Assuming the minimum 10% for the other two required directions, the 0 ° fibers will constitute 80% of the thickness of the panel.

The geometry of the wingbox is dependent on two basic features, the width of the skin and the height of the spars:

- The width of the wingbox skin changes along the span, as can be seen in Figure 12.1. Furthermore, it was discovered that the ratio between the width and the local chord length was also not constant, but followed a linear distribution.
- The height of the spar is dependent on the thickness to chord ratio of the wing profile. This ratio does change along the span of the wing according to Figure 12.8. By inspecting the wing profiles given by Orlita and Vos, the height of the spar was found to be approximately 83% of the maximum airfoil thickness. This can also be seen in Figure 12.9.

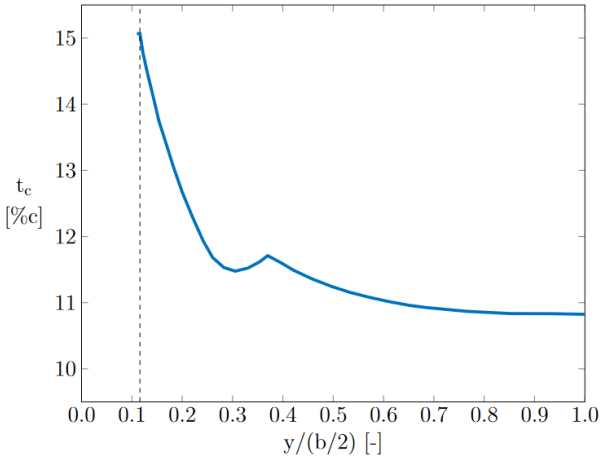

Figure 12.8: Thickness to chord ratio [73]

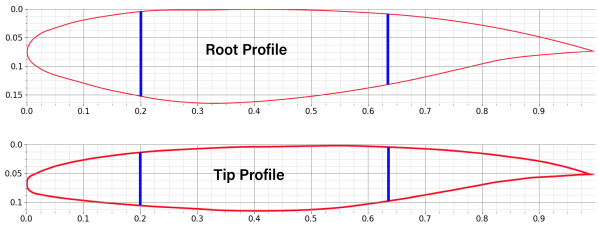

Figure 12.9: Approximate wing profiles at the root and tip of the wing

12.2.2 Shear Stress

The shear flows along the cross-section were calculated using the directions defined in Figure 12.10. It can be seen that in this case, shear flows are defined as positive when acting in a counterclockwise direction. The cross-sectional area of the wing was modelled as a thin-walled closed section, requiring Equation 12.19 for calculation. Due to the symmetrical cross-section $I_{xy} = 0$. It was decided to use the principle of superposition and to separate the problem in two subproblems with uni-axial shear loading. By having only one of the loads, a strategic cut to the structure can be made so that the redundant shear flow q_{s0} is directly equal to 0. The simplified equations are defined in Equation 12.20 and Equation 12.21.

$$q_s = q_b + q_{s0} = -\frac{V_y I_{yy} - V_x I_{xy}}{I_{xx} I_{yy} - I_{xy}^2} \int_0^s ty ds - \frac{V_x I_{xx} - V_y I_{xy}}{I_{xx} I_{yy} - I_{xy}^2} \int_0^s tx ds + q_{s0} \tag{12.19}$$

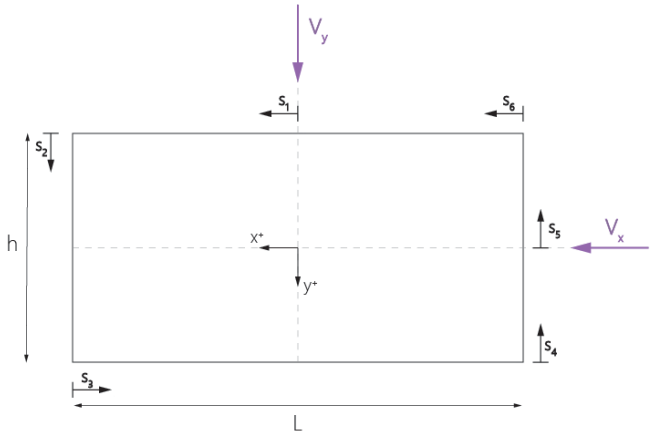

$$q_{sY} = -\frac{V_y}{I_{xx}} \int_0^s t y ds \quad (12.20)$$

$$q_{sX} = -\frac{V_x}{I_{yy}} \int_0^s t x ds \quad (12.21)$$

Figure 12.10: Shear flow coordinate system

The loads script discussed in Section 12.1 also outputs the torque created by the shear forces, which do not act through the shear centre of the section. The torque creates an additional shear flow through the cross section that needs to be considered using Equation 12.22, where A_m stands for the enclosed area of the cross-section.

$$q = \frac{T}{2 \cdot A_m} \quad (12.22)$$

By summing the three components of the shear flow: V_y, V_x and torque, the total shear flow along each region can be obtained. By further dividing with the thickness of each region, the shear stress τ along each region can be obtained.

12.2.3 Bending Stresses

The bending stresses are expected to be the most accentuated due to the large magnitude of the lift force that is experienced by the wing. The bending Equation 12.23 is used, where M_x and M_y are outputs of the wing load analysis script. For the calculation of the normal stress σ_z, the moments of inertia also include the stringers' contributions.

$$\sigma_z = \frac{(M_x I_{yy} - M_y I_{xy})\, y + (M_y I_{xx} - M_x I_{xy})\, x}{I_{xx} I_{yy} - I_{xy}^2} \quad (12.23)$$

12.2.4 Results

One of the outputs of the stresses program is the distribution of the maximum stress experienced by each cross-section location with respect to the spanwise location. By identifying the maximum stresses that the wing box experiences, it can be determined whether or not the wing will be able to support all the loading. Using the material properties described in Section 12.2.1, the thicknesses of the skin and the spars were adjusted until the maximum stresses were reduced below the allowable ones. It was noticed that the limiting case in the deign was the shear strength of the material, which required considerable increase of the thicknesses. The spar thickness was determined to have 14 mm, while the skin 11.25 mm. Thus, the maximum shear stress could be reduced to 140 MPa, below the allowable 152 MPa. It is important to note that, as described in Section 12.2.1, these thicknesses represent only 80% of the final thicknesses of the panels.

Subsequently, it was investigated whether this configuration can support the maximum compression stress or if further adjustments to the thicknesses or stringer parameters are necessary. It was decided to look at the compressive stress, not at the tensional stress since this would be the critical case for the bending stress due to the poorer performance of fibers in compression. The highest compressive stress was registered at 410.26 MPa, well below the prescribed 1300 MPa allowable strength. The final distribution of the shear strength with respect to the span location can be seen in Figure 12.11, while the compression stress variation can be seen in Figure 12.12.

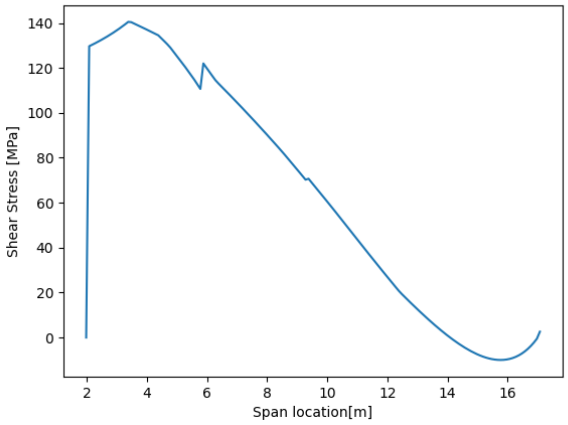

Figure 12.11: Highest shear stress at each span wise location

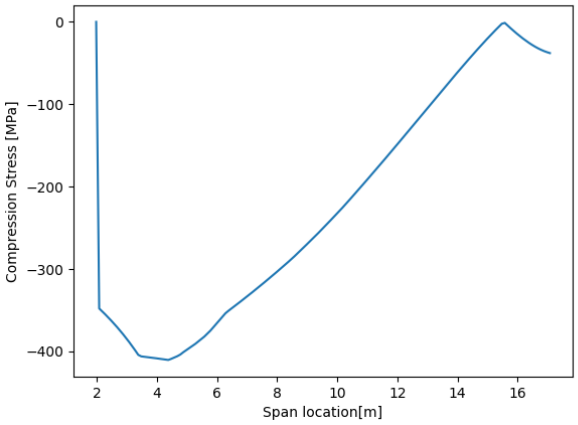

Figure 12.12: Highest compression stress at each span wise location

The other output of the stress analysis is the stress distribution along the cross-section. Figure 12.13 and Figure 12.14 show the shear stress and the bending stress distributions at z = 2.075 m. This span location was chosen aleatory as an example. The loads registered at this location are displayed in Table 12.3.

Table 12.3: Load values at z = 2.075 m

M_x $[kN]$	M_y $[kN]$	V_x $[kN]$	V_y $[kN]$	T$[KN \cdot m]$
7350.73	453.08	153.52	-1235.82	1736.91

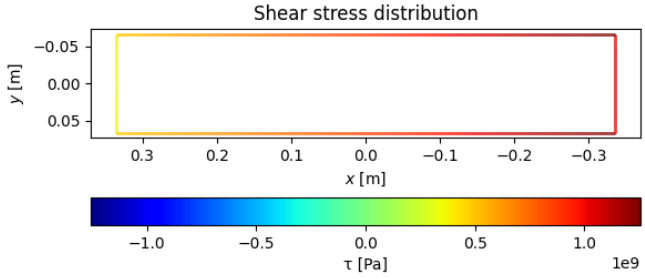

Figure 12.13: Shear stress distribution at z = 2.075 m

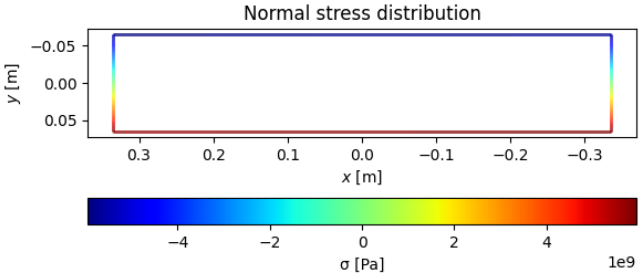

Figure 12.14: Normal stress distribution at z = 2.075 m

12.3 Limitations & Recommendations

Due to the time constraints of the project, the design of the wing box could not be performed in depth. Thus, a series of recommendations based on the current limitations have been drawn out.

Firstly, a more detailed analysis of the composites should be performed. The contribution of the fibers and the matrix should be taken into account, as without them the required thicknesses are overestimated. Additionally, the orientation of the fibers could be optimised for every region of the wing box and can vary along the span as the stresses decrease.

Secondly, the modelling of the wingbox could be done for the complex cross-sectional shape, a trapezoid with two curved sides, instead of a simplified rectangle. Moreover, other elements such as ribs, which would take up some loads, could be considered. Phenomena such as buckling, especially for the upper skin panel, could be considered.

13 | Wing Positioning & Empennage Design

The aim of the analysis proposed in this chapter is to assess if the A320-HACK - considering its changes compared to the A320neo - requires modifications in order to fulfill the stability and controllability criteria. Firstly, the OEW of the aircraft is estimated in Section 13.2, then its centre of gravity (c.g.) range is derived from the loading diagrams in Section 13.3. In Section 13.4, the scissor plot is then constructed and it is assessed if modifications to the horizontal tail or the wing position are necessary, given the new c.g. range. Finally, the landing gear location is analysed and eventual changes are proposed.

13.1 Requirements

The analysis presented in this chapter was performed in order to investigate and verify the following requirements and user recommendations.

UR-PERF-02 The design shall satisfy the CS25 rules.

UG-PERF-03 The flight mechanics characteristics of the aircraft shall be evaluated

UG-SR-01T The issue of ground clearance and tail strike shall be considered

13.2 Operating Empty Weight Estimation

The operating empty weight (OEW) of the A320-HACK was estimated starting from the value of the A320neo and attending to the design choices elaborated in Chapter 11 until Chapter 12.

The mass of the new components (i.e. the LH_2 tanks and the DPU) were added, while the contribution of the APU was removed - given that this item will be replaced by the fuel cell module - then, the mass difference of the new wingbox and the new engines were included. The c.g. at OEW for the A320-HACK was obtained in an analogous way. From the mass of each component and their respective c.g. location, while making use of Equation 13.1, the c.g. of the OEW was obtained. An overview of these modifications, with their respective net mass changes and c.g. locations, is shown in Table 13.1.

Table 13.1: A320-HACK changes compared to the A320neo: added and removed items, together with their respective net mass difference and c.g location

Item	**Mass** [kg] (increase + / decrease -)	**c.g. location** [m] (from the nose)
LH_2 tanks (including pylons and feeding system)	+911	18.7
DPU	+781	32.5
APU	-145	34.6
New engines	+1076	13.6
New wingbox	-915	16.7

The OEW of the A320-HACK results to be 46256 kg (roughly 1696 kg more than the A320neo), with a c.g. location at 34% of the MAC (equivalent to 16.6 m from the aircraft's nose).

13.3 Loading Diagrams and C.G. Range

Based on the aforementioned estimation for the c.g. location at OEW, the contribution of cargo, passengers and fuel (both hydrogen and kerosene) were calculated, and so the loading diagrams for the A320-HACK were obtained, in order to identify the aircraft's c.g. range. This was achieved through the use of Equation 13.1 in an iterative way, where M_i is the mass of a certain movable component and $x_{cg,i}$ is its corresponding centre of gravity location with respect to the aircraft nose.

$$x_{cg} = \frac{\sum_i (x_{cg,i} \cdot M_i)}{\sum M_i} \tag{13.1}$$

All the required dimensions and distances were retrieved and eventually measured from the technical drawings of the A320neo [74], especially from the aircraft side view and the cabin top view Figure 13.1. Furthermore, the centre of gravity locations in terms of MAC can be expressed with respect to the aircraft's nose using Equation 13.2.

$$x[m] = x_{LEMAC} + MAC \cdot x[\%MAC] \tag{13.2}$$

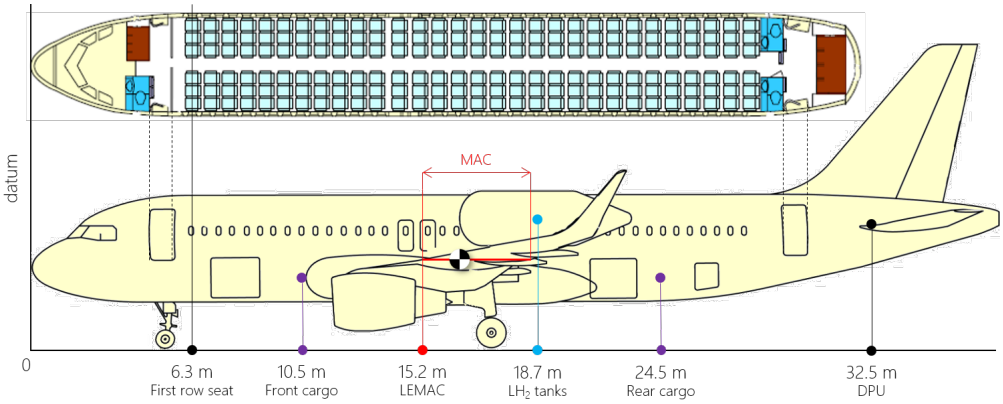

Figure 13.1: Side and cabin top view of the A320-HACK (adapted from [74])

In order to obtain the loading diagrams, the contributions of the movable items were added in the following order: cargo, passengers and lastly fuel. The characteristics (mass and c.g. location) of cargo and fuel are summarised in Table 13.2.

Table 13.2: Movable items mass and centre of gravity location for the A320-HACK

Item	(max) Mass [kg]	c.g. location [m] (from the nose)
Front cargo	3402	10.5
Rear & Bulk cargo	6033	24.5
Kerosene	12884	16.1
Hydrogen	2690	18.7

Note that the c.g. for cargo was assumed to correspond to the cargo compartment number one, while the c.g. for both kerosene and hydrogen were assumed to coincide with their respective tank's c.g. Furthermore, for kerosene, the centre of gravity location was estimated assuming a trapezoidal tank, located between the front spar (25% MAC from the leading edge) and the rear spar (80% MAC from the leading edge) and extending in span-wise direction from the tip to the root of the wing.

For passengers, it was considered a single class configuration, with 180 seats distributed in 30 rows. The mass of each passenger was estimated to be 71 kg (M_{pas}), and the so-called "window-aisle rule" was followed: thus, first the two window seats for each row (one by one) were added, then the two middle seats and lastly the two aisle ones. Moreover, the c.g. location of each row (x_n) was estimated by adding to the distance between the aircraft's nose and the first row ($x_{FirstRow} = 6.3m$) the seat pitch ($\Delta x_{seat} = 0.71m$), as shown in Equation 13.3.

$$x_n = x_{\text{FirstRow}} + n \cdot \Delta x_{\text{seat}} \tag{13.3}$$

Then, at each iteration, the new mass of the aircraft and the new c.g. location were obtained using Equation 13.4 and 13.5.

$$M_n = M_{n-1} + 2n \cdot M_{pas} \qquad (13.4) \qquad x_{cg,n} = \frac{M_{n-1} \cdot x_{cg,n-1} + 2M_{pas} \cdot x_n}{M_n} \qquad (13.5)$$

Note that, by definition of the loading diagram, the passengers - as well as the cargo - were loaded starting both from the front and from the back of the aircraft, in order to identify the most critical conditions in terms of c.g. excursion.

Following the above mentioned procedure, the loading diagrams of the A320-HACK were obtained. Figure 13.2a depicts a common operational condition, while Figure 13.2b shows an unusual loading case (maximum cargo capacity) that however allows to identify the most forward and after position of the aircraft centre of gravity, so the critical c.g. range. The loading conditions of the two diagrams are summarised in Table 13.3.

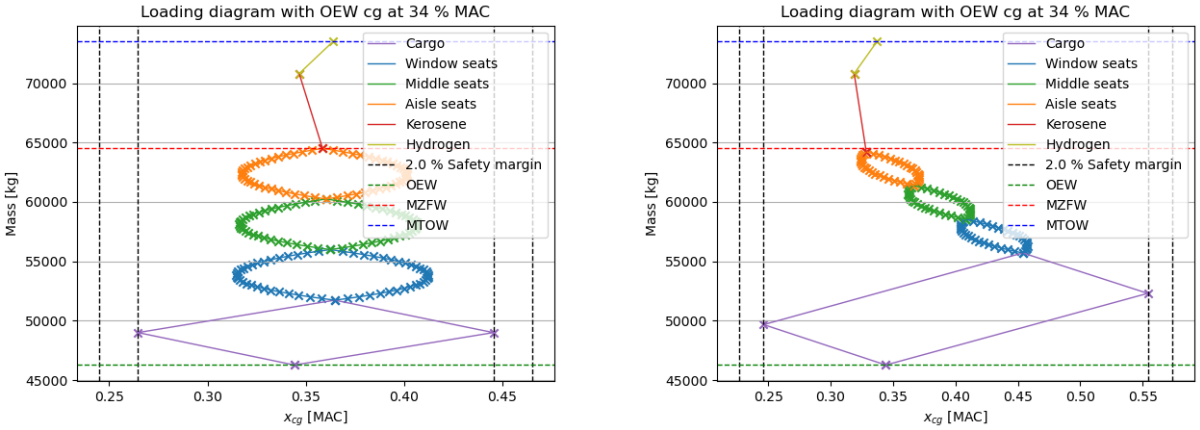

(a) Common loading condition

(b) Critical loading condition

Figure 13.2: Loading diagrams for the A320-HACK

Table 13.3: Conditions for the loading diagrams shown in Figure 13.2a and 13.2b

Diagram	**Front cargo** $[kg]$	**Back cargo** $[kg]$	**Kerosene** $[kg]$	**Hydrogen** $[kg]$	**Passengers**	**c.g. range** $[\%MAC]$ (including a 2% safety margin)
Figure 13.2a	2730	2730	6302	2690	180	24.5-46.6
Figure 13.2b	3402	6033	6587	2690	120	22.6-57.4

Therefore, the most forward c.g. position of the A320-HACK corresponds to 22.6% of the MAC, while the most after at 57.4% (including a 2% safety margin).

13.4 Scissor Plot

The scissor plot (or X plot) was constructed in order to compare the calculated c.g. range for the A320-HACK with the maximum allowable one, as defined by the stability and controllability criteria. The procedures presented in this section are described in deeper detail in the course *Systems Engineering & Aerospace Design* [75]; therefore, in case of further interest, the reader is advised to consult the aforementioned source.

13.4.1 Stability

Firstly, the stability curve is defined by Equation 13.6, where $\bar{x}_{cg}$ is the centre of gravity location, $\bar{x}_{ac}$ the aerodynamic centre location normalised over the mean aerodynamic chord, $C_{L\alpha_h}$ the tail's lift gradient, $C_{L\alpha_{A-h}}$ the aircraft's lift gradient excluding the tail, $d\varepsilon/d\alpha$ the wing's downwash gradient effect on the tail, $S_h l_h / S\bar{c}$ the horizontal tail's volume coefficient and $(V_h/V)^2$ the tail/wing speed ratio, while 0.05 is

simply a static margin.

$$\bar{x}_{cg} = \bar{x}_{ac} + \frac{C_{L\alpha_h}}{C_{L\alpha_{A-h}}}\left(1 - \frac{d\varepsilon}{d\alpha}\right)\frac{S_h l_h}{S\bar{c}}\left(\frac{V_h}{V}\right)^2 - 0.05 \tag{13.6}$$

In order to generate the stability curve, Equation 13.6 can be re-arranged in the form of a linear function, as expressed by Equation 13.7, where S_h/S is the horizontal tail over wing surface ratio, l_h the tail arm and $\bar{c}$ simply the mean aerodynamic chord.

$$\frac{S_h}{S} = \frac{1}{\frac{C_{L\alpha_h}}{C_{L\alpha_{A-h}}}\left(1 - \frac{d\varepsilon}{d\alpha}\right)\frac{l_h}{\bar{c}}\left(\frac{V_h}{V}\right)^2}\bar{x}_{cg} - \frac{\bar{x}_{ac} - 0.05}{\frac{C_{L\alpha_h}}{C_{L\alpha_{A-h}}}\left(1 - \frac{d\varepsilon}{d\alpha}\right)\frac{l_h}{\bar{c}}\left(\frac{V_h}{V}\right)^2} \tag{13.7}$$

All the numerical values for the parameters in Equation 13.7 are presented in Table 13.4, while the procedures adopted to calculate them are briefly outlined thereafter.

Table 13.4: Numerical values for the parameters appearing in Equation 13.7

Parameter	Value	Parameter	Value	Parameter	Value	Parameter	Value
$C_{L\alpha_h}$ [-]	4.749	$\frac{d\varepsilon}{d\alpha}$ [-]	0.4	$\bar{c}$ [m]	4.312	$\bar{x}_{ac}$ [-]	0.172
$C_{L\alpha_{A-h}}$ [-]	6.336	l_h [m]	17.674	$(\frac{V_h}{V})^2$ [-]	0.85		

The tail's lift gradient was calculated using Equation 13.8, the aircraft's lift gradient excluding the tail was obtained using Equation 13.9 and 13.10 (and 13.11). In these equations, $C_{L\alpha_w}$ is the lift slope of the wing, b_f the fuselage width, b the wingspan, S_{net} the net wing surface area, A the wing's aspect ratio, A_h the horizontal tail's aspect ratio and η the airfoil efficiency coefficient (assumed to be constant and equal to 0.95).

$$C_{L\alpha_h} = \frac{2\pi A_h}{2 + \sqrt{4 + \left(\frac{A_h\beta}{\eta}\right)^2\left(1 + \frac{\tan^2\Lambda_{0.5C_h}}{\beta^2}\right)}} \tag{13.8}$$

$$C_{L\alpha_{A-h}} = C_{L\alpha_w}\left(1 + 2.15\frac{b_f}{b}\right)\frac{S_{net}}{S} + \frac{\pi}{2}\frac{b_f^2}{S} \tag{13.9}$$

$$C_{L\alpha_w} = \frac{2\pi A}{2 + \sqrt{4 + \left(\frac{A\beta}{\eta}\right)^2\left(1 + \frac{\tan^2\Lambda_{0.5C_w}}{\beta^2}\right)}} \tag{13.10}$$

$$\beta = \sqrt{1 - M_{cruise}^2} \tag{13.11}$$

Furthermore, the downwash gradient was computed using a semi-empirical formula (Equation 13.12), where K_{ϵ_Λ} and $K_{\epsilon_{\Lambda=0}}$ are found using Equation 13.13 and 13.14 (in which r and m_{tv} are geometrical parameters, defined in Figure 13.3).

$$\frac{d\epsilon}{d\alpha} = \frac{K_{\epsilon_\Lambda}}{K_{\epsilon_{\Lambda=0}}}\left(\frac{r}{r^2 + m_{tv}^2}\frac{0.4876}{\sqrt{r^2 + 0.6319 + m_{tv}^2}} + \left[1 + \left(\frac{r^2}{r^2 + 0.7915 + 5.0734m_{tv}^2}\right)^{0.3113}\right]\left\{1 - \sqrt{\frac{m_{tv}^2}{1 + m_{tv}^2}}\right\}\right)\frac{C_{L\alpha_w}}{\pi A} \tag{13.12}$$

$$K_{\epsilon_\Lambda} = \frac{0.1124 + 0.1265\Lambda_{1/4} + 0.1766\Lambda_{1/4}^2}{r^2} + \frac{0.1024}{r} + 2 \tag{13.13}$$

$$K_{\epsilon_{\Lambda=0}} = \frac{0.1124}{r^2} + \frac{0.1024}{r} + 2 \tag{13.14}$$

The parameter $(V_h/V)^2$ is equal to 0.85 for the A320 tail configuration, while the aerodynamic centre of the aircraft x_{ac} was obtained utilizing a semi-empirical method, shown in Equation 13.15.

$$\left(\frac{\bar{x}_{ac}}{\bar{c}}\right)_{w+f} = \left(\frac{\bar{x}_{ac}}{\bar{c}}\right)_w + -\frac{1.8}{C_{L\alpha A-h}}\frac{b_f h_f l_{fn}}{S\bar{c}} + \frac{0.273}{1+\lambda}\frac{b_f c_g (b - b_f)}{\bar{c}^2 (b + 2.15b_f)}\tan\Lambda_{1/4} \tag{13.15}$$

Equation 13.15 includes the contribution of the wing, the contribution of the fuselage, as well as the contribution from the podded engines. In this expression, b_f and h_f are respectively the fuselage width and height, l_{fn} the distance from the aircraft's nose to the wing's intersection with the fuselage, c_g is

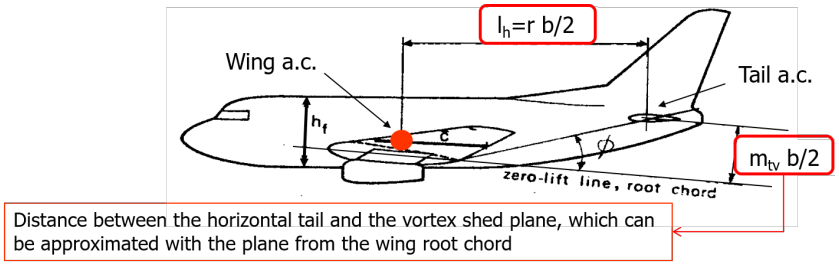

Figure 13.3: Geometrical parameters r and m_{tv}, used to estimate the downwash gradient [75]

the geometric chord (defined as S/b), λ the taper ration, b the wingspan and $\Lambda_{c/4}$ the wing sweep angle at quarter chord. Furthermore, there is an additional contribution given by the engine nacelles defined by Equation 13.16, where k_n is a constant determined by the engines' location and b_n the diameter of the engines' nacelles.

$$\Delta_n \frac{x_{ac}}{\bar{c}} = \sum k_n \frac{b_n^2 l_n}{S\bar{c}\left(C_{L_{\alpha_{A-H}}}\right)} \tag{13.16}$$

Note that the method and equations adopted here do not allow to take into account the effect on stability of the wing mounted hydrogen tanks. Considering that nacelles mounted after the quarter chord have a stabilising effect, it is qualitatively expected that the tanks will have such an influence. However, it is not possible to quantify their contribution at this stage of the design, and therefore further analysis - and more sophisticated methodologies - are required, and thus recommended for later phases of the project. In any case, the stability line was obtained following the above outlined procedure, and can be visualised in Section 13.4.3.

13.4.2 Controllability

Secondly, the controllability curve is defined by Equation 13.17, which is the non-dimensional moment equilibrium equation around the centre of gravity for trim condition. This equation can be re-arranged in the form of a linear function, which is shown in Equation 13.18.

$$C_m = C_{m_{ac}} + C_{L_{A-h}}\left(\frac{x_{cg} - x_{ac}}{\bar{c}}\right) - \frac{C_{L_h} S_h l_h}{S\bar{c}}\left(\frac{V_h}{V}\right)^2 = 0 \tag{13.17}$$

$$\frac{S_h}{S} = \frac{1}{\frac{C_{L_h}}{C_{L_{A-h}}}\frac{l_h}{\bar{c}}\left(\frac{V_h}{V}\right)^2}\bar{x}_{cg} + \frac{\frac{C_{m_{ac}}}{C_{L_{A-h}}} - \bar{x}_{ac}}{\frac{C_{L_h}}{C_{L_{A-h}}}\frac{l_h}{\bar{c}}\left(\frac{V_h}{V}\right)^2} \tag{13.18}$$

All the numerical values for the parameters in Equation 13.18 are presented in Table 13.5, while the procedures adopted to calculate them are briefly outlined thereafter.

Table 13.5: Numerical values for the parameters appearing in Equation 13.18

Parameter	Value	Parameter	Value	Parameter	Value	Parameter	Value
$C_{L\alpha_h}$ [-]	4.749	l_h [m]	17.674	$(\frac{V_h}{V})^2$ [-]	0.85	$\bar{x}_{ac}$ [-]	0.131
$C_{L\alpha_{A-h}}$ [-]	6.336	$\bar{c}$ [m]	4.312	$C_{m_{ac}}$ [-]	-0.703		

In these equations, C_{L_h} is the horizontal tail's lift coefficient, $C_{L_{A-h}}$ is the lift coefficient of the aircraft excluding the tail and $C_{m_{ac}}$ is the moment coefficient around the aircraft's aerodynamic centre. For the A320, C_{L_h} is equal to -0.8, given that the stabilizer is adjustable. Next, $C_{L_{A-h}}$ is equal to the maximum

lift coefficient required during flight, which corresponds to the C_L during landing. Lastly, $C_{m_{ac}}$ is defined by Equation 13.19, which comprises different contributions that are defined in Equation 13.20, 13.21 and 13.22.

$$C_{m_{ac}} = C_{m_{ac_w}} + \Delta_f C_{m_{ac}} + \Delta_{fus} C_{m_{ac}} + \Delta_{nac} C_{m_{ac}} \tag{13.19}$$

$$C_{m_{ac_w}} \approx C_{m_{0_{airfoil}}} \cdot \frac{A\cos^2(\Lambda)}{A + A\cos(\Lambda)} \tag{13.20}$$

$$\Delta_{fus} C_{m_{ac}} = -1.8 \cdot \left(1 - \frac{2.5 b_f}{l_f}\right) \cdot \frac{\pi b_f l_f h_f}{4 S \bar{c}} \cdot \frac{C_{L_0}}{C_{L_{\alpha_{A-h}}}} \tag{13.21}$$

$$\Delta_f C_{m_{ac}} = \mu_2 \left\{ -\mu_1 \cdot \Delta C_{l_{\max}} \cdot \frac{c'}{c} - \left[C_L + \Delta C_{l_{\max}} \left(1 - \frac{S_{wf}}{S}\right)\right] \cdot \frac{1}{8} \cdot \frac{c'}{c} \cdot \left(\frac{c'}{c} - 1\right) \right\} + 0.7 \cdot \frac{A}{1 + \frac{2}{A}} \cdot \mu_3 \cdot \Delta C_{l_{\max}} \cdot \tan\left(\Lambda_{1/4}\right) \tag{13.22}$$

In Equation 13.20, all the parameters are known from the aircraft's geometry, except the $C_{m_{0_{airfoil}}}$ which was assumed to be -0.15 based on reasonable estimations for supercritical airfoils. In Equation 13.21, all the parameters are known from the aircraft's geometry and the previous discussion for stability, except for C_{L_0} (the lift coefficient of the flapped wing at zero angle of attack), which was estimated through the analysis of the aircraft at landing condition. In Equation 13.22, $\Delta C_{l_{\max}}$ is the increase in lift generated by the flaps, c' is the wing's chord with fully extended flaps while c is the wing's chord with retracted flaps, the parameters μ_1, μ_2 and μ_3 - which are a function of the flap type and geometry - were estimated from charts from Torenbeek [76], shown in Figure 13.4a, 13.4b and 13.4c.

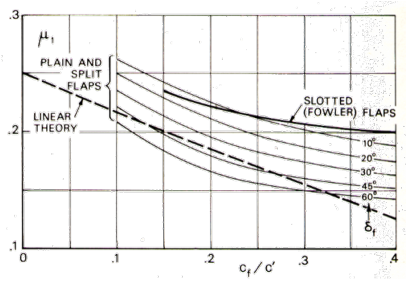

(a) μ_1 as function of flap chord over flapped wing chord

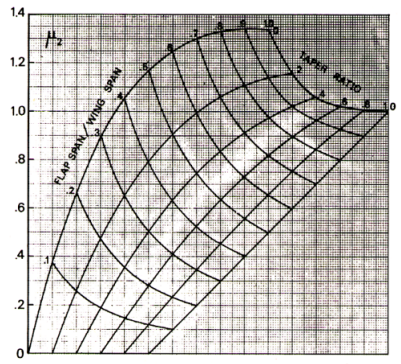

(b) μ_2 as function of flap span/wing span and taper ratio

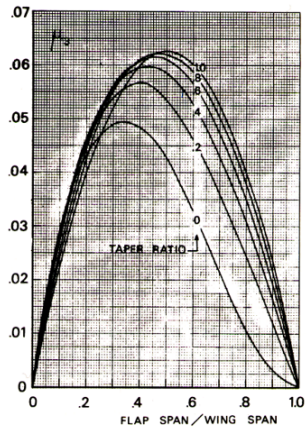

(c) μ_3 as function of flap span/wing span and taper ratio

Figure 13.4: Graphs for estimating μ_1, μ_2 and μ_3 in Equation 13.22 [76]

The controllability line was obtained following the above outlined procedure, and can be visualised in Section 13.4.3.

13.4.3 Plots, Modifications & Iteration

The stability and controllability curves obtained with the procedures explained in the previous sections are plotted in Figure 13.5a. Note that also the neutral stability line is plotted, which is obtained by simply removing the static margin (0.05) from Equation 13.6 (or 13.7); in fact, the neutral stability line is defined for stick fixed conditions, applying the 0.05 factor allows to account for other constraints [75].

In order for the aircraft to be stable, the entire c.g. range needs to lie to the left of the stability curve. On the other hand, in order to be controllable, the entire c.g. range needs to be to the right of the controllability curve. Thus, the design region lies in between the two curves.

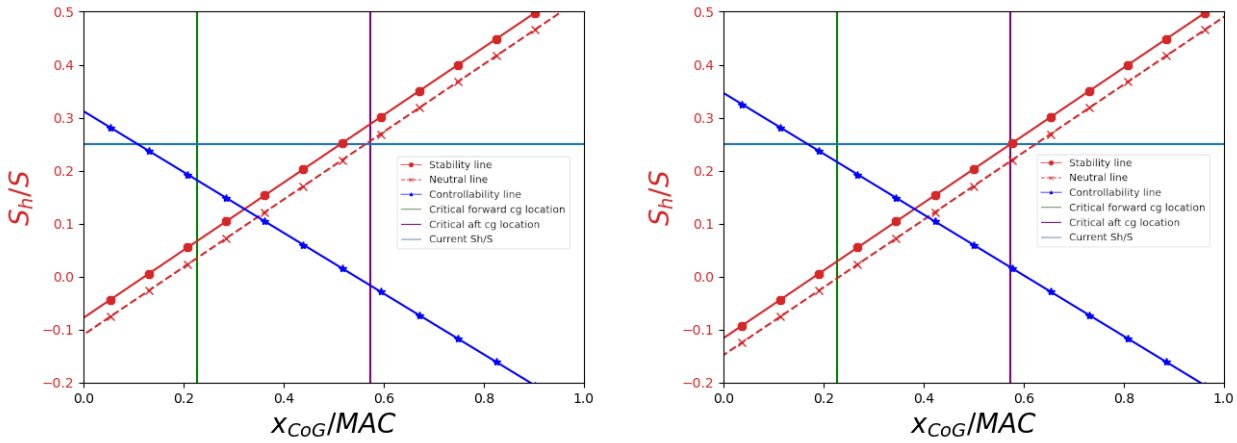

(a) No modifications

(b) 6% MAC wing shift (backward)

Figure 13.5: X plots for the A320-HACK, including c.g. range and the A320neo's Sh/s (equal to 0.25)

As can be seen in Figure 13.5a, the c.g. range of the A320-HACK (defined by the green and purple lines) does not fulfill the stability requirement (since it extends to the right of the curve), assuming to retain the same horizontal tail of the A320neo (so the same S_h/S of 0.25). Therefore, the aircraft design needs to be iterated in order to meet this requirement. Now, at this stage, three main viable solutions are considered: the first one being shifting the wing position, the second one modifying the horizontal tail size, and the third one combines the previous two in order to achieve the optimal design point. In Figure 13.5b, the second option is shown, so the wing was shifted by 6% of the MAC backward (equivalent to roughly 26 cm). The c.g. range was re-evaluated, although it turned out to remain almost unvaried, given the rather small wing shift. This option is particularly appealing since it allows to retain the same horizontal tail of the A320neo, therefore avoiding the necessity of designing new components and thus incurring in additional development costs. However, considering again Figure 13.5b, the optimal solution would be to further shift the wing backward and to reduce the horizontal tail's size. In any case, as it will be further explained in Section 13.6, further and more sophisticated analyses are required in this regard, in order to define the best design option.

Landing Gear

In order to determine the location of the main landing gear, pitch angle limit and the tip back angle and the landing gear's stowaway space in the wing needed to be evaluated. It was assumed that the A320neo's pitch angle, i.e. maximum nose up attitude of the aircraft, was constrained by a 15° limit due to the fact that its tip back was found to be only 13°, based on estimates from the aircraft's schematics. The critical aft cg location of the A320-HACK was found to be at 58.8% of MAC. This is a rearward propagation of 16.8% relative to the critical aft cg location of A320neo at 42% of MAC. This would compromise the pitch angle limit (β), as seen in Figure 13.6, of the aircraft since it would fail to meet the Pitch angle (β) > Max[Tip back angle] (θ), 15°] criteria. Therefore, in order to meet this requirement and to prevent the aircraft from tipping over during landing/take-off, the position of the landing gear is also moved further aft by 6% of MAC, i.e. 26 cm. Since, the wing is also moved by the same amount, this would minimise the redesign of the landing gear stowaway space or the kink in the aircraft's wing.

13.5 Verification & Validation

The above presented methodologies to construct the loading diagrams and the scissor plots were implemented in Python, and the resulting codes were then verified and - to a certain extent - validated. The verification was mainly performed to rule out possible errors in the codes, and thus ensure the models' correctness. This phase was mainly carried out through manual procedures, by dividing the codes in units - mostly coinciding with single functions - and checking the calculations by hand. Plus, a simple sensitivity analysis was also performed, in order to evaluate if the models behaved as expected as a consequence of parameters alterations, whose specific consequences were known.

The validation was carried out in order to evaluate the suitability of the developed models for the

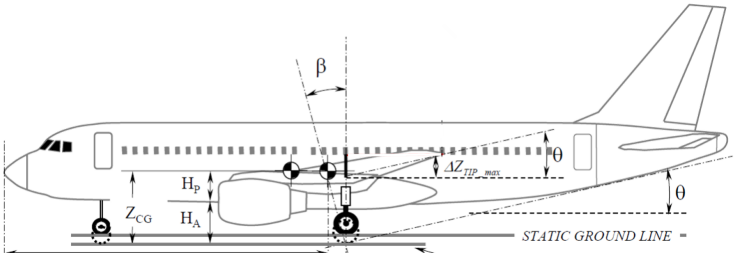

Figure 13.6: Depiction of aircraft's pitch β and tipback angle θ [75]

intended purposes, and their capability to represent reality in a sufficiently accurate way. In order to achieve this, the codes were run with different input parameters, for which the outcomes were known from the aforementioned course [75]; then, the obtained values were compared with the reference ones and discrepancies were not detected.

Overall, while the codes were verified and validated, it is important to recognize that they provide a rather approximate representation of reality, which is however deemed sufficient considering the rather conceptual nature of this project.

13.6 Limitations & Recommendations

The main limitation of this analysis - as already mentioned in Section 13.4 - lies in the fact that the contribution of the wing-mounted tanks was not considered while constructing the scissor plot, given that the adopted methodology does not give the possibility to take into account such an unusual feature. While it can be qualitatively said the wing-mounted tanks should positively contribute to stability, no such considerations can be made for controllability and - in any case - more sophisticated and quantitative analyses are required. Furthermore, while it has been verified that the tail does not end up in the wake of the tanks at high angle of attacks in straight flight, further analyses need to be performed in order to verify that the same holds true for sideslipping flight or for more articulated and/or unusual manoeuvres and flight conditions. Indeed, there is a possibility that the entire tail configuration needs to be reviewed and potentially modified, eventually ending up with a crucifix or a T-tail configuration. Moreover, also the vertical tail design needs to be revised and eventually amended. Overall, what has been presented in this chapter is a preliminary and not comprehensive analysis, suited for the scope of this DSE and the allocated time frame. However, progressing further in the project will require to carefully investigate the wing-mounted tanks' impact on stability and controllability characteristics, and eventually to make design modifications accordingly. Lastly, also the implications in terms of lateral stability need to be addressed and investigated. These recommendations can be summarised in the following three main points:

- Consider tank contribution on stability and controllability with more sophisticated methodologies
- Consider lateral stability characteristics
- Re-evaluate the entire tail configuration

Part IV

A320-HACK Analysis

14 | Aerodynamics

The aerodynamic characteristics of the A320-HACK are assessed because it is important to understand the impact of the hydrogen tanks on the flow of air over the aircraft. First, some basic geometrical characteristics involved in the flow of air over the wing are computed in Section 14.1. Then the overall increase in drag coefficient due to the incorporation of the tanks is computed in Section 14.2. Then, Section 14.3 touches upon the limitations from this analysis and the recommended approach for future design stages.

14.1 Geometrical Characteristics

The top view of the A320-HACK was analysed to obtain the mean aerodynamic chord (MAC) and aspect ratio (AR) of the wing. For this purpose, consider Figure 14.1, due to the fact that the wing is composed out of two trapezoids, the MAC is computed by interpolating between the inner section and outer section MACs [1]. Furthermore, the aspect ratio of the wing was computed using Equation 14.1, which takes into account the presence of sharklets on the tips of the wing [2].

$$AR = \frac{b^2}{S}(1 + 1.9\frac{h_{sharklet}}{b}) \tag{14.1}$$

The resulting geometrical properties of the aircraft are reported in Table 14.1. Some values in the table were obtained from the *Jane's All the World's Aircraft: Development & Production* database[3].

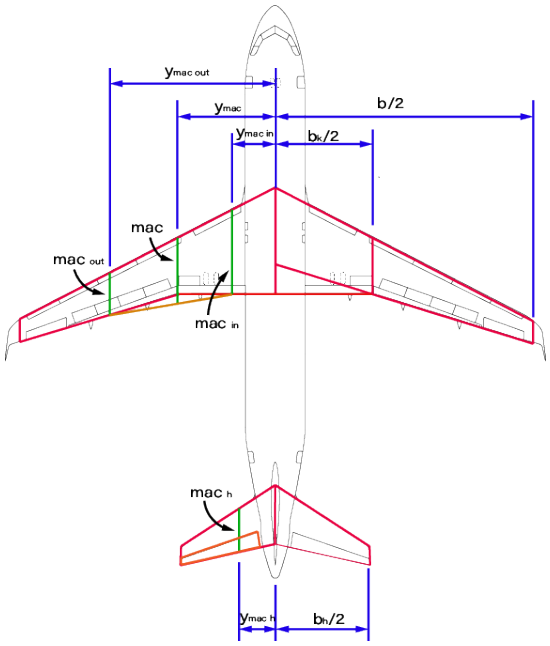

Figure 14.1: Top view o the A320-HACK showing the mean aerodynamic chord of the wing and horizontal tail.

Table 14.1: Geometrical characteristics of the A320-HACK relevant to aerodynamics

Variable	Value	Unit
S	122.4	m^2
S_h	31	m^2
S_v	21.5	m^2
MAC	4.3	m
y_{MAC}	6.47	m
$XLEMAC$	15.21	m
MAC_h	2.73	m
y_{MAC_h}	2.52	m
$XLEMAC_h$	36.2	m
AR	10.73	-
Λ_{LE}	27	deg
Γ	6	deg

14.2 Drag Penalty

The drag penalty is assumed to be an increase in zero-lift drag coefficient. The two added tanks on top of the wing do not have a significant lift-induced component. Using the method from [72] it was found that $C_{D_{i_{tank}}}$ is two orders of magnitude smaller than $C_{D_{0-tank}}$. Therefore, the zero-lift drag coefficient of

[1] AE2111-II, Aerospace Design and Systems Engineering Elements II, Aircraft aerodynamic analysis - fundamentals, F. Oliviero

[2] AE2111-II, Aerospace Design and Systems Engineering Elements II, Aircraft aerodynamic analysis Lift & Drag, F. Oliviero

[3] https://customer.janes.com, accessed:17-May-2020

the tanks is simply added to that of the original A320neo. Using the method from Roskam [72], $C_{D_{0_{tank}}}$ is computed with Equation 14.2. In this expression, the wetted area is obtained through Equation 14.3[2].

$$C_{D_{0_{tank}}} = 2 \times 1.3 C_{f_{tank}} \left[1 + \frac{60}{(l_t/d_t)^3} + 0.0025 \cdot (l_t/d_t)\right] \cdot \frac{S_{wet_{tank}}}{S} \tag{14.2}$$

$$S_{wet_{tank}} = \frac{\pi d_t}{4}\left\{\frac{1}{3L_{nose}^2}\left[\left(4L_{nose}^2 + \frac{d_t^2}{4}\right)^{1.5} - \frac{d_t^3}{8}\right] - d_t + 4L_{body} + 2\sqrt{L_{tail\ cone}^2 + \frac{d_t^2}{4}}\right\} \tag{14.3}$$

Sun, Hoekstra, and Ellerbroek estimated the components of the drag polar for the A320 aircraft, which are assumed to be the same as for the A320neo [77]. These values are used to compute the drag coefficients for the A320-HACK by adding the contribution of the tanks. The results from this paper are reported in Table 14.2 together with the newly computed values of the A320-HACK

Table 14.2: Zero-lift drag coefficients of the A320neo and A320-HACK [77]

	$C_{D_{0_{tanks}}}$	$C_{D_{0_{clean}}}$	$C_{D_{0_{TO}}}$	$C_{D_{0_{app}}}$	$C_{D_{0_{land}}}$	$C_{D_{0_{taxi}}}$	e
A320neo	-	0.023	0.078	0.053	0.120	0.055	0.992
A320-HACK	0.0027	0.0257	0.0807	0.0557	0.1227	0.0577	0.992

Using the values of Table 14.2, it is possible to create a drag polar and a plot for L/D as a function of lift coefficient. The simplified drag polar is given by Equation 14.4. The lift over drag ratio is computed by simply taking the ratio between the lift and drag coefficients. These two are shown in Figure 14.2.

$$C_D = C_{D_0} + \frac{C_L^2}{\pi A R e} \tag{14.4}$$

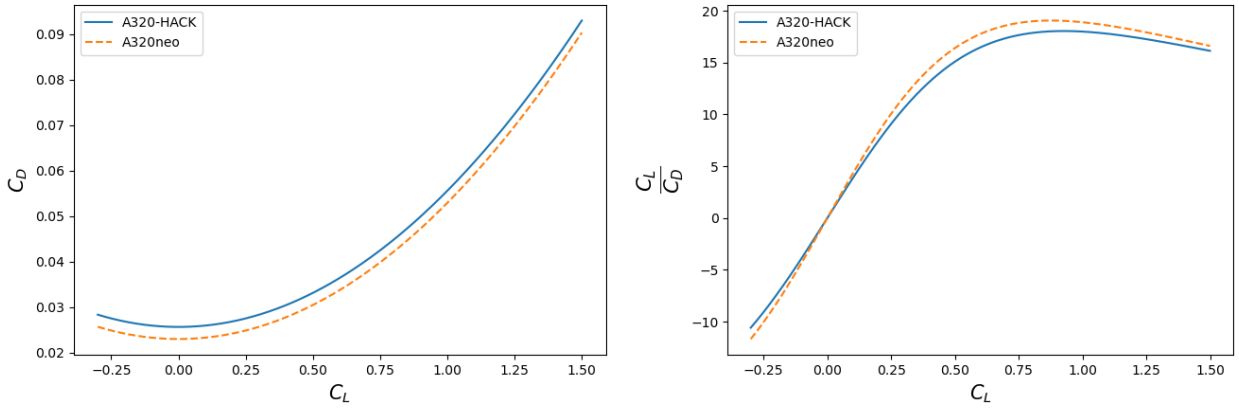

(a) Drag polar

(b) Lift over drag ratio

Figure 14.2: Drag coefficient and lift over drag ratio as a function of lift coefficient for the A320neo and A320-HACK

The lift and drag coefficients at the start of cruise are obtained to determine the required thrust during flight. This is computed assuming that the aircraft takes off with maximum take off weight and using the following fuel fractions: $M_{ff_{TO}} = 0.995$ and $M_{ff_{climb}} = 0.980$. For the cruising altitude of 11280 $[m]$ and a Mach number of 0.78, the following result is obtained:

$$C_L = \frac{2 M_{ff_{TO}} M_{ff_{climb}} MTOW}{\rho V^2 S} = \frac{2 \cdot 0.995 \cdot 0.98 \cdot 73500 \cdot g_0}{0.348 \cdot 230^2 \cdot 122.4} = 0.622$$

Using the drag polar for the A320-HACK, the drag coefficient at the start of cruise (for the C_L of 0.622) becomes 0.0372. With this drag coefficient, the total drag at cruise is $D_c = 42.07\ kN$, which is a 7.68% increase compared to A320neo. The lift to drag ratio for the A320-HACK is therefore, $L/D = 16.7$.

14.3 Limitations and Recommendations

A very important aspect which has been left out from the aerodynamic analysis is the effect which the tank fairing and pylon have on the flow characteristics on top of the wing. Obert studied the aerodynamic design of transport aircraft, hence is work is used for the analysis of the flow over the wing [78].

Firstly, swept wings experience boundary layer cross-flow because the boundary layer moves outboard towards the tip (see Figure 14.3). Therefore, the airflow has a velocity component which is perpendicular to the chord, and hence the tank's pylon is disturbing this flow over the wing. This phenomenon will have to be studied in the future, because flow separation could occur at the outboard side of the pylon. Secondly, the spanwise distribution of the local lift and lift coefficient are also affected by the tanks. Namely, the highest local lift coefficient occurs in between the 60% and 70% of the half span, as can be seen in Figure 14.4. The tanks are located at 55%, close to the location of the highest local C_L. Therefore, the pylon shall be positioned and sized such that the pressure distribution is disturbed as little as possible.

Taking into account the previous design consideration, the third aspect is the distribution of the pressure coefficient along the chord of the A320. The basic wing section of the A320 was designed to minimise the rear loading and to maximise the front loading. The modification can be seen in Figure 14.5, where the arrows show the geometrical changes and the changes in pressure coefficient. For the A320, this means that the airflow over the first half of the upper surface shall remain as undisturbed as possible. The tank pylon has not been designed in terms of chordwise location, but it is recommended that the pylon is located as close to the trailing edge as possible.

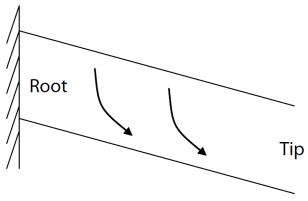

Figure 14.3: Boundary layer moving outboard, causing cross-flow [78]

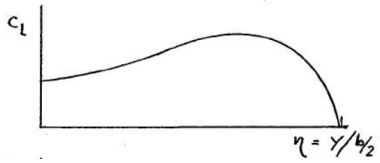

Figure 14.4: Distribution of the local lift coefficient over the half span of the wing [78]

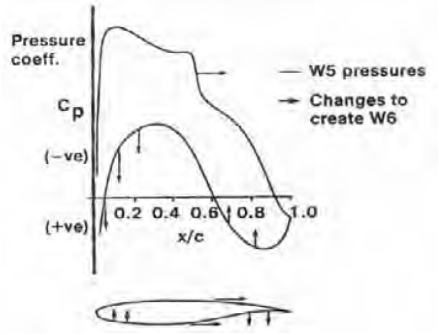

Figure 14.5: Changes applied in the design of the wing section for the A320 [78]

Finally, some drag reduction techniques were studied in order to compensate for the added drag from the tanks and pylon. Because cold hydrogen is being transported through the wing, it could be possible to cool down the upper surface of the wing, as this is favourable for laminar boundary-layer stability and for the delay of transition from laminar to turbulent flow (reducing zero-lift drag) [79]. Nevertheless, this technique requires more research because in the case of cross-flow over swept wings, wall cooling is less effective [80]. It is recommended that research is done on the effects of surface cooling on the boundary layer stability of swept wings.

15 | Performance

The A320-HACK was designed to improve certain aspects such as emissions whilst at the same time maintain other performance parameters such as range, passenger and cargo capacities of the A320neo. Furthermore, in this chapter the performance of the A320-HACK shall be analysed. In Section 15.2 the weight breakdown of the A320-HACK can be found. In the subsequent sections, the range, climb and take-off performance is analysed. Furthermore, for the performance analysis from a sustainability point of view, refer to Chapter 16.

15.1 Requirements

The A320-HACK was designed to comply with the following performance requirements.

UR-PERF-01 A successor to the A320neo aircraft shall be designed with the HACK system.

UR-PERF-02 The design shall satisfy the CS25 rules.

UR-PROP-01 The amount of energy stored in H_2 shall not exceed 1/2 of the energy content in kerosene.

SR-PERF-02 The aircraft shall be able to transport 180 passengers excluding the crew.

SR-PERF-03 The aircraft shall have a harmonic range of 3200 [km] equal to that of the A320neo (WV50).

15.2 Weight Breakdown

To assess the performance of the A320-HACK in comparison to that of the A320neo it is necessary to know their weight breakdown. Thus, this can be found on Table 15.1. The OEW of the A320-HACK was computed as described in Section 13.2. Moreover, in order to comply with the requirement **SR-PERF-02**, it was decided to keep the same MPLW. In addition, the MTOW was also kept the same as the A320neo, since the landing gear was not redesigned.

Table 15.1: Comparison between the weight breakdown of the A320-HACK and the A320neo [kg]

Parameter	A320-HACK	A320neo
OEW	46256	44560
PL_{max}	18240	18240
MZFW	64496	62800
Fuel @ PL_{max}	9003	10700
MTOW	73500	73500

15.3 Flight Profile

The A320-HACK was designed for a range equal to 3200 [km]. The former is the harmonic range of the A320neo. Furthermore, the cruise altitude of 11600 m and the cruise speed to 230 m/s was used for the analysis. The LTO cycle includes the mission phases of taxi, take off, climb out (until 900 m), approach and landing. Besides cruise, also this phase of the flight was analysed from an emission point of view (discussion can be found in Chapter 16).

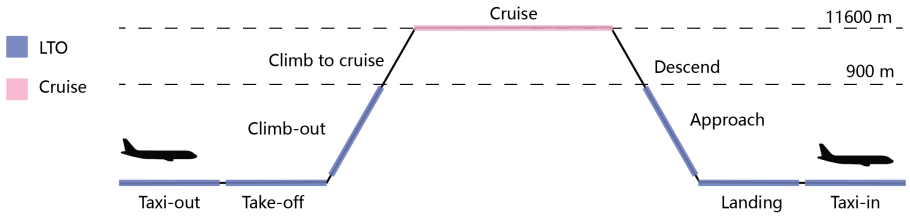

Figure 15.1: Flight profile diagram

15.4 Payload Range Diagram

The range of an aircraft depends on its aerodynamic performance, on its engine efficiency, on its weight and finally on the speed at which it can fly.

While taking into consideration not only the analysis on engine efficiency and engine parameters, which can be found on Chapter 10, but also to the weight breakdown detailed in Section 15.2, the payload range diagram of the A320-HACK was compared to that of a future A320neo. To compute the range, the Breguet's range equation was used. In Equation 15.1, R is the range in km, V_{cruise} is the cruise speed in m/s, TSFC is the thrust specific fuel consumption during cruise in $kg/N/s$, $\frac{L}{D}$ is the

lift over drag, g_0 is the gravitational acceleration at sea level and finally $m4/m5$ is the ratio between the mass of the aircraft at the beginning and at the end of cruise.

$$R = \frac{V_{cruise}}{TSFC \cdot g_0} \cdot \frac{L}{D} \cdot \ln\left(\frac{m4}{m5}\right) \tag{15.1}$$

Moreover, in order to construct the payload-range diagrams, three different ranges were computed. These are summarized in Table 15.2.

Table 15.2: Ranges which were analysed

Range name	Definition
Harmonic Range	The aircraft flies with MPLW
Maximum Fuel Range	The aircraft flies with maximum fuel, but not maximum payload
Ferry Range	The aircraft flies with maximum fuel but zero payload

The parameters used in the construction of the payload range diagrams set out in Table 15.3 and the result is illustrated in Figure 15.2.

Table 15.3: Parameters used in the construction of the A320-HACK's and A320neo's payload range diagram

Parameter	**A320-HACK**	**Future A320neo**
V_{cruise} $[m/s]$	230	230
$\frac{L}{D}$ [-]	16.71	17.98
TSFC $[kg/N/s]$	$7.48 \cdot 10^{-6}$	$13.15 \cdot 10^{-6}$

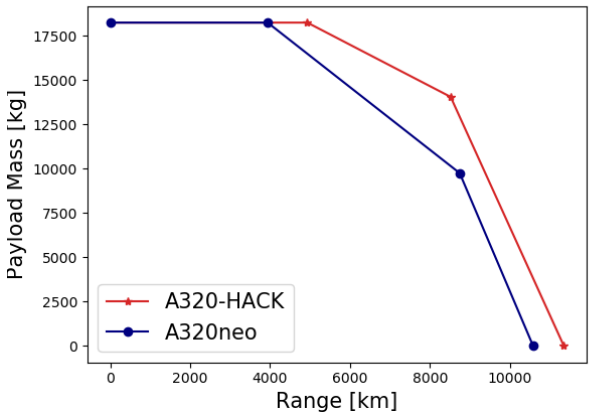

Figure 15.2: Payload Range of a future A320neo and the A320-HACK

As can be seen in Figure 15.2, the range of the A320-HACK is larger than that of A320neo of the future. Thus, the A320-HACK complies with the requirement SR-PERF-03.

Table 15.4: Ranges of the A320-HACK while running on hydrogen and kerosene versus a future version of the A320neo

Parameter	A320-HACK	Future A320neo
Harmonic Range $[km]$	4930	3940
Max fuel Range $[km]$	8500	8740
Ferry Range $[km]$	11300	10600

Verification

To verify that the simulation correctly constructs the payload-range diagram, the parameters of the current A320neo were fed into the program. Table 15.5 summarizes the parameters used and Table 15.6 displays the results.

Table 15.5: Parameters used for the payload-range diagram verification

Parameter	A320neo
V_{cruise} $[m/s]$	230
$\frac{L}{D}$ [-]	17.98
TSFC $[kg/N/s]$	$16.68 \cdot 10^{-6}$

Table 15.6: Verification of the payload diagram plots

Range	Reference $[km]$[62]	Program $[km]$	Error [%]
Harmonic Range	3200	3013	5.8
Maximum Fuel Range	6900	6684	3.13
Ferry Range	8000	8091	1.14

The maximum discrepancy between the reference data and the program's output of 5.8 % can be considered negligible and thus, the program is verified.

15.5 Take-Off, Climb and Landing

Take-Off

The take-off distance is composed of the runway distance and the ground distance covered until the aircraft reaches 15 m of altitude. Furthermore, with the assumption that the take-off phase lasts 1 min (The duration of each flight phase for the considered mission can be found on Table 10.4), based on the acceleration during take-off and thus the associated velocity profile, it was possible to compute the runway distance. For the take off distance covered airborne a similar approach was followed. Once the rate of climb was known, the ground distance covered was computed with Equation 15.2. GD is the ground distance in m, V is the velocity in the beginning of climb, which was taken to be equal to the lift off speed of 84.5 m/s (Refer to Section 10.2.2), h is the altitude, in this case 15 m and finally ROC is the rate of climb in m/s.

$$GD = \frac{V \cdot h}{ROC} \tag{15.2}$$

From the previous computations a take off distance equal to 1992 m was obtained (1859 m for the runway distance and 133 m for the airborne distance). This is slightly larger than the A320neo's take-off distance, which is equal to 1850 m[1]. Nevertheless, this should not cause any issues, since the runway at the Rotterdam Airport is equal to 2200 m.

Climb

In Section 10.2.2 the thrust required per flight phase was analysed. In this section, also the ROC was computed. Based on the time the climb phase is expected to last, namely 20 min, and the altitude the aircraft is required to climb to (11600 m), a value equal to 9.66 m/s was obtained.

Landing

Like the take off distance the landing distance is also composed of two parts. The first part is the airborne phase, which starts once the aircraft reaches 15 m. The second part starts as soon as the aircraft touches the ground and ends once the aircraft has been brought to rest. In order to size for the maximum landing distance, it was assumed that the weight of the aircraft at landing is equal to the MLW. Since the weight is directly proportional to the stall speed, V_s, which subsequently is related to the minimum approach speed, V_{ap} through Equation 15.3, a larger landing weight implies a larger minimum approach speed, which consequently implies a larger landing distance. Moreover, if the MLW of the A320-HACK is considered to be the same as that of the A320neo, 66300 kg, then V_s is equal to 53.73 m/s. Thus, the maximum landing distance can be computed with Equation 15.4[81]. A value equal to 1688.09 m was obtained, which is 328 m larger than the landing distance of the A320neo[1]

$$V_{ap} = 1.3 \cdot V_s \tag{15.3}$$

$$s_L = 0.548 \cdot V_s^2 \tag{15.4}$$

15.6 Hydrogen/Kerosene only Performance

One of the major goals of the A320-HACK is to ease the transition of aviation from a fully kerosene dependent industry, to a hydrogen dependent industry. As such, a requirement was set on the maximum

[1] https://www.globalair.com/aircraft-for-sale/Specifications?specid=639, accessed:21-Jun-2021

amount of hydrogen the A320-HACK should have on board, Nevertheless, it is of relevance to explore the boundaries of the possibility of the A320-HACK allowing for a short-range fully hydrogen flight. Note that due to the requirement on the maximum amount of hydrogen the A320-HACK should be designed to carry, UR-PROP-01, as detailed in Chapter 10. Thus, the range for when the aircraft flies with MPLW has the same value as the range for maximum fuel weight. Therefore, Table 15.7 displays not only the harmonic range of the A320-HACK, but also its ferry range, when flying with only hydrogen. As can be seen, the A320-HACK can fly for instance from Amsterdam to Bologna, while only using hydrogen.

In addition, it might be that some airports do not have access to hydrogen, thus it is also interesting to analyse the performance of the A320-HACK under this scenario. For this, Figure 15.3 displays the payload-range diagram of the A320-HACK while consuming only hydrogen and while consuming only kerosene.

Table 15.7: Ranges of the A320-HACK when running only on hydrogen or only on kerosene

Range	A320-HACK-Hydrogen	A320-HACK-Kerosene
Harmonic Range [km]	1238	3284
Maximum Fuel Range [km]	1238	5460
Ferry Range [km]	1714	7342

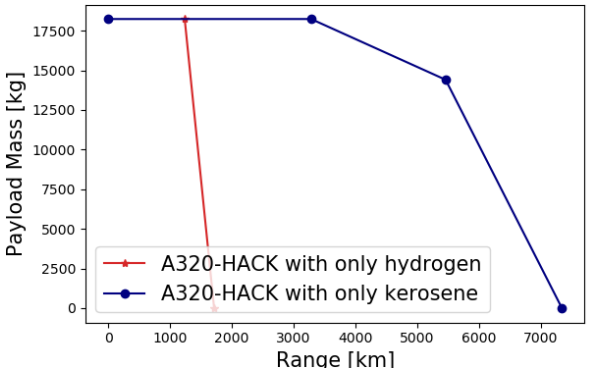

Figure 15.3: Payload Range diagram for the A320-HACK operating only on hydrogen and only on kerosene

16 | Sustainability

As elaborated in Chapter 2, one of the goals of the A320-HACK is to pave the way to a sustainable aviation industry. In this chapter both the emissions and the climate impact of a future with the A320-HACK shall be compared to those of a future with a more efficient version of the A320neo.

16.1 Requirements

Below are the sustainability requirements.

SR-SUST-01 The cruise emissions of NO_x, CO, unburnt hydrocarbon and soot emission shall be at least 30% lower than A320neo.

SR-SUST-02 The NO_x, CO, unburnt hydrocarbon and soot emission for the Landing and Take-Off (LTO) cycle shall be reduced by at least 50% when compared to the A320neo.

SR-SUST-04 The noise-level contour of A320-HACK shall be at maximum 85 decibel, same as for the A320neo.

16.2 Climate Change Model

The climate change model used to assess the climate impact of A320-HACK was constructed based on the model presented by P. Proesmans and Roelof Vos [82]. This model takes the emissions (CO2, H2O, NOx, soot and contrails) of a typical mission, computes their associated radiative forcing and outputs the change in atmospheric temperature over the years for each emission species. Moreover, from the change in atmospheric temperature over the years, the total average temperature response (ATR_H) can be computed. In Equation 16.1, H stands for the number of years the change in temperature due to the aircraft emissions is considered. For this analysis, it is considered to be 100 years as it allows for both

the assessment of long-lived species (CO_2) and short-lived species (NOx)[82].

$$ATR_H = \frac{1}{H}\int_0^H \Delta T(t)\,dt \tag{16.1}$$

Along with assessing the emissions in $[kg]$, this metric was used in Chapter 10, in the A320-HACK's engine design, to check if the sustainability requirements were met. In this section, this shall be explored further.

16.2.1 Utilization rate

To estimate the annual emissions of a certain species, the number of missions performed in a year and the amount of emissions in kg per mission must be known. Equation 16.2 depicts this relationship. U(t) represents the utilization rate; the number of missions flown per year. While e_i represents the emissions in kg of species *i* during a typical mission. Chapter 10, elaborates on how the emissions were obtained.

$$E_i(t) = e_i \cdot U(t) \quad i = CO_2, H_2O, NOx, soot \tag{16.2}$$

Considering **UR-EB-01**, the A320-HACK must enter into service in 2035, therefore throughout this section, this was taken as the value t_0. Furthermore, it is considered that the A320-HACK will operate for 40 years, meaning after 40 years all A320-HACK should be retired. As elaborated in Chapter 4, Airbus's single-aisle aircraft fly all over the globe, and so will A320-HACK. Table 16.1 depicts the market share of Airbus, for each region for the years 2016, 2021 and 2019. The values for 2019 were obtained by interpolating between the values of 2016 and 2021. Furthermore, one should not ignore the impact the Covid-19 pandemic had and is having in the aviation industry. According to IATA's 20 year forecast[1], the number of flights per region shall return to the values of 2019, depicted in Table 16.1, either in 2023 or 2024. For North America, Latin America and Asia/Pacific this recovery is expected to occur already in 2023, while for the remaining regions only in 2024.

Table 16.1: Global market share per region

Region	Asia/Pacific	North America	Europe	Latin America	Middle East	Africa	World
2016 [%][2]	35	24	26	7	5	2	100
2021 [%][3]	38.64	22.72	23.62	5.71	7.41	1.9	100
2019 [%]	37.18	23.23	24.57	6.22	6.44	1.94	100
2019 flights[million]	14.35	8.97	9.48	2.4	2.48	0.748	38.9[4]

Moreover, the aviation industry and associated traffic will grow[1]. However, this shall not occur homogeneously throughout the world. Attending to the different growth rates (GR), Table 16.2 shows the forecast for the world's traffic by 2035.

Table 16.2: Flights per region by 2035

Region	Asia/Pacific	North America	Europe	Latin America	Middle East	Africa	World
GR 2021-2039 [%][1]	4.5	1.7	2.0	2.9	3.6	3.6	3.2
2035 flights [million]	24.34	10.97	11.79	3.38	3.67	1.1	55.3

[1] https://www.iata.org/contentassets/e938e150c0f547449c1093239597cc18/pax-forecast-infographic-2020-final.pdf, retrieved 14-Jun-2021

[2] https://www.iata.org/en/pressroom/pr/2017-10-09-01/,accessed:15-Jun-2021

[3] https://financesonline.com/number-of-flights-worldwide/,accessed: 15-Jun-2021

[4] https://www.statista.com/statistics/564769/airline-industry-number-of-flights/, accessed:15-Jun-2021

During the period of 2018-2028 it is expected that the narrow body segment will account for 56% of the global commercial aircraft market[5]. Thus, from the 55.3 million flights expected to happen in 2035, 30.9 million are expected to be narrow body (NB). Furthermore, for the same period, Table 16.3 depicts the NB market share (percentage of total NB flights in the world per region) and the expected NB flights by 2035 per region. Note that it is assumed that after 2035, the NB flights remain equal to 56 % of the total flights and the NB market share per region remains equal to the values on Table 16.3.
In addition, it is expected that by 2035, 8% of the flights use hydrogen, while in 2050 this number is expected to rise to 40% [83]. Although, in the beginning of the transition to an aviation industry with hydrogen, the HACK concept might be the majority of the hydrogen flights, over time it is expected that other hydrogen aircraft enter the market. Therefore, taking this into account leads to the estimation that by 2050 the A320-HACK should represent 25% of the total amount of flights.

Table 16.3: Narrow body flights per region

Region	Asia/Pacific	North America	Europe	Latin America	Middle East	Africa	World
NB market share[5]	43	18.4	20.3	7.9	8	1.8	100
NB flights 2035 [million]	13.31	5.7	6.3	2.5	2.5	0.6	30.9

Figure 16.1 depicts the number of A320-HACK missions expected over the years, based on the previous analysis. For comparison, it was considered that the future A320neo would also perform the same number of missions. Furthermore, the number of missions were considered instead of the fleet size because to compute the total amount of annual emissions, the number of missions per year are required. The fleet size does not directly translate into the number of flights flown.

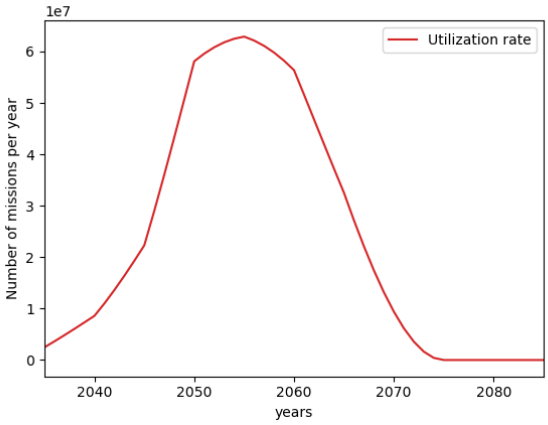

Figure 16.1: Expected number of missions over the years

16.2.2 Emissions Effect

The emissions' species which were considered for the analysis are CO_2, H_2O, NOx and soot. Due to the large uncertainty in the estimation of the climate impact of contrails, these were not considered in the ATR computation. This is briefly discussed later in this section.

Carbon dioxide

Carbon dioxide is a long-lived species, for which its environmental effects do not depend on the geographical location at which it is emitted. From the CO_2 emissions, one can compute the change in CO_2 atmospheric concentration in *ppmv*, denoted as $\Delta\chi_{CO_2}(t)$, in Equation 16.3 [82, 84]. Furthermore, Table 16.4 contains the coefficients α and τ to be used in Equation 16.4 [84].

$$\Delta\chi_{CO_2}(t) = \int_{t_0}^{t} G\chi_{CO_2}(t-t') \cdot E_{CO_2}(t')\, dt' \quad (16.3)$$

$$G_{\chi CO_2}(t) = \sum_{i=1}^{5} \alpha_i \cdot e^{\frac{-t}{\tau_i}} \quad (16.4)$$

[5] https://rb.gy/n96qna,accessed: 14-Jun-2021

Table 16.4: Coefficients of the impulse response function $G_{\chi CO_2}$ for the CO_2 concentration[84]

i	1	2	3	4	5
α_i **[ppmv/kg]**	$0.067 \cdot 10^{-12}$	$0.1135 \cdot 10^{-12}$	$0.152 \cdot 10^{-12}$	$0.0970 \cdot 10^{-12}$	$0.041 \cdot 10^{-12}$
τ_i **[-]**	∞	313.8	79.8	18.8	1.7

The normalized radiative forcing (RF) of CO_2 was computed with Equation 16.5. χ_{CO_2} represents the background CO_2 concentration, which is assumed to be equal to 444 *ppmv* as forecasted in a study by Mathew Smith and Samuel Myers [85].

$$RF* = \frac{1}{\ln 2} \cdot \ln \frac{\chi_{CO_2} + \Delta\chi_{CO_2}(t)}{\chi_{CO_2}} \tag{16.5}$$

Nitrogen Oxides

Unlike CO_2, the NO_x climate impact depends both on the altitude and geographical location at which they are emitted [86]. In this model the altitude effect was accounted for, the geographical location effect was not. When released into the atmosphere, NO_x emissions have two main effects. In the long term, they contribute to the reduction in methane, CH_4 and long-lived ozone O_3L, which has a cooling effect. On the other hand, NO_x emissions lead to the formation of short-lived ozone O_3S in the troposphere and lower stratosphere, which has a warming effect.

To account for the altitude effect, the results present in a study by Dallara and Kroo were used [86]. In this study, the altitude effect or otherwise called forcing factor (s_i in Equation 16.6 and $s_{NO_x-O_{3s}}$ in Equation 16.8), was calculated based on the RF per emissions at a specific altitude, normalized by the fleetwide average RF. The RF per emission as a function of the altitude was obtained from a study by Köhler et al. on the aircraft NO_x emissions[87]. Note that, the forcing factors were not available for an altitude smaller than 5742 *m*, therefore for these lower altitudes the forcing factors are assumed to be constant and equal to the value at 5742 *m*. Furthermore, according to Dallara and Kroo, this should have a small effect in the final radiative forcing results, as below 5742 *m* the magnitude of the forcing factors are small and only a small portion of the flight is flown at this altitude. Ultimately, Equation 16.6 was used to compute the RF of CH_4 and O_3L , where G_i is the impulse response of NOx, which was computed with Equation 16.7. Table 16.5 contains the coefficients used.

$$RF_i(t,h) = s_i(h) \int_{t_0}^{t} G_i(t-t') \cdot E_{NO_x}(t')\, dt' \tag{16.6}$$

$$G_i(t) = A_i e^{\frac{-t}{\tau_i}} \quad i = CH_4, O_3L \tag{16.7}$$

Table 16.5: Coefficients of the impulse response function $G_i(t)$ for the CH_4 and O_3L

Parameter	A_{CH_4} $[W/m^2/kg_{NOx}]$	A_{O_3L} $[W/m^2/kg_{NOx}]$	τ_n $[years]$
Value	1.0	1.37	1.14

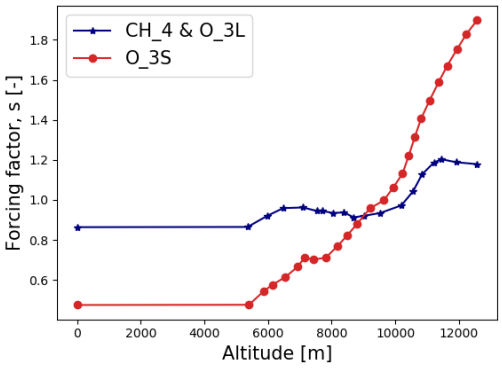

Figure 16.2: Forcing factor as a function of the altitude [86]

As far as the short-lived ozone is concerned, its radiative forcing was computed with Equation 16.8. Again, the forcing factor $s_{NO_x-O_{3s}}$ was calculated based on the plot in Figure 16.2 and the value for $\frac{RF_{ref}}{E_{ref}}$ can be found on Table 16.6.

$$RF_{NO_x-O_{3s}}(t,h) = s_{NO_x-O_{3s}}(h) \cdot \left(\frac{RF_{ref}}{E_{ref}}\right) \cdot E_{NO_x}(t) \tag{16.8}$$

Water, Soot

To account for other short-lived species such as water vapour and soot, Equation 16.9 was used. The radiative forcing for these species was modelled in a similar way to that of short-lived ozone, however the altitude forcing factor was not considered [82]. Moreover, in Table 16.6 one can find the values for $(RF_{ref}/E_{ref})_i$.

Table 16.6: Parameters to compute RF of H_2O,O_3S and $soot$

Parameter	$\frac{RF_{ref}}{E_{ref_{H_2O}}}$	$\frac{RF_{ref}}{E_{ref_{O_3S}}}$	$\frac{RF_{ref}}{E_{ref_{soot}}}$
Value $[W/m^2/kg_{NOx}]$	$7.43{\cdot}10^{-15}$	$1.01{\cdot}10^{-11}$	$5.0{\cdot}10^{-10}$

$$RF_i(t) = (\frac{RF_{ref}}{E_{ref}})_i \cdot E_i(t) \quad i = H_2O, soot \tag{16.9}$$

Contrails

The effect of contrails to climate change is still uncertain. Nevertheless, their effect has been shown to be quite significant [88]. Furthermore, contrails form under very specific situations. If the hot engine exhaust air saturates with respect to liquid water when mixing with the surrounding air, contrails are formed[89]. The mixing process can be modeled with a straight line in a diagram of ambient temperature versus water vapor partial pressure[82]. The slope of the mixing line can be computed with Equation 16.10.

$$G = \frac{EI_{H_2O} \cdot p \cdot c_p}{\epsilon \cdot Q(1-\eta)} \tag{16.10}$$

Nevertheless, in order to have a significant climate impact, contrails must persist in the atmosphere. For this to happen the following conditions must be met: First, the ambient temperature must be below a critical temperature(T_C). Secondly, the partial pressure of the mixed exhaust must be in between the saturation pressure with respect to liquid water and the saturation pressure with respect to ice[89]. Furthermore, the A320-HACK not only uses hydrogen, but also has a larger engine efficiency than that of the A320neo (refer to Chapter 10). Thus, contrail formation is going to be larger. Although contrails were not included in the ATR computation in Section 16.2.3 the conditions for which contrails can be formed for the A320-HACK's engine shall be compared to those of the A320neo's engine and a small discussion on their expected impact shall be given.

Combined effect

To grasp the combined radiative forcing of the considered species, Equation 16.11 was used. Eff_i is the efficacy of a specific species and it is the ratio between the species climate sensitivity and the climate sensitivity of CO_2[82]. The considered values can be found on Table 16.7. RF_{2*CO_2} has a value of 3.7 W/m^2 for a doubling in the CO_2 ratio [90].

$$RF*(t) = \sum_{i}^{allspecies} RF*_i(t) = \sum_{i}^{allspecies} [Eff_i \cdot \frac{RF_i(t)}{RF_{2*CO_2}}] \tag{16.11}$$

Table 16.7: Climate efficacies for considered species

Species i	CO_2	H_2O	O_3	$soot$	CH_4
Eff_i	1.0	1.37	1.14	0.7	1.18

Furthermore, Equation 16.12 was used to compute the change in temperature over the years, due to the considered emission species. In the former, G_T is the impulse response function [91].

$$\Delta T(t) = \int_{t_0}^{t} G_T(t-t') \cdot RF*(t')\, dt' \tag{16.12}$$

$$G_T(t) = \frac{2.246}{36.8} e^{\frac{-t}{36.8}} \tag{16.13}$$

16.2.3 Emissions & Climate Change Analysis

In order to size the main engine, analysis which can be found in Chapter 10, the emissions during LTO and cruise of the A320neo and the A320-HACK were compared. Furthermore, for the LTO cycle the

comparison between the A320neo and the A320-HACK can be found on Table 16.8. For this phase of the mission it was found that the A320-HACK is able to meet the sustainability requirement of reducing the NOx, soot, UHC and CO emissions by 50%. In Table 16.9, the same comparison can be found for the cruise phase of the flight. Also, for this phase the sustainability requirements were met. Note that, to attain the values on Table 16.8 and Table 16.9 the mission's range was considered to be 3000 $[km]$.

Table 16.8: Comparison between the LTO cycle emissions of the A320neo and the A320-HACK

Species	CO_2	CO	H_2O	NOx	$soot$	UHC
A320neo LTO $[kg]$	2224.55	28.9	1803	235	0.109	0.021
A320-HACK LTO $[kg]$	333	1.29	1963	48.4	0.00133	0.00217
Difference [%]	-92.2	-95.5	+8.9	-79.4	-98.8	-87.7

Table 16.9: Comparison between the cruise emissions of the A320neo and the A320-HACK.

Species	CO_2	CO	H_2O	NOx	$soot$	UHC
A320neo Cruise $[kg]$	28736	83.5	12053	1448.5	0.14	0.14
A320-HACK Cruise $[kg]$	8339.7	3.56	14335.8	855	0.054	0.054
Difference [%]	-70.97	-95.7	+19	-40.9	-61.4	-61.4

As far as the climate change is concerned, it was found that for 40 years of operations, the A320-HACK would lead to an ATR value of 0.010 $[K]$, while for the A320neo this value is equal to 0.043 $[K]$, which amounts to a reduction of 76.7 %. This is also supported by Figure 16.3 and Figure 16.4. These display the change in atmospheric temperature over the years due to the different emission species. Note how the change in atmospheric temperature due to water vapor emissions is slightly higher for the A320-HACK than for the A320neo.

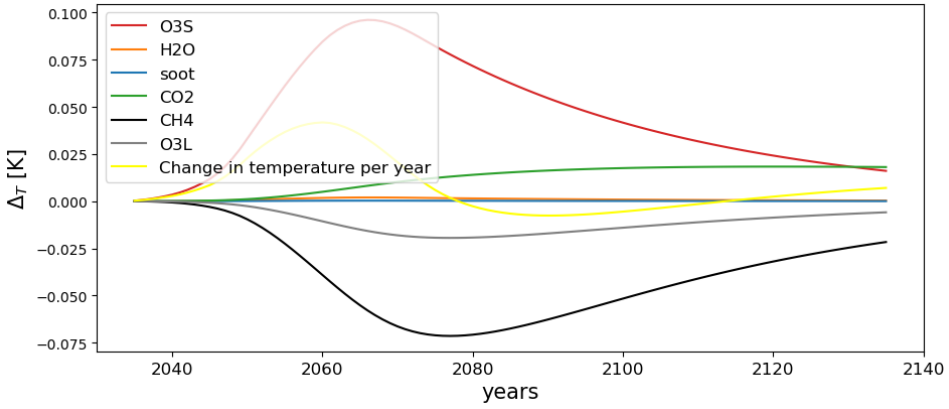

Figure 16.3: Change in temperature over time due to 40 years of A320-HACK operations

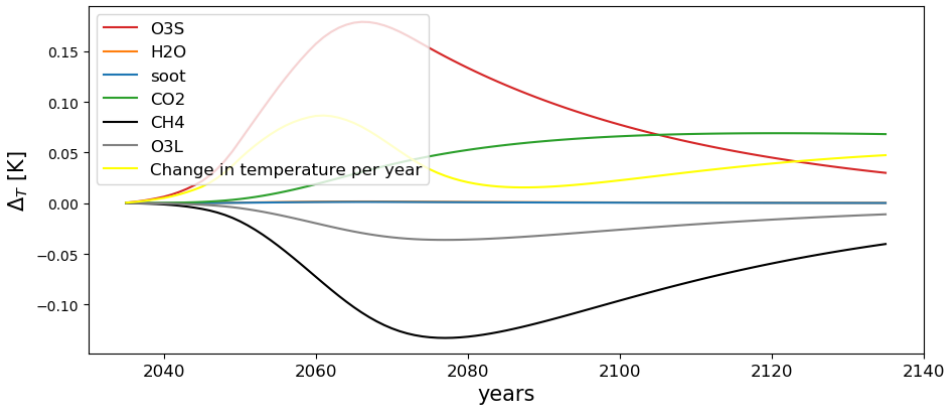

Figure 16.4: Change in atmospheric temperature over time due to 40 years of A320neo operations

As explained in Section 16.2.2 the contrails' climate effect was not taken into account to construct Figure 16.3 and Figure 16.4. Thus, the aforementioned analysis does not take into account that the combustion of hydrogen increases the probability of contrails being formed. Furthermore, the highest atmospheric temperature at which contrails can form for the A320-HACK shall increase with respect to the A320neo. Thus, this implies a larger portion of the flight can gather the required conditions for contrails to be formed.

16.2.4 Verification & Validation

To verify the climate model, the results from a study by Robert Sausen and Ulrich Schumann were taken as reference[84]. Although, the data provided is relatively outdated it still allows to see if the climate model is in line to the expected behaviour. The annual emissions of CO2 in Tg used to verify the model can be found on Table 16.10. Furthermore, the data available for the change in CO_2 concentration, radiative forcing and change in atmospheric temperature consisted of only a few data points. Note that to quantify the error between the reference data and the model's output Equation 16.14 was used.

$$Error = \frac{Reference - Model}{Model} \cdot 100 \tag{16.14}$$

Table 16.10: Annual CO2 emissions [Tg] for the years between 1940 and 1995 [84]

Decade	0	1	2	3	4	5	6	7	8	9
Year										
1940	7.7	8.3	9.0	9.7	10.5	11.3	12.3	13.2	14.3	15.4
1950	16.7	18.0	19.4	21.0	22.7	24.5	26.5	28.6	30.9	33.3
1960	36.0	39.5	43.5	45.9	48.0	51.3	55.6	65.6	74.3	77.8
1970	78.0	90	96	99.4	96	96.1	96.4	102.1	105.7	110.1
1980	110.9	109.3	110.5	112	119.5	123.4	129.9	135.6	141.4	146.5
1990	146.9	143.4	142.0	144.1	150	154.3				

As can be seen in Table 16.11, Table 16.12 and Table 16.13, the error in CO_2 concentration reached a maximum of 6.4%, for the CO_2 radiative forcing the maximum error is of 9.06 % and for the change in atmospheric temperature due to CO_2 emissions it is of 33.79 %. The former was taken into account when analysing the climate change results in Section 16.2.3.

Table 16.11: Verification of change in CO_2 concentration

Year	$(\Delta\chi_{CO_2})_{ref}$ [ppmv]	$(\Delta\chi_{CO_2})_{model}$ [ppmv]	Error [%]
1950	0.05	0.053	5.97
1970	0.35	0.372	6.40
1990	1.13	1.20	6.02
1992	1.22	1.29	6.01
1995	1.37	1.30	5.08

Table 16.12: Verification of Radiative forcing of CO_2

Year	$RF_{CO_{2ref}}$ $[W/m^2]$	$RF_{CO_{2model}}$ $[W/m^2]$	Error [%]
1950	0.001	0.0009	9.06
1970	0.007	0.0064	8.74
1990	0.021	0.020	2.26
1992	0.022	0.022	0.69
1995	0.024	0.022	7.19

Table 16.13: Verification of change in temperature due to CO_2

Year	$\Delta T_{CO_{2ref}}$ $[K]$	$\Delta T_{CO_{2model}}$ $[K]$	Error [%]
1950	0.0	$7.436 \cdot 10^{-5}$	
1970	0.001	$9.06 \cdot 10^{-4}$	9.37
1990	0.003	$4.135 \cdot 10^{-3}$	37.83
1992	0.004	$4.62 \cdot 10^{-3}$	15.59
1995	0.004	$5.35 \cdot 10^{-3}$	33.79

16.2.5 Limitations & Recommendations

One of the biggest limitations of the climate model is that it does not take into account the change in atmospheric temperature due to the formation of contrails. Thus, for the future phases of the design this aspect should be implemented into the climate change model. Furthermore, the sustainability analysis was also performed at discrete points during a typical mission, meaning the conditions at which the aircraft is flying, namely fuel flow, velocity, etc. were not evaluated more than twice per mission phase (climb, cruise,etc.). In addition, it is relevant to analyse the change in climate impact depending on the geographical region the A320-HACK is flying.

16.3 Life-Cycle

In Section 16.3.1, the life-cycle of the aircraft components is analysed. Section 16.3.2 covers the life-cycle analysis from an operational point of view.

16.3.1 Components Life-Cycle

Considering the manufacturing process, CFRP have a considerable impact on the environment compared to traditional metals. CFRP production is about 14 times more energy intensive than the production of conventional steel [92]. It is thus of utmost importance to ensure green energy sources for the production of CFRP in order to reduce climate impact. Although in disadvantage when it comes to the sustainability of the production, over the whole life-cycle, using CFRP leads to a considerable decrease in emissions. As an example, the initial manufacturing 1 ton of carbon fiber creates 20 ton of CO_2. If 20% of the fuselage of an aircraft is replaced with CFRP, each ton of CFRP will lead to a save of 1400 ton of CO_2 over a life-cycle of 10 yrs[6]. Thus, over the whole life-cycle of the product, CFRP leads to considerably lower CO_2 emissions.

In terms of end-of life, thermoplastic composites, such as the ones used in the wing box of the A320-HACK, offer great potential in terms of recyclability. Previously used composite parts can be mechanically recycled by shredding and then used to make new parts through, for example, compression moulding. Sometimes, recycling can lead to degradation in the properties of the material[7], requiring to integrate

[6] https://www.torayca.com/en/aboutus/abo_003.html, retrieved 22-Jun-2021
[7] https://www.nccuk.com/sustainable-composites, retrieved 22-Jun-2021

the reused material in less demanding applications. One of the most popular applications for reused thermoplastics is in cements, where a decrease of up to 16% is shown in the carbon footprint[8] compared to traditional cement manufacturing processes. Materials with improved properties can be obtained by mixing reused material with raw materials, allowing for a wider range of applications. Recycling of composites is not only green, but also economically advantageous, especially for carbon fiber based composites[9].

16.3.2 Operations Life-Cycle

Transport of hydrogen aspect; The A320-HACK's performance in terms of emissions is better than that of the A320neo, as detailed in Section 16.2.3. It was computed that over an operational life of 40 years, the A320-HACK would cause an average temperature increase of ... With regards to the hydrogen production itself, as detailed in Chapter 17, green methodologies would have an extremely low environmental impact. Several countries in North Africa and Australia are already investing in hydrogen economy to make the best use of their relatively low domestic energy needs and an abundance of renewable energy resources. Nevertheless, supplying airports with hydrogen - depending on the transportation means - can have an impact in this regard. However, the use of dedicated liquid hydrogen shipping vessels and hydrogen powered trucks will contribute to reduced emissions. In terms of emissions, the ideal solution would be to produce green hydrogen on-site, this option, however is not economically sound particularly on small scale and on the short term.

16.4 Noise

The A320-HACK should not have a higher noise level than that of A320neo. The impact of the engine modifications on its noise footprint was not analysed in a high level of detail. However, for turbofan engines, the noise mainly stems from the fan, compressor, and exhaust. The introduction of the geared fan in HACK's engine was assumed not to have a major impact on its noise level. This is because LEAP-1A and PW1100G have similar fan diameters of 78 and 81 $inch$ and bypass ratios (BPR), of 11 and 12. However, their noise is similar at around the 83 dB in terms of Effective Perceived Noise Level (EPNL)[10]. This is despite the fact that PW1100G is a geared turbofan engine . According to [93], "the fan noise can be reduced as high as 10 dB by the increase of bypass ratios" in terms of Sound pressure level (SPL). A higher bypass ratio also lowers the nozzle exit velocities and thus the exhaust noise [94]. Since the bypass ratio of the A320-HACK's engine is 40.6% higher than that of LEAP-1A, a similar noise reduction was assumed from the former to the latter.

The original Auxiliary Power Unit (APU) of the A320neo, Honeywell 131-9A, was a conventional gas generator[95]. The C130-Hercules APU has similar specifications as the Honeywell 131-9A. The C130H APU produces 125.7 dB[11]. A normal conversation is about 60 dB [96]. This means that the sound of C130H APU is $(e^{\frac{125.7-60}{10}}) = 713$ times more intense than normal speech. A fuel cell on the other hand, only produces 40-50 dB[12] at 1 m distance. This is 63% less intensive than normal speech. When comparing the C130H to a fuel cell, one can experience a sound intensity (as measured in W/m^2) reduction by a factor of $(e^{\frac{125.7-50}{10}}) = 1939$. However, this reduction applies to the idle phase only as in a nominal mission that is where the APU is used. Thus, in the remaining phases of the mission, the Dedicated Power Unit (DPU) contributes to an increase in noise although not significantly.

The noise levels are mainly relevant during the landing and take-off, with fan noise being a predominant factor in both phases as seen in Figure 16.5. As seen above, by the use of higher BPR, the fan noise

[8] https://tinyurl.com/3na4x7x9, accessed: 22-Jun-2021

[9] https://www.compositesworld.com/articles/recycled-thermoplastic-composites-for-production, accessed: 22-Jun-2021

[10] https://publicapps.caa.co.uk/docs/33/CAP1869QuotaCountvalidationstudy31Jan2020.pdf, retrieved on 29-Jun-2021

[11] https://www.mjphm.org.my/mjphm/journals/2017%20-%20Special%20Volume%20(1)/NOISE%20EXPOSURE%20AMONG%20MAINTENANCE%20CREWS%20OF%20C130H%20AIRCRAFT%20LEAD%20TO%20THE%20HEARING%20IMPAIRMENT.pdf, accessed:22-Jun-2021

[12] https://energies.airliquide.com/resources-planet-hydrogen/fuel-cell, accessed:22-Jun-2021

levels could be reduced by 10 dB in SPL. However, in order to fully comprehend what this difference will be in comparison to that of A320neo, the reduction in SPL must be converted to reduction in EPNL. Afterall, EPNL is the industry benchmark for maximum noise level for a stage 4 aircraft such as A320neo/A320HACK. Therefore, as an extension to this study, the SPL reduction of the fan noise must be converted into EPNL using the method described by ICAO [13]and compared against noise performance of A320neo.

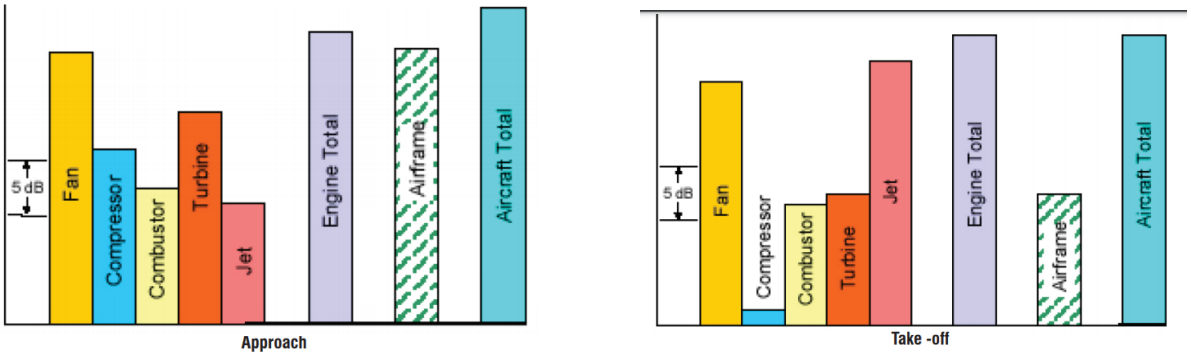

(a) Sources of noise during approach

(b) Sources of noise during approach

Figure 16.5: Relative weights of noise sources during take-off and landing [97]

17 | Operations & Logistics

Introducing a new fuel in a complex industry such as commercial aviation requires to thoroughly consider the implications in terms of infrastructure and operations. This chapter proposes an overview on such aspects: first, the refuelling operations and its safety, as well as the turnaround time of the A320-HACK will be addressed; then, the hydrogen supply chain will be briefly outlined and lastly a case study for the Rotterdam The Hague Airport will be presented.

17.1 Requirements

The considerations presented in this chapter were aimed at investigating and verifying the following requirements and user recommendations.

UR-OPER-01 The impact of refuelling LH_2 on the turn-around time of the aircraft shall not be more than 10 minutes.

UR-SR-04 The passenger evacuation time of A320-HACK shall not be greater than 90 s.

UG-PERF-02 The aircraft refuelling and safety shall be taken into account.

UG-SR-02 The safety of the LH_2 refuelling system shall be addressed.

UG-SUST-01 The supply and production of green hydrogen at the airport shall be investigated.

UG-SR-03 The storage of LH_2 at the airport shall be addressed.

17.2 Refuelling Operations

The ground refuelling system, the turnaround time implications of LH_2 refuelling, and some safety related aspects will be presented in this section.

[13] https://www.icao.int/Meetings/EnvironmentalWorkshops/Documents/Noise-Certification-Workshop-2006/Depitre_4.pdf, retrieved 29-JUN-2021

17.2.1 Refuelling System

The refuelling operation of LH_2 is rather similar to the kerosene one. Refuelling can be done either using tanker trucks (Figure 17.1a) or using hydrant refuelling vehicles (Figure 17.1b) in case of a pipeline system. Once the refuelling equipment is connected to the aircraft inlet, LH_2 is pumped into the tanks and the displaced GH_2 from boil-off is collected. GH_2 is ideally re-introduced in the supply chain, or eventually utilised to directly run hydrogen-powered Ground Support Equipment (GSE) operated within the airport infrastructure (it is indeed rather reasonable to expect that such vehicles will be available in the near future). Two possible refuelling procedures are presented in Figure 17.1a and Figure 17.1b. Although these operations were considered viable and safe at the time of this study, further research into the likely costs incurred in making adaptations to airport infrastructure is recommended in order to further confirm the feasibility and viability of such procedures at different airports.

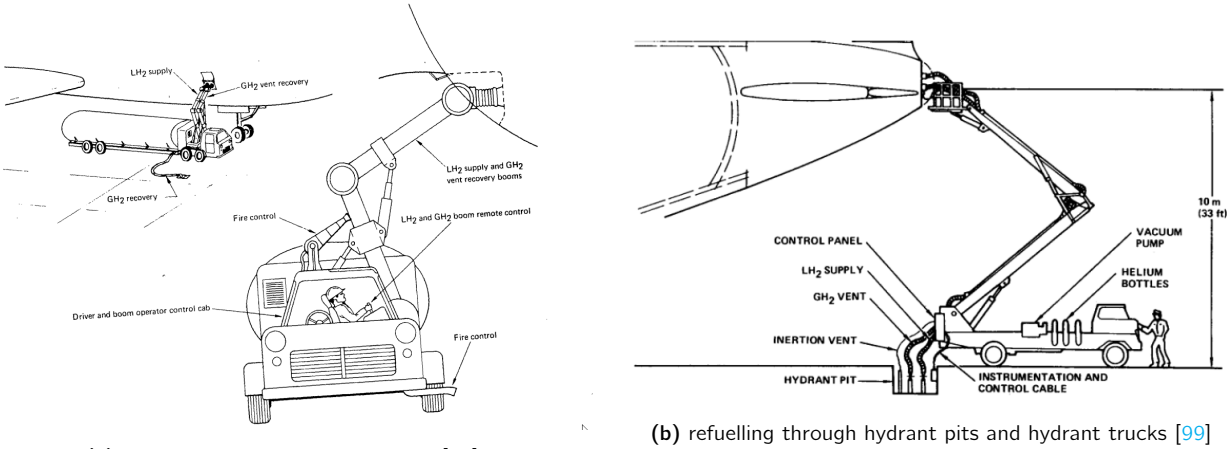

(a) refuelling through a tanker truck [98]

(b) refuelling through hydrant pits and hydrant trucks [99]

Figure 17.1: Liquid hydrogen refuelling procedures

For the A320-HACK specifically, another option for refuelling is available, exploiting the fact that the hydrogen tanks are wing-mounted. Instead of refuelling the empty tanks at the gate, it would be possible to swap them with pre-filled ones. This procedure seems rather convenient and could be even less time-consuming than traditional refuelling. However, at this stage of the project, it is complex to estimate the feasibility and duration of such operation. The design of the tanks and their connection interface with the wings has not yet reached the level of detail required to quantify the practicality of this procedure. It must be also noted that, given the tanks' location on the upper wing surface, swapping them may turn out to be rather convoluted due to the presence of suspended loads and may add to turnaround time (TRT) as a result. Plus, it would also be necessary to verify the required GSE could fit in the TRT without clashing with other vehicles. Overall, given that - again - it is not yet possible to estimate the time required for swapping the tanks, it is not feasible to compare this procedure to the standard refuelling. Therefore, for the purpose of this study, the traditional refuelling procedure will be considered, although it is recommended to investigate the possibility to swap tanks during later phases of the project.

17.2.2 Turnaround Time & Ramp Layout

The A320-HACK has to be refuelled with hydrogen and kerosene, and thus - compared to the current A320s - involves additional operations that impact the aircraft's TRT and the ramp layout. The former is especially crucial for costs and competitiveness, indeed, even a 10 minutes prolongation could lead to a 2% increase of the total cost for short-haul flights [83]. Therefore, it is important to integrate the new required operations while minimising their effect on the TRT, also considering the limit posed by UR-OPER-01.

The TRT and the ramp layout of the A320-HACK were defined starting from the ones of the A320neo, which are described in detail in [62]. The main difference consists of the additional LH_2 refuelling phase, and the shortened kerosene refuelling time given the smaller capacity. On the other hand, the following

operations remain mostly unchanged: passengers disembarking and boarding, cargo unloading and loading, catering, cabin cleaning and all the other general procedures.

The LH_2 refuelling time was estimated as follows. Firstly, it was assumed that by 2035 the refuel rate for liquid hydrogen will reach a value of around 1000 L/min, which is realistically achievable granted that sufficient assets are invested into R&D [83]. Secondly, akin to the Airbus's approach to estimated A320neo TRT, it was assumed that the tanks are filled at roughly 80% of their maximum capacity. As already explained, the A320-HACK has two wing-mounted tanks (max usable capacity of 16771 L each, so 13417 L at 80%)). In order to minimise the impact of hydrogen refuelling on the TRT, this activity is performed from two different locations, partially at the same time. The entire right wing-mounted tank and part of the left wing-mounted tank (5526 L) are refueled from the right hand side of the aircraft, positioning the required Ground Support Equipment (GSE) underneath the wing, similarly to what already happens for kerosene. refuelling takes 29 minutes, plus 5 min were added both before and after this operation, in order to position and prepare the GSE. Usually, for kerosene only 2.5 min are allocated before and after the refuelling, though hydrogen requires more elaborate procedure, as discussed in Section 19.4.2, and longer intervals were defined as a result.

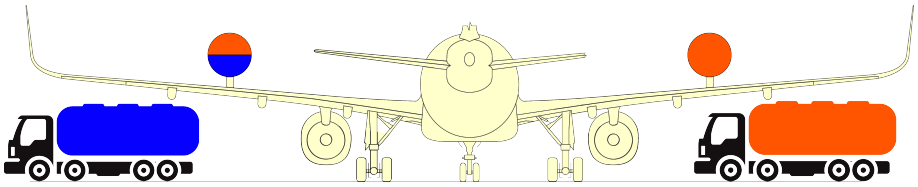

Figure 17.2: Representation of a LH_2 refuelling event, the truck on the right hand side refuels the right tank and part of the left one to optimize the turnaround time

The remaining capacity of the left wing-mounted tank (roughly 7900 L), as depicted in Figure 17.2 will be refueled from the right hand side of the aircraft, again positioning the required GSE underneath the wing. This activity takes 18 minutes (10 minutes for positioning/removal of the GSE and 10 minutes for the actual refuelling) and is completely performed while passengers are not on board, given that it could partially obstruct an eventual evacuation considering the position of the GSE on the left hand side of the aircraft. Since the aim is not to increase the current turnaround time - where passengers are not on board for only 18.5 minutes - the time available for this operation was constrained and so part of the left tank is refueled, as explained above, from the right hand side.

Similarly, the kerosene refuelling time was estimated assuming a rate of 1250 L/min [62] and to fill 80% of the total capacity (equal to 15900 L). Thus, 10 min (plus 2.5 min before and after for GSE positioning) are necessary in order to fill the tanks at 80% (12725 L).

Overall, compared to the A320neo, the turnaround time of the A320-HACK has not increased and still remains 44 min, and the refuelling phase constitutes a critical path. These operations (both for kerosene and LH_2) run in parallel to other activities (including passenger disembarking and boarding), given that no specific concern of any matter has been identified. Indeed, kerosene refuelling is already allowed to be performed while passengers are boarding, on board or disembarking [100], and LH_2 refuelling does not seem to raise any problematic in this regard [31]. The turnaround sequence for the A320-HACK is depicted in Figure 17.3.

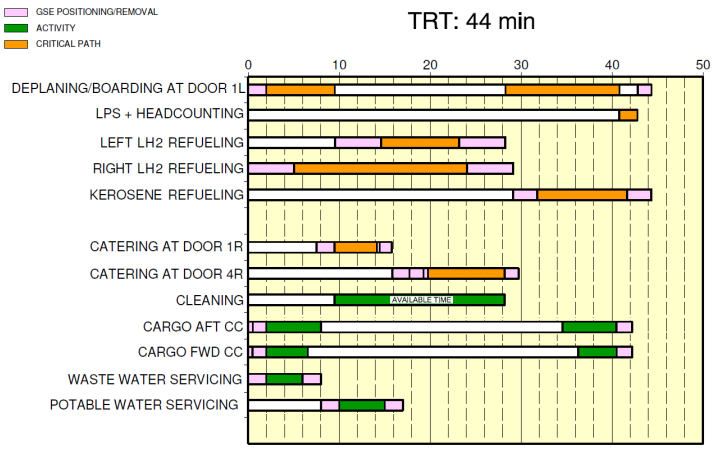

Figure 17.3: Full servicing turnaround time chart for the A320-HACK (adapted from [62])

Additionally, the ramp layout of the A320-HACK was analysed and it was verified that the LH_2 GSE could actually fit without clashing with other operations or equipment. The ramp layout of the A320-HACK is depicted in Figure 17.4, while the corresponding abbreviations for the GSE are listed in Table 17.1.

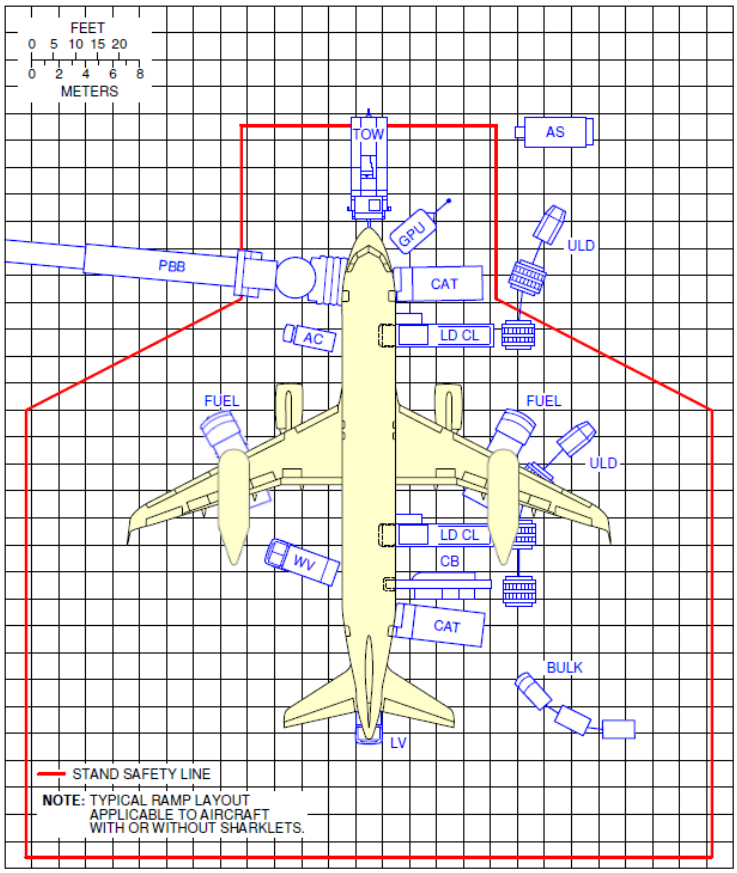

Figure 17.4: Ramp layout for the A320-HACK (adapted from [62])

Table 17.1: Ground Support Equipment (GSE) abbreviations [62]

AC	Air conditioning unit
AS	Air start unit
BULK	Bulk train
CAT	Catering truck
CB	Conveyor belt
FUEL	Fuel tanker
GPU	Ground power unit
LDCL	Lower deck cargo loader
LV	Lavatory vehicle
PBB	Passenger boarding bridge
TOW	Tow tractor
ULD	Unit Load Device
WV	Portable water vehicle

Lastly, it is important to mention that the additional turnaround tasks required by the A320-HACK were set up considering the aircraft evacuation plan (shown in Figure 17.5), which should remain unobstructed. The left hand side of the aircraft is indeed completely free when passengers are boarding, on board and disembarking, thus allowing for a safe evacuation in case of emergency.

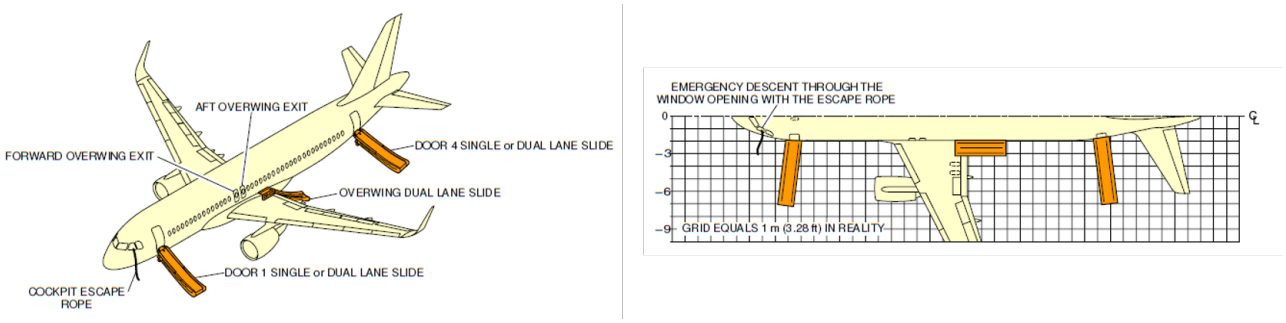

Figure 17.5: Emergency evacuation devices for the A320neo and A320-HACK [62]

17.2.3 Safety & Handling

This section briefly outlines the hazardous features of hydrogen, and touches upon how these could be addressed during operations such as refuelling. So far, no specific regulations have been set up, and even studies about the safety risks related to LH_2 operations are rather scarce in literature [101].

Firstly, liquid hydrogen has an extremely low temperature, that could lead to thermal contraction of the materials used for the equipment. Secondly, these materials can be embrittled by hydrogen, which also has a very high permeability. These aspects can cause failure in the equipment and thus lead to a leakage. Permeability issues can be addressed during the equipment design, implementing double-wall structures and performing periodical leak tests. Embrittlement can be controlled using weld joints and installing vacuum gauges to spot eventual issues. Thermal contraction can be approached by setting up cool-down procedures. However, despite these measures, a leakage can still take place and eventually lead to either an explosion or a fire. The former can be mitigated using a rupture disc and a gas detector. The latter instead, first needs to be identified with a UV detector - as a hydrogen flame is invisible - and then put off with an extinguisher system. All the aforementioned preventive and mitigative measures need to be considered while designing the operations equipment and setting up the related procedures.

Further, hydrogen has an extremely high buoyancy, implying that - in case of leakage - it rapidly mixes with the ambient air to a level below the flammability threshold (4% by volume of air) [102]. Hydrogen has a high flammability, although it must be said that in case of fire it will cause less damage due to lower temperatures and strength of the flame compared to kerosene [103]. The high buoyancy of hydrogen is rather favourable during refuelling operations, because once released, the gas would quickly dissolve in the atmosphere reducing the risk of ignition. Furthermore, since refuelling doesn't take place in a confined space, there is no risk of hydrogen accumulation, which could lead to physiological risks such as asphyxiation.

Although hydrogen is a non-toxic substance, it is classified as an asphyxiant, and it is associated with certain physiological hazards. First, eventual LH_2 splashes on the skin cause serious frostbite or hypothermia. Therefore, other than minimising the probability of spillages, personnel shall operate with a personal protective equipment (PPE) able to mitigate the effects of eventual LH_2 splashes. Furthermore, inhaling cold vapour or gas leads to respiratory discomfort and eventually to asphyxiation. Therefore, measure to prevent this occurrence need to be implemented while setting up the operational procedures.

Overall, it can be said that hydrogen is neither more dangerous nor safer compared to other fuels, it simply has peculiar properties and thus has to be handled accordingly by employing adequate crew training and safety procedures [102].

17.3 Hydrogen Supply Chain

Introducing a new fuel in the aviation industry is a great logistical challenge, given the extension of the current infrastructure and thus the costs of eventual modifications - besides the difficulties related to handling hydrogen. The aim of this section is to outline the supply chain of hydrogen to airports, briefly addressing all the currently available options for production, transportation and storage. A schematic representation of the hydrogen supply chain, from production up to refuelling, is depicted in Figure 17.6.

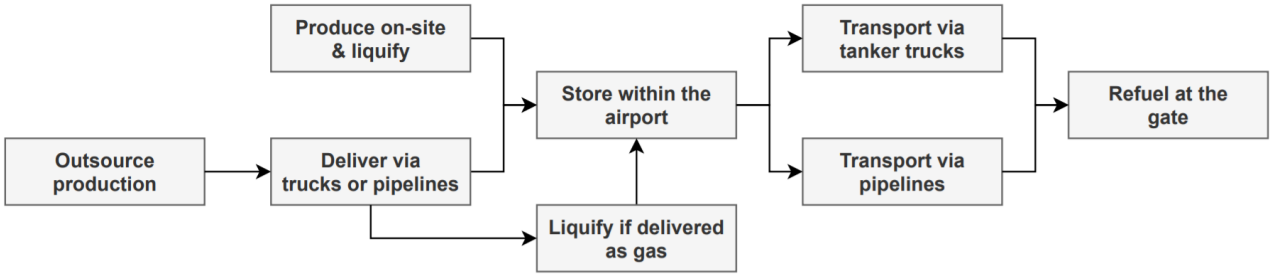

Figure 17.6: Schematic representation of the hydrogen supply chain for commercial aviation

17.3.1 Hydrogen Production Methods

Although hydrogen is the most abundant element on Earth, it is only found incorporated in more complex molecules, due to its high reactivity. Hence, hydrogen needs to be isolated through specific production processes. These are divided in three categories - grey, blue and green - based on the energy source and methodology adopted for its production [104].

Grey hydrogen - which currently constitutes 96% of the total H_2 production [104] - is obtained from hydrocarbons such as natural gas or coal, through carbon intensive methodologies (Steam Methane Reforming (SMR) and coal gasification). Processes to generate grey hydrogen are highly intensive in terms of CO_2 (roughly 9 kg of CO_2 for 1 kg of H_2 [105]), though their cost is rather low, since they are already highly developed and established (the TRL is quite high, and the overall efficiency of the process can be up to 76% [105]). Given its environmental footprint and the availability of cleaner alternatives, it is reasonable to expect that grey hydrogen might be slowly replaced by more sustainable options.

Blue hydrogen is produced through the same procedures as for grey hydrogen, though most of the carbon emissions are captured via Carbon Capture and Storage (CCS) methods (such processes can capture up to 99% of the generated CO_2 [105]). Therefore, compared to grey hydrogen, the blue one is far less pollutant but also more expensive, given the lower TRL. Blue hydrogen is often regarded as an intermediate step towards completely carbon free processes, which are introduced hereafter.

Green hydrogen is produced through extremely low or zero-emission processes, exploiting renewable energy to perform electrolysis. Thus, green hydrogen can boast a low environmental impact, plus it has a higher degree of purity compared to grey and blue hydrogen[1]. Nonetheless, it is still the most expensive option, given its lower TRL [104]; the overall process efficiency is expected to exceed 70% within the end of the current decade [106].

Note that other possibilities are available for hydrogen production. In fact, hydrogen can also be produced exploiting nuclear energy or from biomass gasification. Nevertheless, for the time being, these options result less viable or convenient than the ones mentioned before. Producing hydrogen from nuclear[2] is still at an early development phase, while capital and feed-stock costs still need to be reduced for biomass processes[3].

For sustainability reasons, either blue or green hydrogen are preferred, especially in case of implementing production facilities within airports' infrastructure. Moreover, the large-scale adoption of hydrogen in aviation triggers an increase in hydrogen demand, which should ideally be satisfied by implementing sustainable solutions. Consequently, the hydrogen adoption in aviation should also further back and drive the development of blue and green hydrogen technologies, decreasing costs and increasing efficiency.

17.3.2 Production Site & Transportation

Considering the hydrogen supply chain for commercial aviation, it is possible to generate hydrogen on-site at the airport or to outsource the production. Each option has its advantages and disadvantages, and

[1] https://www.tno.nl/en/focus-areas/energy-transition/roadmaps/towards-co2-neutral-industry/hydrogen-for-a-sustainable-energy-supply/15-things-you-need-to-know-about-hydrogen/, accessed:13-May-2021

[2] https://www.energy.gov/ne/articles/could-hydrogen-help-save-nuclear, accessed:13-May-2021

[3] https://www.energy.gov/eere/fuelcells/hydrogen-production-biomass-gasification, accessed:13-May-2021

the optimal solution depends on the airport. In this section, each option is briefly outlined.

On-site production offers great logistic advantages as it eliminates the use of fuel tankers that help cut down emissions and a complex hydrogen supply chain. Alder, however, concludes that the energy, water, capital costs and spacial constraints of an airport would make it infeasible for an on-site production and liquefaction facility to accommodate the needs of a wide-scale adoption of LH_2 at the airport [107]. The cost competitiveness of this option is highly dependent on the location of the airport if a low-carbon energy source is available [83]. In addition, the economies of scale also play a role in the cost of hydrogen, as smaller airports with a lower demand will struggle to secure the capital required for the plant installation. This is investigated further in Section 17.4.3. The applicability of this option is limited by the availability of facilities/space of the airport, as a hydrogen plant requires an extensive surface area. Another aspect that needs to be considered is the high development cost that might not be efficiently amortized in case of airports with a low amount of required hydrogen. Moreover, smaller production plants tend to be more expensive to operate compared to larger ones.

From a transportation point of view, outsourcing becomes more complicated and costly than the on-site production. Delivery can be done via hydrogen carrying trucks or pipelines for gas hydrogen. For the latter, the liquefaction process along with its costs and facilities must be considered, plus a pipeline network would need to be built. By using trucks, the infrastructure adjustments required from the airports' side are considerably reduced. In the near future, while the hydrogen demand per airport will be low, it is expected that transportation by truck will be the most viable option [83]. One advantage of using trucks is the fact that commercial LH_2 carrying trucks are already available on the market [108], allowing airports to begin offering hydrogen services sooner. The pipeline system will take longer to implement. For reference, it is forecasted that in 2040, in Europe, the hydrogen network will extend to 39700 km across 21 countries[4]. However, if the airport's hydrogen demand is increased, pipelines are expected to be preferred over trucks for large airports due to increased ground traffic and operational challenges. In terms of emissions, the pipeline alternative has an advantage as currently only diesel powered trucks are available. In the future, the emissions' discrepancy might be reduced if trucks which run on alternative fuels are introduced. Lastly, pipelines are more reliable, quiet and safe.

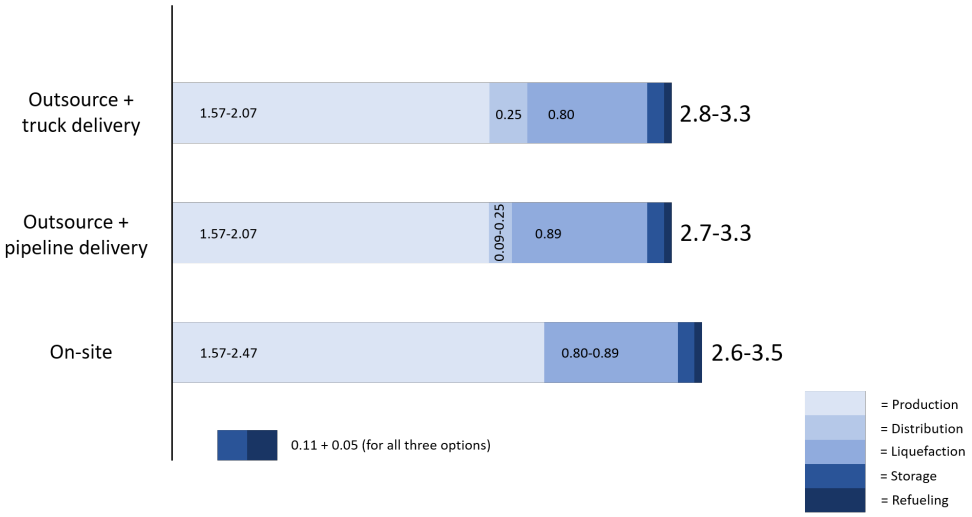

Figure 17.7: Overview of the possible supply options for hydrogen with respective forecasted costs for 2040 (expressed in USD per kg of H_2), compiled with data from [83]

According to a recent study [83], for all the supply pathway options depicted in Figure 17.6, the forecasted costs for 2040 will be rather similar, from around 2.6 to 3.5 USD per kilogram of H_2. This is mainly because when the transportation costs are absent, they are compensated by the higher costs of producing on-site. Indeed, on-site production would most likely happen on smaller scale, which usually implies a

[4] https://www.reuters.com/business/sustainable-business/europe-could-operate-40000-km-hydrogen-pipelines-by-2040-operators-2021-04-13/, accessed:12-May-2021

cost increase. Nevertheless, also the overall efficiency of the process must be considered: in this regard, the last option would have a total efficiency around 60% [83], while the first two pathways - given the transportation phase - would most likely score below this value. An overview of the aforementioned options, together with their respective forecasted costs range, are show in Figure 17.7. In any case, it is important to realise that - even in the most optimistic scenario - hydrogen is going to be significantly more expensive than kerosene per kWh at the inception of A320-HACK which will amount to a 9% in fuel costs per passenger kilometre [83].

17.3.3 Storage

Once the hydrogen is liquefied on-site or the liquid hydrogen is transported to the airport, it will be stored in the cryogenic fuel storage tanks. These tanks will be built with a capacity to store the amount of LH_2 needed for two days of operation. This decision stems from balancing the efforts to minimise the losses due to evaporation and to mitigate the effects of disruptions in the supply of LH_2. The ideal shape for such tanks is spherical, since this minimises the surface-to-volume ratio, and hence the heat transfer. While NASA has been able to achieve evaporation rates of 0.05% /day with integrated refrigeration and storage methods[109], on a smaller scale these rates range between 0.1% and 0.3% per day[109]. However, the storage efficiencies of the tanks with no active cooling is at present only estimated to be 66.6% and is forecasted to be improved to 83% by 2040[110]. Using these efficiencies and the estimated LH_2 used in daily operations, the required tank volumes are calculated and presented in Table 17.2. Instead of venting the vapour hydrogen, however, it will be collected and used as a fuel for the airside trucks and maintenance vehicles or recycled by sending it to the liquefaction facility.

17.4 Rotterdam The Hague Airport Case Study

As discussed, the hydrogen supply chain is organized in multiple ways. Hence, it is not possible to establish a universal operations and logistics plan, as this varies - among others - with the airport size, air traffic volumes, the development of a hydrogen network in the region and the eventual regulations. For the purpose of this project, a case study for the implementation of hydrogen services was conducted for the Rotterdam The Hague Airport.

17.4.1 Required Fuel Estimation

Firstly, the quantity of hydrogen that will be used by the airport over a certain time span was estimated. For this, the current usage of kerosene was estimated, converted in energy usage and then it was forecasted that a portion of this will be provided by LH_2. Based on this quantity, it is possible to analyse the hydrogen supply chain for the airport.

The current monthly requirement of kerosene for the airport was estimated based on an available dataset of commercial flights operated in January 2020[5]. However, this is not a complete reflection of the critical fuel requirement as January is generally not a month with high flights demand. Therefore, additional corrections were applied and this data set was used to obtain a distribution of the operated routes and their respective aircraft (depicted in Figure 17.8).

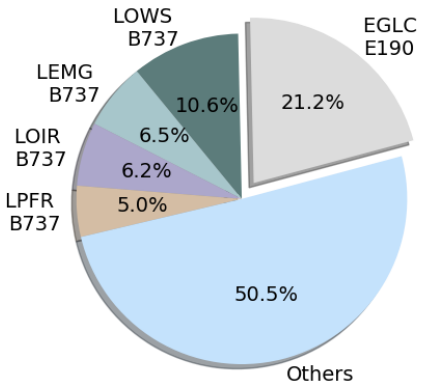

Figure 17.8: Distribution of flights for the Rotterdam The Hague Airport, based on January 2020 figures[5]

Using these percentages, the numbers were scaled to a more representative period, namely May 2019; the most intensive month of the year in terms of traffic[6]. Thus, the data from January 2020 - comprising 321 flights - was scaled to take into account the 858 flights of May 2019. Then, knowing which aircraft is operated on a certain route, the fuel flows of the correspondent engines were retrieved from the ICAO Emissions Databank[7]; plus, knowing the cruise velocity of the aircraft and the distance of the routes, the cruise time was determined. Later, by multiplying the duration of each flight phase by the correspondent fuel flow, the amount of kerosene burnt per flight was computed. It is important to realize that this process is based on an idealized method that does not take into account any inefficiencies. Therefore, an additional factor of 23% accounting was applied to compensate the aforementioned assumption [111]. After using this procedure for all the flights in the distribution, a monthly kerosene requirement of 3050 $tons$ was estimated.

This value is valid for the year 2019, however, since this case study considers two future scenarios - namely 2035 and 2050 - the estimation was adjusted in order to take into account current trends and thus be valid for his scope. Firstly, fuel efficiency constantly increases due to technical advancements. According to Kharina and Rutherford [112], the fuel burn is reduced at an average yearly rate of roughly 1%, therefore, the estimation was adjusted accordingly. Secondly, air traffic volumes are constantly growing, for the Netherlands this happens at a yearly rate of about 1.5% [113]. Thus, the estimation was corrected accordingly. However, the pandemic hardly impacted commercial aviation, which is expected to recover to pre-pandemic level only by 2024[8]. Therefore, for this case study, it was assumed that the estimation for kerosene consumption calculated for 2019 will be reached again in 2024, then, the two aforementioned corrections (for fuel efficiency and air traffic increase) were applied using a compounding formula. As a result, for 2035, a kerosene monthly usage of 3220 $tons$ was estimated, while a value just below 3500 $tons$ was obtained for 2050.

Next, in order to assess the amount of hydrogen necessary, the kerosene estimation was converted into energy equivalent, and it was assumed that this total energy requirements will be partially satisfied by hydrogen in the two future scenarios. In this way, it was possible to obtain the monthly quantity of hydrogen required (in terms of energy, weight and volume). Based on [83], it was assumed that roughly 8% of the energy required in the form of fuel will be provided by hydrogen in 2035, this fraction was considered to grow up to 40% in 2050. Therefore, a hydrogen usage equivalent to just under 3100 MWh (about 90 $tons$ of LH_2) was obtained for 2035, while a value of roughly 16600 MWh (about 500 $tons$ of LH_2) was found for 2050.

The steps and results presented above are summarised in Table 17.2, the following constants were used for the calculations: 12 kWh/kg as kerosene energy density, 33.6 kWh/kg as hydrogen energy density and 71 kg/m^3 as LH_2 mass density.

Table 17.2: Monthly estimation of fuel required at the Rotterdam Airport

Year	**Kerosene** [$tons$]	**Energy Equivalent** [MWh]	**Predicted LH_2 fraction of total energy**	**LH_2 Energy Equivalent** [MWh]	**LH_2 weight** [$tons$]	**LH_2 volume** [m^3]
2019	3050	36600	-	-	-	-
2035	3220	38650	8%	3100	90	1300
2050	3500	41600	40%	16600	500	7000

[5] https://zenodo.org/record/4737390, accessed:17-May-2021

[6] https://www.rotterdamthehagueairport.nl/wp-content/uploads/Totaal-per-maand-2019-januari-2020.pdf, accessed:17-May-2021

[7] https://www.easa.europa.eu/domains/environment/icao-aircraft-engine-emissions-databank, accessed:17-May-2021

[8] https://www.eurocontrol.int/press-release/new-eurocontrol-four-year-forecast-finds-air-traffic-not-expected-reach-2019-levels, accessed:03-Jun-2021

17.4.2 Hydrogen Supply Chain for 2035 & 2050

Considering the estimated quantities of hydrogen required by the airport (both for 2035 and 2050), as well as the hydrogen production facilities existing in the region[9], the most sensible choice seems to outsource hydrogen and deliver it to the airport in liquid form via tanker trucks. Indeed, realising an on-site production and/or liquefaction plant would not be economically sensible, given that - as explained before - costs are significantly higher for small-scale plants. While supplying hydrogen via a pipeline may sound as a reasonable option, this would imply the necessity of a liquefaction facility at the airport, which would not be economically convenient.

The required hydrogen will be provided by the production facilities that are - or will be - operative in the area of the Port of Rotterdam[9]. Green and blue hydrogen plants are expected to be realised in the near future, and these should be able to ensure the supply of the hydrogen required by the airport. For example, Shell is developing the Rotterdam Green Hydrogen Hub, a plant capable of generating between 50 and 60 $tons$ of hydrogen daily and supposed to start operations in 2023[10]. Furthermore, the H-vision[11] plan targets to have an operative blue hydrogen plant by late 2026. In addition, there may also be the possibility to utilise green hydrogen produced overseas, in areas such as North Africa where, lower energy demands and higher availability of renewable sources attribute to an expected cost of 1 $\$ct/kWh$ by 2030 [114]. It will then be shipped to the port via LH_2 carriers, similar to the ones tested for transport between Japan and Australia [12].

To calculate the number of trucks necessary to supply the hydrogen requirement, a tanker truck capacity of 30 m^3 was assumed. This figure was defined considering that a traditional kerosene tanker truck can carry around 40 m^3 and that - for LH_2 - roughly 30% of this total available volume would be taken up by insulation, thus leaving the remaining 70% ($\approx$30 m^3) for hydrogen. Based on this consideration, it was estimated that 45 truck loads per month (1.5 per day) will be required to supply the necessary quantity in 2035. This number of truck loads increases up to 235 per month ($\approx$8 per day) to meet the hydrogen requirement in 2050. These figures are summarised in Table 17.3.

Table 17.3: Liquid hydrogen supply estimations for the Rotterdam Airport

Year	Monthly LH_2 requirement [m^3]	Truck load capacity [m^3]	Monthly number of truck loads	Daily number of truck loads
2035	1300	30	45	$\approx$1.5
2050	7000	30	235	$\approx$8

In terms of airport infrastructure, no major changes will be required, it will only be necessary to integrate a rather small facility to store LH_2. Taking into account the relatively low amount of hydrogen consumption, as well as the quasi-uninterrupted supply from close-by plants, the LH_2 storage tanks will likely need to host just a 24/48h consumption, in order to make up for eventual disruptions in the supply chain. This means that - considering the 48h limit - storage tanks will need to contain roughly 90 m^3 in 2035, and about 470 m^3 in 2050. Therefore, for 2035 a spherical storage tank with a diameter of roughly 6.5 m would be required. For 2050, roughly five spherical tanks of the same size would be required, or eventually fewer with larger diameter (these numbers were obtained assuming that 70% of the total tank volume can be used for hydrogen, the rest being reserved mainly for insulation). Therefore, in terms of surface area, a lot of around 40 m^2 would need to be allocated for the storage tank; in 2050, the required surface area would be around five times as large. The aforementioned figures are briefly summarised in Table 17.4.

Table 17.4: Liquid hydrogen storage facility estimations for the Rotterdam Airport

[9] https://www.portofrotterdam.com/en/doing-business/port-of-the-future/energy-transition/hydrogen-in-rotterdam, accessed:07-Jun-2021

[10] https://www.shell.com/energy-and-innovation/new-energies/hydrogen.html, accessed:07-Jun-2021

[11] https://www.h-vision.nl/en, accessed:07-Jun-2021

[12] https://global.kawasaki.com/en/corp/newsroom/news/detail/?f=20191211_3487, accessed:21-Jun-2021

Year	Storage capacity $[m^3]$	Hydrogen volume over total tank volume	Spherical tank volume $[m^3]$	Spherical tank diameter $[m]$	Number of tanks	Required surface area $[m^2]$
2035	90	70%	130	6.5	1	40
2050	470	70%	130	6.5	5	200

Since the area needed for hydrogen storage tanks is rather small, they can easily be integrated into the airport infrastructure, provided that there is adequate ventilation. One of such locations at the Rotterdam airport is identified and is seen in the Figure 17.9.

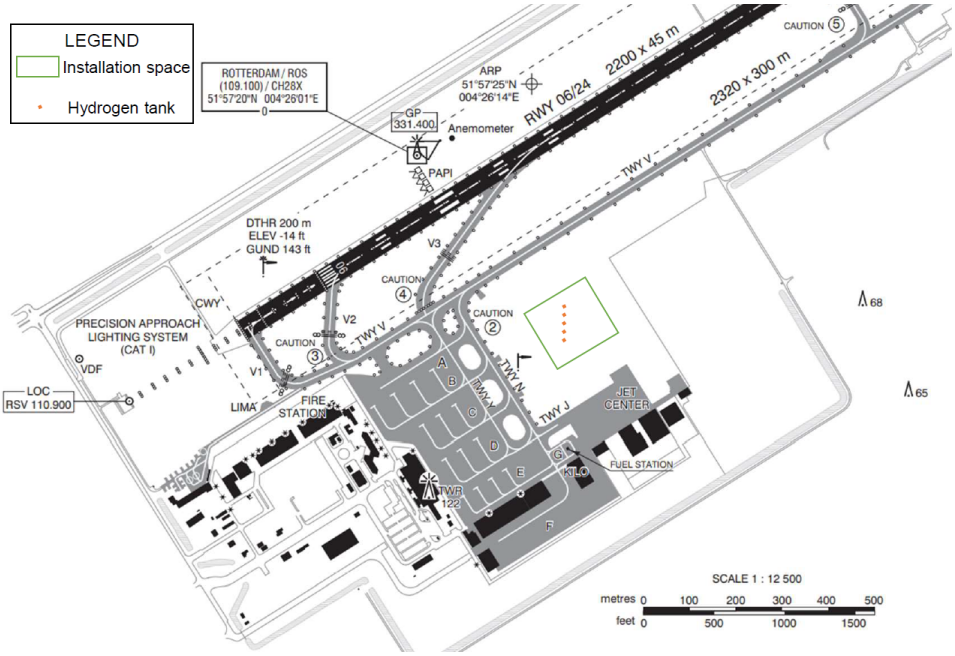

Figure 17.9: Possible locations of Hydrogen storage tanks at the Rotterdam Airport[13]

17.4.3 On-Site Liquefaction of Hydrogen

As previously explained, it is more convenient to directly supply LH_2 to the airport instead of delivering GH_2 and then liquefying it on-site. In order to reach this conclusion, an analysis was performed, and its results are briefly presented in this section. Several liquefaction methods, their energy consumption and their associated costs were considered and analysed.

The work needed to liquefy 1 kg of hydrogen in an ideal cycle of isothermal compression and isentropic expansion is 3.23 kWh [115]. However, the energy consumed by the current state of the art liquefaction facility in Leuna is as much as 11.9 kWh/kg_{LH_2} [116]. Several studies have examined different thermodynamic refrigeration cycles that could improve the efficiency of the liquefaction process at larger scale and concluded that specific power consumption of 5.29 - 10.85 kWh/kg_{LH_2} could be achieved [117, 118, 119, 120, 121]. However, the capacities of these plants range from 170 - 860 t_{LH_2}/day. In addition, these studies were also only theoretical in nature and the capacity of the largest liquefaction facility at this moment is merely 13.5 t_{LH_2}/day. Essler concludes that it would be feasible to liquefy hydrogen on a medium scale, with a capacity of 40-50 t_{LH_2}/day, with a specific power consumption of 6.4 kWh/kg_{LH_2} via the improvement of the compressor efficiency by raising the exit temperature of the compressed hydrogen from 80K to 130K and by using mixed refrigerant cascade [122]. This project aims to demonstrate this by setting up a research plant [14]. However, since a modest amount of 3 $tons/day$ of LH_2 is projected to be needed at the airport in 2035 and 16.5 $tons/day$ later in 2050, the specific

[13] https://www.dutchvacc.nl/charts/, accessed:22-Jun-2021
[14] https://cordis.europa.eu/project/id/278177/reporting, accessed:21-Jun-2021

power consumption of 6.4 kWh/kg_{LH_2} could never be achieved.

Despite this significant reduction in power consumption relative to the plants operating at present, the energy required for liquefaction alone will be 11 GWh in 2035 and 47.5 GWh in 2050. These estimates were calculated based on the specific power consumption of 10 kWh/kg_{LH_2} in 2035 due to meagre operational loads in 2035, an improved 8 kWh/kg_{LH_2} due to higher consumption in 2050, as seen in Table 17.5 together with the projections of LH_2 usage as seen in Table 17.3. Rotterdam airport, as part of the Royal Schiphol group is, and will be powered for the next 12 years, entirely by the Dutch wind farms [15]. However, it is unknown whether the energy supplier, Eneco, will be able to extend the supply of this green energy to the liquefaction facility as this would represent a 5% and 20% increase in the energy consumption for 2035 and 2050 respectively, relative to the present 230 GWh supplied to the group.

In addition to that, the capital required to install a plant described [101] is found to be in excess of €90 million. The amount of LH_2 projected to be used at this airport will mean that the capital investment will never be repaid without pricing the LH_2 produced at the facility out of the market[123]. Therefore, on-site liquefaction of hydrogen is not a viable solution for an airport of the scale similar to that of Rotterdam airport. For larger airports, with a demand for $50 t_{LH_2}/day$ or more, this might still be a worthy option, particularly as the displaced vapour hydrogen collected from the aircraft's fuel tanks can also be re-liquefied on site.

Table 17.5: Specific energy consumption of liquefaction vs plant's operational loads [101]

	Plant Capacity: 50 $[tons/day]$			
Operating load factors [%]	**100**	**75**	**50**	**25**
Specific energy consumption $[kWh/kg_{LH_2}]$	6.76	7.18	7.40	10.20

17.5 Limitations & Recommendations

The first limitation of the analyses presented in this chapter is related to the refuelling operations. The presented considerations are based on rather dated (albeit the latest available) studies, which deemed such procedures viable and safe; however, no such procedure, and no system to perform them have been designed and implemented so far. Furthermore, for the TRT estimations, based on literature, it was assumed that by 2035 it will be possible to refuel LH_2 at a rate comparable to the current kerosene one. Also in this case, no equipment able to fulfill this requirement is available, and the forecast is based on the assumption that such technology will be developed in the next decade. Overall, it seems that - although these refuelling procedures seem feasible - substantial efforts and investments are required in order to make them actually practicable in the desired time frame.

The second limitation is related to the hydrogen supply chain. Indeed, the Rotterdam The Hague Airport case study was set up assuming that the current hydrogen-related projects will be completed within the set time frame. However, in case delays should occur, there might be the chance that no LH_2 would be available by 2035 as forecasted, and so the estimations here presented might turn out to be unrealistic.

Finally, two aspects have not been thoroughly considered, namely the public perception of hydrogen and its higher costs compared to traditional fuels. For what concerns the former, mixed public views were recorded by various studies, and many are still influenced by some historic accidents, such as the Hindenburg disaster[16]. For the latter, it is undeniable that - even in the most optimistic scenarios - hydrogen, especially at early stages, will be significantly more expensive than kerosene. Therefore, while hydrogen might be appealing from a sustainability standpoint, its economic drawbacks might discourage

[15] https://news.schiphol.com/royal-schiphol-group-fully-powered-by-dutch-wind-farms-from-2018/?, accessed:09-Jun-2021

[16] https://www.weforum.org/agenda/2019/04/why-don-t-the-public-see-hydrogen-as-a-safe-energy-source/ , accessed:21-Jun-2021

its adoption from a business perspective, and thus slow down its spread. It is therefore reasonable to expect that a bold support in terms of policy and governmental funds might be necessary to ramp up this technology (like it is happening with other technologies, such as electric private transport). Another funds-related aspect emerges also from the airport case study: while it is clear that adapting the infrastructure will require significant investments, it is not fully clear what party will be responsible to make them.

Overall, in order to provide answers to the aforementioned aspects, more interdisciplinary studies are required; in particular, it is necessary to further deepen the policy related aspects and in general to consider in a more comprehensive way all the stakeholders.

18 | Costs

Before producing a new aircraft, a cost analysis is conducted to analyse the feasibility of the project. This chapter gives an overview of the different steps that were taken in the cost analysis of the A320-HACK.

18.1 Requirements

There are two requirements related to the financial part of the project. They are stated below [11]:

UR-COST-01 The total development cost of the aircraft shall not exceed 5 billion euros.

UR-COST-02 The production cost of the aircraft shall not exceed 15% than that of A320neo.

18.2 Cost for Manufacturer

The costs for the manufacturer (Airbus) consist of the development and production costs. After that a break-even analysis is conducted.

18.2.1 Development Cost

Markish [124] found a way to estimate the cost per kg for the following subsystems: wing, empennage, fuselage, landing gear, engines, systems and payload. The systems consist mostly of the following: fuel weight, flight control, Auxiliary Power Unit, instrumentation, avionics, hydraulics and electrics [125]. The hydrogen (H_2) system consists of two mounted tanks (one on each wing) mounted on top of the wing, as has been explained in Section 9.2. Therefore, the development cost of the H_2 system will use the same unit price per kg as the one allocated to the wing.

As the A320-HACK is based on the A320neo, some of the parts stay the same or very similar. This will reduce the development cost for those parts. Markish found a method to take the engineering similarities into account. The reduction factors are as follows: -20% for engineering, -50% for manufacturing and support, lastly, -5% for tool design and fabrication. However, the A320-HACK uses hydrogen, to account for the potentially more complicated designs, it was decided to add the factor to the development cost where the largest changes in the design occur. It is implemented for the wing, because of the use of composites and the integration of the podded hydrogen tanks; and the engines: use of a hybrid fuel system and combustion chamber redesign.

The development cost can be found by multiplying the weights of the different subsystems (see Table 18.1 and Figure 18.1) with the cost per kg (including the reduction/addition factor) found by Markish [124] and then correcting it with the correct inflation factor[1][2] to 2021. The certification cost is also included in the development cost and is 150 million USD[3]. All the development costs are stated in Table 18.2 and the cost distribustion can be found in Figure 18.2.

[1] Inflation: 1 USD in 2002 is equal to 1.5 USD in 2021.

[2] https://www.usinflationcalculator.com/, accessed:20-Jun-2021

[3] https://www.plm.automation.siemens.com/global/pl/our-story/customers/tlg-aerospace/51461/, accessed:25-Jun-2021

Table 18.1: Mass of the different subsystems considered in the cost analysis [kg]

Subsystem	Mass [kg]
Wing	8,235
H_2 system	3,217
Empennage [125]	1,211
Fuselage [125]	6,868
Landing gear [125]	2,790
Engines	6,464
Systems [125]	8,868
Payloads	18,240

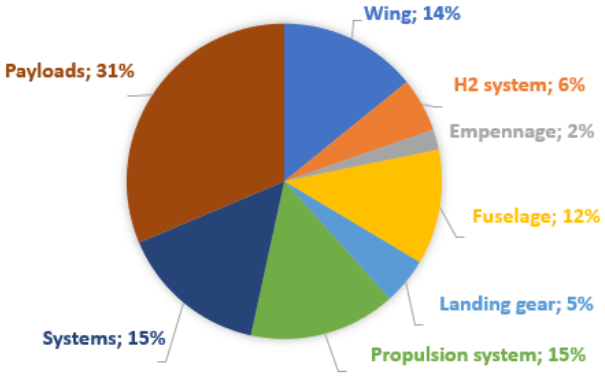

Figure 18.1: Weight distribution of the A320-HACK

Table 18.2: Development cost breakdown [$MUSD$] corrected to 2021 inflation

	Engineering cost [$M\ USD$]	Material and equipment cost [$M\ USD$]	Tool design cost [$M\ USD$]	Tool fabrication cost [$M\ USD$]	Support cost [$M\ USD$]	Total cost [$M\ USD$]
Wing	193.4	54.8	43.8	145.3	25.7	463.0
H2 system	128.9	36.5	29.2	96.8	17.2	308.6
Empennage	66.8	10.4	20.8	69.0	4.9	171.9
Fuselage	233.2	36.4	72.7	241.0	17.1	600.4
Landing gear	7.4	1.2	2.3	7.6	0.5	18.9
Engines	120.8	37.7	27.8	92.0	17.7	296.0
Systems	322.0	50.3	100.4	332.6	23.6	828.9
Payloads	207.7	32.5	64.8	214.7	15.3	535.0
Certification	-	-	-	-	-	150
Total	1,280.2	259.7	361.8	1,199	122	3,372.7

Requirement *UR-COST-01* stated that the development cost shall not exceed 5 billion €. The development cost of the A320-HACK estimated to be about 3.37 billion USD, which equals 2.77 billion €. This is only 55% of the maximum allowed budget for the development cost, thus it complies with requirement *UR-COST-01*.

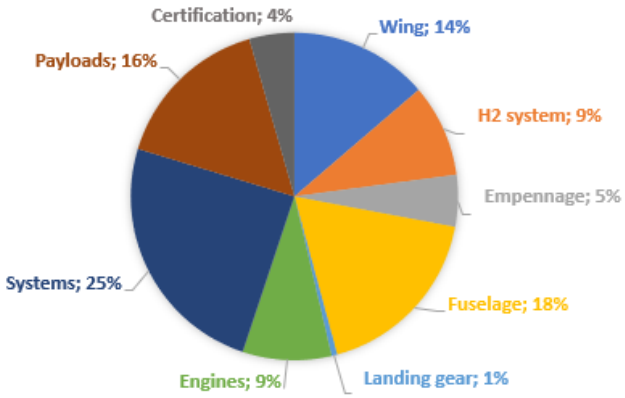

Figure 18.2: Development cost distribution of the A320-HACK

18.2.2 Manufacturing Cost

Requirement *UR-COST-02* states that the manufacturing cost cannot be higher than 15% of the manufacturing cost of the A320-neo. Airbus had a profit margin of 3.29%[4] pre-Covid (Q4 of 2011 - Q3 of 2019). The Covid-19 pandemic has not been taken into account as the profit was very negative (-11.4% in Q3 of 2020), however its profit is increasing again and will recover soon[4].

The A320neo has a list price of 110.6 million *USD* [126], using the previously determined profit margin, one can find that the manufacturing cost of the A320neo should be around 107.4 million *USD*. The requirement stated that the manufacturing cost of the A320-HACK can be 15% higher, resulting in a maximum manufacturing cost of 123.5 million *USD* for the A320-HACK.

The manufacturing cost has been estimated by using Markish method. It consists of three parts: labour, material and other [124]. To account for the use of composites in the wing, the manufacturing costs has been increased by 10%. The engine manufacturing cost has also been increased by 10% to account for the dual fuel system. The final assembly might be more complicated because of the wing mounted tanks above the wing. Therefore, a 3% increase in manufacturing cost has been implemented. The fuel cell and battery costs are added to the list. This was done because a "conventional" aircraft does not use a fuel cell, thus the cost per kg estimated by Markish does not take that into account.

The total manufacturing cost for the A320-HACK can be estimated using the mass per subsystem from Table 18.1 and the cost per kg estimated by Markish [124] scaled to 2021 *USD*. The cost of the engine has been estimated as follows. The list price of the LEAP-1A engine was approximated to be 13.6 million *USD*[5] A 20% profit margin[6] was deducted from the list price, resulting in 10.9 million *USD*.The unit price was found by dividing it by the LEAP-1A engine weight and then adding a 10% increase to account for the hydrogen modification. The manufacturing costs for the subsystems are listed in Table 18.3 and the distribustion is displayed in Figure 18.3.

Table 18.3: Manufacturing cost breakdown [*M USD/kg*] corrected to 2021 inflation [124]

	Labour [*M USD/kg*]	**Material [*M USD/kg*]**	**Other [*M USD/kg*]**	**Total [*M USD/kg*]**
Wing	18.2	6.1	1.8	26.1
H_2 system	6.5	2.2	0.6	9.3
Empennage	5.2	1.6	0.5	7.3
Fuselage	7.6	2.1	0.8	10.5
Landing gear	1.0	0.9	0.1	2.0
Engines	11.5	9.2	7.3	28.0
Systems	7.4	2.1	0.8	10.3
Payloads	14.7	3.6	1.5	19.8
Final assembly	8.2	0.6	0.3	9.1
Fuel cell system	-	-	-	0.02
Total	80.3	28.4	13.7	122.3

[4] https://www.macrotrends.net/stocks/charts/EADSY/airbus-group/profit-margins, accessed:17-Jun-2021

[5] https://www.businesswire.com/news/home/20140713005026/en/American-Airlines-selects-CFM%E2%80%99s-advanced-LEAP-1A-engine-to-power-100-A320neo-aircraft, accessed:08-Jun-2021

[6] https://www.flightglobal.com/engines/ge-aviations-2018-profit-jumps-20-as-leap-production-lifts/131230.article, accessed:22-Jun-2021

The manufacturing cost of the A320-HACK is estimated to be 122.3 million *USD*, which equals 100.3 million €. This is an increase of 14.2% compared to the A320neo, thus requirement *UR-COST-02* is met.

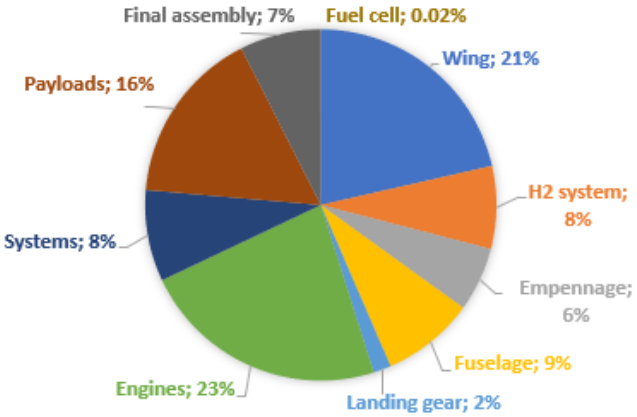

Figure 18.3: Manufacturing cost distribution of the A320-HACK

18.2.3 Total Cost for Manufacturer

The total cost for the manufacturer (Airbus) consists of the development cost of the program (2.77 billion €) and the manufacturing cost of aircraft itself. The manufacturing cost is dependent on the fleet size of the project. The A320's entry into service (EIS) in 1988[7] and in 2015 there were 8600 A320 aircraft ordered. As 2015 is about 30 years after the EIS of the A320, one can assume that the total fleet over 30 years is about 8600 aircraft. Hydrogen is currently a new technology and airlines are not familiar with it. Thus, there is a chance that not all airlines will purchase a hydrogen powered aircraft, resulting in a smaller A320-HACK fleet. The team assumed that the A320-HACK fleet would be only 50% of that of the A320, resulting in 4300 aircraft in 30 years. Therefore, the total manufacturing cost will become 100.3 million € times 4300 aircraft. This equals 431.3 billion €. Combining the development cost and the total manufacturing cost, the A320-HACK project will cost Airbus 434 billion €.

18.2.4 Break-Even Analysis

For the break-even analysis starting in 2035, a net present value analysis was performed, using the following formula where NPV is defined as the net present value, C_0 the initial investment, C the cashflow in the year n, and r the discount rate; the cost of borrowing money.

$$NPV = -C_0 + \frac{C_n}{(1+r)^n} \tag{18.1}$$

Using this method, the present value of the investment was calculated, and the break-even point determined. A discount rate of 6% was used as this is the lower boundary of the range 6-12% which is the average range of discount rates.[8] Taking the lower boundary means that the interest rate on the cost of capital is assumed to be on the lower side for airbus, because of the long history and trust that Airbus established with its financiers. The development cost in the analysis was taken as the initial investment. Then for the yearly cashflows, the following formula was used:

$$CF = (\text{List Price - Manufacturing Cost}) \cdot \#\text{AC sold} \tag{18.2}$$

[7] https://www.aerospace-technology.com/projects/a320/, accessed:18-Jun-2021
[8] https://www.oldschoolvalue.com/investing-strategy/explaining-discount-rates/, accessed:18-Jun-2021

The list price in the years 2035-2039 inclusive is 3.3% higher than the manufacturing cost, as previously mentioned. However starting from 2040, it is assumed that Airbus aims to make a profit of 6% (almost double) as popularity of the program is increased. Assuming that airbus delivers as many aircraft as have been ordered, with none remaining unsold yearly, a starting value of 10 aircraft manufactured per month has been chosen, keeping in mind that both production facilities in Europe and North America will be used. Assuming that in the following year, the number of aircraft produced increases by 5% with respect to the previous year, as the production rate is increased, the break-even point occurs after 848 aircraft have been sold, in 2041. This is visualised in Figure 18.4.

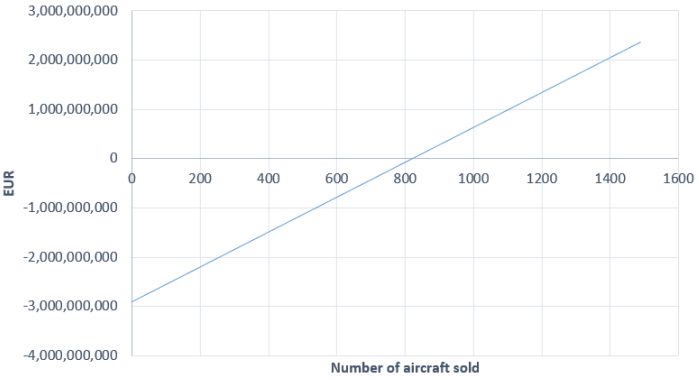

Figure 18.4: Break-Even graph

18.3 Cost for Airline

This section will estimate the costs related to operating an A320-HACK. It consists of the acquisition, operational and disposal costs.

18.3.1 Acquisition Cost

The acquisition cost consists of the manufacturing cost and the profit. The manufacturing cost was previously found to be 100.3 million € and Airbus had a profit of 3.29% (pre-Covid)[4]. Therefore, the acquisition cost will become $100.3 \cdot 103.29\% = 103.6$ million € for one aircraft. Note that the acquisition cost is the same thing as a list price.

18.3.2 Operational cost

Cost per Block Hour

The cost per block hour is the total cost an airline has per hour of flight. It consists of the crew, fuel, aircraft, maintenance, insurance and other costs. The cost per block hour for an A320 operated by an American airline is around 4,360 USD[9]. The A320-HACK will use a mixture of hydrogen and kerosene as propellant, thus the cost per block hour will change.

The price for 1 kg of hydrogen is around 1.5-3.5 USD/kg for blue hydrogen, and between 2.5-10 USD/kg for green hydrogen [127]. Jet-A fuel (kerosene) will cost an airline €0.5/kg[10]. Due to the carbon tax, the Jet-A fuel price will increase. It is estimated to increase by 34.5%[11]. The fuel price per block hour can be estimated as follows, where X is the chosen type of fuel.

$$\text{Fuel cost per block hour} = \frac{\text{Amount of Fuel X} \cdot \text{Price X}}{\text{Hours of flight}} \tag{18.3}$$

The cost per block hour for the airliner can be found in Table 18.4. The last column displays the price difference with respect to the A320neo estimated in 2035.

Table 18.4: Cost per block hour for different types of fuel [USD] forecasted for 2035

Aircraft	Type of fuel	Hydrogen fuel price [USD]	Cost per block hour	Difference wrt. A320neo [%]
A320neo	Kerosene	-	4577	-

[9] https://www.planestats.com/bhsn_2018dec, accessed:17-Jun-2021

[10] https://www.iata.org/en/publications/economics/fuel-monitor/, accessed:25-Jun-2021

[11] https://www.statista.com/statistics/496358/aviation-kerosene-retail-prices-projection-uk/, accessed:25-Jun-2021

A320-HACK	Kerosene + LH_2	1.5	4400	-3.9
	Kerosene + LH_2	2.5	4740	+3.6
	Kerosene + LH_2	3.5	5081	+11.0
	Kerosene + LH_2	10	7296	+59.4

As seen in Table 18.4, the cost per block hour increases by maximum 11% when using blue hydrogen. When using green hydrogen the increase in price starts at 11% and can go up to 59.4%. Therefore, it is suggested to choose blue hydrogen. This increase in the cost is translated to an increase in the ticket price.

Example Mission Cost

A flight from Amsterdam (AMS) to Rome (FCO), will take about two hours of flight, thus resulting in two block hours. Assuming the airline selects to use blue hydrogen at a price of 2.5 USD/kg, the operating cost will be $2.5 \cdot 4740 = 9498$ USD or €7774.

Total Operational Costs

An aircraft has an average life time of 30 years and a total of 135,000-165,000 flight hours[12]. This analysis will consider a life time of 30 years and 140,000 flight hours. The operational cost of the A320-HACK is equal to the cost per block hour times the flight hours. The total operational cost is estimated to be between 616 million USD (505 million €) and 711 million USD (583 million €) per aircraft for 30 years of operation.

If an airline would have 10 A320-HACKs using blue hydrogen (2.5 USD/kg), then the total operational cost would be $10 \cdot 4740 \cdot 140,000 = 6.64$ billion USD or 5.44 billion €.

18.3.3 Disposal Cost

The disposal cost is 10% of the acquisitions cost [128] or 1% of the Life Cycle Cost (LCC) [129]. For this analysis, the 10% of the acquisitions cost will be used. The disposal cost of one A320-HACK will be equal to 10.4 million €.

For an airline with 10 A320-HACKs, the disposal cost will be equal to 103.6 million € or the acquisitions cost of one extra A320-HACK.

18.3.4 Total Cost for Airlines

The total cost for the airline exists of the acquisition, operational and disposal costs, as stated in Equation 18.4.

$$C_{total_{airline}} = (C_{acq} + C_{ops} + C_{disp}) \cdot \#\text{ A320-HACKs} \tag{18.4}$$

Assuming an airline operates 10 A320-HACKs using blue hydrogen at 2 USD/kg, then the total cost will become equal to $10 \cdot (103.6 + 6.6 + 0.1 \cdot 103.6) \cdot 10^6 = 6.58$ billion €.

18.4 Cost for Airport

As mentioned in Section 17.4, for the Rotterdam airport case study, LH_2 will be outsourced and delivered to the airport via tanker trucks. The average cost of point-to-point (plant to airport) delivery cost is estimated to be around 0.35 $ per kg of LH_2 for distances lower than 50 $[km]$.[130]

Thus, with a yearly LH_2 requirement of €15,600 in 2035, the point-to-point delivery cost of LH_2 is 387,600$. The storage station costs are estimated to be around 0.28 $ per kg for a LH_2 station with a capacity of 3000 kg/day, which is the storage amount estimated in 2035. The larger the station capacity although the slightly larger land area required, the hydrogen dispensed is significantly higher, thus offering a lower cost per kg of LH_2 stored. (For reference, for a station with a 500 kg/day storage capacity, the cost is 0.70 $ per kg) [130]. The storage costs per day in 2035 for the Rotterdam airport then amount to 841 $ per day, and annually, this would result in around 307,000 $. Thus, as a rough estimate, the

[12] https://www.flexport.com/blog/decommissioned-planes-salvage-value/, accessed:18-Jun-2021

cost for the Rotterdam airport in the year 2035, should be around 687,000 $, which is around € 577,000. Now, the airport can deduct some of these costs because of the reduced CO_2 emissions due to the HACK system of the A320-HACK, and the use of only the DPU for the taxiing procedures. For every tonne of CO_2 that an airport reduces, it receives one 'credit' as a proof of this reduction and it is equal to € 50[13].

Seeing as the A320-HACK has a reduction of around 2 tonnes of CO_2 per flight, as shown in Table 16.8, it would receive € 100 per A320-HACK take-off or landing.Thus with an average of 17 flights per day taking off or landing from the Rotterdam airport with the A320-HACK, the airport could break-even on its LH_2 storage cost of 841 $ per day, every day. This is a start to reducing its increased annual cost.

19 | RAMS Characteristics

The RAMS characteristics study is the analysis of the Reliability, Availability, Maintainability and Safety of the A320-HACK. Since the new aircraft is derived from the A320neo, this chapter will mainly focus on the impact of newly developed and redesigned subsystems on the RAMS of the product.

19.1 Reliability

Reliability can be defined as the probability that a system will operate as intended for a given time frame. In more quantitative terms, it can be defined by Equation 19.1 (where T_{tot} is the total evaluation period and M_{repair} the downtime period for corrective maintenance) and Equation 19.2 (where λ is the failure rate and t the time).

$$\text{Re} = \frac{T_{\text{total}} - M_{\text{repair}}}{T_{\text{total}}} \qquad (19.1) \qquad\qquad \text{Re}(t) = e^{-\lambda t} \qquad (19.2)$$

Reliability of an articulated system is determined by the reliability of its single subsystems, plus by their complexity as well as their arrangement. Systems (or elements of a single system) can be indeed designed to be either in series or in parallel; in the former case, a single element failure causes the entire system to fail, while in the latter the entire system fails only if all the components fail. Parallel systems are therefore preferable to enhance reliability, and this aspect was taken into account during the design phase. Therefore, multiple level of redundancy were implemented for certain systems of the A320-HACK.

For example, to make up for an eventual DPU failure, each engine is equipped with a generator, thus achieving a triple redundancy. Regarding the hydrogen fueling system - aside from the double tank configuration - each tank is equipped with two boost pumps, plus two additional pumps are placed in the centre to supply the DPU and eventually transfer LH_2 between the two tanks; therefore, a two level redundancy has been implemented for the hydrogen feeding system. All these systems have never been developed for an aircraft before, therefore it is difficult to quantify their failure rate and thus their reliability at this stage of the project.

Furthermore, several systems which are currently hydraulics in the A320neo will be electrified in the A320-HACK. This will also have an advantage in terms of reliability, given that such systems are less prone to failure compared to their hydraulics counterparts as the mechanical complexity is reduced. Plus, also in this case an appropriate level of redundancy was implemented.

Overall, the reliability of the new components and especially the hydrogen related ones, need to be further investigated, as implementations of such systems - and thus testing - are still at a rather low readiness level or even not yet existing for aviation applications specifically. Albeit, there are some existing studies and estimations for failure of hydrogen system components (such as cryogenic valves and sub-components) adopted in different applications [131]. In any case, in order to meet the high industry standard in terms of reliability efforts need to be spent into R&D of these components before the aircraft's launch in 2035.

[13] https://www.cleanenergywire.org/news/study-finds-co2-price-50-euros-tonne-would-be-socially-balanced-germany, accessed:28-Jun-2021

19.2 Maintainability

An appropriate way to analyse the maintainability of this aircraft redesign will be to identify the key changes to the subsystems and the topology and then explore ways to rate the maintainability of the A320-HACK in terms of the industry standard line maintenance checks that are classified into four main categories, ranging from A-D, based on the frequency and the complexities of the tasks involved as seen in Table 19.1.

Table 19.1: Maintenance check intervals for A320

A check [Flight hours]	**B check**	**C check** [Flight hours]	**D check** [months]
60	n/a	6000	72

19.2.1 Hydrogen Distribution Architecture

Whilst it true that the addition of the on-board LH_2 storage and distribution systems will increases the frequency and the costs of maintenance. The modular nature of the LH_2 tanks makes will, however, make the maintenance easier and reduce downtime. The additional maintenance costs is not expected to be more than 6% [83].

19.2.2 Electrification

Besides the improved efficiency, the electric actuators also offer increased reliability which reduces the need for extensive preventive and regular maintenance schedules. When the electronics are installed within, these actuators also act as standalone components and reduce dependencies on other components and lowers maintenance costs[1]. Therefore, having these electric systems replace the hydraulic systems in the landing gear actuation, elevators and the rudder of the aircraft will contribute to the ease and reduced costs of the maintenance. It was evident that the reductions in maintenance checks of up to 66% can be achieved through widescale electrification of the aircraft architecture[1].

19.2.3 Introduction of DPU

Due to the absence of moving parts, the fuel cell centred Dedicated Power Unit (DPU) will need to undergo a significantly reduced maintenance. The airliners operating the aircraft would not benefit from reduced maintenance costs but arguably an even greater downtime costs, as discussed in [132]. In contrast, however, these systems are susceptible to degradation from high voltage [133]. This means that they may need to be replaced faster and this could attribute to a slight increase in maintenance and downtime costs that need to be investigated further.

19.2.4 Detection Procedures

The first step in the maintenance procedure is determining the state of subsystems. Non-destructive testing procedures need to be laid down in order to identify possible faults that require technical assistance. For the storage tanks, some of the possible measurements are the pressure inside the vessel, the temperature in the vacuum jacket and the relative humidity in the venting stacks. These measurements could outline a possible fuel leakage or degradation of the insulation. Leaks or degradation of the motor at the level of the cryogenic tanks can be identified by measuring the discharge temperatures, the flow rates, the consumption and the vibrations [134].

19.3 Availability

As operators are generating revenue from the availability of the aircraft, it is important to assure it is on a similar level to the A320neo. First, the availability represents the percentage of aircraft's lifetime when it is usable, and can be defined by the Equation 19.3 [2] with T_{total} - the total amount of time the aircraft

[1] https://www.boeing.com/commercial/aeromagazine/articles/qtr_4_06/AERO_Q406_article4.pdf, accessed:18-Jun-2021

[2] https://www.tebodin.bilfinger.com/fileadmin/tebodin/Area_Middle_East/Articles/Services_-_RAM_study.pdf, accessed:18-Jun-2021

could be used, and $M_{preventive}$ and M_{repair} being the time used for preventive maintenance and repair activities. Important to note that this characteristic is closely related to the reliability of the product and its subcomponents.

$$Av = \frac{T_{total} - M_{preventive} - M_{repair}}{T_{total}} \tag{19.3}$$

19.3.1 Hydrogen Storage System

The new hydrogen tanks and related components are extra pieces that will need to be checked, hence slightly increasing the maintenance time ($M_{preventive}$) during regular checks. However, in case of damage, these will not impact availability greatly as these components are not integral to the airframe and are easily accessible. Therefore, the tanks and other pieces can be replaced by other parts while being repaired.

19.3.2 Electrification and DPU

As was stated previously in Section 19.2, the replacement of hydraulic subsystems by electric ones results in an overall reduced maintenance time, and therefore positively contributes to the availability of the airplane. Similarly, as the APU replacement by DPU results in shorter maintenance, it will lower the time dedicated for regular checks, beneficial for availability. The replacement of DPU due to degradation could potentially occur during the C and D-type checks, when the airplane is partially disassembled.

19.3.3 Hydrogen Fuel Supply

In the early stages, there may be cases when the hydrogen fuel is not available at a given airport. This should not be of great concern to the overall availability of the airplane as it can still can be operate to 2/3 of its potential using kerosene, and will impact availability only in case of long-range missions. As for the DPU being inoperative, the electricity on-board could still be provided by the engines. The likelihood of hydrogen unavailability will decrease with time.

19.4 Safety

Safety is determined by all the factors that protect the equipment and people in case of an incident. The safety of the A320-HACK will be discussed for the subsystems which are modified with respect to the A320neo.

19.4.1 On-board Hydrogen System Safety

The on-board hydrogen system consists out of the cryogenic tanks and feeding systems. For the cryogenic tanks, multiple design choices were made having safety in mind.

The location of the tanks allows for distance between the passengers and the tanks. Even though a fire is not ignited, hydrogen leaks can lead to respiratory issues such as asphyxiation. Thus, it is essential to keep the tanks isolated from the passengers.

Tank puncture can occur when sharp objects hit the tanks, leading to an immediate failure of the tank. For the A320-HACK, such objects can be debris from the engine charged with extremely high energies as described in Section 9.2.7. The current design mitigated any possible failure caused by the engine debris by placing the tanks more aft. Due to the external position of the tanks, the CS25.631 requirement referring to bird strike impact was also accounted for. The fairing of the tanks were designed to absorb the bird impact without any damage, thus protecting the tanks.

Tank ruptures can be caused by tank leaks. Due to the low boil-off temperature of the hydrogen and the high temperature difference between the inside of the tank and the outside environment, liquid hydrogen will quickly expand as it leaves the tank, possibly leading to a rupture of the tank. Two scenarios are possible [31]. In case the hydrogen is not ignited, the spilled fuel will become gaseous and spread rapidly within the atmosphere. If the hydrogen is ignited, it will burn on the surface of the wing. Thus, it is necessary to design a wing that would not collapse under the generated heat. However, the burning time of hydrogen is extremely brief compared to other fuels [31]. It is necessary to determine if the ignition of kerosene or the ignition hydrogen will lead to the most critical thermal shock on the wing and design for that case. For safety precautions, the tank will be equipped with a leakage detection system.

In case a leak is discovered, the tank shall be vented as soon as possible and the aircraft shall land at the nearest location. Additionally, regular checks need to be performed on the tanks in order to address any present cracks that could lead to a rupture scenario.

The insulation system was designed to ensure the cryogenic storage of the hydrogen for 36 h as dictated by UR-SR-01. Thus, if the insulation is in a good state, no boil-off should occur during the duration of the mission. If the MLI insulation is damaged in any way, for example if the vacuum jacket is lost, gaseous hydrogen will start to rapidly build-up in the tank, leading to an increase in pressure. If the pressure increases too much, the tank will burst. As a safety measure, the tank is equipped with a pressure sensor, a rupture disk and a venting valve. In case the pressure increases, reaching p_{vent}, the venting procedure will begin, thus reducing the pressure in the tank.

Besides the hydrogen storage system, the feeding system safety also needs to be considered. Leaks are prone to happen at seals and fittings such as valves for example. These critical locations in the fuel paths must be equipped with leakage detectors. In case of a leakage detected along the feeding system, the hydrogen supply from the tank must be interrupted at once.

19.4.2 Hydrogen Refuelling Safety

The cryogenic temperatures of liquid hydrogen have as consequence that if any substances are trapped in, they will solidify. These solid bits can then plug the tank outlet. Additionally, if any air gets in when the vacuum seal is broken down, the hydrogen might ignite in the tank or along the refuelling system. In order to prevent this, the hydrogen system needs to be purged. In addition, the oxygen and the water vapour trapped at the exposed inlet of the refuelling adapters pose a grave danger if they were to enter the tank where large concentrations of hydrogen is present, it would result in a highly flammable concoction of gases. To prevent this, therefore, the connection between the refuelling tanker's hose outlet and the aircraft's fuelling adapter must be evacuated and purged before any fuel is pumped. Installation of appropriate sensors to detect the concentration of air, water vapour and oxygen together with adequate crew training protocols will contribute to the improvement of safety during this operational procedure.

19.4.3 DPU Safety

One of the main issues that can occur with fuel cells is clogging due to air impurities, which can reduce the efficiency of the fuel cell. In order to prevent this, multiple air filters need to be installed along the air intake path [3]. Specifically, for the selected PEMFC, the purity of the intake hydrogen also needs to be considered for the same efficiency purposes [135]. Thus, a filtering system to separate the hydrogen from common impurities such as carbon monoxide, hydrogen sulphide and ammonia.

The DPU is responsible for providing the electrical power required by the aircraft. As discussed in Section 20.1, the A320-HACK will have the cabin pressurisation, along with primary control surfaces such as the rudder or the elevator electrified. If these systems become non-functional due to lack of electrical power, extreme safety hazards can occur. As a safety measure, in case the DPU is unavailable for any reason, the main engines will provide the required power.

20 | A320-HACK System Diagrams

After the design of subsystems of the A320-HACK, the functioning of the whole system needs to be investigated. This chapter offers an overview on the subsystem relations within the aircraft. The power distribution system is discussed in Section 20.1. Section 20.2 offers an overview of other systems of the A320-HACK through a hydraulics diagram, data handling diagram and hardware-software diagrams.

[3] https://www.freudenberg-filter.com/en/world-of-automotive/products/fuel-cell-solutions/, accessed:18-Jun-2021

20.1 Electrical System

Before the electric block diagram of the aircraft is presented, differences in the electrification degree between A320neo and A320-HACK are mentioned. In an attempt to reduce the mechanical complexity of the A320-HACK and reduce engine bleed-air required for various systems which reduce the efficiency of the engine, several systems of the A320neo were electrified. The brakes, landing gear, nose steering, rudder and elevator are electrically actuated on A320-HACK. Electrically actuated brakes eliminate delays in braking due to leaking brake hydraulic fluid, and also reduces the aircraft weight. (The B787-8 saves 64kg compared to the B777 because of the electric brakes[1]). The E-rudder concept set to be delivered by Airbus in 2024 will be implemented which will "replace spoiler-elevator computers, yaw-damper, and rudder-trim actuators, and travel limiter unit) and install a new rudder-pedal unit in the cockpit, new rudder-position sensors, and back-up control module".[2] Additional features powered by electricity are electrically heated blankets on the leading edge of the wing, and inlet of the engine, referred to as the Ice Protection System (ICS), and electro-chromatic dimmable windows. Finally, the cabin pressurization system of the A320-HACK doesn't rely on engine bleed-air as the A320neo, but rather on a compressor driven by the air outside the aircraft coming in through an inlet.[3] The air pressurized by this system is also used for the fuel cell operation as previously described, and the system as a whole, referred to the Environmental Control System (ECS).

The power required for these systems is shown in Table 20.1. These values have been estimated by taking as a baseline, the power required values from a study regarding electrification of the A320neo. Additional power is required for the ice control system which was not included in the study, but can be seen in the table [136].

Table 20.1: Total power required for the A320-HACK

Phase	Taxi-out	Take-off	Climb	Cruise	Descent	Landing	Taxi-in
Power Required Baseline[kW]	206	101	235	282	245	107	206
Ice Control System Power Required [kW]	5	5	30	60	30	5	5
Total Power Required [kW]	211	106	265	342	275	112	211

Thus, the two integrated drive generators (IDGs) rated at 90kVa of the A320neo, no longer deliver sufficient power for the A320-HACK, as the total power required in cruise is around 342 [kW]. It has been chosen to replace these with two variable starter frequency generators (VSFGs) rated at 200 kVa. VSFGs have an efficiency at the output of generator of 53% when compared to the 34% of the IDGs[137]. To note again, the engine generators will provide the backup power, as the dedicated power unit is the main source of power. Although the power per generator is around twice of the original generators, the power density in the year 2035 is estimated to be double compared to that in 2020, thus there should be no weight increase due to the different generators [138]. An overview of the electrical system is now presented, where the colours of the elements have no meaning:

[1] https://thepointsguy.com/guide/6-features-that-set-the-787-dreamliner-apart-from-the-rest/, accessed:10-Jun-2021

[2] https://www.flightglobal.com/air-transport/airbus-switching-a320neo-family-from-mechanical-to-electronic-rudder-control/143203.article, accessed:10-Jun-2021

[3] https://www.boeing.com/commercial/aeromagazine/articles/qtr_4_07/article_02_2.html, accessed:10-Jun-2021

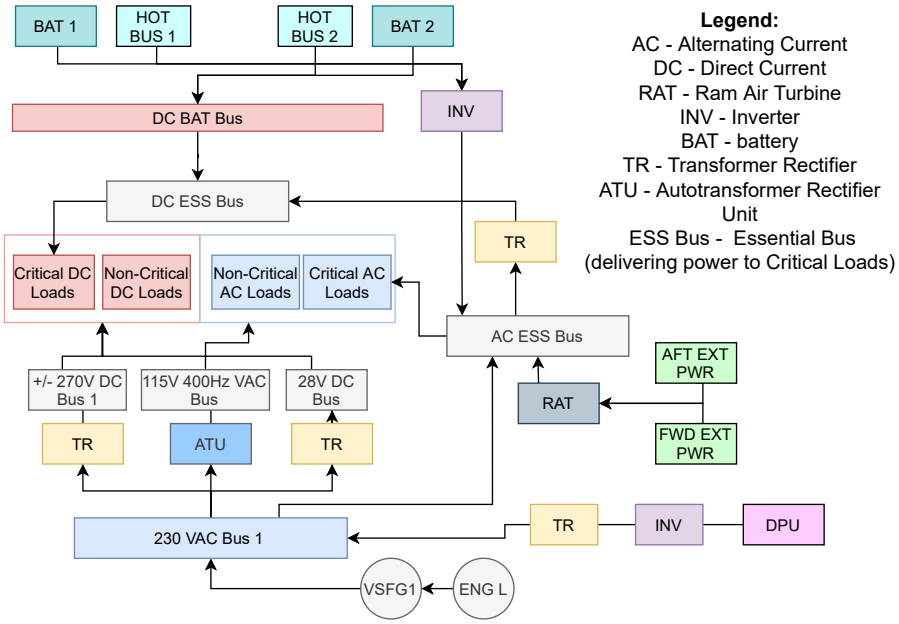

Figure 20.1: A320-HACK electrical diagram

20.2 Handling Systems

The hardware and software block diagrams, as shown in Figure 20.3 and Figure 20.2, illustrate the relations between the components of the aircraft, and the flow of information. Only the specific interfaces of the A320-HACK are included in these diagrams.

In Figure 20.5, the hydraulics diagram adapted from the A320neo diagram is shown[4]. The hand pump has been removed, as the cargo door will now be electrically actuated, and an electric pump in the green line is added for the systems in the green box.

The data handling diagram, as illustrated in Figure 20.4 offers a visual overview of the flow of data within the A320-HACK system.

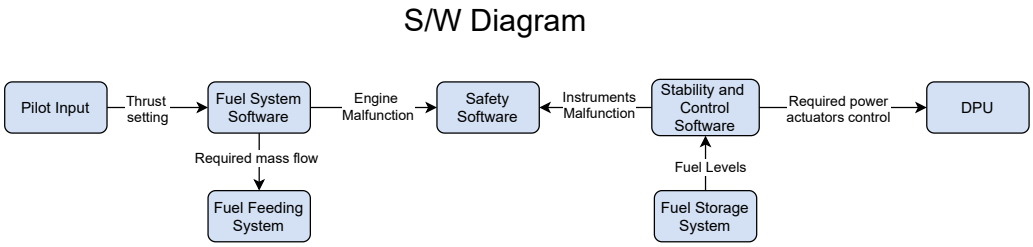

Figure 20.2: A320-HACK software diagram

[4] https://safetyfirst.airbus.com/app/themes/mh_newsdesk/pdf/safety_first_04.pdf, accessed:08-Jun-2021

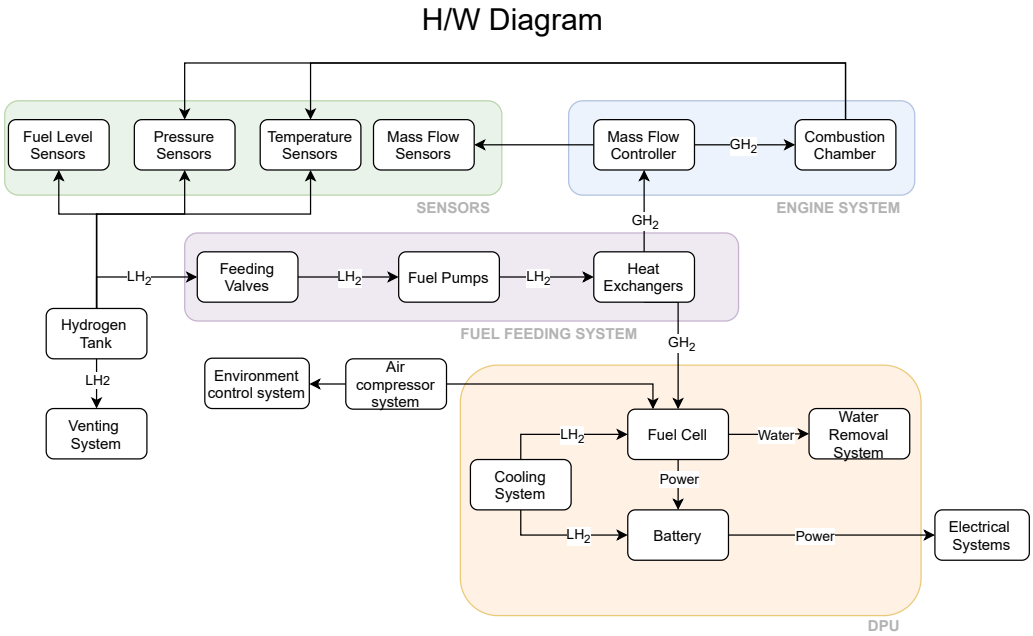

Figure 20.3: A320-HACK hardware diagram

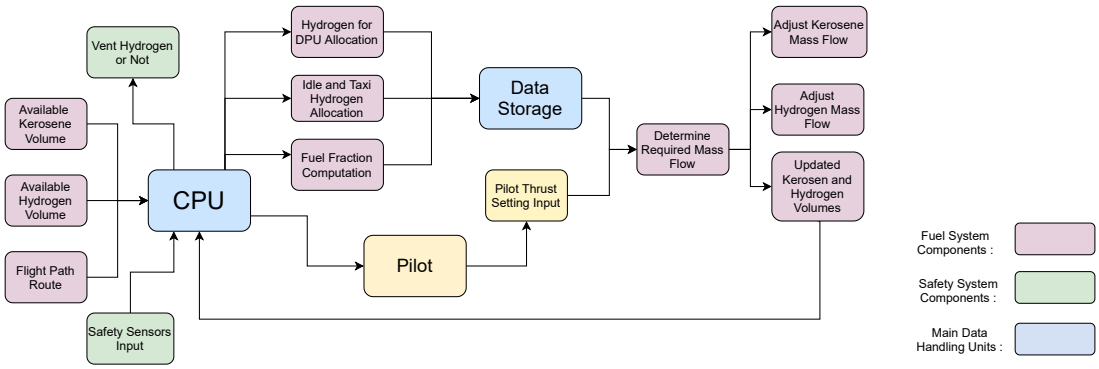

Figure 20.4: A320-HACK Data Handling Diagram

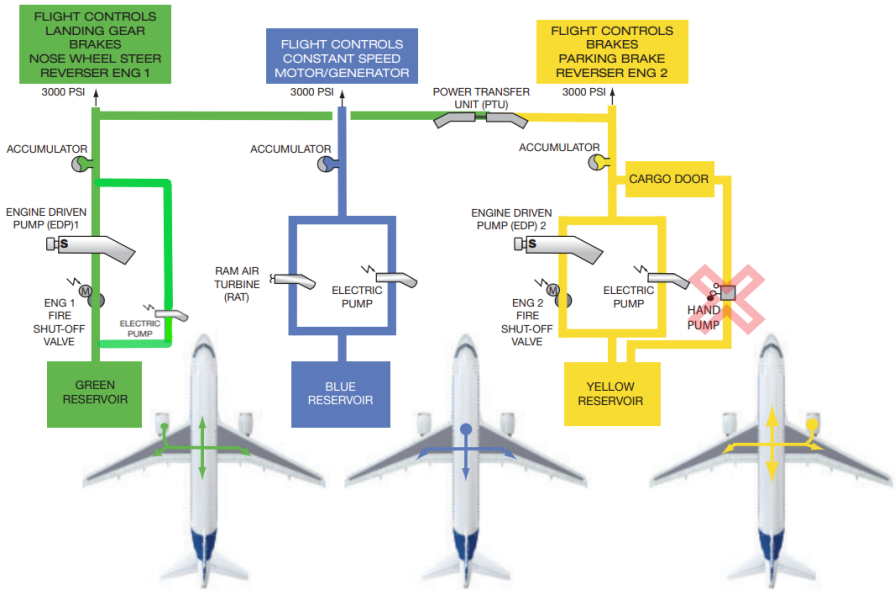

Figure 20.5: A320-HACK hydraulics diagram

21 | Project Development

Looking ahead, it is important to define and plan all the tasks and steps that will be pursued after the end of DSE. This chapter looks into the next phases of the A320-HACK project. Section 21.1 evaluates when the technology readiness level of the novel systems included in the A320-HACK design. Section 21.2 presents the manufacturing processes for key parts, while Section 21.3 offers a timeline of the post-DSE phases of the project.

21.1 TRL Roadmap

For the following technologies present on the A320-HACK, the Technology Readiness Level is determined, and presented in Table 21.1. A description of the levels can be found in Figure 21.1 and the number of years for the technology to reach maturity in Figure 21.2 [1]

Table 21.1: TRL Levels [139]

Technology	TRL	Years to reach maturity
DPU	2	15
Hydrogen Assisted Combustion of Kerosene (HACK)	2	15
Ultra High BPR ($\geq$ 15)[2]	5	7
LH2 Storage Tank [3]	5	11
Aluminium vacuum shell MLI [139]	6	11
Cabin Air Compressor System	9	0
E-rudder	7	5
Lean Direct Injection (LDI)	2	15
Primary Structure of Carbon Fiber Reinforced Thermoplastic	7	10

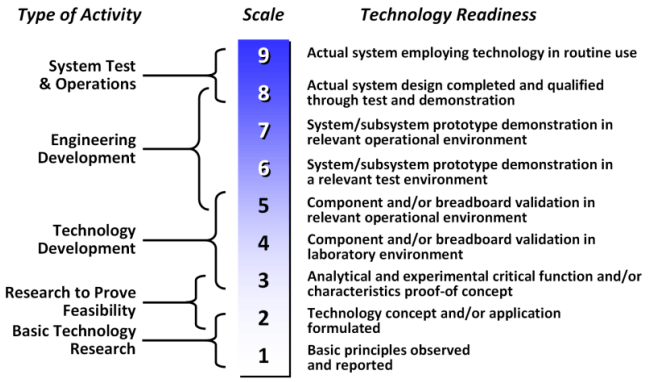

Figure 21.1: TRL description

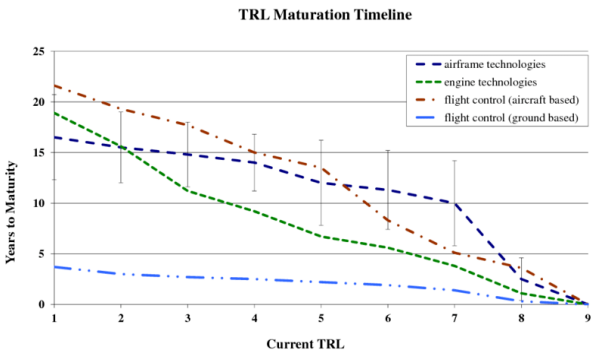

Figure 21.2: TRL vs years to maturity [140]

The LDI and DPU technologies are still at the phase where only research has been performed to demon-

[1] https://www.spacefaringamerica.com/?p=29, accessed:17-Jun-2021

[2] https://www.iata.org/en/programs/environment/technology-roadmap/, accessed:17-Jun-2021

[3] https://www.pnnl.gov/main/publications/external/technical_reports/PNNL-21473.pdf, accessed:17-Jun-2021

strate its feasibility, thus receiving a TRL of 2. Also, the HACK technology received a TRL of 2, as this technology is only currently being researched. Looking at Figure 21.2 it can be seen that for engine technologies with a TRL of 2, 15 years are allocated to reach maturity (the A320-HACK is scheduled for EIS in 2035, thus these technologies can be implemented). The cabin air compressor system has a TRL of 9 since this is already in used on the B787 dreamliner, and requires no further maturity.[4] For the E-rudder and other electrified flight controls, a TRL of 7 was given, as the E-rudder system is set to be launched in 2024, and a conservative estimate of 5 years for the technology to mature, corresponds to a TRL of 7. A primary structures using carbon fiber reinforced thermoplastic (CFRTP) is being investigated by many parties, and was already being incentivized by Airbus in 2009 [5]. At the moment, the ENLIGHTEN project has been launched to industrialize the technology [6]. Furthermore, NLR's project STUNNING is also looking into further developing this technology [7]. For these reasons, CFRTP structures are given a TRL of 7.

21.2 Production Plan

The production of the A320-HACK needs to change considerably from that of A320neo in some subsystems. Therefore, the manufacturing procedures used to manufacture the modified parts are presented. The wingbox structure is produced using an automated tape laying technique (Section 21.2.1), the cryogenic tank is produced using welding techniques (Section 21.2.2), and the manufacturing of other parts is explained in Section 21.2.3. The assembly of the A320-HACK is presented in Section 21.2.4.

21.2.1 Manufacturing of the Wingbox

The wingbox is manufactured from carbon fiber reinforced thermoplastic, and therefore a new manufacturing technique needs to be adopted. The trend to use thermoplastic materials is partly motivated by their capability to be processed in-situ. This means that as the thermoplastic tape (a prepreg) is being placed, it is also being heated and consolidated against the surface of the part, hence no post-processing is required. This material property is being exploited by Coriolis, as they are producing multiple robotic arms capable of creating complex parts by adding layers of thermoplastic composite [8]. Also, NLR's STUNNING project has recently produced the largest single thermoplastic piece ever made (a fuselage panel) as part of an EU project[9], confirming the efforts to certify large thermoplastic parts.

This automated technology, which reduces manufacturing time and cost compared to autoclaved parts, has already been investigated for the production of a wingbox by Oliveri et al. [141]. Based on the work from this paper, a manufacturing process for the wingbox was set up and is presented in Figure 21.3.

21.2.2 Manufacturing of the Cryogenic Tanks

The cryogenic tanks, due to their size, cannot be made out of one aluminium piece. The main technique is to stir-weld the caps to the cylindrical body after they have been formed from aluminium sheets. The process is described in detail in Figure 21.4.

21.2.3 Recommended Manufacturing Techniques

The manufacturing process applied to other parts is not given in such detail due to the time limitations from this project. Nevertheless, it is interesting to consider that some part could also used advanced manufacturing processes as presented in Section 21.2.1:

[4] https://www.boeing.com/commercial/aeromagazine/articles/qtr_4_07/article_02_2.html, accessed:17-Jun-2021

[5] https://www.toraytac.com/media/eb39bfaf-d733-4f08-a73e-8eef5b3034f9/aUWLgQ/TAC/Documents/Articles/Toray_CW_TAPAS-2.pdf, accessed:23-Jun-2021

[6] https://www.compositesworld.com/news/enlighten-program-launched-to-speed-thermoplastic-composites-industrialization, accessed:23-Jun-2021

[7] https://www.nlr.org/news/nlrs-stunning-project-departs-for-next-generation-composite-planes/, accessed:22-Jun-2021

[8] https://www.coriolis-composites.com/fiber-placement-machines/, accessed:22-Jun-2021

[9] https://www.nlr.org/news/nlrs-stunning-project-departs-for-next-generation-composite-planes/, accessed:22-Jun-2021

The fuselage panels can also be manufactured using automated tape laying processes [10], increasing the overall use of recyclable thermoplastic composites. The best scenario would be to overtake the structural efficiency of the newest A350 [11]. Frames and other stiffening elements such as ribs, longerons and stringers could be optimized by using a large proportion of unidirectional fibers which are also placed via automated processes [12]. The production of engines is left to other companies specialized in the field.

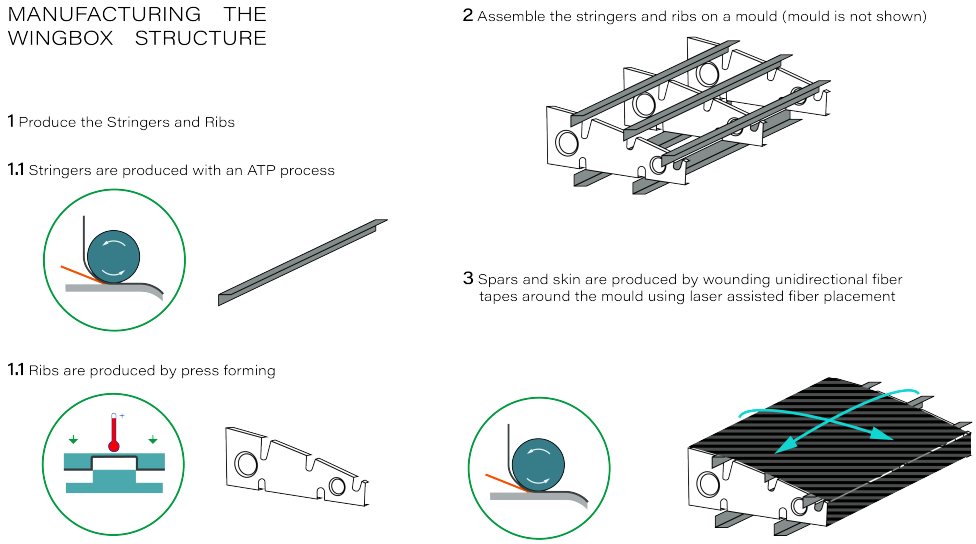

Figure 21.3: Wingbox production using automated tape laying of thermoplastics

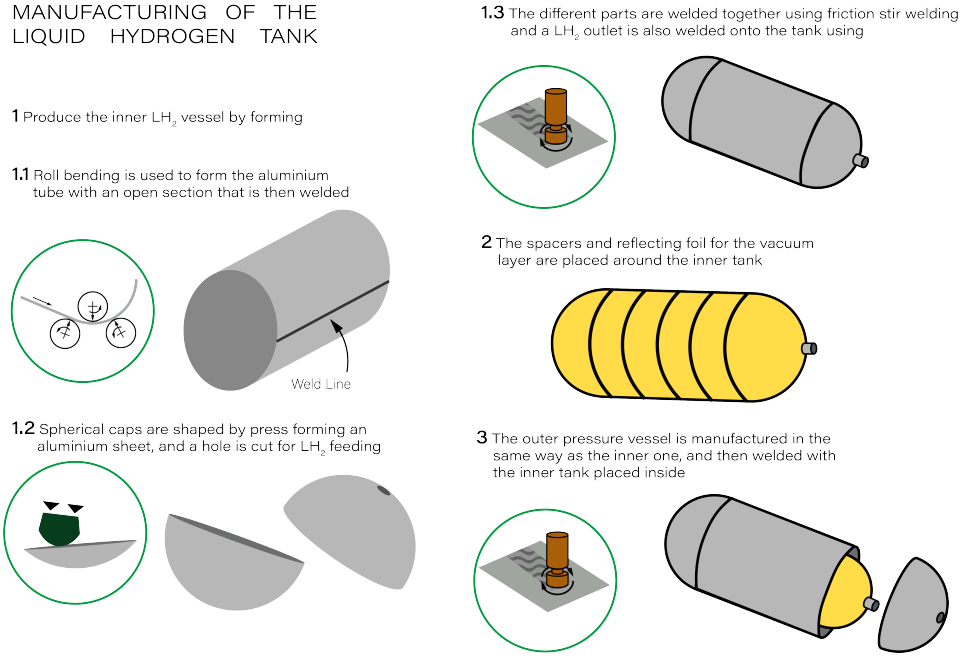

Figure 21.4: Hydrogen tank production

21.2.4 A320-HACK Assembly

The assembly plan is presented in Figure 21.5. It shows how the main steps in the process follow each other, without specifying the associated time or assembly technique. Since the material of the wingbox has changed completely, the assembly of this part to the fuselage is considered. In the case that thermoplastic is also used for the centre wingbox and fuselage, the welding of the wing onto the centre

[10] https://www.coriolis-composites.com/industries/aerospace/large-complex-parts/, accessed:22-Jun-2021
[11] https://www.airbus.com/aircraft/passenger-aircraft/a350xwb-family.html, accessed:22-Jun-2021
[12] https://www.coriolis-composites.com/industries/aerospace/complex-frames-structures/, accessed:22-Jun-2021

fuselage is considered to be the optimal alternative [142]. This decreases the amount of rivets and bolts used in the aircraft, reducing the structural weight. In the case that only the wing is using composites, the preferred technique is the use of rivets and bolts.

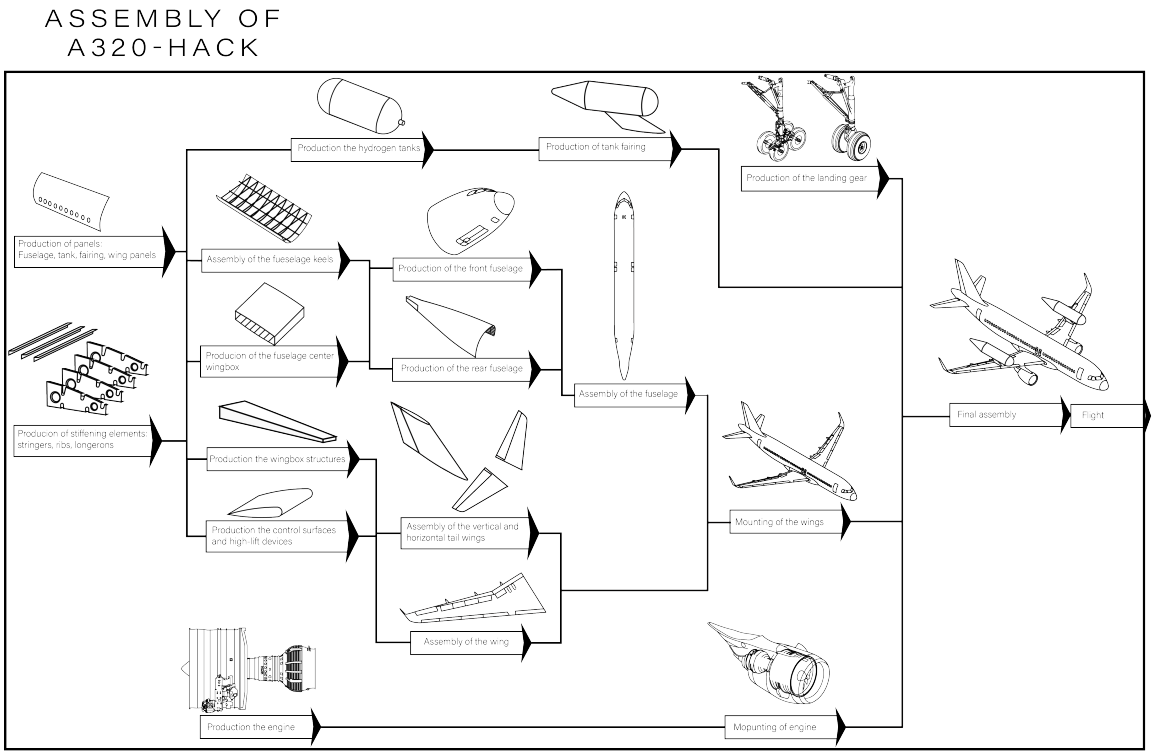

Figure 21.5: Assembly plan of the A32-HACK

21.3 Project Development Plan

The project design & development Logic, depicted in Figure 21.6, presents the general milestones that will occur after the DSE phase, while the project Gantt chart, shown in Figure 21.7, expands on them and adds a preliminary timeline to the post-DSE activities.

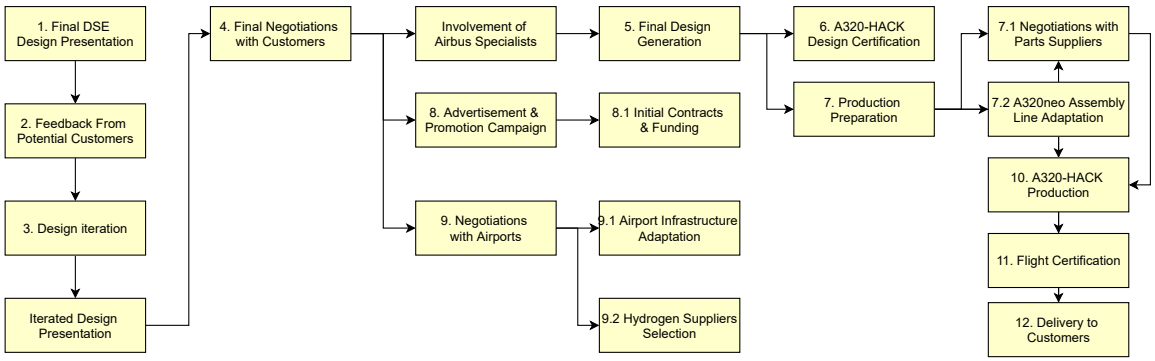

Figure 21.6: Project Design & Development Logic Diagram

As presented in Figure 21.7, the post-DSE phase of the project begins with the Final Design Presentation. The main tasks that follow are related to finalizing the design, certification and production. For 2021, monthly divisions were used as the activities can be more accurately predicted and last less time. For the rest of the timeline, trimestrial and semestrial time divisions were used as later activities have a longer duration.

First, the A320-HACK design needs to be further developed and certified. Aspects such as structure and aerodynamics of new tanks, engine redesign will have to be further investigated, along with all the other subsystems. Stability and flight dynamics changes due to the new tanks and weight shifts also need to

	Phase	Start Date	End Date	Duration	2021	2022	2023	2024	2025	2026	2027
					June July Aug. Sep. Oct. Nov. Dec.		Jan-June July-Set Oct-Dec		Jan-June July-Dec	Jan-June July-Dec	Jan-June July-Dec
1	Final DSE Design Presentation	30/Jun	01/Jul	2 days	* *						
2	Acquiring Feedback From Potential Customers	02/Jul	03/Jul	2 days	*						
3	Design Iteration	04/Jul	Sep/21	2 months							
4	Negotiating Final Design with Customers	Sep/21	Oct/21	1 month							
5	Generation of the Final Design	Oct/21	Oct/23	2 years							
6	Design Certification	Nov/23	May/25	1.5 years							
7	Production Preparation	Jan/22	Jul/26	4.5 years							
7.1	Negotations with Manufacturing Suppliers	Jan/22	Jul/26	4.5 years							
7.2	A320neo Production Line Adaptation	Jan/23	Jul/25	2.5 years							
7.3	A320neo Assembly Line Adaptation	Jan/24	Jul/26	2.5 years							
8	Advertisment and Promotional Campaign	Jun/25	Jan/35	10 years							
8.1	Initiate Contracts and Funding	Jun/25	Dec/25	7 months							
9	Negotiations with airports	Jan/27	Dec/28	2 years							
9.1	Airport Infrastructure Adaptation	Jan/27	Dec/28	2 years							
9.2	Selecting Hydrogen suppliers	Jan/27	Dec/28	2 years							
9.2.1	Negotiations with Hydrogen Suppliers	Jan/27	Dec/27	1 year							
9.2.2	Establish supply chain	Jan/28	Dec/28	1 year							
10	A320-HACK Production & Assembly	Jan/25	Dec/31	7 years							
11	Flight Certification	Jan/32	Dec/34	3 years							
11.1	Compliance Demonstration	Jan/32	Jun/34	2.5 years							
11.2	Technical Closure and Issue of Approval	Jun/34	Dec/34	6 months							
12	First Delivery to the Customer	Jan/35	Jan/35	-							

(a) Years 2021 to 2027

	Phase	Start Date	End Date	Duration	2028	2029	2030	2031	2032	2033	2034	2035
											Jan-June July-Dec	Jan-June July-Dec
1	Final DSE Design Presentation	30/Jun	01/Jul	2 days								
2	Acquiring Feedback From Potential Customers	02/Jul	03/Jul	2 days								
3	Design Iteration	04/Jul	Sep/21	2 months								
4	Negotiating Final Design with Customers	Sep/21	Oct/21	1 month								
5	Generation of the Final Design	Oct/21	Oct/23	2 years								
6	Design Certification	Nov/23	May/25	1.5 years								
7	Production Preparation	Jan/22	Jul/26	4.5 years								
7.1	Negotations with Manufacturing Suppliers	Jan/22	Jul/26	4.5 years								
7.2	A320neo Production Line Adaptation	Jan/23	Jul/25	2.5 years								
7.3	A320neo Assembly Line Adaptation	Jan/24	Jul/26	2.5 years								
8	Advertisment and Promotional Campaign	Jan/24	Jan/35	11 years								
8.1	Initiate Contracts and Funding	Jun/25	Dec/25	7 months								
9	Negotiations with airports	Jan/27	Dec/28	2 years								
9.1	Airport Infrastructure Adaptation	Jan/27	Dec/28	2 years								
9.2	Selecting Hydrogen suppliers	Jan/27	Dec/28	2 years								
9.2.1	Negotiations with Hydrogen Suppliers	Jan/27	Dec/27	1 year								
9.2.2	Establish supply chain	Jan/28	Dec/28	1 year								
10	A320-HACK Production & Assembly	Jan/25	Dec/31	7 years								
11	Flight Certification	Jan/32	Dec/34	3 years								
11.1	Compliance Demonstration	Jan/32	Jun/34	2.5 years								
11.2	Technical Closure and Issue of Approval	Jun/34	Dec/34	6 months								
12	First Delivery to the Customer	Jan/35	Jan/35	-								*

(b) Years 2028 to 2035

Figure 21.7: Project's Gantt chart

be quantified. Certification duration could reduce because the A320-HACK is based on the previously certified A320neo, however, it will also involve the testing of the new HACK system, which might lengthen the process. Considering these two effects, an average value of 1.5 yrs[13] can be estimated for this task.

Next, production preparation for the fabrication of the new A320-HACK need to kick-off. This process begins once about 25% of the structural design is completed [143]. For the A320-HACK this will happen by the end of 2021 since it is heavily derived from the A320neo. In 2022 the negotiations with the manufacturing suppliers can start. This is a long process given that about 80% of Airbus' activities come from suppliers[14].

Once the negotiations have started, it is estimated that around January 2023 the production adaptations can start. These ensure the new or adapted parts of the A320-HACK can be manufactured. The assembly line will begin adaptation one year later, allowing for a margin from the adaptation of the first parts. Overall, this process occurs until mid 2026. The four and a half years of work are guaranteed to ensure a safe process is created for this new aircraft concept.

Additionally, advertisement is typically a phase that can start as soon as the design is finalised and has commenced certification. The promotional campaign continues until the aircraft enters service and generally extends after that. However, the Figure 21.7 only includes advertisement up until the first delivery to the customer, which will last 11 years. As just reasoned, promotional campaigns can go on

[13] https://rb.gy/l3z5hz, accessed:04-May-2021

[14] https://www.airbus.com/be-an-airbus-supplier.html, accessed:04-May-2021

for a very long time. For comparison, even though the A320neo was announced on December 2010[15], its first flight was in 2014[16] and the first delivery only in 2016[17]. This accounts for six years between the first announcement and the first delivery.

Next, negotiating with airports is a critical step for the success of the mission. It is essential that the negotiation process starts during the early production phase so that all necessary infrastructure are in place once the aircraft enters service. Having more airports facilitating the use of hydrogen will have a decisive effect on securing contracts with customers. These negotiations are assumed to be in the order of years as airports need to be convinced to construct a new infrastructure.

The first aircraft usually rolls out of the manufacturing plant few years after the go-ahead date [143]. But in the case of the A320-HACK, more intensive redesign work has to be performed because of the hydrogen integration. Mid 2025, once the design has been certified and in the last year of production preparations, the fabrication will start. This process will continue until approximately the end of 2030. The process is lengthy due to added caution when handling with a hybrid design: more validation tests will have to be performed to guarantee the safety of the aircraft, and the production and assembly of the new propulsion system is likely to require more than two years given its complexity[18].

The flight certification phase refers to certification process that follows after the production of the aircraft, respectively compliance demonstration and technical closure and issue of approval[19]. The compliance demonstration is the most extensive phase of the design certification. EASA estimates this process to take around 5 years for large aircraft[19]. However, due to the fact that the current design is an adaptation, the duration is expected to decrease. A similar case was constituted by the certification of A320neo for which 3000 *hrs* of testing were conducted[20]. By taking into account this data, it can be expected that the compliance demonstration will take about 2.5 years. An additional half a year is estimated for the technical closure and issue of approval.

Finally, the first delivery to the customer can be performed after the flight certification is finalised. Here, Airbus will start compensating for the costs attributed to the A320-HACK program. The break-even point will depend on the amount of trust the market puts on the new hybrid design involving hydrogen.

22 | Conclusion

The purpose of this report was to present the conceptual design of the A320-HACK, a narrow body airliner - powered by a hybrid propulsion system based on the HACK concept - envisioned to be the successor for the A320neo. Various concepts were investigated and then, after a thorough trade-off, a design concept was chosen and further analysed. The A320-HACK will retain the configuration of a traditional airliner, however, it will have tanks for liquid hydrogen mounted on the upper sides of the wings. Therefore, it will be based on the existing A320 family, although several modifications - which were analysed and designed in this report - will be implemented. First, it will have a new propulsion system, together with a feeding system and dedicated tanks for liquid hydrogen. Then, the traditional APU will be replaced by a fuel cell module (DPU), which is another completely new component. In addition, the wignbox will be redesigned and produced out of composites. Lastly, components such as the brakes, landing gear, nose steering, rudder and elevator will be electrically actuated, in order to reduce mechanical complexity.

[15] https://www.airbus.com/newsroom/press-releases/en/2010/12/airbus-offers-new-fuel-saving-engine-options-for-a320-family.html, accessed:05-Jun-2021

[16] https://www.airbus.com/newsroom/press-releases/en/2014/09/first-a320neo-successfully-completes-first-flight.html, accessed:06-May-2021

[17] https://www.airbus.com/newsroom/press-releases/en/2016/01/first-a320neo-delivery-opens-new-era-in-commercial-aviation.html, accessed:06-May-2021

[18] http://www.madehow.com/Volume-1/Jet-Engine.html, accessed:06-May-2021

[19] https://www.easa.europa.eu/domains/aircraft-products/aircraft-certification, accessed:04-May-2021

[20] https://www.airbus.com/newsroom/press-releases/en/2014/09/first-a320neo-successfully-completes-first-flight.html#media-list-image-image-all_ml_0-1, accessed:06-May-2021

Overall, the A320-HACK will match the market positioning of the A320neo; it will have the same passenger capacity of 180 passengers, and a higher harmonic and maximum fuel ranges (4938 km and 8500 km respectively). Furthermore, the novel HACK concept will offer the flexibility of running on both kerosene and hydrogen, separately or simultaneously. While running on both fuels, the emissions will decrease significantly, with an estimated reduction of 71% in terms of CO_2 and 41% in terms of NO_x. Additionally, if the route is shorter than 1238 km, the flight can be performed exclusively on hydrogen, resulting in a CO_2-free journey. Thus, the climate change impact of the A320-HACK will be substantially lower compared to the A320neo: in terms of ATR over a period of 40 years, the reduction is estimated to reach a value of 76.7%. Furthermore, the fuel consumption is also expected to decrease significantly, up to an estimated 44%, reducing operating costs. Lastly, the development cost of the A320-HACK is estimated to be € 2.77 billion, while the list price of a single unit is expected to be around € 103.6 million.

The presented design fulfills the pre-defined requirements, which are summarised in Table 22.1. The time span of this project did not allow to deeply analyse every single aspect; thus, the compliance with few requirements has not yet been verified (indicated as NA in the table) and it is left for further phases of the project. In addition, all the user guidelines listed in Chapter 3 were appropriately addressed throughout the course of the report.

Table 22.1: Compliance matrix for the A320-HACK project

Req. code	Description	Compliance	Chapter
UR-PERF-01	Design a successor for the A320neo using the HACK system	Yes	-
UR-PERF-02	Compliance with CS25 regulations	NA	-
UR-PROP-01	Energy stored in $H_2 \leq 50\%$ of energy stored in kerosene	Yes, equal to 50%	Chapter 8
SR-PERF-02	180 pax capacity	Yes	Chapter 13 & 15
SR-PERF-03	at least 6300 km of max fuel range	Yes, 8500 km	Chapter 15
UR-SR-01	LH_2 tanks, 36 hours without boil-off at 45°C	Yes	Chapter 9
UR-SR-04	Passengers evacuation time $\leq$ 90 s	Yes, unchanged wrt A320neo	Chapter 17
SR-SUST-01	30% cruise emissions reduction wrt the A320neo	Yes, 90%	Chapter 16
SR-SUST-02	50% LTO emissions reduction wrt the A320neo	Yes, 50%	Chapter 16 & 10.4.2
SR-SUST-04	Noise-level contour, max 85 decibel	Yes	Chapter 16
UR-OPER-01	TRT impact of LH_2 refueling, $\leq$ 10 min	Yes, TRT unchanged wrt A320neo	Chapter 17
SR-OPER-03	Idle and taxi powered by H_2 only	Yes	Chapter 8
UR-COST-01	Development cost $\leq$ 5B euros	Yes, € 2.77B	Chapter 18
UR-COST-02	Production cost increase wrt the A320neo $\leq$ 15%	Yes, € 100.3M	Chapter 18
UR-EB-01	EIS by 2035	Yes	Chapter 21

Bibliography

[1] J. Hill, E. Nelson, D. Tilman, S. Polasky, and D. Tiffany. "Environmental, Economic, and Energetic Costs, and Benefits of Biodiesel and Ethanol Biofuels". In: *Proceedings of the National Academy of Sciences of the United States of America* Vol. 103 (Aug. 1, 2006), pp. 11206–10. DOI: 10.1073/pnas.0604600103.

[2] M. M. Hasan and M. M. Rahman. "Performance and emission characteristics of biodieseldiesel blend and environmental and economic impacts of biodiesel production: A review". In: *Renewable and Sustainable Energy Reviews* Vol. 74 (July 1, 2017), pp. 938–948. DOI: 10.1016/j.rser.2017.03.045.

[3] D. Dewanji, A. G. Rao, M. Pourquie, and J. P. van Buijtenen. "Study of Swirling Air Flow Characteristics in a Lean Direct Injection Combustor". In: ASME Turbo Expo 2010: Power for Land, Sea, and Air. American Society of Mechanical Engineers Digital Collection, Dec. 22, 2010, pp. 499–510. DOI: 10.1115/GT2010-22602.

[4] D. Dewanji and A. G. Rao. "Spray combustion modeling in lean direct injection combustors, Part II: Multi-point LDI". In: *Combustion Science and Technology* Vol. 187, No. 4 (2015). Publisher: Taylor & Francis, pp. 558–576. DOI: 10.1080/00102202.2014.958476.

[5] R. A. Gangoli, F. Yin, and v. B. J. P. "A hybrid engine concept for multi-fuel blended wing body". In: *Aircraft Engineering and Aerospace Technology: An International Journal* Vol. 86, No. 6 (Jan. 1, 2014). Ed. by R. Singh. Publisher: Emerald Group Publishing Limited, pp. 483–493. DOI: 10.1108/AEAT-04-2014-0054.

[6] *Certification Specifications and Acceptable Means of Compliance for Large Aeroplanes (CS-25)*. Dec. 15, 2020.

[7] Airbus. *Global Market Forecast - Cities, Airports and Aircraft 2019-2038*. Airbus, 2019.

[8] D. S. Lee, D. W. Fahey, A. Skowron, M. R. Allen, U. Burkhardt, Q. Chen, S. J. Doherty, S. Freeman, P. M. Forster, J. Fuglestvedt, A. Gettelman, R. R. De León, L. L. Lim, M. T. Lund, R. J. Millar, B. Owen, J. E. Penner, G. Pitari, M. J. Prather, R. Sausen, and L. J. Wilcox. "The contribution of global aviation to anthropogenic climate forcing for 2000 to 2018". In: *Atmospheric Environment* Vol. 244 (Jan. 1, 2021), p. 117834. DOI: 10.1016/j.atmosenv.2020.117834.

[9] T. Cooper, I. Reagan, C. Porter, and C. Franzoni. *Global Fleet and MRO Market Forecast 2021-2031*. Oliver Wyman.

[10] Boeing. *737 MAX: Airplane Characteristics for Airport Planning*. D6-38A004. Boeing Commercial Airplanes, Feb. 2021, p. 199.

[11] Dr. Arvind Gangoli Rao. *Project Guide Design Synthesis Exercise: A320 - HACK*. Delft: TU Delft, Apr. 15, 2021. 58 pp.

[12] N. ALBOSHMINA. *Ammonia Cracking with Heat Transfer Improvement Technology*. 2019.

[13] P. C. Rao and M. Yoon. "Potential Liquid-Organic Hydrogen Carrier (LOHC) Systems: A Review on Recent Progress". In: *Energies* Vol. 13, No. 22 (Jan. 2020), p. 6040. DOI: 10.3390/en13226040.

[14] C. A. Sofia, D. H. Tota, G. Nico, G. Martino, H. Marek, N. Mikhail, S. R. Sara, U. Elena, v. S. M. Johan, and V. Datta. *Midterm Review: Thorough Midterm Review for the A320-HACK project by Group 11*. Delft, The Netherlands: TU Delft, May 28, 2021, p. 72.

[15] T. Saaty and L. Vargas. "The Analytic Network Process". In: Sept. 10, 2006, pp. 1–26. ISBN: 978-0-387-33859-0. DOI: 10.1007/0-387-33987-6_1.

[16] A. Uranga, M. Drela, D. K. Hall, and E. M. Greitzer. "Analysis of the Aerodynamic Benefit from Boundary Layer Ingestion for Transport Aircraft". In: *AIAA Journal* Vol. 56, No. 11 (2018), pp. 4271–4281. DOI: 10.2514/1.J056781.

[17] S. Ravikanth, M. SaiDheeraj, L. Farooq, and A. Ramesh. "A Effect of Elevator Deflection on Lift Coefficient Increment". In: *IJMER* Vol. 5, No. 6 (June 2015), p. 17.

[18] "A Calculation Method for Over-the-Wing Engines within Conceptual Aircraft Design". In: (2019). Artwork Size: 11 pages Medium: application/pdf Publisher: Deutsche Gesellschaft für Luft- und Raumfahrt - Lilienthal-Oberth e.V. Version Number: 1.0, 11 pages. DOI: 10.25967/480177. (Visited on 06/04/2021).

[19] NATO. *AGARD Lecture Series*. 43. Google-Books-ID: W_Jjd5RRpnMC. North Atlantic Treaty Organization, 1970. 710 pp.

[20] X.-w. Sun, Z.-y. Guo, and W. Huang. "Passive zero-boil-off storage of liquid hydrogen for long-time space missions". In: *International Journal of Hydrogen Energy* Vol. 40, No. 30 (Aug. 10, 2015), pp. 9347–9351. DOI: 10.1016/j.ijhydene.2015.05.184.

[21] J. E. Fesmire and W. L. Johnson. "Cylindrical cryogenic calorimeter testing of six types of multilayer insulation systems". In: *Cryogenics* Vol. 89 (Jan. 1, 2018), pp. 58–75. ISSN: 0011-2275. DOI: 10.1016/j.cryogenics.2017.11.004.

[22] D. Verstraete, P. Hendrick, P. Pilidis, and K. Ramsden. "Hydrogen fuel tanks for subsonic transport aircraft". In: *International Journal of Hydrogen Energy*. Hyceltec 2009 Conference Vol. 35, No. 20 (Oct. 1, 2010), pp. 11085–11098. DOI: 10.1016/j.ijhydene.2010.06.060.

[23] R. G. Ross. "Quantifying MLI Thermal Conduction in Cryogenic Applications from Experimental Data". In: *IOP Conference Series: Materials Science and Engineering* Vol. 101 (Dec. 18, 2015), p. 012017. ISSN: 1757-8981, 1757-899X. DOI: 10.1088/1757-899X/101/1/012017.

[24] D. Singh, A. Pandey, M. K. Singh, L. Singh, and V. Singh. "Heat radiation reduction in the cryostat with multilayer insulation technique". In: *Journal of Instrumentation* Vol. 15, No. 7 (July 27, 2020), P07032–P07032. DOI: 10.1088/1748-0221/15/07/P07032.

[25] V. Kazymyrovych. *Very high cycle fatigue of engineering materials : A literature review*. Karlstad University, 2009.

[26] A. Abass, A. Hammadi, and B. Faisal. "Fatigue Life Estimation of Aluminum Alloy 2024-T4 and Fiber Glass-Polyester Composite Material". In: Vol. 3 (June 1, 2016), pp. 1760–1764. ISSN: 2395-0056.

[27] D. Verstraete. "The Potential of Liquid Hydrogen for long range aircraft propulsion". In: (Apr. 2009).

[28] M. F. Ashby. "Chapter 4 - Material Property Charts". In: *Materials Selection in Mechanical Design (Fourth Edition)*. Ed. by M. F. Ashby. Oxford: Butterworth-Heinemann, Jan. 1, 2011, pp. 57–96. DOI: 10.1016/B978-1-85617-663-7.00004-7.

[29] Hampus Larsson. *Bird strike analysis: An Analytical Approach*. Stockholm, Sweden: KTH Royal Institute of Technology, 2015, p. 65.

[30] M. Avalle, G. Belingardi, and R. Montanini. "Characterization of polymeric structural foams under compressive impact loading by means of energy-absorption diagram". In: *International Journal of Impact Engineering* Vol. 25, No. 5 (May 1, 2001), pp. 455–472. ISSN: 0734-743X. DOI: 10.1016/S0734-743X(00)00060-9.

[31] G. Daniel Brewer. *Hydrogen Aircraft Technology*. Florida, US: CRC Press, Inc., 1991. 445 pp.

[32] J. W. Choi, Y. J. Kim, K. H. Lee, H. I. Kim, K. Y. Han, and J. H. Park. *Liquid hydrogen properties*. KAERI/TR–2723/2004. Korea Atomic Energy Research Institute, 2004.

[33] *Liquid Hydrogen Fuelled Aircraft System Analysis*. GRD1-1999-10014. Germany: Airbus Deutschland GmbH, Sept. 24, 2003.

[34] P. Ghoshdastidar. *Heat Transfer*. 2nd Edition. Oxford University Press, 2012.

[35] *A320 - Flight Crew Operations Manual: Fuel Content*.

[36] J. Wink, R. Hermsen, R. Huijsman, C. Akkermans, L. Denies, F. Barreiro, A. Schutte, A. Cervone, and B. Zandbergen. "Cryogenic rocket engine develpment at Delft aerospace rocket engineering". In: Space propulsion. 2016.

[37] M. Voskuijl. *AE2230-I Flight and Orbital Mechanics*. 2019.

[38] S. Paramasivam. "Analysis of Aerodynamic Characteristics of a Supercritical Airfoil for Low Speed Aircraft". In: *International Journal of Research in Engineering and Technology* Vol. 03 (June 25, 2014), pp. 179–183. DOI: 10.15623/ijret.2014.0306033.

[39] H. Rick. *Gasturbinen und Flugantriebe*. Berlin, Heidelberg: Springer Berlin Heidelberg, 2013. DOI: 10.1007/978-3-540-79446-2.

[40] S. Farokhi. *Aircraft Propulsion*. Google-Books-ID: 1dMeAQAAIAAJ. Wiley, 2009. 828 pp.

[41] J. van Buijtenen, W. Visser, T. Tinga, S. Shakariyants, and F. Montella. *Reader of Aero Engine Technology, AE4238*. Aug. 2018.

[42] A. J. Lampe. *A Discourse of the Bleedless and Bleed Air Gas Turbine Engines*. University of Colorado, p. 12.

[43] A. Gangoli Rao and Feijia Yin. *AE4238 Aero Engine Technology*. 2020.

[44] K. G. Kyprianidis. "Future Aero Engine Designs: An Evolving Vision". In: *Advances in Gas Turbine Technology*. Rijeka, Croatia, 2011, pp. 3–24.

[45] U. Michel. "The Benefits of Variable Area Fan Nozzles on Turbofan Engines". In: 49th AIAA Aerospace Sciences Meeting including the New Horizons Forum and Aerospace Exposition. Vol. AIAA-2011-0226. Orlando, Florida, Jan. 4, 2011. DOI: 10.2514/6.2011-226.

[46] R. J. M. Elmendorp. *PrandtlplaneARchitecture for the Sustainable Improvement of Future AirpLanes - Feasibility study on the use of very large bypass ratio turbofan engines for the PrandtlPlane*. TU Delft, Jan. 2020.

[47] C. Svoboda. "Turbofan engine database as a preliminary design tool". In: *Aircraft Design* Vol. 3, No. 1 (Mar. 1, 2000), pp. 17–31. DOI: 10.1016/S1369-8869(99)00021-X.

[48] S. Eelman, I. del Pozo y de Poza, and T. Krieg. "Fuel Cell APUs in Commercial Aircraft an Assessment of SOFC and PEMFC Concepts". In: 24th International Congress of the Aeronautical Sciences. Garching, 2004, p. 10.

[49] I. M. M. Saleh. *Modelling, Simulation and Performance Evaluation: PEM Fuel Cells For High Altitude UAS*, p. 260.

[50] J. Zhang, Z. Xie, J. Zhang, Y. Tang, C. Song, T. Navessin, Z. Shi, D. Song, H. Wang, D. P. Wilkinson, Z.-S. Liu, and S. Holdcroft. "High temperature PEM fuel cells". In: *Journal of Power Sources* Vol. 160, No. 2 (2006), pp. 872–891. DOI: 10.1016/j.jpowsour.2006.05.034.

[51] K. Spencer. *Investigation of Potential Fuel Cell Use in Aircraft*. Dec. 2013.

[52] T. Aicher, B. Lenz, F. Gschnell, U. Groos, F. Federici, L. Caprile, and L. Parodi. "Fuel processors for fuel cell APU applications". In: *Journal of Power Sources*. Selected papers from the Ninth Ulm Electrochemical Days Vol. 154, No. 2 (Mar. 21, 2006), pp. 503–508. DOI: 10.1016/j.jpowsour.2005.10.026.

[53] W. Winkler and P. Nehter. *System analysis of Fuel Cell APUs for Aircraft applications*. Sept. 1, 2005.

[54] P. Aguiar, D. J. L. Brett, and N. P. Brandon. "Solid oxide fuel cell/gas turbine hybrid system analysis for high-altitude long-endurance unmanned aerial vehicles". In: *International Journal of Hydrogen Energy* Vol. 33, No. 23 (Dec. 1, 2008), pp. 7214–7223. ISSN: 0360-3199. DOI: 10.1016/j.ijhydene.2008.09.012.

[55] M. D. Fernandes, S. T. de P. Andrade, V. N. Bistritzki, R. M. Fonseca, L. G. Zacarias, H. N. C. Gonçalves, A. F. de Castro, R. Z. Domingues, and T. Matencio. "SOFC-APU systems for aircraft: A review". In: *International Journal of Hydrogen Energy* Vol. 43, No. 33 (Aug. 16, 2018), pp. 16311–16333. ISSN: 0360-3199. DOI: 10.1016/j.ijhydene.2018.07.004.

[56] D. Daggett, S. Eelman, and G. Kristiansson. "Fuel Cell APU". In: *AIAA International Air and Space Symposium and Exposition: The Next 100 Years*. _eprint: https://arc.aiaa.org/doi/pdf/12660. American Institute of Aeronautics and Astronautics. DOI: 10.2514/6.2003-2660.

[57] S. Shamim, B. Choudhary, and J. Anwer. "A review on recent advances in proton exchange membrane fuel cells: Materials, technology and applications". In: *Advances in Applied Science Research* Vol. 6 (Oct. 9, 2015), pp. 89–100.

[58] M. H. S. Bargal, M. A. A. Abdelkareem, Q. Tao, J. Li, J. Shi, and Y. Wang. "Liquid cooling techniques in proton exchange membrane fuel cell stacks: A detailed survey". In: *Alexandria Engineering Journal* Vol. 59, No. 2 (Apr. 1, 2020), pp. 635–655. DOI: 10.1016/j.aej.2020.02.005.

[59] R. O'Hare, S.-W. Cha, W. Colella, and F. Prinz. *Fuel Cell Fundamentals*. third edition. Wiley, 2016.

[60] J. Larminie and A. Dicks. *Fuel Cell Systems Explained*. second edition. Wiley, 2003.

[61] X. Xia. "Dynamic power distribution management for all electric aircraft". In: (Jan. 2011). Accepted: 2011-10-05T15:07:20Z Publisher: Cranfield University.

[62] *A320 Aircraft Characteristics Airport and Maintenance Planning*. France: Airbus, Dec. 1, 2020.

[63] *Flight Crew Operating Manual: A320 - Water/waste*. Airbus.

[64] D. Fluorochemicals. "Thermodynamic Properties of HFC-134a". In: (), p. 34.

[65] A. Franco. "Optimum design of bipolar plates for separate air flow cooling system of PEM fuel cells stacks". In: *Heat and Mass Transfer* Vol. 51, No. 12 (Dec. 1, 2015), pp. 1691–1703. DOI: 10.1007/s00231-015-1530-6.

[66] S. Longo, M. Cellura, F. Guarino, M. Ferraro, V. Antonucci, and G. Squadrito. "Chapter 6 - Life Cycle Assessment of Solid Oxide Fuel Cells and Polymer Electrolyte Membrane Fuel Cells: A Review". In: *Hydrogen Economy*. Ed. by A. Scipioni, A. Manzardo, and J. Ren. Academic Press, Jan. 1, 2017, pp. 139–169. DOI: 10.1016/B978-0-12-811132-1.00006-7.

[67] M. Sauermoser, N. Kizilova, B. G. Pollet, and S. Kjelstrup. "Flow Field Patterns for Proton Exchange Membrane Fuel Cells". In: *Frontiers in Energy Research* Vol. 8 (2020). Publisher: Frontiers. DOI: 10.3389/fenrg.2020.00013.

[68] B. Mechatronica. "Thermal management for batteries in E-mobility applications". June 14, 2018.

[69] S. Fuchss, A. Michaelides, O. Stocks, and R. Devenport. "The Propulsion System of the New Jaguar I-Pace". In: *MTZ worldwide* Vol. 80, No. 1 (Jan. 1, 2019), pp. 18–25. DOI: 10.1007/s38313-018-0123-4.

[70] *EVTV Monitor/Controller For Tesla Model S Battery Modules*. 2017.

[71] *Model X Emergency Response Guide*. 2016.

[72] J. Roskam. *Airplane Design Part VI: Preliminary Calculations of Aerodynamic, Thrust and Power Characteristics*. DARcorporation, 1985. 584 pp.

[73] M. Orlita and R. Vos. "Cruise Performance Optimization of the Airbus A320 through Flap Morphing". In: *17th AIAA Aviation Technology, Integration, and Operations Conference*. 17th AIAA Aviation Technology, Integration, and Operations Conference. Denver, Colorado: American Institute of Aeronautics and Astronautics, June 5, 2017. DOI: 10.2514/6.2017-3264.

[74] *Ground Operations Manual, Airbus Industrie A320/A321*. LTU International Airways.

[75] F. Oliviero and E. Gill. *AE3211-I Systems Engineering & Aerospace Design*. 2020.

[76] E. Torenbeek. *Synthesis of subsonic airplane design*. Publisher: Delft University Press. Delft: Delft University Press, Dec. 31, 1982. ISBN: 90-247-2724-3.

[77] J. Sun, J. M. Hoekstra, and J. Ellerbroek. "Aircraft Drag Polar Estimation Based on a Stochastic Hierarchical Model". In: Eight SESAR Innovation Days. The Netherlands: TU Delft, Dec. 2018, p. 8.

[78] E. Obert. *Aerodynamic Design of Transport Aircraft*. Delft, The Netherlands: IOS Press, 2009. ISBN: 978-1-58603-970-7.

[79] A. L. Braslow. "A review of factors affecting boundary-layer transition". In: *NASA Technical Note D-3384* (1966), p. 30.

[80] P. Hemmen. "Towards Practical Hybrid Laminar Flow Control: Boundary Layer Stability with Suction and Scalability of Pressure Losses across Perforated Sheets". Master Thesis. Delft, The Netherlands: Delft University of Technology, 2018.

[81] J. Melkert, R. Vos, and B. Zandbergen. *AE1222-II Aerospace Design & Systems Engineering Elements*. 2019.

[82] P. Proesmans and R. Vos. "Airplane Design Optimization for Minimal Global Warming Impact". In: *AIAA Scitech 2021 Forum* (2021). Publisher: American Institute of Aeronautics and Astronautics Inc. (AIAA). DOI: 10.2514/6.2021-1297.

[83] *Hydrogen-powered aviation: A fact-based study of hydrogen technology, economics, and climate impact by 2050*. Belgium: Clean Sky 2 JU, Fuel Cells, and Hydrogen 2 JU, May 2020. DOI: 10.2843/471510.

[84] R. Sausen and U. Schumann. "Estimates of the Climate Response to Aircraft CO2 and NOx Emissions Scenarios". In: (2000), p. 32. DOI: 10.1023/A:1005579306109.

[85] M. R. Smith. "Impact of anthropogenic CO2 emissions on global human nutrition". In: *Nature Climate Change* Vol. 8 (2018), p. 8.

[86] E. S. Dallara, I. M. Kroo, and I. A. Waitz. "Metric for Comparing Lifetime average Climate Impact of Aircraft". In: *AIAA Journal* Vol. 49, No. 8 (Aug. 2011), pp. 1600–1613. DOI: 10.2514/1.J050763.

[87] M. O. Köhler, G. Rädel, O. Dessens, K. P. Shine, H. L. Rogers, O. Wild, and J. A. Pyle. "Impact of perturbations to nitrogen oxide emissions from global aviation". In: *Journal of Geophysical Research: Atmospheres* Vol. 113 (D11 2008). DOI: 10.1029/2007JD009140.

[88] G. Volker, L. Bock, U. Burkhardt, K. Dahlmann, K. Gierens, L. Hüttenhofer, S. Unterstrasser, A. Gangoli Rao, A. Bhat, F. Yin, T. Reichel, C. Paschereit, and L. Yeshayahou. "Assessing the climate impact of the AHEAD multi-fuel blended wing body". In: *Meteorologische Zeitschrift* Vol. 26 (Dec. 8, 2017), pp. 711–725. DOI: 10.1127/metz/2016/0758.

[89] U. Schumann. "Influence of propulsion efficiency on contrail formation". In: *Aerospace Science and Technology* Vol. 4, No. 6 (Sept. 1, 2000). Publisher: Elsevier Masson, pp. 391–401. DOI: 10.1016/S1270-9638(00)01062-2.

[90] I. P. on Climate Change. *Climate change 2007: the physical science basis: contribution of Working Group I to the Fourth Assessment Report of the Intergovernmental Panel on Climate Change*. Cambridge ; New York, 2007. 996 pp.

[91] V. Grewe and A. Stenke. "AirClim: an efficient tool for climate evaluation of aircraft technology". In: *Atmospheric Chemistry and Physics* Vol. 8, No. 16 (Aug. 11, 2008), pp. 4621–4639. DOI: 10.5194/acp-8-4621-2008.

[92] S. Das. "Life cycle assessment of carbon fiber-reinforced polymer composites". In: *The International Journal of Life Cycle Assessment* Vol. 16, No. 3 (Mar. 1, 2011), pp. 268–282. DOI: 10.1007/s11367-011-0264-z.

[93] R. Xue, J. Jiang, X. Zheng, J.-l. Gong, and A. Jackson. "Study of Noise Reduction Based on Optimal Fan Outer Pressure Ratio and Thermodynamic Performance for Turbofan Engines at Conceptual Design Stage". In: *International Journal of Aeronautical and Space Sciences* Vol. 21, No. 2 (June 1, 2020), pp. 439–450. DOI: 10.1007/s42405-019-00236-8.

[94] M. Gorji-Bandpy and M. Azimi. "Technologies for jet noise reduction in turbofan engines". In: *Aviation* Vol. 16, No. 1 (Apr. 5, 2012). Number: 1, pp. 25–32. DOI: 10.3846/16487788.2012.679770.

[95] *APS 300 Auxiliary Power Unit*. 2006.

[96] R. B. Norton. "Defence Infrastructure Organisation". In: (), p. 29.

[97] L. Leylekian, M. Lebrun, and P. Lempereur. "An overview of aircraft noise reduction technologies." In: *Aerospace Lab*, No. 6 (June 2014). DOI: 10.12762/2014.AL07-01.

[98] *An exploratory study to determine the integrated technological air transportation system ground requirements of liquid-hydrogen-fueled subsonic, long-haul civil air transports.* The Boeing Commercial Airplane Company, 1976.

[99] G. D. Brewer and R. E. Morris. "Tank and Fuel Systems Considerations for Hydrogen Fueled Aircraft". In: *SAE Transactions* Vol. 84 (1975). Publisher: SAE International, pp. 3088–3103.

[100] *Flight Operations Briefing Notes, Ground Handling, Refueling with Passengers on Board*. Blagnac, France: Airbus, 2007.

[101] G. Hankinson and B. J. Lowesmith. *Qualitative Risk Assessment of Hydrogen Liquefaction, Storage and Transportation*. Loughborough: Loughborough University, Oct. 31, 2013. (Visited on 06/07/2021).

[102] V. Molkov. *Fundamental of Hydrogen Safety Engineering I*. 2012.

[103] S. Rondinelli, A. Gardi, R. Kapoor, and R. Sabatini. "Benefits and challenges of liquid hydrogen fuels in commercial aviation". In: *International Journal of Sustainable Aviation* Vol. 3 (Jan. 1, 2017), p. 200. DOI: 10.1504/IJSA.2017.086845.

[104] *Innovation Insights Brief | 2019, New Hydrogen Economy - Hope or Hype?* World Energy Council, 2019.

[105] N. Muradov. "17 - Low-carbon production of hydrogen from fossil fuels". In: *Compendium of Hydrogen Energy*. Ed. by V. Subramani, A. Basile, and T. N. Vezirolu. Woodhead Publishing Series in Energy. Oxford, Jan. 1, 2015, pp. 489–522. DOI: 10.1016/B978-1-78242-361-4.00017-0.

[106] F. Scheepers, M. Stähler, A. Stähler, E. Rauls, M. Müller, M. Carmo, and W. Lehnert. "Temperature optimization for improving polymer electrolyte membrane-water electrolysis system efficiency". In: *Applied Energy* Vol. 283 (Feb. 1, 2021), p. 116270. DOI: 10.1016/j.apenergy.2020.116270.

[107] H. Alder P. "Hydrogen in air transportation. Feasibility study for Zurich airport, Switzerland". In: *International Journal of Hydrogen Energy* Vol. 12, No. 8 (Jan. 1, 1987), pp. 571–585. ISSN: 0360-3199. DOI: 10.1016/0360-3199(87)90016-4.

[108] C. Amy and A. Kunycky. *Hydrogen as a Renewable Energy Carrier for Commercial Aircraft*. Oct. 12, 2019.

[109] J. Andersson and S. Grönkvist. "Large-scale storage of hydrogen". In: *International Journal of Hydrogen Energy* Vol. 44, No. 23 (May 3, 2019), pp. 11901–11919. DOI: 10.1016/j.ijhydene.2019.03.063.

[110] J. Davies, F. Dolci, D. Klassek-Bajorek, R. Ortiz Cebolla, and E. Weidner. "Current status of Chemical Energy Storage Technologies". In: *Publications Office of the European Union, Luxembourg,* (2020). DOI: 10.2760/280873.

[111] T. G. Reynolds. "Air traffic management performance assessment using flight inefficiency metrics". In: *Transport Policy*. Air Transportation and the Environment Vol. 34 (July 1, 2014), pp. 63–74. DOI: 10.1016/j.tranpol.2014.02.019.

[112] A. Kharina and D. Rutherford. *Fuel Efficiency Trends for New Commercial Jet Aircraft: 1960 to 2014*. Washington DC: The International Council of Clean Transportation (ICCT), 2015.

[113] *European Aviation in 2040, Challenges of Growth*. Belgium: European Organisation for the Safety of Air Navigation (EUROCONTROL), 2018.

[114] F. Wouters, D. S. Rachidi, and D. B. Ikken. *A North Africa - Europe Hydrogen Manifesto*. Munich: Dii Desert Energy Industry Network, Nov. 2019.

[115] W. A. Amos. *Costs of Storing and Transporting Hydrogen*. NREL/TP-570-25106, ON: DE00006574, 6574. National Renewable Energy Laboratory (U.S.), Jan. 27, 1999, NREL/TP–570–25106, ON: DE00006574, 6574. DOI: 10.2172/6574.

[116] H. Rezaie, M. Ziabasharhagh, and M. Mafi. "A review of hydrogen liquefaction, current situation and its future". In: Feb. 21, 2021.

[117] H. Matsuda and M. Nagami. *Study of large hydrogen liquefaction process*. Nippon Sanso Corp, 1997.

[118] H. Quack. "Conceptual design of a high efficiency large capacity hydrogen liquefier". In: *AIP Conference Proceedings* Vol. 613, No. 1 (May 10, 2002), pp. 255–263. DOI: 10.1063/1.1472029.

[119] G. Valenti and E. Macchi. "Proposal of an innovative, high-efficiency, large-scale hydrogen liquefier". In: *International Journal of Hydrogen Energy* Vol. 33, No. 12 (June 1, 2008), pp. 3116–3121. DOI: 10.1016/j.ijhydene.2008.03.044.

[120] C. Baker and R. Shaner. "A study of the efficiency of hydrogen liquefaction". In: *International Journal of Hydrogen Energy* Vol. 3, No. 3 (Jan. 1, 1978). Publisher: Pergamon, pp. 321–334. DOI: 10.1016/0360-3199(78)90037-X.

[121] D. O. Berstad, J. H. Stang, and P. Nekså. "Large-scale hydrogen liquefier utilising mixed-refrigerant pre-cooling". In: *International Journal of Hydrogen Energy*. Novel Hydrogen Production Technologies and Applications Vol. 35, No. 10 (May 1, 2010). DOI: 10.1016/j.ijhydene.2010.02.001.

[122] J. Essler and a. et al. *Report on Technology Overview and Barriers to Energy- and Cost-Efficient Large Scale Hydrogen Liquefaction*. 1.1. June 2012.

[123] K. Stolzenburg and R. Mubbala. *Hydrogen Liquefaction Report*. 2013.

[124] J. Markish. "Valuation Techniques for Commercial Aircraft Program Design". In: (2002), p. 153.

[125] L. Cöllen. "Standardized Geometry Formats for Aircraft Conceptual Design and Physics-based Aerodynamics and Structural Analyses". Stockholm, Sweden, Sept. 2011.

[126] Airbus. *Airbus Aircraft 2018 Average List Prices*. 2018.

[127] D. Powell. *Focus on Blue Hydrogen*. Aug. 2020.

[128] D. P. Raymer. *Aircraft design: A conceptual approach*. Washington DC: American Institute of Aeronautics and Astronautics, 1989.

[129] J. Roskam. *Airplane Design VIII: Airplane Cost Estimation: Design, Development, Manufacturing and Operating*. Airplane Design v. 1. DARcorporation, 2002.

[130] C. Yang and J. Ogden. "Determining the lowest-cost hydrogen delivery mode". In: *International Journal of Hydrogen Energy* Vol. 32, No. 2 (Feb. 1, 2007), pp. 268–286. DOI: 10.1016/j.ijhydene.2006.05.009.

[131] J. Fydrych and G. Consogno. "A maintenance strategy for a multi-valve cryogenic distribution system". In: *IOP Conference Series: Materials Science and Engineering* Vol. 278 (Dec. 2017), p. 012014. DOI: 10.1088/1757-899X/278/1/012014.

[132] R. Saltolu, N. Humaira, and G. nalhan. "Aircraft Scheduled Airframe Maintenance and Downtime Integrated Cost Model". In: *Advances in Operations Research* Vol. 2016 (2016), pp. 1–12. DOI: 10.1155/2016/2576825.

[133] V. Suboti, N. H. Menzler, V. Lawlor, Q. Fang, S. Pofahl, P. Harter, H. Schroettner, and C. Hochenauer. "On the origin of degradation in fuel cells and its fast identification by applying unconventional online-monitoring tools". In: Vol. 277 (Nov. 1, 2020), p. 115603. DOI: 10.1016/j.apenergy.2020.115603.

[134] K. Groth and C. Correa-Jullian. "Liquid Hydrogen Storage System FMEA and Data Requirements for Risk Analysis". In: Nov. 2, 2020. DOI: 10.3850/978-981-14-8593-0_5714-cd.

[135] D. Imamura, D. Ebata, Y. Hshimasa, M. Akai, and S. Watanabe. "Impact of Hydrogen Fuel Impurities on PEMFC Performance". In: *SAE Transactions* Vol. 116 (2007). Publisher: SAE International, pp. 621–626. DOI: 10.1149/1.3210713.

[136] S. C. Tan. *Electrically Assisted Propulsion & Power Systems for Short-Range Missions: Electrification of a Conventional Airbus A320neo*. 2018.

[137] G. A. Whyatt and L. A. Chick. *Electrical Generation for More-Electric Aircraft Using Solid Oxide Fuel Cells*. PNNL-21382, 1056768. Apr. 1, 2012. DOI: 10.2172/1056768.

[138] V. Madonna, P. Giangrande, and M. Galea. "Electrical Power Generation in Aircraft: Review, Challenges, and Opportunities". In: Vol. 4 (May 7, 2018), pp. 646–659. DOI: 10.1109/TTE.2018.2834142.

[139] G. L. Mills, B. Buchholtz, and A. Olsen. "Design, fabrication and testing of a liquid hydrogen fuel tank for a long duration aircraft". In: ADVANCES IN CRYOGENIC ENGINEERING: Transactions of the Cryogenic Engineering Conference - CEC, Volume 57. Spokane, Washington, USA, 2012, pp. 773–780. DOI: 10.1063/1.4706990.

[140] P. Nolte, A. Apffelstaedt, V. Gollnick, and T. Rötger. "Quantitative Assessment of Technology Impact on Aviation Fuel Efficiency". In: (June 20, 2012).

[141] V. Oliveri, G. Zucco, D. Peeters, G. Clancy, R. Telford, M. Rouhi, C. McHale, R. M. OHiggins, T. M. Young, and P. M. Weaver. "Design, Manufacture and Test of an In-Situ Consolidated Thermoplastic Variable-Stiffness Wingbox". In: *AIAA Journal* Vol. 57, No. 4 (Apr. 2019), pp. 1671–1683. DOI: 10.2514/1.J057758.

[142] D. Stavrov and H. E. N. Bersee. "Resistance welding of thermoplastic composites-an overview". In: *Composites Part A: Applied Science and Manufacturing* Vol. 36, No. 1 (Jan. 1, 2005), pp. 39–54. DOI: 10.1016/j.compositesa.2004.06.030.

[143] J. Sinke. "Organization of the production process". In: *Production of Aerospace Systems*. Delft: TU Delft.

A | Engine Cycle Analysis & Design

A.1 Engine Parameters

Table A.1: A320-HACK's engine parameters for take-off

Parameter	η_{inlet}	η_{LPC}	η_{HPC}	η_{mech}	η_{cc}	η_{HPT}	η_{LPT}	$(\eta_{noz})_{core}$	$(\eta_{noz})_{fan}$
HACK's value	0.995	0.93	0.988	0.995	0.9995	0.95	0.96	0.995	0.998
Relative difference [%]	0.51	1.11	1.05	0.51	0.45	2.14	2.13	0.46	0.77
Parameter	η_{fan}	Π_{fan}	Π_{LPC}	Π_{HPC}	Π_{cc}	BPR	OPR	$TIT\ [K]$	
HACK's value	0.95	1.35	1.7	18.78	0.955	15.61	44.70	1,570	
Relative difference [%]	2.20	-3.57	-15.00	57.42	1.60	40.59	33.81	14.12	

A.2 Engine Cycle Analysis Results

Table A.2: Complete engine cycle analysis for cruise and lift-off for the A320-HACK. Temperatures are given in K and pressures in *bar*. Mass flows are in *kg/s*, velocities in *m/s*, and thrust in *kN*. Power is in *MW*

Lift-off						**Cruise**					
$T_{0,0}$	292	$p_{0,3}$	45.59	$p_{0,7}$	1.48	$T_{0,0}$	243	$p_{0,3}$	14.77	$p_{0,7}$	0.70
$p_{0,0}$	1.06	OPR	43.10	T_8	635	$p_{0,0}$	0.308	OPR	48.12	T_8	647
$T_{0,2}$	292	$T_{0,4}$	1,571	p_8	1.01	$T_{0,2}$	243	$T_{0,4}$	1547	p_8	0.38
$p_{0,2}$	1.06	$p_{0,4}$	43.54	v_8	379.89	$p_{0,2}$	0.307	$p_{0,4}$	14.10	v_8	498
$T_{0,21}$	319	$\dot{m}_{fuel}$	0.377	T_{18}	291	$T_{0,21}$	268	$\dot{m}_{fuel}$	0.163	T_{18}	223
$p_{0,21}$	1.43	ϕ_{PZ}	0.35	p_{18}	1.01	$p_{0,21}$	0.42	ϕ_{PZ}	0.39	p_{18}	0.22
$T_{0,25}$	375	$T_{0,45}$	1,140	v_{18}	237.20	$T_{0,25}$	350	$T_{0,45}$	1184	v_{18}	299
$p_{0,25}$	2.43	$p_{0,45}$	11.51	T_{core}	9.18	$p_{0,25}$	0.997	$p_{0,45}$	4.61	T_{core}	5.28
$T_{0,16}$	319	$T_{0,5}$	698	T_{fan}	73.09	$T_{0,16}$	268	$T_{0,5}$	756	T_{fan}	15.70
$p_{0,16}$	1.42	$p_{0,5}$	1.48	T_{total}	82.27	$p_{0,16}$	0.42	$p_{0,5}$	0.71	T_{total}	20.98
$T_{0,3}$	874	$T_{0,7}$	698			$T_{0,3}$	771	$T_{0,7}$	756		
W_{fan}	14.02	W_{LPC}	1.73	W_{HPC}	15.31	W_{fan}	4.93	W_{LPC}	0.99	W_{HPC}	5.01
W_{HPT}	15.39	W_{LPT}	15.82			W_{HPT}	5.03	W_{LPT}	5.94		

Table A.3: Engine cycle analysis for list-off and cruise for the A320-HACK. Velocities are in $[m/s]$, temperatures are given in K and pressures in *bar*. Altitude is in m, mass flows are in *kg/s*, and thrust, F_N, in *kN*. TSFC is given in $g/kN/s$

Idle						**Taxi out**					
v_0	3.40	h	0			v_0	12.93	h	0		
$T_{0,3}$	863.21	$p_{0,3}$	43.68	$\dot{m}_{air}$	48.51	$T_{0,3}$	863.44	$p_{0,3}$	43.72	$\dot{m}_{air}$	186.97
$\dot{m}_{fuel}$	0.017	$\dot{m}_{H_2}$	0.017	$\dot{m}_{ker}$	0	$\dot{m}_{fuel}$	0.067	$\dot{m}_{H_2}$	0.067	$\dot{m}_{ker}$	0
T_{PZ}	1,685	$T_{0,4}$	1,473	$p_{0,4}$	41.71	T_{PZ}	1,685	$T_{0,4}$	1,473	$p_{0,4}$	41.75

F_N	9.97	$F_{N,fan}$	9.92	$F_{N,core}$	0.05	F_N	36.73	$F_{N,fan}$	36.64	$F_{N,core}$	0.09
$TSFC$	1.74	ϕ_{PZ}	0.277	$\phi_{overall}$	0.202	$TSFC$	1.82	ϕ_{PZ}	0.277	$\phi_{overall}$	0.202

Table A.4: Engine cycle analysis for list-off and cruise for the A320-HACK. Temperatures are given in K and pressures in *bar*. Altitude is in m, mass flows are in kg/s, and thrust, F_N, in kN. TSFC is given in $g/kN/s$

Climb						**Approach**					
M_0	0.496	h	5,800			M_0	0.469	h	5,800		
$T_{0,3}$	812.32	$p_{0,3}$	26.38	$\dot{m}_{air}$	289.32	$T_{0,3}$	807.598	$p_{0,3}$	25.93	$\dot{m}_{air}$	300.257
$\dot{m}_{fuel}$	0.539	$\dot{m}_{H_2}$	0.169	$\dot{m}_{ker}$	0.37	$\dot{m}_{fuel}$	0.221	$\dot{m}_{H_2}$	0.069	$\dot{m}_{ker}$	0.152
T_{PZ}	3,140	$T_{0,4}$	2,548	$p_{0,4}$	25.19	T_{PZ}	1,749	$T_{0,4}$	1,505	$p_{0,4}$	24.76
F_N	46.93	$F_{N,fan}$	27.86	$F_{N,core}$	19.07	F_N	36.29	$F_{N,fan}$	29.86	$F_{N,core}$	6.42
$TSFC$	11.48	ϕ_{PZ}	0.887	$\phi_{overall}$	0.647	$TSFC$	6.09	ϕ_{PZ}	0.35	$\phi_{overall}$	0.256

Table A.5: Engine cycle analysis for taxi in right after landing for the A320-HACK. Temperatures are given in K and pressures in *bar*. Altitude is in m, mass flows are in kg/s, and thrust, F_N, in kN. TSFC is given in $g/kN/s$

Taxi in					
M_0	0.15	h	0		
$T_{0,3}$	867.07	$p_{0,3}$	44.36	$\dot{m}_{air}$	488.56
$\dot{m}_{fuel}$	0.175	$\dot{m}_{H_2}$	0.175	$\dot{m}_{ker}$	0
T_{PZ}	1,690	$T_{0,4}$	1,477	$p_{0,4}$	42.36
F_N	81.00	$F_{N,fan}$	80.81	$F_{N,core}$	0.19
$TSFC$	2.16	ϕ_{PZ}	0.277	$\phi_{overall}$	0.202

Table A.6: Percentage different for A320-HACK with respect to A320neo when running A320-HACK on kerosene only

Phase	**Relative Difference**				
	Mass TSFC	Energy TSFC	Thermal efficiency	Propulsive efficiency	Total efficiency
Kerosene Only					
Taxi-out	-18.54%	-18.54%	3.01%	0.002%	0.46%
Lift-off	-19.57%	-19.57%	3.31%	0.0002%	1.78%
Cruise	-12.67%	-12.67%	2.35%	0.008%	2.45%
Hydrogen Only					
Taxi-out	-70.84%	-18.63%	3.04%	0.002%	0.46%
Take-off	-71.19%	-19.59%	3.43%	-0.0002%	1.77%
Cruise	-68.70%	-12.65%	2.38%	0.007%	2.45%

B | Fuel cell membrane calculations

This chapter will give more information about the equations used in Chapter 11 and how they were derived. This section is structured as follows: first, some general parameters are calculated. Then, the equations need to compute ohmic overpotential are stated.

Table B.1: Known physical properties of PEMFC [59]

Physical properties	Symbol	Values	Unit
Thermodynamic voltage	E_{thermo}	1	$[V]$
Operating current density	j	0.5	$[A/cm^2]$
Temperature[1]	T	363	[K]
Hydrogen mole fraction	x_{H_2}	0.9	[-]
Oxygen mole fraction	x_{O_2}	0.19	[-]
Cathode water mole fraction	x_{H_2O}	0.1	[-]
Cathode pressure[1]	p^C	1	$[atm]$
Anode pressure[1]	p^A	1	$[atm]$
Transfer coefficient	α	0.5	[-]
Exchange current density	j_0	0.0001	$[A/cm^2]$
Electrolyte thickness[1]	t^M	183	$[\mu m]$
Anode thickness	t^A	350	$[\mu m]$
Cathode thickness	t^C	350	$[\mu m]$
Dry density of Nafion 117	ρ_{dry}	0.0021	$[kg/cm^3]$
Nafion equivalent weight	M_m	1	$[kg/mol]$
Electro-osmothic drag coefficient saturated Nafion	n_{drag}^{SAT}	2.5	[-]
Gas constant	R	8.314	$[J/molK]$
Faraday constant	F	96,485	$[C/mol]$

B.1 General Parameters

This section will calculate some general parameters needed to find the operating voltage of a fuel cell using the given parameters in Table B.1.

The vapour pressure, when fully saturated, can be found by using Equation B.1 [59], where p_{SAT} is in bar and T in K (see Table B.1). Thus, the vapour pressure equals 0.691 atm.

$$p_{SAT} = 10^{-2.1794+0.02953(T-273)-9.1837\cdot10^{-5}(T-273)^2+1.4454\cdot10^{-7}(T-273)^3} \tag{B.1}$$

The water vapor activity (a_w) in the Nafion 117 is given by Equation B.2 [59], where x_{H_2O} is given in Table B.1 and $x_{H_2O,SAT}$ can be found using Equation B.3 [59].

$$a_w = \frac{p_{H_2O_w}}{p_{SAT}} = \frac{x_{H_2O} \cdot p_{total}}{x_{H_2O,SAT} \cdot p_{total}} \tag{B.2}$$

$$x_{H_2O,SAT} = \frac{p_{SAT}}{p_{operating}} \tag{B.3}$$

The water content (λ) in the Nafion 117 membrane is given by the following two equations [59]:

$$\lambda = 14a_w \text{ for } 0 < a_w \leq 1 \tag{B.4}$$

$$\lambda = 10 + 4a_w \text{ for } 1 < a_w \leq 3 \tag{B.5}$$

[1] Adapted to A320-HACK

The water vapor activity (a_w) was previously calculated using Equation B.2 and equals 0.439. This means that $\lambda = 14 \cdot 0.4396 = 6.154$. The water diffusivity (D_λ) in the Nafion 117 membrane can be calculated using Equation B.6 [59].

$$D_\lambda = e^{2416\left(\frac{1}{303}-\frac{1}{T}\right)} \cdot (2.562 - 0.33\lambda + 0.0264\lambda^2 - 0.000671\lambda^3) \cdot 10^{-6} \text{ for } \lambda > 4 \ (cm^2/s) \tag{B.6}$$

The binary gas diffusion coefficient can be found by using Equation B.7 [59].

$$p \cdot D_{ij} = a \left(\frac{T}{\sqrt{T_{ci}T_{cj}}}\right)^b (p_{ci}pcj)^{1/3}(T_{ci}T_{cj})^{5/12}\left(\frac{1}{M_i}+\frac{1}{M_j}\right)^{1/2} \tag{B.7}$$

where p is the total pressure (1 atm), T the temperature (363 K), M_i, M_j are the molecular weights (g/mol) of species i and j, $T_{ci}, T_{cj}, p_{ci}, p_{cj}$ are the critical temperatures and pressures of the species. All values can be found in Table B.2. For pairs of non-polar gases, $a = 2.745 \cdot 10^{-4}$ and $b = 1.823$. Pairs involving H_2O (polar) and a non-polar gas, one can use $a = 3.640 \cdot 10^{-4}$ and $b = 2.334$.

Table B.2: Critical properties of polar and non-polar gases [59]

Substance	Molecular weight (g/mol)	T_c (K)	p_c (atm)
H_2	2.016	33.3	12.80
Air	28.964	132.4	37.0
O_2	31.999	154.4	49.7
N_2	28.013	126.2	33.5
H_2O	18.015	647.3	217.5

Table B.3: D_{ij} results

	Value $[cm^2/s]$
D_{H_2,H_2O}	2.011
D_{O_2,H_2O}	0.396
D_{O_2,N_2}	0.295

The effective diffusivity (D_{ij}^{eff}) can be expressed as $D_{ij}^{eff} = \epsilon^{1.5} D_{ij}$ [59], where ϵ is the porosity, usually 0.4. Figure B.1 shows the layout of a PEMFC. One can distinguish three parts, namely the anode, electrolyte and cathode. Section "a" and "b" are used for the anode calculations. Similarly, "c" and "d" are for the cathode side.

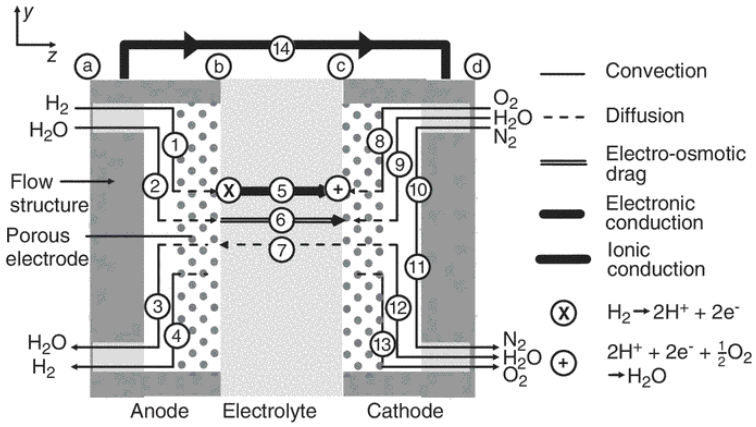

Figure B.1: Breakdown of a PEMFC membrane [59]

To account for H_2 and H_2O in the PEMFC anode, Equation B.8 and B.9 can be used [59]. Note that $J^A_{H_2O}$ is unknown.

$$J^A_{H_2} = \frac{-p^A D^{eff}_{H_2,H_2O}}{RT}\frac{dx_{H_2}}{dz} \tag{B.8}$$

$$J^A_{H_2O} = \frac{-p^A D^{eff}_{H_2,H_2O}}{RT}\frac{dx_{H_2O}}{dz} \tag{B.9}$$

Using the flux balance at the anode side for H_2 and H_2O, Equation B.10 and B.11 have the following solutions [59]. Please note that α^* has an asterisk. This is done to prevent confusion with known transfer coefficient (α).

$$x_{H_2}(z) = x_{H_2}\big|_a - z\frac{jRT}{2Fp^A D^{eff}_{H_2,H_2O}} \tag{B.10}$$

$$x_{H_2O}(z) = x_{H_2O}\big|_a - z\frac{\alpha^* jRT}{2Fp^A D^{eff}_{H_2,H_2O}} \tag{B.11}$$

The H_2 and H_2O concentrations at the anode-membrane interface are calculated by using Equation B.12 and B.13 [59]. The "a" and "b" stand for anode the anode-interface. Namely "a" is at the beginning and "b" is at the end of the anode as can be seen in Figure B.1.

$$x_{H_2}\big|_b = x_{H_2}\big|_a - t^A \frac{jRT}{2Fp^A D^{eff}_{H_2,H_2O}} \quad \text{(B.12)} \qquad x_{H_2O}\big|_b = x_{H_2O}\big|_a - t^A \frac{\alpha^* jRT}{2Fp^A D^{eff}_{H_2,H_2O}} \quad \text{(B.13)}$$

Similarly, one can find the O_2 and H_2O concentrations at the cathode-membrane interface "c" (see Figure B.1) using Equation B.14 and B.15 [59].

$$x_{O_2}\big|_c = x_{O_2}\big|_d - t^C \frac{jRT}{2Fp^C D^{eff}_{O_2,H_2O}} \quad \text{(B.14)} \qquad x_{H_2O}\big|_c = x_{H_2O}\big|_d - t^C \frac{(1+\alpha^*)jRT}{2Fp^C D^{eff}_{O_2,H_2O}} \quad \text{(B.15)}$$

B.2 Ohmic Overpotential Calculations

Before one can find the ohmic overpotential, one needs to calculate the water profile in the membrane, the membrane resistance and the unknown α^*. The water flux in membrane can be calculated using: Equation B.16.

$$J^M_{H_2O} = 2n^{SAT}_{drag}\frac{j}{2F}\frac{\lambda}{22} - \frac{\rho_{dry}}{M_m} D_\lambda \frac{d\lambda}{dz} \quad \text{(B.16)}$$

The water content (λ) is stated in Equation B.17 [59].

$$\lambda(z) = \frac{11\alpha^*}{n^{SAT}_{drag}} + C\exp\left(\frac{j\cdot M_m \cdot n^{SAT}_{drag}}{22F\rho_{dry}D_\lambda} z\right) = 4.4\alpha^* + C\exp\left(\frac{0.000561\cdot j\cdot z}{D_\lambda}\right) \quad \text{(B.17)}$$

Using Equation B.17 one can find the water content (λ) at the anode- and cathode-membrane interface, "b" and "c" respectively [59].

$$\lambda|_b = \lambda(0) = 4.4\alpha^* + C \quad \text{(B.18)} \qquad \lambda|_c = \lambda(t^M) = 4.4\alpha^* + C\exp\left(\frac{0.000561\cdot j\cdot z}{D_\lambda}\right) \quad \text{(B.19)}$$

Since $a_w\big|_b = \frac{p^A x_{H_2O}\big|_b}{p_{SAT}}$, combining Equation B.13 and B.4 gives Equation B.20 [59]

$$\lambda|_b = 14a_w\big|_b = 14\frac{p^A}{p_{SAT}}\left(x_{H_2O}\big|_a - t^A\frac{\alpha^* jRT}{2Fp^A D^{eff}_{H_2,H_2O}}\right) \quad \text{(B.20)}$$

Similarly, one can compute the cathode side using Equation B.21

$$\lambda|_c = 10 + 4a_w\big|_c = 10 + 4\frac{p^C}{p_{SAT}}\left(x_{H_2O}\big|_d + t^C\frac{(1+\alpha^*)jRT}{2Fp^C D^{eff}_{O_2,H_2O}}\right) \quad \text{(B.21)}$$

Now, when setting Equation B.18 equal to Equation B.20 and Equation B.19 equal to B.21, one can find $\alpha^* = 0.483$ and $C = 3.793$.
The conductivity of the Nafion 117 membrane is determined by Equation B.22 [59].

$$\sigma(z) = \left\{0.005193\left[4.4\alpha + C\exp\left(\frac{0.000561j}{D_\lambda}\cdot z\right)\right]\right\}\cdot\exp\left(1268\left[\frac{1}{303} - \frac{1}{T}\right]\right) \quad \text{(B.22)}$$

Total area-specific resistance of membrane is equal to Equation B.23 [59]. Finally, the ohmic overvoltage can be found by using Equation B.24 [59].

$$ASR_m = \int_0^{t_m}\frac{dz}{\sigma(z)} \quad \text{(B.23)} \qquad \eta_{ohmic} = j\cdot ASR_m \quad \text{(B.24)}$$

C Detailed Organisational Diagrams

- 1 Conduct Market Analysis
  - 1.1 Evaluate Customers
  - 1.2 Evaluate Market Share
  - 1.3 Evaluate Market Trends
  - 1.4 Evaluate Design Competitiveness
- 2 Design Aircraft
  - 2.1 Derive Requirements
    - 2.1.1 Create RDT
    - 2.1.2 Validate Requirements
  - 2.2 Perform Risk Asessment
    - 2.2.1 Assess Technical Risk
    - 2.2.2 Create Contingency Plan
  - 2.3 Construct Budget Breakdown
    - 2.3.1 Construct Cost Breakdown
    - 2.3.2 Construct Engineering Budget Breakdown
  - 2.4 Identify Design Options
    - 2.4.1 Create DOT
    - 2.4.2 Create Subsystem DOT
  - 2.5 Perform Trade-off
    - 2.5.1 Establish Trade-Off Criteria
    - 2.5.2 Establish Trade-Off Weights
  - 2.6 Perform Subsystem Design
    - 2.6.1 Design Propulsion Subsystem
    - 2.6.2 Design HLD
    - 2.6.3 Design Landing Gears
    - 2.6.4 Design Control Surfaces
  - 2.7 Verify and Validate
    - 2.7.1 Verify Code
    - 2.7.2 Verify Requirements
    - 2.7.3 Validate Code
  - 2.8 Assess Design Compliance
    - 2.8.1 Check Compliance with CS25
  - 2.9 Construct CAD Models
  - 2.10 Create Technical Drawings
- 4 Manufacture Aircraft
  - 4.1 Procure Materials
    - 4.1.1 Procure Recycled Materials
    - 4.1.2 Procure Metal Alloys
    - 4.1.3 Procure Composites
  - 4.2 Create List of Inventory
  - 4.3 Select Required Equipment
  - 4.4 Set-up Production Lines
    - 4.4.1 Produce Parts in Batches
    - 4.4.2 Carry Sub Assembly
  - 4.5 Facilitate Assembly
    - 4.5.1 Transport Sub-assembly to Assembly Points
    - 4.5.2 Set-up Stations Along Production Line
    - 4.5.3 Perform Final Assembly
  - 4.6 Perform Tests
    - 4.6.1 Perform Statics Structural Tests
    - 4.6.2 Perform Flight Tests
    - 4.6.3 Perform NDT
- 6 Deliver Aircraft to Customer
  - 6.1 Schedule Ferry Flight
  - 6.2 Perform Ground Inspection
  - 6.3 Perform In-flight Subsystems Check
  - 6.4 Fix Any Faults
  - 6.5 Issue Airworthiness Certificate
  - 6.6 Transfer of Title Deeds
- 8 Retire Aircraft
  - 8.1 Disassemble Aircraft
    - 8.1.1 Evaluate Value of Parts
    - 8.1.2 Document Parts' Materials
    - 8.1.3 Remove Valuable Parts
    - 8.1.4 Desmantle Remaining Parts
  - 8.2 Reuse Aircraft Parts
    - 8.2.1 Identify non-resuable Parts
    - 8.2.2 Repair Parts
      - 8.2.2.1 Check State Valuable Parts
      - 8.2.2.2 Check State Non-valuable Parts
      - 8.2.2.3 Repair Valuable Parts
      - 8.2.2.4 Repair Non-valuable Parts
    - 8.2.3 Sell Parts
      - 8.2.3.1 Sell Valuable Parts to Customers
      - 8.2.3.2 Sell Non-valuable Parts to other markets
  - 8.3 Recycle Aircraft
    - 8.3.1 Identify Recyclable Parts
    - 8.3.2 Recycle Parts
  - 8.4 Dispose of Remaining Waste
    - 8.4.1 Identify Hazardous Materials
    - 8.4.2 Decontaminate Hazardous Waste
    - 8.4.3 Identify Suitable Disposal Options

- **Perform Mission**
  - **1** Conduct Market Analysis
  - **2** Design Aircraft
  - **3** Certify Design
  - **4** Manufacture Aircraft
  - **5** Perform Compliance Demonstration
  - **6** Deliver Aircraft to Customer
  - **7** Operate Aircraft
  - **8** Retire Aircraft

- **7** Operate Aircraft
  - **7.1** Ensure Pre-flight Operations
    - **7.1.1** Establish communication with Departure/Ground control
    - **7.1.2** Perform Pre-flight Inspection
      - **7.1.2.1** Check Airframe
      - **7.1.2.2** Check Blades
      - **7.1.2.3** Check Instruments
    - **7.1.3** Load Cargo
      - **7.1.3.1** Fill in the Weight Balanace Form
      - **7.1.3.2** Ensure Stability Margin is not exceeded
      - **7.1.3.3** Secure Cargo Itself
    - **7.1.4** Load Cabin Payload
      - **7.1.4.1** Load Passengers and Cabin Luggage
      - **7.1.3.2** Load Catering Trolleys
      - **7.1.4.3** Ensure Stability Margin is not exceeded
    - **7.1.5** Refuel kerosene
      - **7.1.5.1** Locate Tanks
      - **7.1.5.2** Access Tanks
      - **7.1.5.3** Ensure Compatability with the Airports Refueling System
      - **7.1.5.4** Record Kerosene Mass
    - **7.1.6** Refuel H2
      - **7.1.6.1** Locate Tanks
      - **7.1.6.2** Access Tanks
      - **7.1.6.3** Ensure Compatability with the Airports Refueling System
      - **7.1.6.4** Record Kerosene Mass
    - **7.1.7** De-icing
  - **7.2** Ensure In-flight Operations
    - **7.2.1** Establish Tower Communication
    - **7.2.2** Main engine switch on
      - **7.2.2.1** Adapt H2/ kerosene ratio
    - **7.2.3** Taxi
      - **7.2.3.1** Provide onboard safety instructions
      - **7.2.3.2** Adapt H2/ kerosene ratio
    - **7.2.4** Take-off
      - **7.2.4.1** Ensure take-off within take-off distance
      - **7.2.4.2** Activate HLDs
      - **7.2.4.3** Deliver maximum engine power
      - **7.2.4.4** Accelerate to V1
      - **7.2.4.5** Ensure load factor is comfortable for the passengers
      - **7.2.4.6** Adapt H2/ kerosene ratio
      - **7.2.4.7** Turn on climate control
        - **7.2.4.7.1** Provide Oxygen supply
        - **7.2.4.7.2** Pressurise cabin
    - **7.2.5** Climb
      - **7.2.5.1** Retract the Landing gear
      - **7.2.5.2** Deliver maximum engine power
      - **7.2.5.3** Maintain climb angle
      - **7.2.5.4** Maintain climb rate
      - **7.2.5.5** Ensure load factor is comfortable for the passengers
      - **7.2.5.6** Adapt H2/ kerosene ratio
      - **7.2.5.7** Maintain climate control
    - **7.2.6** Cruise
      - **7.2.6.1** Ensure longitudinal static stability
      - **7.2.6.2** Ensure lateral static stability
      - **7.2.6.3** Ensure directional stability
      - **7.2.6.4** Ensure load factor is comfortable for the passengers
      - **7.2.6.5** Adapt H2/ kerosene ratio
      - **7.2.4.7** Maintain climate control
    - **7.2.7** Descend
      - **7.2.7.1** Activate HLDs
      - **7.2.7.2** Deploy Landing gear
      - **7.2.7.3** Set Descent Angle
      - **7.2.7.4** Maintain Descent Rate
      - **7.2.7.5** Ensure load factor is comfortable for the passengers
      - **7.2.7.6** Adapt H2/Kerosene Ratio
      - **7.2.7.7** Maintain climate control
    - **7.2.8** Land
      - **7.2.8.1** Reduce Descent Rate
      - **7.2.8.2** Activate Speed Brakers
      - **7.2.8.3** Land First on Main Wheels
      - **7.2.6.4** Ensure load factor is comfortable for the passengers
      - **7.2.8.5** Ensure Airframe Resistance
      - **7.2.8.6** Adapt H2/Kerosene Ratio
      - **7.2.8.7** Maintain climate control
    - **7.2.9** Switch Main Engine OFF
  - **7.3** Ensure Post-flight Operations
    - **7.3.1** Unload Cargo
      - **7.3.1.1** Ensure Stability Margin is not exceeded
    - **7.3.2** Unload Cabin Payload
      - **7.3.2.1** Ensure Stability Margin is not exceeded
    - **7.3.3** Post-flight inspection
      - **7.3.3.1** Check for Potencial Damage
  - **7.4** Ensure Maintenance
    - **7.4.1** Store Flight History Data
    - **7.4.2** Schedule Maintenance
      - **7.4.2.1** Identify Parts which Need Maintenance
    - **7.4.3** Perform Maintenance
    - **7.4.4** Update Maintenance Logs
  - **7.5** Withstand Critical Scenarios
    - **7.5.1** Perform Emergency Landing
    - **7.5.2** Perform Flight with One Inoperative Engine

LVL 1 | LVL 2 | LVL 3 | LVL 4 | LVL 5

1 Conduct Market Analysis → 2 Design Aircraft → 3 Certify Design → 4 Manufacture Aircraft → 5 Perform Compliance Demonstration → 6 Deliver Aircraft to Customer → 7 Operate Aircraft → 8 Retire Aircraft

REF 1 Conduct Market Analysis → 1.1 Evaluate Customers → 1.2 Evaluate Market Share → 1.3 Evaluate Market Trends → 1.4 Evaluate Design Competitiveness → REF 2 Design Aircraft

REF 2 Design Aircraft → 2.1 Derive Requirements → 2.2 Perform Risk Assessment → 2.3 Construct Budget Breakdown → 2.4 Identify Design Options → 2.5 Perform Trade-off → 2.6 Perform Subsystem Design → 2.7 Verify and Validate → 2.8 Assess Design Compliance → 2.9 Construct CAD Models → 2.10 Create Technical Drawings → REF 3 Certify Design

REF 4 Manufacture Aircraft → 4.1 Procure Materials → 4.2 Create List of Inventory → 4.3 Select Required Equipment → 4.4 Set-up Production Lines → 4.5 Facilitate Assembly → 4.6 Perform Tests → REF 5 Perform Compliance Demonstration

REF 4.1 Procure Materials → 4.1.1 Procure Recycled Materials → 4.1.2 Procure Metal Alloys → 4.1.3 Procure Composites → REF 4.2 Create List of Inventory → 4.3 Select Required Equipment → 4.4 Set-up Production Lines

REF 4.4 Set-up Production Lines → 4.4.1 Produce Parts in Batches → 4.4.2 Carry Sub Assembly → REF 4.5 Facilitate Assembly → 4.5.1 Transport Sub-assembly to Assembly Points → 4.5.2 Set-up Stations Along Production Line → 4.5.3 Perform Final Assembly → REF 4.6 Perform Tests → 4.6.1 Perform Statics Structural Tests → 4.6.2 Perform Flight Tests → 4.6.3 Perform NDT → REF 5 Perform Compliance Demonstration

REF 6 Deliver Aircraft to Customer → 6.1 Schedule Ferry Flight → 6.2 Perform Ground Inspection → 6.3 Perform In-flight Subsystems Check → 6.4 Fix Any Faults → 6.5 Issue Airworthiness Certificate → 6.6 Transfer of Title Deeds → REF 7 Operate Aircraft

REF 8 Retire Aircraft → 8.1 Disassemble Aircraft → 8.2 Reuse Aircraft Parts → 8.3 Recycle Aircraft → 8.4 Dispose of Remaining Waste

REF 8.1 Disassemble Aircraft → 8.1.1 Evaluate Value of Parts → 8.1.2 Document Parts' Materials → 8.1.3 Remove Valuable Parts → 8.1.4 Desmantle Remaining Parts → REF 8.2 Reuse Aircraft Parts

REF 8.2 Reuse Aircraft Parts → 8.2.1 Identify non-resuable Parts → OR → REF 8.3 Recycle Aircraft / 8.2.2 Repair Parts → 8.2.3 Sell Parts

REF 8.2.2 Repair Parts → AND → 8.2.2.1 Check State Valuable Parts / 8.2.2.2 Check State Non-valuable Parts → OR → REF 8.2.3 Sell Parts / 8.2.2.3 Repair Valuable Parts → 8.2.2.4 Repair Non-valuable Parts

REF 8.2.3 Sell Parts → 8.2.3.1 Sell Valuable Parts to Customers → 8.2.3.2 Sell Non-valuable Parts to other markets

REF 8.3 Recycle Aircraft → 8.3.1 Identify Recyclable Parts → OR → REF 8.4 Dispose of Remaining Waste / 8.3.2 Recycle Parts

REF 8.4 Dispose of Remaining Waste → 8.4.1 Identify Hazardous Materials → 8.4.2 Decontaminate Hazardous Waste → 8.4.3 Identify Suitable Disposal Options

LVL 1 LVL 2 LVL 3 LVL 4

REF

7 Operate Aircraft → **7.1** Ensure Pre-flight Operations → **7.2** Ensure In-flight Operations → **7.3** Ensure Post-flight Operations → **7.4** Ensure Maintenance → **7.5** Withstand Critical Scenarios → REF **8** Retire Aircraft

REF

7.1 Ensure Pre-flight Operations → **7.1.1** Establish Communication with Ground Control → **7.1.2** Perform Pre-flight Inspection → AND → (**7.1.3** Load Cargo; **7.1.4** Load Cabin Payload) → **7.1.5** Refuel kerosene → **7.1.6** Refuel H2 → **7.1.7** De-icing → REF **7.2** Ensure In-flight Operations

REF

7.2 Ensure In-flight Operations → **7.2.1** Establish Tower Communication → **7.2.2** Switch Main Engine ON → **7.2.3** Taxi → **7.2.4** Take-off → **7.2.5** Climb → **7.2.6** Cruise → **7.2.7** Descend → **7.2.8** Land → **7.2.9** Taxi → **7.2.10** Switch Main Engine OFF → REF **7.3** Ensure Post-flight Operations

REF

7.3 Ensure Post-flight Operations → **7.3.1** Unload Cargo → **7.3.2** Unload Cabin Payload → **7.3.3** Post-flight inspection → REF **7.4** Ensure Maintenance

REF

7.4 Ensure Maintenance → **7.4.1** Store Flight History Data → **7.4.2** Schedule Maintenance → **7.4.3** Perform Maintenance → **7.4.4** Update Maintenance Logs → REF **7.5** Withstand Critical Scenarios

REF

7.5 Withstand Critical Scenarios → **7.5.1** Perform Emergency Landing → **7.5.2** Perform Flight with One Inoperative Engine